Université de Montréal

Effet des contraintes élastiques sur la cinétique de séparation de phases dans les alliages

par
Danny Perez

Département de Physique
Faculté des arts et des sciences

Thèse présentée à la Faculté des études supérieures
en vue de l'obtention du grade de Philosophiæ Doctor (Ph.D.)
en Physique

Décembre, 2006

Université de Montréal
Faculté des études supérieures

Cette thèse intitulée:

Effet des contraintes élastiques sur la cinétique de séparation de phases dans les alliages

présentée par:

Danny Perez

a été évaluée par un jury composé des personnes suivantes:

Normand Mousseau,	président-rapporteur
Laurent J. Lewis,	directeur de recherche
Alain Rochefort,	membre du jury
Ronald Miller,	examinateur externe

Thèse acceptée le: 18 Décembre 2006

RÉSUMÉ

On ne saurait surestimer l'importance technologique des alliages dans nos sociétés modernes. En effet, ils font partie intégrante de toutes les facettes de l'activité industrielle, en passant par les transports, la construction et l'énergie, sans oublier les technologies émergentes. Cependant, tout comme les humains auxquels ils rendent de précieux services, les alliages sont sujets au vieillissement, lequel cause une dégradation de leurs performances avec le temps. Ce phénomène est dû à l'instabilité de leur microstructure, de laquelle dépendent plusieurs de leurs propriétés utiles. Le développement de stratégies menant à la stabilisation des microstructures est donc d'un intéret technologique considérable. Cette thèse est consacrée à l'étude théorique d'une classe d'alliages démontrant une stabilité accrue : les alliages multiphases élastiquement inhomogènes. Dans ce cas, la microstructure est composée d'inclusions d'une phase donnée enchassées dans une matrice d'une différente phase. Nous cherchons à comprendre les mécanismes physiques leur conférant ces propriétés enviables.

La réalisation de cet objectif demande la mise au point de modèles numériques permettant la simulation de la microstructure des alliages. À cet effet, nous proposons un modèle novateur basé sur une généralisation multi-échelle de la théorie classique de la fonctionnelle de la densité. À l'aide de ce modèle, nous procédons à une étude systématique de l'impact de l'élasticité sur le comportement des inclusions composant la microstructure de ces alliages multiphases. Ces résultats démontrent que deux avenues peuvent mener à la stabilisation : i) à travers la composante interfaciale de l'interaction élastique ou ii) à travers les interactions élastiques entre inclusions. Dans le premier cas, l'élasticité permet un couplage entre la structure globale de l'interface (liée à la forme de l'inclusion) et sa structure locale (à l'échelle atomique). Nous démontrons que ce couplage induit des oscillations du potentiel chimique des inclusions lors de leur croissance. Ces oscillations permettent initialement une évolution normale de la microstructure, mais l'arrêtent complètement après un certain temps. Dans le second cas, nous montrons que les interactions défavorisent les grosses inclusions en induisant un accroisse-

ment de leur potentiel chimique. Leur croissance est donc ralentie au profit des plus petites inclusions, menant à une diminution du taux d'évolution jusqu'à la stabilisation complète de la microstructure par le biais du mûrissement inverse.

Mots clés : alliage, microstructure, mûrissement, stabilisation, simulation numérique.

ABSTRACT

The technological importance of alloys in modern societies cannot be overstated. Indeed, they are part of all aspects of industry, from transports, building, and energy to emergent technologies. However, like the humans they serve, alloys are subject to aging, i.e., the gradual degradation of their performances as a function of time. This phenomenon is due to the inherent instability of their microstructure, of which depend numerous macro-scale properties. The development of strategies to stabilize the microstructure of alloys is thus of considerable technological interest. This thesis is concerned with a particular class of materials showing excellent stability properties, the so-called elastically inhomogeneous multiphase alloys, where the microstructure is composed of inclusions of a given phase embedded within a matrix of a different phase. Our goal is to understand the physical processes confering these important properties to this class of alloys.

The realisation of this objective relies on the development of reliable numerical models to simulate the microstructural evolution of alloys. To this end, we propose a novel approach based on a multiscale generalization of the classical time-dependent density-functional theory. Using our model, we carry out a systematic study of the impact of elasticity on the coarsening behavior of the inclusions composing the microstructure of these multiphase systems. Our results demonstrate that two pathways may lead to stabilization : i) through interfacial elasticity effects or ii) through elastic interactions between inclusions. In the first case, elasticity couples the global interface structure (the general shape of the inclusion) to its local, atomic-scale structure. We show that this coupling induces oscillations in the chemical potential of the inclusion during growth and that these oscillations are able to force a transition from a normal coarsening state at early time to a stabilized state at later time. In the second case, we show that elastic interactions induce a slowing down in the growth of the large inclusion by increasing their chemical potential relative to the smaller ones. This leads to an overal slowing down of the dynamics, until complete stabilization is achieved through inverse coarsening.

Key words : alloy, microstructure, coarsening, stabilization, numerical simulation.

TABLE DES MATIÈRES

LISTE DES FIGURES

LISTE DES NOTATIONS ET DES SYMBOLES

$\mathcal{A}_i^\alpha$:	Activité des atomes de type α au site i
CVM :	Cluster variation method (méthode variationnelle par amas)
D :	Distance entre inclusions
$\Delta E_{\text{elastic}}^{\text{A}->\text{B}}$:	Énergie élastique de substitution
$\Delta\mu$:	$\mu^B - \mu^A$
δ_l :	Amplitude du mode l
$\epsilon^{\alpha,\beta}$:	Contribution chimique de l'interaction entre des atomes de types α et β
F :	Énergie libre
FRI :	Fractional rate of increase (taux d'accroissement fractionnel)
GT :	Gibbs-Thomson
HI-LM :	Hard inclusion at low interface misfit (inclusion dure à bas désaccord d'interface)
HI-HM :	Hard inclusion at high interface misfit (inclusion dure à grand désaccord d'interface)
h_i^α :	Champs externe local affectant les atomes de type α au site i
$k^{\alpha,\beta}$:	Constante de rappel pour l'interaction entre des atomes de types α et β
LSW :	Lifshitz, Slyozov et Wagner
$M_{i,j}$:	Mobilité pour la diffusion entre les sites i et j
μ_i^α :	Potentiel chimique des atomes de type α au site i
$P(\mathbf{n},t)$:	Fonction de distribution des états au temps t
$P^{\text{loc}}(\mathbf{n},t)$:	Approximation TDDFT à la fonction de distribution des états au temps t
p_i^α :	Occupation moyenne du site i par des atomes de type α
QCM :	Quasicontinuum method (méthode du quasicontinuum)
R :	Rayon
R_{eq} :	Rayon équivalent

SI-LM : Soft inclusion at low interface misfit
(inclusion molle à bas désaccord d'interface)

SI-HM : Soft inclusion at high interface misfit
(inclusion molle à grand désaccord d'interface)

$\sigma^{\alpha,\beta}$: Paramètre de maille d'équilibre pour l'interaction entre des atomes de types α et β

T : Température

TDDFT : Time-dependent density-functional theory
(théorie de la fonctionnelle de la densité dépendante du temps)

$V_{i,j}^{\alpha,\beta}$: Énergie d'interaction entre deux atomes de type α et β situés au sites i et j, respectivement.

$w_{i,j}$: Taux de transition pour l'échange des atomes situés aux sites i et j

LISTE DES TABLEAUX

LISTE DES ANNEXES

REMERCIEMENTS

Je voudrais, dans un premier temps, remercier mon directeur de recherche, le professeur Laurent J. Lewis du département de physique de l'Université de Montréal pour sa rigueur, son support constant, sa disponibilité malgré sa lourde charge de travail et pour son efficacité, ma foi, surprenante ! Mais j'aimerais surtout le remercier pour toutes les opportunités qu'il m'a offertes tout au long de mon séjour au département, opportunités qui m'ont permis de tirer le meilleur de mes études graduées et de ressortir grandi de cette expérience.

Je tiens aussi à remercier tous mes collègues, particulièrement Patrick et Ralf, mais aussi mes (nombreux) autres collègues de bureau : Catherine, Xavier, Sébastien, Louis-Alexandre, Nassima, Alexis, les stagiaires avec qui j'ai eu l'honneur de travailler : Danahé, Elizabeth, Delphine, Laurent, et tous les autres étudiants que j'ai eu le plaisir de côtoyer au fil des ans. Merci aussi aux autres professeurs du groupe, Normand et Michel, qui, par leur présence et leur judicieux choix d'étudiants, ont su rendre l'ambiance de travail à la fois motivante et sereine.

Je me dois aussi de mentionner l'excellent travail de tous les professionnels du RQCHP qui m'ont permis de compter sur un environnement de travail informatique hors pair.

Sur une note plus personnelle, j'aimerais remercier ma famille, particulièrement ma mère et mon frère, pour m'avoir accompagné et soutenu pendant toutes ces années. Et, les derniers mais non les moindres, un gros merci à tous les pot(e)s : Carl, Daniel, Evelyne, François, Julie, Karine, Marc G., Marc L., Rebecca, Stéphane, Yannick, pour leur constant rappel des nombreux avantages qu'il y a à sortir du bureau de temps en temps !

Finalement, j'aimerais remercier le Conseil de recherche en sciences naturelles et en génie du Canada (CRSNG) et le Fonds québécois de la recherche sur la nature et les technologies (FQRNT) pour leur support financier.

INTRODUCTION

Depuis des millénaires, les métaux accompagnent l'homme dans son cheminement à travers l'histoire. Le début de cette relation se perd en fait dans la nuit des temps. En effet, on a recensé au Moyen-Orient des utilisations du cuivre remontant à environ 10 000 ans. Cette percée technologique a permis à la civilisation d'effectuer des pas de géant en rendant possible, par exemple, la mise au point d'outils efficaces et durables. Très tôt, on s'est rendu compte qu'il était possible, et même avantageux, de mélanger différents métaux pour obtenir de nouveaux matériaux aux capacités dépassant celles de leurs constituants pris individuellement. Pensons par exemple au bronze (alliage de cuivre et d'étain) dont on trouve des traces à partir du quatrième millénaire avant Jésus-Christ. Dû à sa dureté et à sa durabilité, cet alliage fit dès lors partie intégrante de tous les aspects de la vie courante : on l'utilisa dans la confection de vaisselle, de bijoux, d'armes, d'armures et d'outils en tous genres. Il revêt une telle importance qu'il a donné son nom à une des trois périodes de l'histoire préhistorique des civilisations : l'Âge du bronze. C'est à partir de cette époque que débute l'urbanisation des sociétés, forçant ainsi de nombreux changements sociaux et politiques. Plus près de nous, on ne peut passer sous silence le rôle considérable occupé par l'acier (constitué principalement de fer et de carbone) dans toutes les facettes de la vie industrielle moderne. On oublie par contre fréquemment que le travail du fer remonte à environ 6 000 ans en Égypte. La maîtrise des procédés fut très laborieuse, les alliages basés sur le fer ne se substituant à grande échelle aux alliages de cuivre que près de 3 000 ans après. Il faudra même attendre jusqu'aux années 1870 pour que l'acier devienne véritablement abordable, permettant ainsi la deuxième révolution industrielle. De nos jours, l'acier occupe un rôle central dans l'économie. À preuve, plus d'un milliard de tonnes de cet alliage sont produites chaque année.

L'acier constitue un exemple parfait pour illustrer l'infinie diversité des propriétés des matériaux obtenus par alliage. Par exemple, l'ajout de nickel rend l'acier inoxidable, alors que l'ajout de manganèse améliore sa résistance mécanique. Bien que la nature des éléments entrant dans la composition du mélange soit d'une im-

portance capitale, on ne doit pas négliger l'importance de la concentration relative des différents ingrédients. Par exemple, dans l'acier, l'ajout de chrome en faible concentration (entre 1 et 4%) améliore la dureté de l'alliage ; par contre, en quantité supérieure, il rend plutôt le matériau cassant. Il est donc possible d'obtenir toute une gamme de matériaux aux propriétés différentes en variant la nature et les proportions des différents éléments.

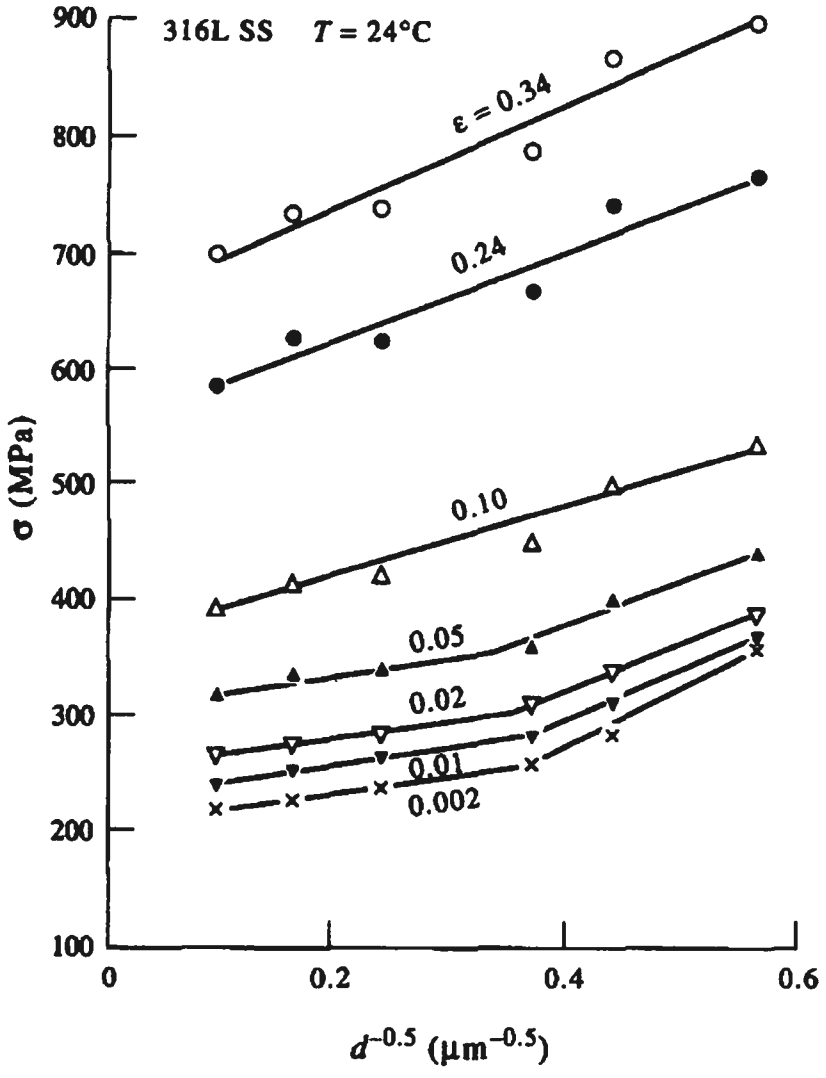

FIG. 1 – Résistance en tension (*yield strength*) d'un échantillon d'acier 316L en fonction de la taille moyenne des grains pour différents étirements ϵ. Figure tirée de la référence [36].

La composition chimique est donc un facteur déterminant en ce qui concerne les

propriétés des matériaux. Il n'est toutefois pas le seul : une place centrale doit aussi être réservée à la microstructure. Prenons encore une fois pour exemple l'acier. Lors de sa formation, un échantillon d'acier n'est habituellement pas monocristallin, mais est plutôt composé d'un ensemble de grains dont les orientations cristallines relatives diffèrent ; on dit alors que le matériau est polycristallin. Les propriétés de ces grains influencent fortement les propriétés du matériau. Par exemple, la résistance en tension (σ) varie de manière importante en fonction de la taille moyenne des grains, comme on peut le constater dans la figure 1. Dans ce cas, le comportement est décrit par la loi de Hall-Petch [27, 69] :

$$\sigma = \sigma_0 + k/\sqrt{d} \tag{1}$$

où d est la taille moyenne des grains et σ_0 et k sont des constantes liées au matériau. Cette relation illustre clairement l'importance de bien contrôler la microstructure si on désire tirer pleinement profit des capacités du matériau.

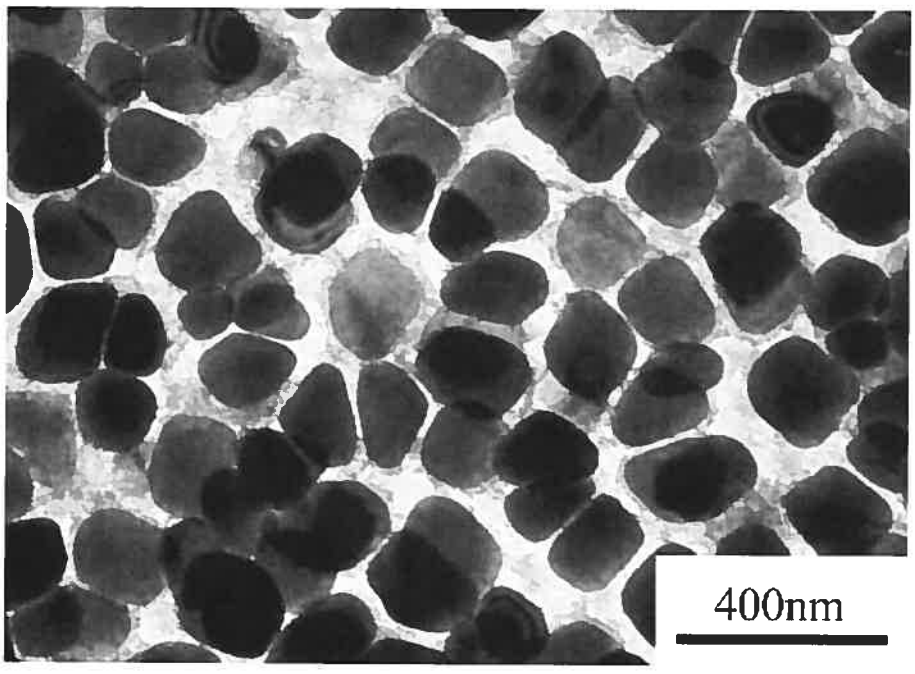

FIG. 2 – Microstructure d'un superalliage de nickel. Figure tirée du site web du département des sciences des matériaux de l'Université de Cambridge [2].

La microstucture des alliages ne se limite pas à la distribution de défauts structuraux, comme les joints de grains de l'exemple précédent. En effet, puisque les alliages sont des mélanges de plusieurs espèces atomiques, la microstructure peut aussi être caractérisée par des variations spatiales dans la concentration des différents composants. Ce phénomène est important car ces variations peuvent être stables sur de longues échelles de temps. Prenons pour exemple un café bien chaud auquel on ajoute du sucre. En faible concentration, le sucre se dissout complètement et le mélange est homogène. Cependant, si on ajoute encore du sucre de manière à ce que la limite de solubilité soit dépassée, l'excédent de sucre se déposera au fond de la tasse. Dans ce cas, on parle d'un phénomène de *séparation de phases*, les deux phases étant ici constituées du café saturé en sucre et du dépôt de sucre. Il se produit un phénomène analogue dans les alliages. Supposons que la composition initiale du système se trouve dans un régime sursaturé. Même si la distribution des différentes espèces est initialement uniforme, la séparation de phases aura éventuellement lieu, causant la formation de petites inclusions riches en éléments excédentaires ; on qualifie alors la microstructure de multiphase. Ces inclusions continueront ensuite à croître, modifiant par le fait même les concentrations chimiques locales ainsi que la structure du matériau.

Bien que ce phénomène puisse a priori sembler néfaste, puisqu'il restreint la gamme des compositions chimiques thermodynamiquement possibles, il peut être mis à profit pour optimiser certaines caractéristiques du matériau. Prenons, par exemple, le cas des superalliages de nickel. Tel qu'illustré à la figure 2, la microstructure est ici composée d'inclusions de type γ' (constituées d'une phase ordonnée de nickel et d'aluminium) enchassées dans une matrice riche en nickel. Lorsqu'on soumet ce matériau à un stress mécanique suffisamment intense, une déformation plastique s'ensuit. La résistance à un tel stress dépend de la facilité avec laquelle des dislocations se propagent dans l'échantillon. Or, comme on peut le voir à la figure 3, les inclusions sont en mesure d'ancrer efficacement les dislocations. En effet, une inclusion se trouve au centre de chacune des boucles observées sur la figure. Comme les dislocations se propagent plus difficilement à travers le milieu, la

résistance du matériau s'en trouve d'autant augmentée. Ce mécanisme est connu sous le nom de "durcissement par inclusions" (*precipitate hardening*).

Ceci n'est qu'un exemple parmi tant d'autres illustrant l'amélioration des performances des alliages par le biais de leur microstructure multiphase. Cependant, cette approche souffre d'un désavantage important : les microstructures multiphases sont habituellement instables. En effet, les inclusions se sont pas des entités fixes et isolées puisqu'elles sont couplées entre elles via la diffusion. Ceci fait en sorte que le nombre, la taille, la forme et la disposition des inclusions varient constamment. Cela implique que, même si la microstructure initiale est optimale, les performances du matériau vont graduellement se détériorer ; c'est ce qu'on appelle le vieillissement. Un exemple de ce phénomène mesuré dans un superalliage de nickel est donné à la figure 4. Les résultats montrent que la résistance du matériau varie fortement en fonction du temps. En effet, on observe un durcissement initial suite à la formation d'inclusions. On remarque la très grande efficacité du durcissement par inclusions : en choisissant correctement la température de mûrissement, il est possible d'accroître la résistance de près d'un facteur trois ! Par contre, cette augmentation est suivie d'un ramollissement graduel. Ici, ce dernier est causé par la perte de cohérence de l'interface entre la matrice et les inclusions (i.e., lorsque le champs de déplacement devient discontinu à l'interface) suite à la croissance de ces dernières, ce qui vient diminuer l'efficacité de l'ancrage des dislocations [59].

Le vieillissement est en fait une des principales limitations inhérentes à l'utilisation de microstructures multiphases pour l'optimisation des performances des matériaux. Pour contourner cet obstacle, il faut soit trouver des systèmes où la microstructure d'équilibre correspond à la microstructure optimale, soit développer des stratégies pour stabiliser le plus possible la microstructure dans l'état désiré. Or, depuis plusieurs années, on a remarqué que certains alliages dits élastiquement inhomogènes — où les paramètres de maille et les constantes élastiques de chacune des phases diffèrent — possèdent une cinétique de séparation de phases très particulière. En effet, on a observé un ralentissement, et même un arrêt complet, du mûrissement chez un grand nombre de membres de cette famille. De plus, on

peut contrôler les propriétés morphologiques de leur microstructure en ajustant leur composition. Ces alliages offrent donc une avenue très prometteuse pour acquérir un contrôle accru sur la microstructure et ainsi améliorer les capacités des matériaux.

Malheureusement, la compréhension des causes physiques menant à la stabilisation de la microstructure multiphase des alliages élastiquement inhomogènes reste partielle. En effet, bien que l'on comprenne que, de manière générale, la stabilisation est le résultat d'une compétition entre la diminution de l'énergie d'interface du système et la diminution de son énergie élastique, les mécanismes précis menant à la stabilisation restent inconnus. L'étude théorique de ce problème est l'objet de la présente thèse.

Ce travail est articulé comme suit : la théorie classique décrivant la séparation de phases et l'évolution des microstuctures multiphases est présentée au chapitre 1. À l'aide de résultats expérimentaux, le chapitre suivant met ensuite en évidence le fait que la théorie classique n'est pas en mesure de décrire correctement le comportement des alliages élastiquement inhomogènes. Une fois identifiées les divergences entre la théorie et l'expérience, nous précisons plus clairement les objectifs de notre étude au chapitre 3. Le corps de la thèse débute véritablement au chapitre 4, où nous proposons un modèle numérique novateur permettant l'étude de l'évolution microstructurale. Ce chapitre contient aussi un étude de l'effet général de l'élasticité sur le comportement d'inclusions isolées, tant au niveau morphologique que thermodynamique ou dynamique. Aux chapitres 5 et 6 nous présentons une étude détaillée de l'impact des effets élastiques interfaciaux sur la morphologie et la thermodynamique des inclusions avant d'en déduire les conséquences sur le mûrissement. Ce modèle de mûrissement est encore raffiné au chapitre 7 pour y inclure les effets des interactions élastiques entre inclusions. Nous procédons ensuite, au chapitre 8, à une revue des résultats obtenus dans cette étude, avant de conclure.

Étant donné la présentation du corps de la thèse sous forme d'articles, de nombreux détails plus techniques concernant l'implémentation du modèle numérique ont dû être omis. Conséquemment, ces détails sont plutôt présentés en annexes. On y propose aussi quelques pistes pour permettre l'amélioration du modèle utilisé au

cours de la présente étude.

FIG. 3 – Structure des dislocations dans un superalliage de nickel de type C263 après un essai de fluage à 160 MPa durant 60 heures à une température de 1073 K obtenue par microscopie électronique à transmission. Figure tirée du site web du département des sciences des matériaux de l'Université de Cambridge [1].

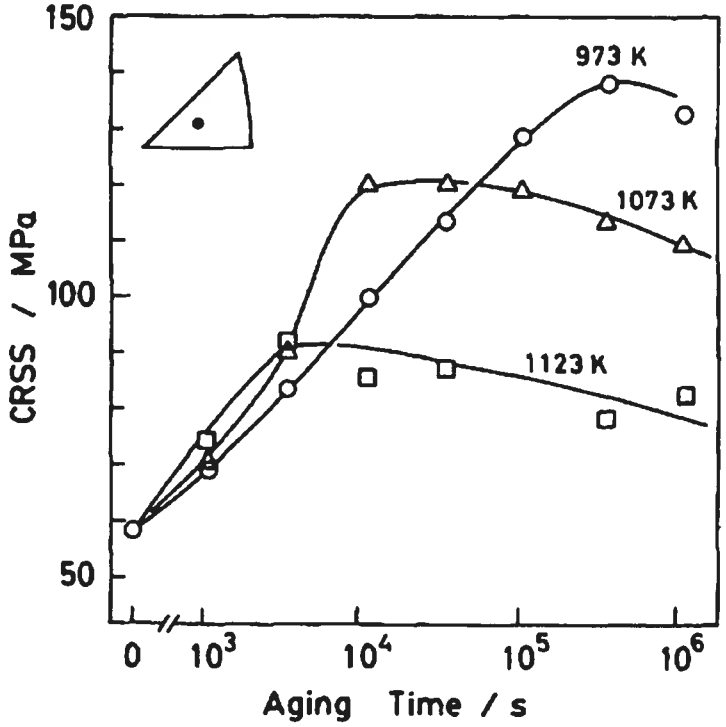

FIG. 4 – Évolution du stress critique de cisaillement en fonction du temps de vieillissement pour un superalliage de nickel Ni-18Al-4Ti (% atomique). Figure tirée de la référence [59].

CHAPITRE 1

LA MICROSTRUCTURE DES ALLIAGES MULTIPHASES : THÉORIE CLASSIQUE DE LA SÉPARATION DE PHASES

L'étude de la séparation de phases dans les alliages en présence d'effets élastiques importants est d'une formidable complexité, étant donné le fort couplage entre la diffusion, la thermodynamique et l'élasticité. Cette complexité est telle qu'aucune théorie analytique n'est disponible pour décrire l'évolution microstructurale dans ce type de systèmes. Les travaux sur le sujet sont donc essentiellement basés sur la modélisation numérique. Par contre, une théorie de la séparation de phases en l'absence d'effets élastiques est disponible depuis plus de 40 ans. Le programme de recherche dans le domaine consiste donc à identifier et à comprendre les écarts par rapport au comportement classique lorsque les effets élastiques entrent en jeu. Il est par conséquent approprié de débuter notre étude en présentant brièvement la théorie générale des phénomènes de séparation de phases. Ceci est l'objet du présent chapitre. Ce dernier comporte trois sections : premièrement, on décrira certains aspects de la thermodynamique des mélanges dans le but de déterminer dans quelles conditions la séparation de phases est possible ; les deux volets suivants s'attardent au parcours suivi par la microstructure entre l'état initial homogène et l'état final stable où la séparation de phases est totale, en débutant par la nucléation de la microstructure et en se tournant ensuite vers son mûrissement. Ce chapitre ne se veut pas une revue exhaustive des différents aspects de la séparation de phases, mais plutôt un bref survol des concepts les plus importants qui seront utiles pour bien situer les résultats principaux de la thèse.

1.1 Thermodynamique de la séparation de phases

Débutons par la thermodynamique des mélanges binaires. L'objectif ici est d'isoler les causes premières de la séparation de phases. À cet effet, considérons un mélange contenant n_A moles d'atomes de type A et n_B moles d'atomes de type B à une température T et à une pression P. L'énergie libre de Gibbs de ce mélange

est :

$$G = G(T, P, n_A, n_B) = n_A\mu_A + n_B\mu_B; \tag{1.1}$$

ou encore, en termes d'énergie par mole,

$$g = G/(n_A + n_B) = c_A\mu_A + c_B\mu_B, \tag{1.2}$$

où les concentrations molaires des différents constituants sont telles que $c_A + c_B = 1$ (dans ce qui suit, on se servira de cette relation pour éliminer c_B de toutes les équations). On a alors, pour les potentiels chimiques μ_A et μ_B :

$$\mu_A = \left(\frac{\partial G}{\partial n_A}\right)_{P,T,n_B} = g + (1 - c_A)\left(\frac{\partial g}{\partial c_A}\right)_{P,T} \tag{1.3}$$

et

$$\mu_B = \left(\frac{\partial G}{\partial n_B}\right)_{P,T,n_A} = g - c_A\left(\frac{\partial g}{\partial c_A}\right)_{P,T}. \tag{1.4}$$

1.1.1 Conditions d'équilibre entre deux phases

Supposons maintenant qu'une séparation de phases soit thermodynamiquement permise dans ce système. Dans ce cas, il faut que deux phases différentes puissent coexister à l'équilibre à la pression et à la température imposées. Dans le cas qui nous occupe, les deux phases correspondent à des régions de différentes concentrations des deux espèces, mais de manière générale il peut s'agir de différents états de la matière (liquide, solide, gaz). Posons l'existence d'une phase α à la concentration $c_A^\alpha = c_\alpha$ (et donc contenant une concentration $c_B^\alpha = 1 - c_\alpha$ en éléments de type B) et d'une phase β à la concentration $c_A^\beta = c_\beta$. Posons aussi que $c_\alpha > c_\beta$ de manière à ce que la phase α soit riche en atomes de type A et que la phase β soit riche en atomes de type B. La coexistence de ces deux phases implique que les potentiels chimiques des différents types d'atomes soient égaux dans les deux phases (par contre, μ_A et μ_B n'ont pas à être égaux entre eux). Donc, d'après les équations 1.3 et 1.4 et puisque $\mu_A^\alpha = \mu_A^\beta$, on doit avoir

$$g^\alpha + (1 - c_\alpha)\left(\frac{\partial g}{\partial c_A}\right)^\alpha_{P,T} = g^\beta + (1 - c_\beta)\left(\frac{\partial g}{\partial c_A}\right)^\beta_{P,T}; \tag{1.5}$$

de même, puisque $\mu_B^\alpha = \mu_B^\beta$,

$$g^\alpha - c_\alpha \left(\frac{\partial g}{\partial c_A}\right)^\alpha_{P,T} = g^\beta - c_\beta \left(\frac{\partial g}{\partial c_A}\right)^\beta_{P,T}. \tag{1.6}$$

Ces deux dernières équations impliquent que

$$\left(\frac{\partial g}{\partial c_A}\right)^\alpha_{P,T} = \left(\frac{\partial g}{\partial c_A}\right)^\beta_{P,T} \tag{1.7}$$

et que

$$(c_\alpha - c_\beta)\left(\frac{\partial g}{\partial c_A}\right)^\alpha_{P,T} = g^\alpha - g^\beta. \tag{1.8}$$

Ces équations représentent les conditions de stabilité des deux phases en contact. Les deux points d'équilibre partagent donc une même tangente sur la courbe de g en fonction de c_A. Pour que ceci soit possible, il faut nécessairement que $\left(\frac{\partial^2 g}{\partial c_A^2}\right)_{P,T}$ passe par zéro en deux points entre c_α et c_β. Remarquons par la même occasion que la concentration moyenne c_A du système doit nécessairement se trouver entre c_α et c_β pour que la séparation en deux phases stables soit possible. On appelle *point critique* le point (T, P, c_A) tel que c_α et c_β coïncident. Ce point sépare donc les régimes de températures et de pressions pour lesquels la coexistence de phases est possible de ceux où elle est interdite.

1.1.2 Conditions de stabilité

Nous avons déterminé les conditions nécessaires pour qu'une coexistence de deux phases soit possible et nous savons même comment calculer leurs concentrations respectives. Il reste maintenant à déterminer dans quelles conditions il sera thermodynamiquement favorable au système d'entamer une telle séparation de phases plutôt que de se maintenir dans un état de mélange homogène. On a mentionné plus haut que, pour que l'équilibre thermodynamique soit atteint à une température et à une pression données, le potentiel chimique de chacune des espèces doit être uniforme dans tout l'échantillon. Pour qu'il soit possible d'atteindre l'équilibre, il faut donc que la diffusion des différentes espèces s'effectue afin d'annuler tout gradient de leur potentiel chimique. On a $J_A \propto -\frac{\partial \mu_A}{\partial r}$, avec J_A le courant

de diffusion des atomes de type A et r une variable de position. On peut réécrire ce courant comme étant :

$$J_A \propto -\frac{\partial \mu_A}{\partial c_A}\frac{\partial c_A}{\partial r}. \tag{1.9}$$

Pour que le courant de diffusion annule tout gradient de concentration $\partial c_A/\partial r$ pour ainsi mener à une distribution uniforme d'atomes de type A à travers l'échantillon, il faut donc que

$$\frac{\partial \mu_A}{\partial c_A} > 0. \tag{1.10}$$

À partir des équations 1.3 et 1.4, on peut montrer que cette condition est équivalente à

$$\left(\frac{\partial^2 g}{\partial c_A^2}\right)_{P,T} > 0. \tag{1.11}$$

Ces équations expriment les conditions de stabilité chimique du mélange homogène. En effet, leur violation implique que les courants de diffusion *amplifient* tout gradient de concentration, même induit par de très faibles fluctuations, menant nécessairement à une séparation entre les phases identifiées plus haut. Remarquons que cette séparation de phases serait ici spontanée. On parle dans ce cas de *décomposition spinodale.*

Un calcul plus rigoureux de cette condition de stabilité peut être effectué en obtenant la variation de l'entropie d'un mélange homogène à l'équilibre en présence de fluctuations et en exigeant que cette variation soit négative (c.f. Reichl [73] pour le détail de cette procédure).

1.1.3 Forme de l'énergie libre

À la lumière de ce qui a été discuté plus haut, il est possible d'identifier la forme générique que doit posséder la courbe $g(c_A)_{P,T}$ pour qu'une séparation de phases se produise. D'après les conditions d'équilibre, il faut que $\left(\frac{\partial^2 g}{\partial c_A^2}\right)_{P,T}$ change de signe deux fois entre c_α et c_β. De plus, on a montré que la séparation de phases n'est possible que pour des concentrations $c_\beta < c_A < c_\alpha$. Les domaines $0 < c_A < c_\beta$ et $c_\alpha < c_A < 1$ sont donc stables face à la séparation de phases et sont, par conséquent, convexes par rapport à c_A. Ces deux conditions impliquent nécessairement que la fonction $g(c_A)_{P,T}$ soit concave dans un intervalle contenu entre c_α et c_β. La fonction

$g(c_A)_{P,T}$ doit donc être d'une forme semblable à celle illustrée à la figure 1.1.

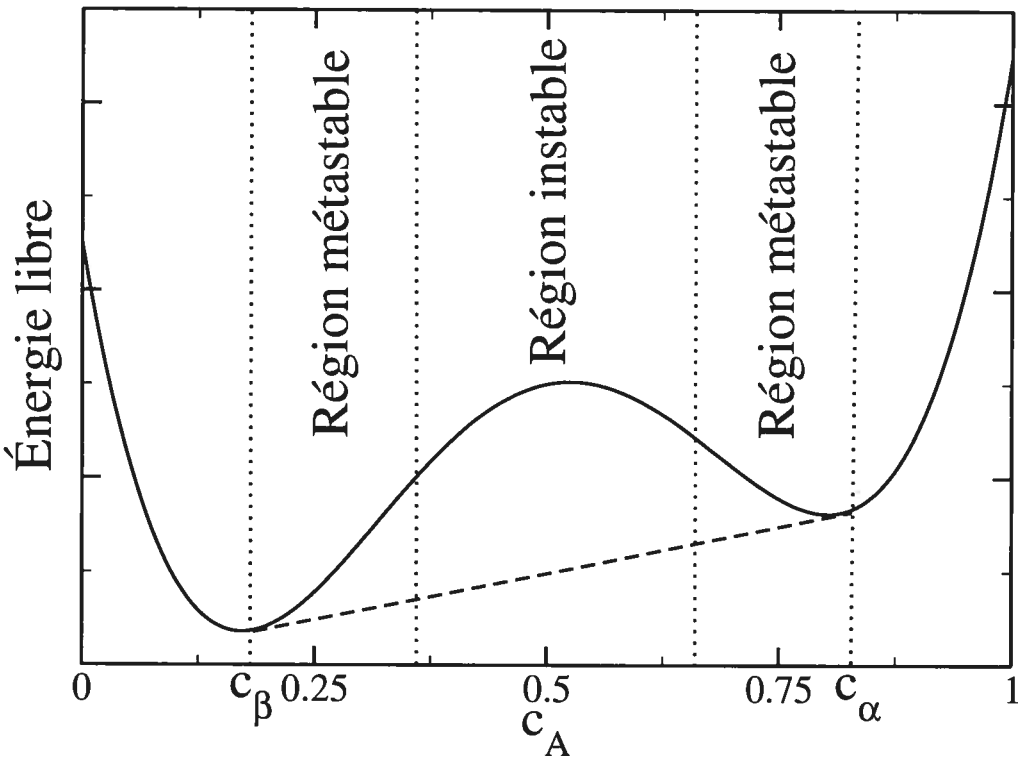

FIG. 1.1 – Représentation schématique de l'énergie libre en fonction de la concentration pour une pression et une température où la séparation de phases est possible.

1.1.4 Condition de métastabilité

En étudiant la figure 1.1, on remarque que la région d'instabilité ne couvre pas toute la région où la séparation de phases serait théoriquement possible. Pour que cette éventualité se réalise dans la région stable restante entre c_α et c_β il faut que l'énergie libre de l'état séparé soit inférieure à celle de l'état homogène. On peut montrer que c'est bien le cas en réécrivant l'énergie libre de l'état séparé sous la forme

$$g = C_\alpha g^\alpha + C_\beta g^\beta, \tag{1.12}$$

où C_α et C_β sont les concentrations des différentes phases telles que $c_A = C_\alpha c_\alpha + C_\beta c_\beta$. Or, ces deux concentrations sont reliées entre elles car on doit avoir $C_\alpha + C_\beta = 1$. L'énergie libre du mélange devient donc

$$g = C_\alpha(g^\alpha - g^\beta) + g^\beta. \tag{1.13}$$

Cette relation est représentée par la ligne hachurée sur la figure 1.1. La forme concave de l'énergie libre dans la région instable fait donc en sorte que l'énergie libre du système séparé soit effectivement plus faible que celle du système homogène. La séparation de phases est donc thermodynamiquement favorable dans tout l'intervalle compris entre c_α et c_β, bien que le mélange homogène soit stable sur une partie de cet intervalle, appellée *région métastable*. Dans cette région, l'état d'équilibre est un état hétérogène composé de deux phases en coexistence, mais la séparation de phases ne survient pas de manière spontanée étant donné la stabilité du mélange homogène. Finalement, on notera que l'équation 1.13 ne comporte aucun terme lié à la présence d'interfaces entre les deux phases. Dans la limite thermodynamique, ce terme est négligeable car proportionnel à l'aire de l'interface entre des phases macroscopiques, alors que les termes en g sont proportionnels à leur volume. Cet argument n'est par contre valide qu'à l'équilibre thermodynamique. Nous verrons dans les prochaines sections que les contributions interfaciales sont en fait très importantes car elles contrôlent la cinétique de l'atteinte de l'équilibre.

1.2 Théorie classique de la nucléation

Maintenant que nous avons établi les conditions thermodynamiques nécessaires à la séparation de phases et les propriétés des différentes phases stables, il reste à déterminer comment la transition entre l'état homogène et l'état thermodynamiquement stable s'effectue. Cette transition se déroule habituellement en deux temps : premièrement, une étape de nucléation où des domaines d'une nouvelle phase se forment à l'intérieur du mélange initialement homogène et, deuxièmement, une étape de mûrissement lors de laquelle le système se dirige vers l'équilibre par l'échange d'espèces entre les différents domaines. Dans la présente section, nous

nous attarderons à la première étape de la transition, telle que décrite par la théorie classique de la nucléation ; le mûrissement sera traité à la section 1.3.

Supposons un système homogène tel que la concentration c_A soit légèrement inférieure à c_α. Pour abaisser son énergie libre, le système aurait avantage à se séparer en deux phases de concentration c_α et c_β. Par contre, cette transition ne peut se faire instantanément. En effet, le transport par diffusion est nécessaire pour modifier la composition chimique locale du mélange. La conversion devrait donc plutôt se dérouler de manière locale, par la nucléation et la croissance de petits domaines. Dans le cas décrit ci-haut, la transformation devrait donc débuter par la formation de petites inclusions de phase β à l'intérieur du mélange homogène.

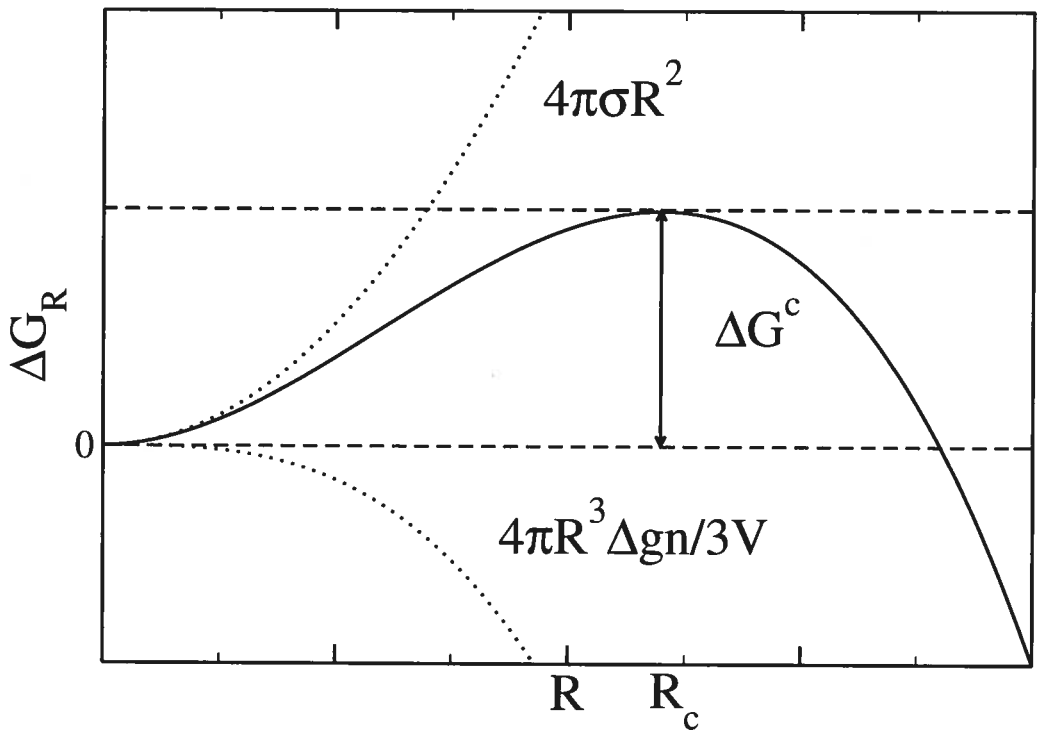

FIG. 1.2 – Représentation schématique de la barrière de nucléation en fonction de la taille d'une inclusion.

Le coût énergétique associé à la nucléation d'une telle inclusion de rayon R est :

$$\Delta G_R = \frac{4}{3}\pi R^3 \Delta g n/V + 4\pi R^2 \sigma, \tag{1.14}$$

avec Δg la différence entre l'énergie libre molaire du système séparé et celle du système homogène, σ l'énergie d'interface par unité d'aire (supposée isotrope) entre les phases α et β, V le volume total du système et $n = n_A + n_B$. Les inclusions sont supposées sphériques car, pour un volume donné, cette forme minimise l'aire de l'interface et donc l'énergie libre de formation. Par conséquent, pour des énergies d'interface anisotropes, la forme optimale n'est plus sphérique. Tel que mentionné plus tôt, cette contribution de l'énergie d'interface n'a pas été considérée dans l'équation 1.13 puisque, dans la limite thermodynamique, cet apport est négligeable devant celui dû aux phases volumiques. Elle doit cependant être prise en considération lorsque le cas d'une inclusion de petite taille est traité. Tel qu'illustré à la figure 1.2, l'équation 1.14 comporte une compétition entre deux termes : la décroissance de l'énergie libre volumique (car Δg est négatif) et l'accroissement de l'énergie d'interface lors de la nucléation. Pour de petites valeurs de R, le terme d'interface domine et le coût de la nucléation est positif. Par contre, ce coût énergétique possède un maximum pour

$$R_c = -\frac{2\sigma V}{\Delta g n}; \tag{1.15}$$

cette taille correspond au *rayon critique* auquel est associée une *barrière de nucléation*

$$\Delta G^c = \frac{16\pi\sigma^3 V}{3n\Delta g^2}. \tag{1.16}$$

Cette dernière est l'énergie que le système doit fournir pour engendrer la séparation de phases. En effet, si une inclusion de rayon $R > R_c$ se forme, il sera favorable pour elle de continuer à croître, puisque cela causera une décroissance de son énergie libre. Par contre, une inclusion plus petite que la taille critique aura plutôt tendance à passer en solution.

Étant donné qu'une barrière d'énergie libre sépare l'état homogène de l'état

comportant un noyau critique, la séparation de phases ne sera pas initiée spontanément mais seulement suite à une fluctuation thermique suffisamment intense. De telles fluctuations surviennent à un taux :

$$J = \Gamma \exp(\Delta G^c / k_B T) \tag{1.17}$$

où Γ est un préfacteur cinétique.

Puisque le nombre d'atomes de type B est conservé, la nucléation de noyaux critiques de phase β a pour effet de réduire la sursaturation dans la matrice, i.e., d'y augmenter la valeur de c_A. À mesure que cette décroissance survient, le taux de nucléation diminue car $\Delta g \to 0$ pour $c_A \to c_\alpha$ (i.e., il n'y a pas de gain d'énergie libre volumique lors de la nucléation si les deux phases sont en équilibre). Comme le taux de nucléation est exponentiellement dépendant de $1/\Delta g$, l'épisode de nucléation cesse rapidement. À ce moment, une distribution d'inclusions disposées de manière *grosso modo* aléatoire s'est formée à travers la matrice. Cependant, tant que $c_A < c_\alpha$, il est favorable pour les atomes de type B de la matrice de diffuser vers les inclusions. Donc, pendant un certain temps encore, l'ensemble des inclusions continuera à croître aux dépens de la matrice, abaissant graduellement la sursaturation ambiante.

Notons finalement que la théorie classique de la nucléation décrite ci-haut n'est valide que pour de faibles niveaux de sursaturation. En effet, tel que démontré à la section 1.1.2, pour des saturations plus importantes (lorsque c_A se trouve en région instable), la séparation de phases ne requiert pas d'épisode de nucléation activée thermiquement mais survient spontanément car la hauteur de la barrière de nucléation tend alors vers zéro (décomposition spinodale).

1.3 Mûrissement et théorie LSW

À mesure que la croissance des premières inclusions se déroule, le degré de sursaturation du milieu ambiant décroît puisque l'état du système ressemble de plus en plus à la coexistence des deux phases α et β. À partir d'un certain moment, le degré de sursaturation devient négligeable et on peut considérer que les inclusions

ont pratiquement atteint l'équilibre local avec leur milieu. Cependant, l'équation 1.14 indique que cet état n'est pas le minimum global d'énergie libre, puisqu'un état constitué d'un seul domaine de phase β en équilibre avec la phase α possèderait une énergie libre encore moindre (car, pour un volume total donné, l'aire de l'interface serait minimisée). Puisque les inclusions ne peuvent plus croître aux dépens du milieu environnant, l'atteinte de l'équilibre global doit survenir suite à un échange de masse entre les différentes inclusions. C'est le début du régime appelé *mûrissement.*

La théorie classique du mûrissement fut développée à la fin des années 50 par Lifshitz, Slyozov et Wagner (LSW) [47, 99]. L'objectif de cette théorie est de décrire l'évolution temporelle d'un ensemble d'inclusions représenté par une fonction de distribution $f(R,t)$. Cette tâche est accomplie en ayant recours à trois hypothèses principales :

1. Les inclusions sont sphériques et l'approximation de la capillarité est valide (la concentration de soluté à l'interface des inclusions est inversement proportionnelle à leur rayon).
2. La dynamique du système est essentiellement mue par la capillarité (i.e., la réduction de l'énergie d'interface).
3. La densité (ou encore la fraction volumique) d'inclusions tend vers 0.

D'un point de vue purement mathématique, l'évolution de f est décrite par une équation de continuité de la forme :

$$\frac{\partial f(R,t)}{\partial t} + \frac{\partial (f \frac{dR}{dt})}{\partial R} = J(R,t) \tag{1.18}$$

où $J(R,t)$ est le taux de nucléation d'inclusions de taille R au temps t. Dans le cadre de la théorie LSW, on suppose $J = 0$, i.e., on considère que le taux de nucléation est déjà négligeable à $t = 0$ et on s'intéresse uniquement à l'évolution des inclusions déjà présentes dans le système à ce moment.

D'un point de vue physique, on doit maintenant déterminer la forme de dR/dt, le taux de croissance d'une inclusion sphérique taille R et de phase β. Dans le cadre du modèle LSW, cette quantité est associée au taux de croissance d'une inclusion

isolée dans un milieu représentatif de l'environnement moyen des inclusions dans le système ; le modèle de LSW est donc une théorie de champ moyen. Cette association est pleinement justifiée en autant que l'hypothèse 3 soit respectée, puisque dans ce cas, les inclusions sont trop éloignées les unes des autres pour que l'environnement près de chacune d'elle soit significativement affecté par la position et la taille des autres inclusions dans le voisinage. Le taux de croissance est alors obtenu en résolvant l'équation de diffusion des atomes de type B dans l'approximation quasi-statique (encore une fois valide grâce à l'hypothèse 3) :

$$\nabla^2 c_B(r) = 0. \tag{1.19}$$

Pour ce faire, on utilise comme condition aux frontières : i) à l'interface de l'inclusion :

$$c_B(r = R) = c_\infty + \frac{\gamma}{R} \tag{1.20}$$

avec $\gamma = (2\sigma/k_B T) v c_\infty$, $c_\infty = (1 - c_\beta)$ la concentration d'équilibre d'atomes de type B autour d'une interface plane et v est le volume atomique moyen dans l'inclusion et ii), à l'infini,

$$c_B(r \to \infty) = c_m \tag{1.21}$$

où c_m est la concentration moyenne d'atomes de type B dans la matrice.

L'équation 1.20 est une forme de l'équation de Gibbs-Thomson qui relie la concentration d'équilibre autour d'une inclusion à son rayon de courbure. L'utilisation d'une telle relation est possible dans le cadre de l'hypothèse 1 du modèle. Qualitativement, cette relation implique que la concentration à l'équilibre d'atomes de type B au voisinage de l'interface d'une inclusion de rayon R est d'autant plus grande que R est petit et que, par conséquent, des courants de diffusion vont se former dans la matrice avec pour effet de transporter des atomes de type B des petites inclusions vers les plus grandes. Ceci resultera en la croissance des plus grandes inclusions et à l'évaporation des plus petites, et donc à la décroissance de l'aire totale des interfaces. Cette idée a été émise par Ostwald en 1897 [64] mais n'a été exprimée clairement sous la forme présentée ici qu'en 1961 par Lifshitz, Slyozov [47] et Wagner [99].

De manière formelle, on obtient, en solutionnant l'équation 1.19, les courants de diffusion d'atomes de type B à l'interface de l'inclusion et, par conséquent, le taux de croissance recherché :

$$\frac{dR}{dt} = \frac{D}{R}\left[c_m - \frac{\gamma}{R}\right] \tag{1.22}$$

où D est la constante de diffusion des atomes de type B à travers la matrice. Ce paramètre a pour seul effet de fixer une échelle de temps caractérisque pour la diffusion. Pour $R \to 0$ on a bien $dR/dt < 0$ et pour $R \to \infty$, $dR/dt > 0$, en accord avec l'argument donné ci-haut. Cette équation montre aussi que la dynamique du modèle de LSW est bel et bien uniquement contrôlée par la capillarité (hypothèse 2), puisque γ y est le seul paramètre libre non-trivial.

Le dernier ingrédient requis pour effectuer l'intégration de l'équation 1.18 est la valeur de c_m. Cette dernière est obtenue grâce à la conservation du nombre d'atomes de type B, i.e., la somme du nombre d'atomes B dans la matrice et de celui dans les inclusions doit être constante. Mathématiquement, cette condition prend la forme :

$$c_0 = c_m(t) + \int_0^\infty \frac{4\pi}{3} R^3 f(R,t) dR. \tag{1.23}$$

Cette dernière équation procure la relation de fermeture recherchée.

Malheureusement, la solution analytique de l'équation 1.18 est inconnue. Par contre, Lifshitz et Slyozov ont montré qu'il est possible d'obtenir une solution dans la limite asymptotique $t \to \infty$. Cette solution comporte plusieurs caractéristiques intéressantes :

1. Le rayon moyen des inclusions augmente comme $\langle R \rangle \propto t^{1/3}$. Dans un système de taille finie, la conservation du nombre d'atomes de type B implique nécessairement que le nombre d'inclusions diminuera avec le temps, jusqu'à ce qu'une seule ne subsiste et que la séparation de phases soit totale. On atteint alors l'équilibre thermodynamique.

2. La forme asymptotique de $f(R,t)$ est indépendante de $f(R,0)$. Il est donc inutile de tenter de modéliser précisément le processus de nucléation si on s'intéresse uniquement au mûrissement.

3. La fonction de distribution asymptotique est auto-similaire lorsque exprimée en fonction de $R/\langle R \rangle$. La forme de la distribution devrait donc être universelle.

Notons aussi que le modèle LSW prévoit implicitement une distribution spatiale aléatoire des inclusions puisque, en vertu de son caractère de champ moyen, ce dernier ne contient aucun mécanisme capable d'induire des corrélations.

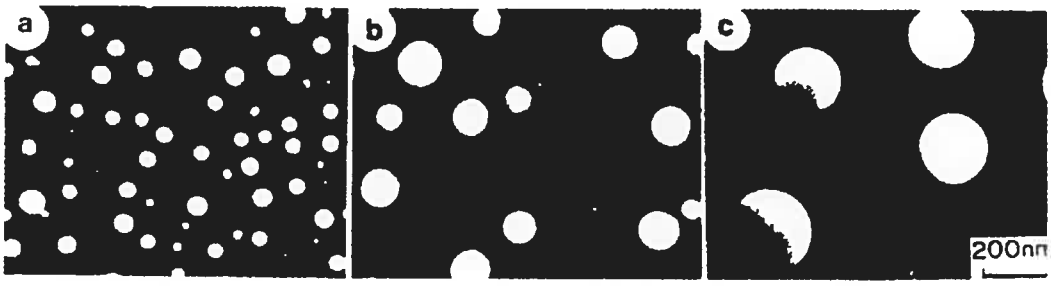

FIG. 1.3 – Développement de la microstructure d'un alliage de Ni-18.2Cr-6.2Al (% atomique) à une température de 1073K pour (a) 8.64×10^4 s, (b) 6.91×10^5 s et (c) 5.2×10^6 s. Figure tirée de la référence [54].

Le modèle LSW est le modèle "canonique" décrivant l'évolution des microstructures multiphases. Ses prédictions sont fréquemment vérifiées expérimentalement dans les alliages multiphases où l'inhomogénéité élastique est faible. Prenons par exemple le cas du Ni-Cr-Al. La figure 1.3 montre que la microstructure de ce système est conforme à ce qui est attendu : les inclusions sont sphériques et distribuées aléatoirement ; à mesure que le temps passe, le nombre d'inclusions diminue et leur taille moyenne augmente. L'analyse quantitative de la microstructure, présentée à la figure 1.4 pour du Ni-Cr-Al et du Ni-Si-Al, démontre que l'accord avec le modèle est excellent. Le volet (a) montre l'évolution de la taille moyenne des inclusions en fonction du temps sur des échelles logarithmiques. Les deux droites superposées aux données expérimentales ont une pente (correspondant à l'exposant de mûrissement) de 0,326 pour le Ni-Cr-Al et de 0.338 pour le Ni-Si-Al, en accord avec la

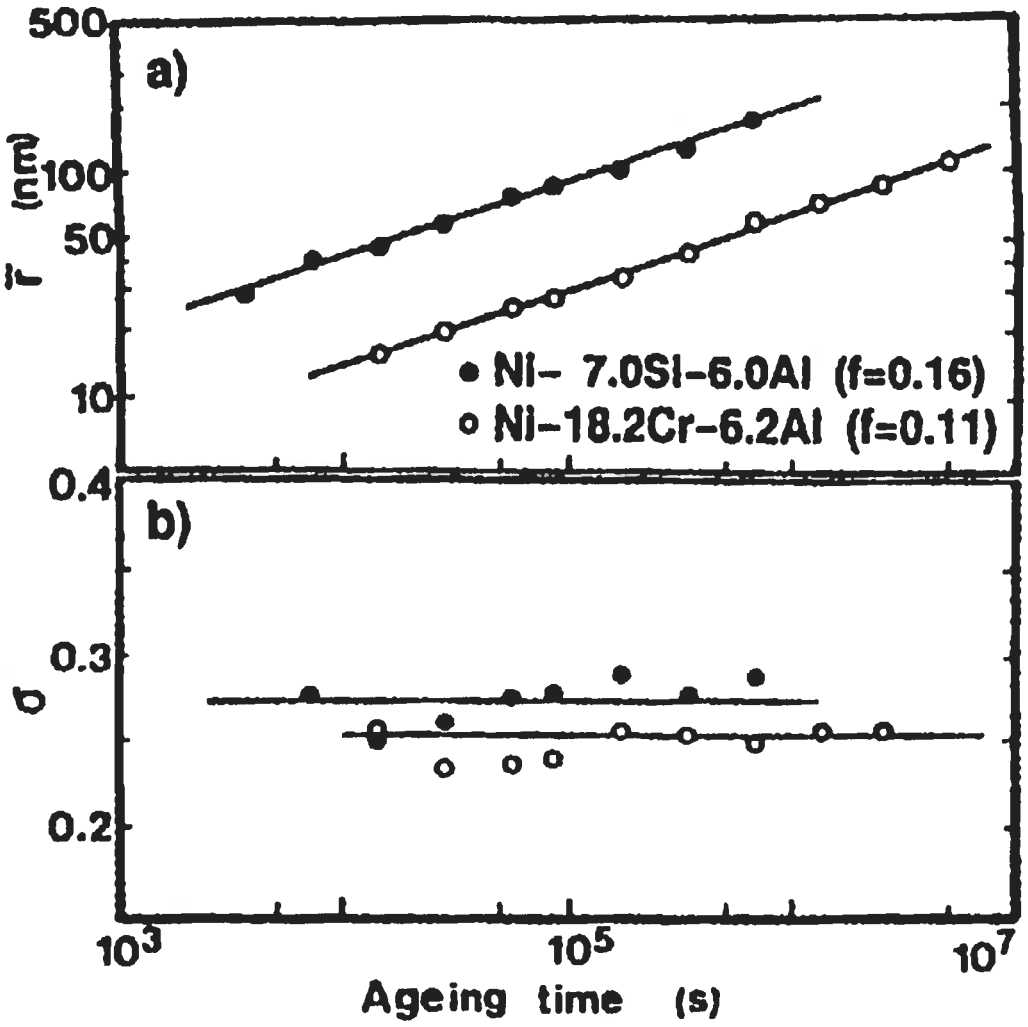

FIG. 1.4 – Évolution temporelle (a) du rayon moyen des inclusions et (b) de la largeur normalisée de la distribution de taille des inclusions pour des alliages de Ni-Si-Al et de Ni-Cr-Al. Figure tirée de la référence [54].

valeur attendue de 1/3. La volet (b) montre l'évolution de largeur de la distribution en taille des inclusions, normalisée par leur taille moyenne. Tel que prévu au point 3, cette largeur normalisée est indépendante du temps, indiquant la nature auto-similaire de la fonction de distribution. La largeur est par contre légèrement plus grande que celle prévue par la théorie LSW (0.215). Des versions raffinées du modèle LSW montrent que cette différence est attribuable à la valeur finie de la fraction volumique des inclusions (0.16 pour le Ni-Si-Al et 0.11 pour le Ni-Cr-Al).

Dans ce chapitre, nous avons résumé brièvement les principaux ingrédients de la théorie classique de la séparation de phases qui ne s'applique qu'à des systèmes

dominés par la capillarité (où la réduction de l'énergie d'interface est le seul moteur de l'évolution microstructurale). Au chapitre suivant, nous allons démontrer, en passant en revue quelques résultats expérimentaux obtenus sur des alliages élastiquement inhomogènes, que des contributions élastiques peuvent drastiquement changer la donne. Nous verrons que certains des comportements observés sont totalement inexplicables dans le cadre de la théorie classique décrite ci-haut.

CHAPITRE 2

LA MICROSTRUCTURE DES ALLIAGES MULTIPHASES ÉLASTIQUEMENT INHOMOGÈNES : OBSERVATIONS EXPÉRIMENTALES

Au chapitre précédent, nous avons exploré les prédictions du modèle classique de la séparation de phases. L'expérience montre cependant que cette théorie classique est incapable de décrire correctement l'évolution de la microstructure dans les alliages élastiquement inhomogènes, tant au niveau de la morphologie des inclusions et de la microstructure en général que de la cinétique du mûrissement. Dans le présent chapitre, nous allons décrire brièvement les principales caractéristiques "anormales" du mûrissement dans ce type d'alliages et, au besoin, relier ces dernières à des violations des hypothèses sous-tendant le modèle classique du mûrissement (cf. section 1.3). En effet, bien que l'hypothèse 2 du modèle LSW soit systématiquement violée, étant donné les contributions élastiques importantes à l'énergie libre, des violations des deux autres hypothèses contribuent probablement aussi au comportement anormal de ce type de matériaux.

2.1 Effets morphologiques

En l'absence d'effets élastiques, la forme adoptée par les inclusions ne devrait dépendre que de la variation angulaire de l'énergie d'interface et devrait donc être indépendante de leur taille. Par exemple, si on pose que l'énergie d'interface est isotrope, comme dans le cadre de la théorie classique, les inclusions devraient maintenir une forme sphérique. Cette prévision est fréquemment violée dans les alliages contraints. Prenons pour exemple les mesures de Maheshwari *et al.* sur un alliage Ni-Al [50]. Dans ce cas, le mûrissement donne lieu à la croissance d'inclusions de Ni_3Al à l'intérieur d'une matrice de Ni. Le désaccord de maille entre les deux phases est d'environ 0.5%. La figure 2.1 donne une image par microscopie électronique d'un alliage contenant 6.25% d'Al (en masse) après un mûrissement de 92.5 heures à 900 K. La forme cuboïdale des inclusions les plus grosses se distingue facilement de la

forme plutôt sphérique adoptée par les plus petites. Cette dépendance en taille de la forme des inclusions est représentée à la figure 2.2 où est tracé le facteur de forme (qui prend la valeur 1 dans le cas d'une inclusion sphérique et $\sqrt{2}/2 \simeq 0.717$ dans le cas d'une inclusion cubique) en fonction de la largeur de l'inclusion (prise comme une moyenne le long des axes [100] et [010]). La tendance à l'adoption d'une forme cubique à mesure que la taille de l'inclusion augmente y est évidente. Un tel changement de forme des inclusions est en violation de l'hypothèse 1 du modèle LSW et donc pourrait venir affecter le mûrissement en modifiant la relation entre c_R et la taille des inclusions.

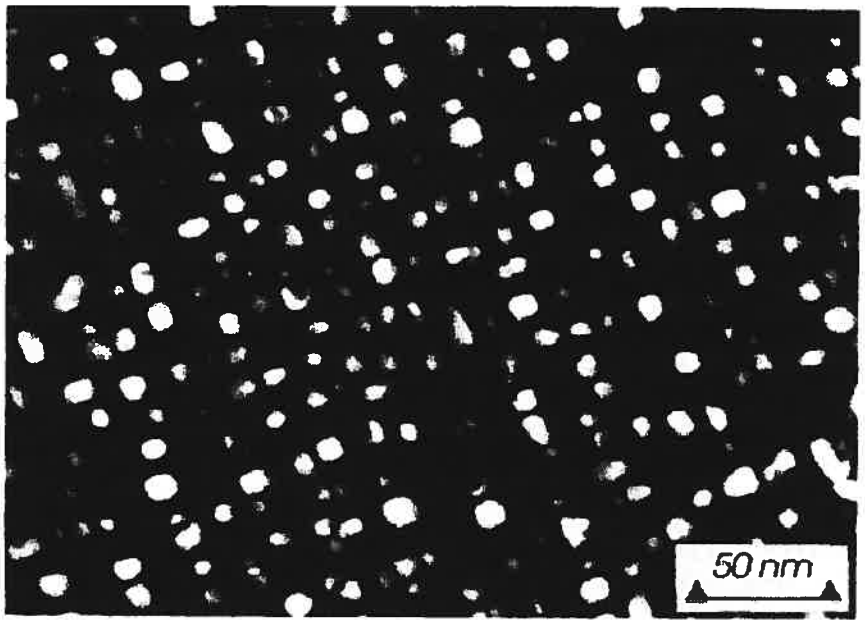

FIG. 2.1 – Image d'inclusions de Ni_3Al dans un alliage Ni-Al contenant 6.25% d'Al (en pourcentage massique) prise à l'aide d'un microscope électronique à transmission. L'alliage a subi un mûrissement de 92.5 heures à 900K. Figure tirée de la référence [50].

En plus d'affecter la morphologie individuelle des inclusions, l'élasticité est aussi en mesure de modifier considérablement la morphologie globale de la microstructure en induisant d'importantes corrélations dans la forme et la taille des inclusions. La figure 2.3 présente un exemple d'une telle microstructure dans du Ni-Al-Mo. Les

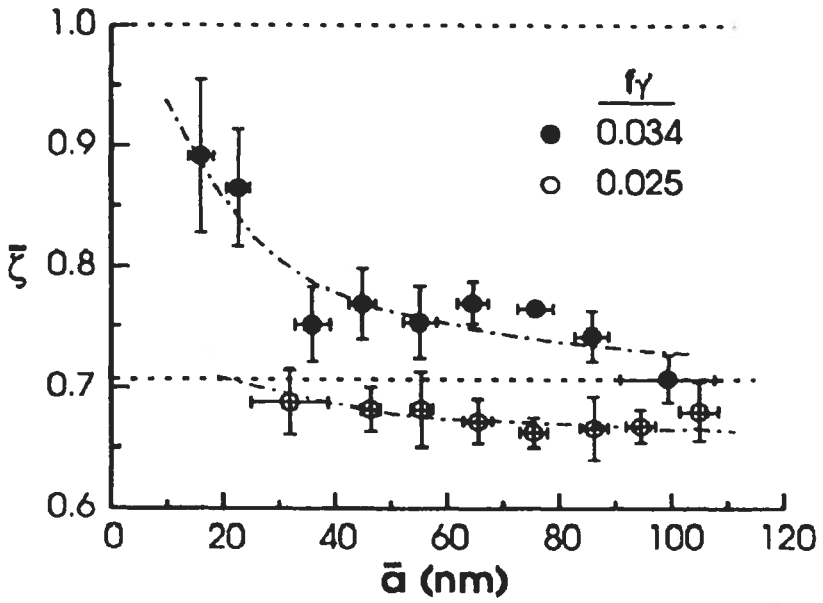

FIG. 2.2 – Variation du facteur de forme en fonction de la taille moyenne des inclusions pour deux fractions volumiques différentes (f_γ), $f_\gamma = 0.034$ correspondant à 5.78% d'Al et $f_\gamma = 0.025$ à 5.72%. Figure tirée de la référence [50].

résultats montrent que de fortes corrélations spatiales se forment à mesure que la microstructure évolue. On note une très forte tendance à l'alignement des inclusions le long de directions cristallographiques précises. De plus, on observe que les tailles d'inclusions voisines sont fortement corrélées (la hauteur d'une inclusion est souvent la même que celle de ses voisines latérales alors que sa largeur est souvent la même que celles de ses voisines du haut et du bas). Cette observation n'est pas prévue par la théorie classique du mûrissement. Ceci est probablement lié à la violation évidente des hypothèses 1 et 3 du modèle LSW (inclusions sphériques et faible fraction volumique). L'apparition de telles corrélations est aussi une indication que l'hypothèse 2 est violée, car un tel ordonnement résulte probablement de la minimisation d'une contribution élastique à l'énergie libre.

Les fortes corrélations observées ci-haut devraient se répercuter dans la distribution en taille des inclusions. Les mesures expérimentales confirment que c'est bel et bien le cas, mais que, contrairement aux autres caractéristiques morphologiques décrites jusqu'à maintenant, les effets varient fortement d'un alliage à l'autre. En

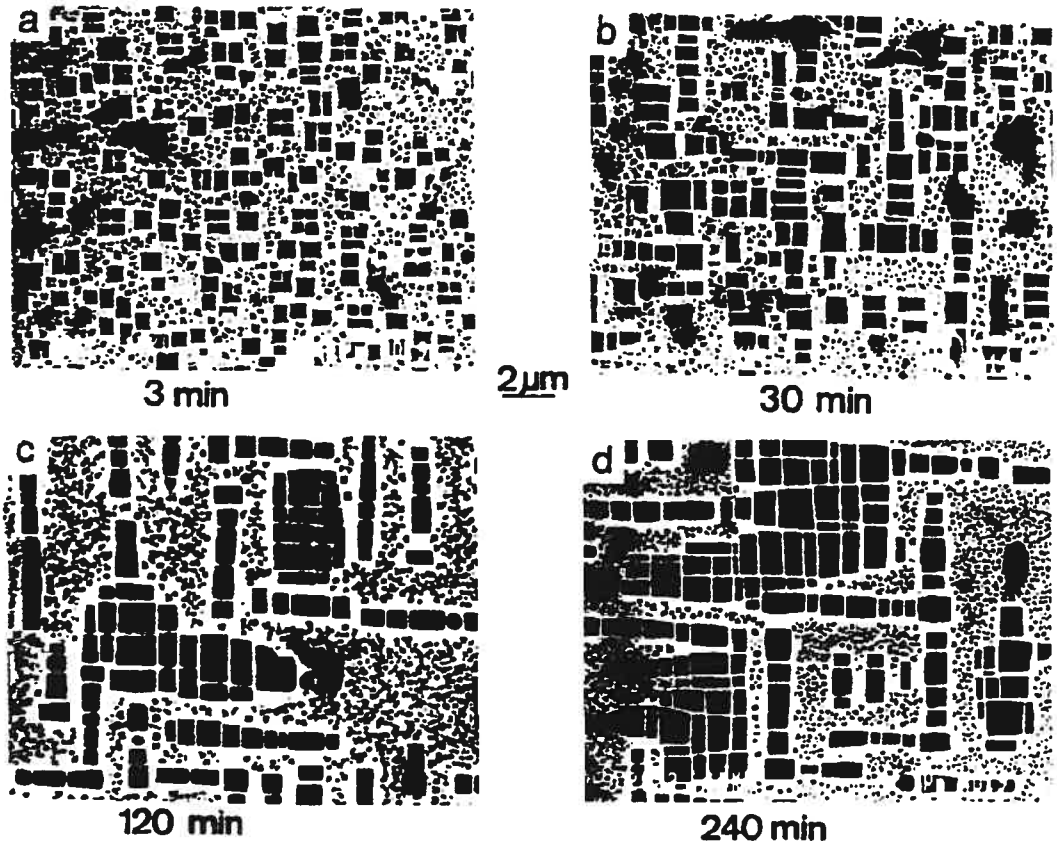

FIG. 2.3 – Évolution de la microstructure d'un alliage Ni-15Al-6Mo (% atomique) à une température de 1453 K. Figure tirée de la référence [8].

effet, tel qu'illustré à la figure 2.4, on observe autant une augmentation qu'une diminution de la largeur de la distribution par rapport à la distribution standard du modèle LSW.

2.2 Effets sur la cinétique du mûrissement

Puisque les effets élastiques influencent de manière importante la morphologie des inclusions durant la séparation de phases, on peut s'attendre à ce que les effets sur la cinétique du processus soient aussi importants. C'est en effet le cas : le mûrissement des microstructures élastiquement inhomogènes se trouve fortement ralenti comparativement à la prédiction du modèle LSW pour des temps de mûrissement assez long. Tel qu'illustré à la figure 2.5, deux types de comportements sont habituellement rapportés : soit l'exposant décrivant le mûrissement est simplement

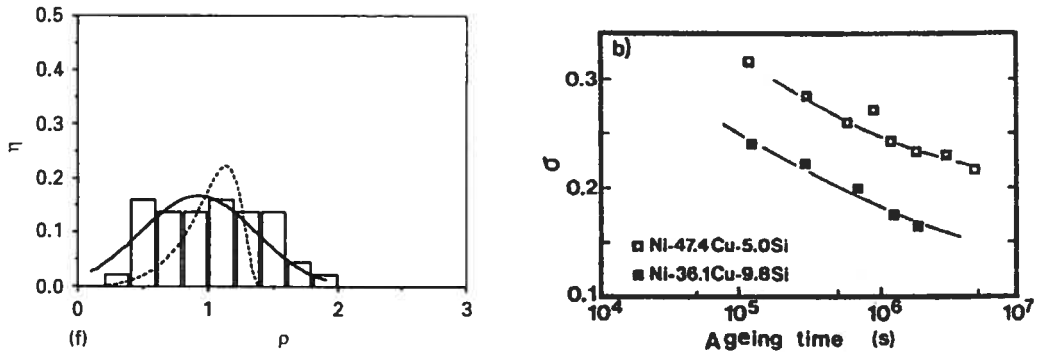

FIG. 2.4 – Effets de l'élasticité sur la distribution en taille des inclusions. Graphique de gauche : Distribution en taille des inclusions dans du IN-713C (superalliage de nickel) en fonction de leur taille normalisée après 20 073 heures de mûrissement à une température de 1223 K. Courbe pointillée : distribution LSW ; courbe continue : distribution gaussienne. Figure tirée de la référence [25]. Graphique de droite : Évolution de la largeur normalisée de la distribution en taille des inclusions dans du Ni-47.4Cu-5.0Si et du Ni-36.1Cu-9.8Si (% atomique). Figure tirée de la référence [54].

réduit — comme dans les superalliages de nickel de type ODS [77] ou celui du Ni-Al-Mo [8] — soit le mûrissement débute avec un exposant donné (parfois très près de $1/3$) mais ralentit subitement par la suite, atteignant même un arrêt complet — comme dans le Ni-Mo [54], le Ni-Cu-Si [54], le superalliage de nickel IN-713C [25], ou encore le Ti-Mo [41]. Il est possible que ces différences de comportement soient simplement dues au fait que les échelles de temps caractéristiques varient d'un système à l'autre et, qu'en conséquence, seule la période de mûrissement normal ou seule la période de stabilisation puisse être observée dans certaines expériences.

Une autre caractéristique des alliages élastiquement inhomogènes est que le comportement lors du mûrissement est fortement dépendant de la fraction volumique des inclusions. On observe, en effet, une décroissance de l'exposant de mûrissement [54, 65] et une décroissance de la taille maximale des inclusions [65] à mesure qu'augmente la fraction volumique, alors qu'en l'absence d'inhomogénéité élastique l'exposant de mûrissement n'est pas affecté. Par exemple, comme le montre le graphique de droite de la figure 2.5, la taille moyenne maximale des inclusions dans le Ni-Cu-Si passe de 16 nm pour une fraction volumique de 0.18 à 12 nm pour une

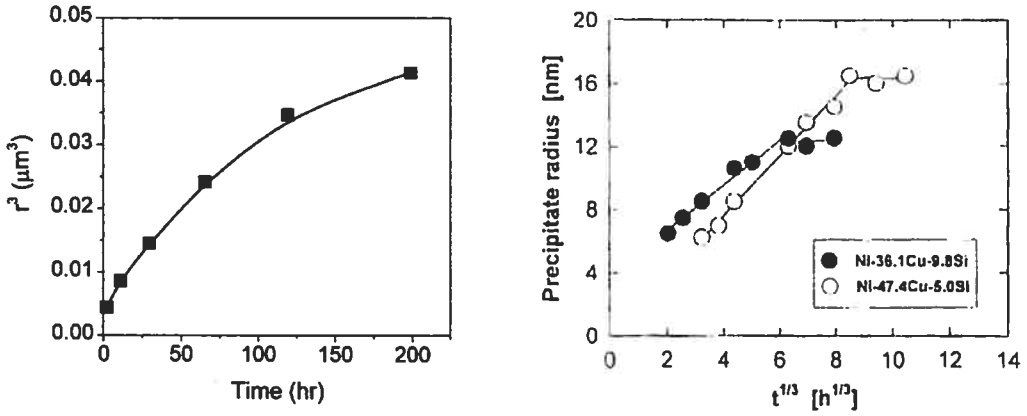

FIG. 2.5 – Effet de l'élasticité sur le mûrissement. Graphique de gauche : rayon moyen des inclusions au cube en fonction du temps pour un alliage ODS à une température de 1223 K. Figure tirée de la référence [77]. Graphique de droite : rayon moyen des inclusions en fonction de $t^{1/3}$ pour deux alliages de Ni-Cu-Si. Cercles pleins : fraction volumique de 0.5 (Ni-36.1Cu-9.8Si) ; cercles vides : fraction volumique de 0.18 (Ni-47.4Cu-5.0Si). Figure tirée de la référence [65].

fraction volumique de 0.5. Les effets d'une violation de l'hypothèse 3 du modèle LSW sont donc importants.

2.3 Intérêt technologique

Tel que mentionné en introduction, les propriétés macroscopiques des matériaux sont intimement liées à leur microstructure. Le design d'alliages passe donc autant par le choix d'une composition chimique que par la mise au point d'une méthodologie de préparation qui permet la formation de la microstructure optimale pour l'application visée. Cependant, même en supposant que cet objectif quelque peu utopique soit réalisé, l'alliage ne conservera ses propriétés idéales que durant un temps limité car, comme nous l'avons vu au chapitre 1, la microstructure est une entité dynamique qui évolue constamment. Puisque la microstructure optimale est rarement la même que la microstructure d'équilibre, les matériaux sont sensibles au vieillissement, ce qui limite leur durée de vie utile. En contrepartie, cela implique aussi que le vieillissement pourrait être éliminé dans le cas où la structure d'équilibre (ou encore, une structure métastable) correspondrait à la microstructure optimale. L'intérêt porté aux alliages multiphases élastiquement inhomogènes provient du fait qu'ils permettent une telle "ingéniérie" des microstructures et de

leurs propriétés cinétiques. En effet, comme nous l'avons montré plus haut, des microstructures stables se forment spontanément dans ces matériaux. De plus, il est possible de contrôler certaines des propriétés de ces états stables (comme la taille moyenne maximale) en variant la fraction volumique des inclusions. Dans quelques alliages, il est possible d'atteindre le même but en modifiant plutôt le désaccord de maille effectif à l'aide d'impuretés. Ces alliages permettent donc, dans une certaine mesure, de relier directement une composition chimique avec une microstructure stable, permettant ainsi une optimisation plus efficace des propriétés des matériaux. Même lorsqu'une telle association entre la structure optimale et une structure stable n'est pas possible, on peut tout de même diminuer l'impact du vieillissement en sélectionnant une composition où le mûrissement est ralenti.

Pour tirer profit de ces avantages, il faut par contre être en mesure de comprendre la nature des effets élastiques et l'origine précise de la stabilisation observée dans ces alliages. Tel qu'explicité au chapitre suivant, ceci est l'objectif général de cette thèse.

CHAPITRE 3

OBJECTIFS ET MÉTHODOLOGIE

La présente étude vise à améliorer la compréhension des effets de l'inhomogénéité élastique sur l'évolution de la microstructure des alliages multiphases et plus particulièrement celle de leur comportement anormal en ce qui concerne leur cinétique de mûrissement. On s'intéresse spécialement à l'origine de la stabilisation de la microstructure observée dans ce type d'alliage.

Cet objectif général est atteint en procédant à une analyse systématique de l'effet de la violation de chacune des prémices du modèle classique du mûrissement proposé par Lifshitz, Slyosov et Wagner, tel que présenté au chapitre 1. De manière plus précise, nous allons tenter de répondre aux questions suivantes :

1. Est-ce que l'approximation de la capillarité, et donc, la relation de Gibbs-Thomson, est toujours valide dans des systèmes élastiquement inhomogènes ? Dans la négative, quels changements doivent-ils y être apportés ?
2. Quel est l'effet sur le mûrissement d'une transition dans la forme des inclusions ?
3. Comment la stabilité des inclusions est-elle affectée par l'élasticité ? Est-ce que leurs propriétés changent lorsque leur taux de croissance devient important ?
4. Comment le mûrissement est-il affecté par les contraintes agissant à l'interface entre les inclusions et la matrice ?
5. Comment le mûrissement est-il affecté par une fraction volumique finie ? Autrement dit, quels sont les effets des interactions entre inclusions ?

Les questions 1 à 3 seront étudiées au chapitre 4, alors que la question 4 sera l'objet des chapitres 5 et 6. Finalement, le chapitre 7 sera consacré à la question 5.

Puisque nous nous intéressons aux mécanismes physiques généraux affectant l'évolution des alliages multiphases élastiquement inhomogènes, il est judicieux d'utiliser comme modèle le système le plus simple montrant les caractéristiques voulues. C'est dans cette optique que nous utilisons dans ce qui suit un alliage binaire générique composé d'atomes de types A et B dans lequel on introduit une

faible proportion de lacunes, nécessaires en tant que médiatrices de la diffusion. Les espèces A et B sont identiques au niveau chimique, mais diffèrent au niveau élastique. De plus, comme la majorité des simulations dans le domaine, nos calculs sont restreints à deux dimensions. Notre impératif de simplicité s'applique aussi aux microstructures utilisées lors des simulations : nos calculs sont restreints à des microstructures contenant un faible nombre d'inclusions. L'utilisation de différentes conditions aux frontières permet toutefois d'étudier ces systèmes simples sous toutes leurs coutures.

Une fois les systèmes modèles définis, leur évolution doit être obtenue à l'aide d'un modèle numérique fiable permettant de simuler leur évolution structurale en ayant recours à un minimum d'hypothèses simplificatrices. Par contre, comme nous le verrons au cours des chapitres suivants, les modèles numériques actuels ne permettent pas de reproduire la diversité des comportements observés expérimentalement (cf. chapitre 2). Nous nous devons donc de sortir des sentiers battus si nous voulons raisonnablement espérer améliorer la compréhension actuelle du problème. À cet effet, nous proposons au chapitre 4 un modèle numérique novateur basé sur une description microscopique de la physique du problème, obtenue à partir de la théorie classique de la fonctionnelle de la densité dépendante du temps, mais utilisant une méthode sophistiquée de résolution adaptative et multi-échelle permettant l'étude de longues échelles de temps et d'espace. Étant donné que le chapitre 4 est constitué d'un article, seuls les éléments essentiels du modèle y sont présentés ; les autres détails numériques sont plutôt décrits aux annexes I à IV. Des stratégies pour améliorer la méthode sont finalement proposées à l'annexe V.

CHAPITRE 4

MODÉLISATION MULTI-ÉCHELLE POUR L'ÉVOLUTION MICROSTRUCTURALE DES MATÉRIAUX MULTIPHASES : APPLICATION À LA CROISSANCE D'INCLUSIONS ISOLÉES EN PRÉSENCE D'ÉLASTICITÉ

Ce chapitre est principalement consacré à l'élaboration du modèle numérique sur lequel est basé l'ensemble de notre étude. Après avoir justifié la nécessité de mettre au point un nouveau modèle microstructural capable de prendre en compte les effets à l'échelle atomique tout en conservant l'efficacité des modèles continus formulés à l'échelle mésoscopique ou macroscopique, nous proposons un modèle novateur basé sur une généralisation multi-échelle de la théorie classique de la fonctionnelle de la densité dépendante du temps. À travers l'étude du comportement d'inclusions isolées, nous démontrons l'efficacité du modèle en comparant les résultats numériques avec quelques prévisions théoriques bien établies, en particulier l'effet de l'élasticité sur la forme d'équilibre des inclusions, l'effet de l'élasticité sur la relation de Gibbs-Thomson et l'effet de la croissance sur la stabilité de l'interface des inclusions. Dans ces trois cas, les résultats du modèle sont en accord avec les prévisions. Le reste du chapitre est consacré à l'étude de l'impact des effets dynamiques (instabilité de forme, piégeage de soluté) sur la relation de Gibbs-Thomson des inclusions et celui des transitions de forme sur le mûrissement. Dans les deux cas, nous observons des effets significatifs, mais incapables d'expliquer la stabilisation de la microstucture observée expérimentalement.

Ce chapitre a fait l'objet d'une publication dans la revue *Physical Review E* [Phys. Rev. E **74**, 031609 (2006)]. En tant que premier auteur de cet article, ma contribution a consisté en :

1. La création du modèle utilisé pour effectuer les calculs numériques.
2. L'implémentation des programmes informatiques nécessaires aux calculs.
3. L'exécution des calculs requis.
4. L'analyse et l'interprétation des données.

5. La rédaction de la version initiale de l'article.

6. La réalisation des modifications suggérées par le co-auteur de l'article.

Multiscale model for microstructure evolution in multiphase materials : application to the growth of isolated inclusions in presence of elasticity

Danny Perez and Laurent J. Lewis

Département de physique et Regroupement Québécois sur les Matériaux de Pointe (RQMP), Université de Montréal, C. P. 6128 Succursale Centre-Ville, Montréal (Québec) H3C 3J7, Canada

We present a novel multiscale model based on the classical lattice time-dependent density-functional theory to study microstructure evolution in multi-phase systems. As a first test of the method, we study the static and dynamic properties of isolated inclusions. Three cases are explored : elastically homogeneous systems, elastically inhomogeneous systems with soft inclusions, and elastically inhomogeneous systems with hard inclusions. The equilibrium properties of inclusions are shown to be consistent with previous results : both homogeneous and hard inclusions adopt a circular shape independent of their size, while soft inclusions are circular below a critical radius and elliptic above. In all cases, the Gibbs-Thomson relation is obeyed, except for a change in the prefactor at the critical radius in soft inclusions. Under growth conditions, homogeneous inclusions exhibit a Mullins-Sekerka shape instability [W. Mullins and R. Sekerka, J. Appl. Phys. **34**, 323 (1963)] , while in inhomogeneous systems, the growth of perturbations follows the Leo-Sekerka model [P. Leo and R. Sekerka, Acta Metall. **37**, 3139 (1989)]. For soft inclusions, the mode instability regime is gradually replaced by a tip growing mechanism which leads to stable, strongly out of equilibrium shapes even at very low supersaturation. This mechanism is shown to significantly affect the growth dynamics of soft inclusions, while dynamical corrections to the growth rates are negligible in homogeneous and hard inclusions. Finally, due to its microscopic formulation, the model is shown to automatically take into account phenomena caused by the presence of the underlying discrete lattice : anisotropy of the interfacial energy, anisotropy of the kinetics, and preferential excitation of shape perturbations commensurate with the rotational symmetry of the lattice.

4.1 Introduction

It is well known that many macroscopic properties of materials, like tensile resistance, electric conductivity, ductility, etc., are directly related to the micro-scale structure. However, the microstructure is a dynamical entity : it evolves continuously, inducing changes in the properties for which the material was initially designed. It is thus of prime importance to understand the forces driving microstructural evolution in order to tailor materials that are able to maintain their properties over long time scales. However, this task has proven formidable because, in "real-life" materials, the observed microstructure is the result of a delicate balance between many competing physical processes. For example, in the common case of two-phase materials, which is the subject of this paper, the microstructure consists of inclusions embedded within a matrix. In general, the inclusions and the matrix will have different physical properties (elastic constants, diffusion constants, lattice parameters, etc.) so that the free energy (which is minimized during microstructural evolution) will have chemical, interfacial, and elastic components. In order to study the formation and evolution of the microstructure, a description of each of these components is required.

The first step toward a complete understanding of the evolution of the microstructure is to identify the equilibrium state toward which simple systems proceed. For two-phase systems without lattice misfit, the shape of an isolated inclusion is strictly driven by interfacial energy considerations and can thus be obtained simply by using a Wolff construction. However, in presence of lattice misfits, the situation is much more complicated. Indeed, the problem of finding the free-energy-minimizing configurations is an old one (see Ref. [22] for a recent review). The basic behavior of these systems is now well established in the simplest cases. For example, in the case of inhomogeneous but isotropic elasticity and isotropic interface energy, isolated spherical hard inclusions are stable for all sizes, i.e., the equilibrium shape of the inclusions is not affected by the elastic contributions to the free energy.[33] However, if the inclusions are softer than the matrix, the spherical shape is only stable at small radius ; at large radius the symmetry is broken and the equilibrium shape becomes increasingly elliptic.[33]

While the structural behavior of isolated inclusions is now well known, much less is known about the relation between their structure and their coarsening behavior. (A notable exception is the recent work of Thornton *et al.* [46, 91] concerning homogeneous and inhomogeneous, anisotropic elasticity with isotropic surface energy). In order to make this connection, the effect of shape changes on the solute concentration, or equivalently on the chemical potential, inside and around the inclusions has to be studied. This information, taking the form of a so-called Gibbs-Thomson relation, is essential to understanding the coarsening dynamics of a system of diffusively interacting inclusions, since it dictates the rate at which a given inclusion of a particular size (and shape) grows or dissolves. However, for the knowledge of the equilibrium properties to be really useful, it must be the case that, at any given time, the microstructure is close to equilibrium. Therefore, the effect of finite growth rates on the coarsening behavior has to be assessed. The morphological consequences of finite growth rates on the inclusions have also been thoroughly investigated,[7, 45, 56, 94, 103] but the relation between shape perturbations and chemical potentials, and hence coarsening behavior, is much less understood. In order to assess the importance of dynamical effects, it is necessary to study the effect of the dynamical corrections on the Gibbs-Thomson relation.

In this paper, we study the equilibrium and dynamical properties of isolated inclusions in the case of homogeneous and inhomogeneous, isotropic elasticity under varying growth rate, and infer the consequences of dynamical corrections on the coarsening behavior of systems of inclusions. This is achieved using a novel two-dimensional, multiscale model based on the classical lattice time-dependent density-functional theory (TDDFT).[19, 74] The focus of this work is twofold : first, we validate the methodology by comparing our observations with theoretical models or numerical simulations (mainly concerning morphological aspects) ; second, we present new results for the connection between morphology and the coarsening behavior of inclusions.

Anticipating our results, we observe that the classical Gibbs-Thomson behavior is obeyed in homogeneous circular inclusions, as expected. Under imposed growth, shape instabilities develop and, for small amplitudes, their behavior is consistent

with the predictions of the Mullins-Sekerka theory.[56] The microscopic resolution of our model enables us to identify an efficient excitation process for modes with the same rotational symmetry as that of the lattice. The impact of growth on the chemical potentials of the inclusions is then characterized, and we show that dynamical corrections to the coarsening behavior are small. Hard inclusions are observed to also exhibit the Gibbs-Thomson behavior. Elasticity is shown to have a stabilizing effect against shape perturbation growth, in agreement with the theory of Leo and Sekerka.[45] In this case also, dynamical corrections to the growth dynamics are small. Finally, for soft inclusions, we observe the expected equilibrium transition between circular and elliptic shapes and quantify its effect on the chemical potentials of the inclusions. Soft inclusions are found to be extremely sensitive to growth conditions : strongly out of equilibrium shapes form and survive even at very low supersaturation. While the behavior predicted by the Leo and Sekerka model is observed at small radii, we find that a new, elastically-induced growth mechanism favoring the growth of tips dominates the evolution at larger sizes. The effect of dynamical corrections on the growth dynamics is shown to be significant in this case, because of the important morphological changes induced by finite growth rates.

The paper is organized as follows. In Section 4.2, we describe the model, its multiscale generalization and the methodology used to solve the relevant system of equations. In Section 4.3, we present the results of our calculations for homogeneous, hard and soft inclusions, respectively. In each case, we describe the equilibrium properties of isolated inclusions, then investigate how these properties are affected by finite growth rates and examine the importance of these corrections on the coarsening rate. Finally, in Section 4.4, we discuss the implication of our results for the description of the coarsening kinetics of a collection of inclusions.

4.2 Methodology

The microstructural evolution of a multiphase material in presence of elastic misfits is an intrinsically multiscale problem : on the one hand, at moderate temperatures, the inter-phase boundary is only a few atomic-layer thick so that

mechanical and chemical properties of the material may vary strongly on a nm length scale; on the other hand, the elastic strain field caused by the presence of the inclusion is very long ranged. Adding to the difficulty is the coupling between thermodynamics, diffusion and elasticity : elastic stresses can affect the local chemical potentials inside the material, thus causing diffusion fluxes that modify the elastic response of the system, and so on.

However, most models proposed so far to study two-phase systems with elastic misfits are essentially single scale — macroscopic sharp-interface models,[35, 79, 91, 98] mesoscopic diffuse interface models (also known as phase-field models),[60, 100, 107] or microscopic Monte Carlo models [21, 26, 42, 43] — and thus suffer from some drawbacks. First, sharp-interface models assume the interfaces to be infinitely thin and structure less, thus lacking internal length scales. These have to be introduced *a posteriori* if scale-dependent effects (like shape transitions as a function of size) need to be taken into account. Also, interphase boundary conditions have to be devised artificially in order to introduce proper physics into the models (e.g., solute concentration vs. interface curvature or strain relations must be specified) which, for simplicity, often rely on some local equilibrium assumption. Relevant physical parameters (diffusion constant, elastic constants, etc.) are also needed as input. Finally, the models do not easily allow for topological changes in the microstructure (merging of inclusions for example).

Diffuse interface methods, for their part, assume that all physical properties of the microstructure vary smoothly on the scale of the grid used in the calculations. However, in typical two-phase microstructures, the interfaces are a only few nm thick. This imposes strong limitations on the possible grid sizes if qualitative results are sought. Even if this requirement is somewhat relaxed, the grid size still needs to be smaller than any other length scale in the system. In presence of elastic effects, this constraint can be severe.[89] Further, these models need external input for the thermodynamic (e.g., bulk free energy vs concentration, chemical potential vs strain), elastic (e.g., elastic constants) and diffusion (e.g., temperature or concentration dependence of the diffusion rates) properties of the material, and the coupling between these properties. Despite these limitations, macro and mesosco-

pic simulations (MMS) are extremely powerful tools since they enable very large systems, composed of many inclusions, to be studied over long durations.

At the other end of the spectrum, Monte Carlo models are formulated directly on the atomic scale, the natural scale for describing interphase boundaries. Further, the thermodynamic and elastic properties are implicitly obtained from the microscopic description of the interactions between atoms. This microscopic description also allows one to specify the microscopic diffusion processes and to automatically take the composition dependence of the diffusion rates into account. However, these nice features come at a very high computational cost, so that such calculations are restricted to small systems over short time scales. Since elastic interactions are long ranged, and their effects usually predominate over interface effects only in the late stages of the coarsening process, Monte Carlo simulations are seldom used in this context. The causes of this inefficiency compared to MMS are fourfold. First, Monte Carlo moves are essentially local in nature so that a large number is required to significantly alter the microstructure, while for MMS, the update steps are global. Second, except at very low temperature, many of the moves are in fact thermal "noise"; thus, while on average they tend to relax the microstructure, on an individual basis they do not contribute significantly to the relaxation process; these thermal fluctuations are already averaged out in MMS, so that every step directly contributes to the structural evolution. Third, the timestep is roughly constant throughout the simulation, independent of the time scale on which the microstructure evolves; in constrast, the timestep for MMS can be adjusted dynamically. Finally, the number of degrees of freedom required to describe the microstructure is very large since all atomic sites are explicitly taken into account, while in MMS one degree of freedom represents a large number of atomic sites.

One way around this efficiency problem is to consider equations for the evolution of the *average* occupation state of each lattice site. This way, thermal fluctuations can be integrated out and global updates of the system become possible. Even if such equations cannot be derived exactly, several approximation schemes have been proposed in recent years to simulate phase separation without elastic misfit (see Refs. [9, 19, 70] for example). While these approaches are able to bypass the

first three drawbacks of the Monte Carlo method, the problem of the large number of degrees of freedom remains. Here, we propose to solve this last point by using a multi-scale generalization of one of the aforementioned schemes, namely the time-dependent density-functional theory of Fisher and collaborators.[19] We also propose an extension of this framework to include the effect of elastic misfits. The remaining part of this section will be organized as follows : first, we outline the derivation of the TDDFT equations and describe how elastic effects can be included within the model; second, the multiscale generalization of the microscopic model is presented; finally, we give a brief description of the algorithmic tools used in our implementation of the model.

4.2.1 The TDDFT formalism

We begin by deriving the main equations of TDDFT. Since a detailed description of the theory is already available in the literature (see Ref. [19] and references therein), only the main steps are outlined here for completeness. Consider a system of interacting particles on a lattice. The state of the lattice sites can be described by an ensemble of occupation numbers n_i^α for α-type particles at site i. Assuming that each site can be occupied by only 1 particle (n_i^α equals either 0 or 1), the dynamics of the system can formally by described by the following master-equation for the probability to find the system in the configuration $\mathbf{n} = \{n_i^\alpha\}$ at time t :

$$\begin{aligned} \frac{dP(\mathbf{n},t)}{dt} &= \frac{1}{2}\sum_{i,j\in nn(i)} [w_{i,j}(\tilde{\mathbf{n}})P(\tilde{\mathbf{n}},t) \\ &\quad -w_{i,j}(\mathbf{n})P(\mathbf{n},t)] \end{aligned} \tag{4.1}$$

Here, it is assumed that a configuration evolves in time through successive exchanges of nearest-neighbors particles [$nn(i)$ denotes the set of nearest-neighbors of site i]. These exchanges proceed at rate $w_{i,j}(\mathbf{n})$; $\tilde{\mathbf{n}}$ represents a configuration which differs from $\mathbf{n}$ only by the exchange of the occupation numbers of sites i and j. From Eq. 4.1, a local master-equation describing the dynamics of the *average* occupation numbers $p_i^\alpha = \langle n_i^\alpha \rangle_t$ [where $\langle\rangle_t$ denotes an average with respect to the

distribution $P(\mathbf{n},t)$] is obtained :

$$\frac{dp_i^\alpha}{dt} = \sum_{j\in nn(i),\beta} \langle J_{i,j}^{\beta,\alpha}\rangle_t - \langle J_{i,j}^{\alpha,\beta}\rangle_t, \tag{4.2}$$

with the diffusion fluxes defined as :

$$J_{i,j}^{\beta,\alpha}(\mathbf{n}) = n_i^\beta n_j^\alpha w_{i,j}(\mathbf{n}). \tag{4.3}$$

The problem now is to evaluate the average diffusion fluxes. The main assumption of TDDFT is that the full non-equilibrium distribution function $P(\mathbf{n},t)$ can be approximated by the local equilibrium distribution function $P^{\text{loc}}(\mathbf{n},t)$ of the system under an external, site-dependent field h_i^α :

$$P^{\text{loc}}(\mathbf{n},t) = \frac{1}{Z(t)} \exp\left\{-\frac{1}{k_B T}\left[H(\mathbf{n}) + \sum_{i,\alpha} h_i^\alpha n_i^\alpha\right]\right\}, \tag{4.4}$$

where H is the Hamiltonian of the system, and $Z(t)$ is such that $\sum_{\mathbf{n}} P^{\text{loc}}(\mathbf{n},t) = 1$. The problem of computing the non-equilibrium distribution function in configuration space is now replaced by that of determining the $\{h_i^\alpha\}$ in real space. This is achieved by requiring consistency between $P^{\text{loc}}(\mathbf{n},t)$ and the $\{p_i^\alpha(t)\}$. The idea behind this assumption is that high-order correlations should relax rapidly compared to the site occupation averages ; hence, after a short initial transient, the high-order correlation functions should take values close to the ones they would relax to if the average occupations were kept constant by some external constraint. The validity of this assumption has been confirmed by Chen[9] who has shown that the dynamics of a system where pair-correlation functions are allowed to evolve following their own equations of motion is quantitatively very similar to that of a system where instantaneous equilibrium of the pair correlation functions relative to the site occupation averages is assumed. Further, it was shown [37] that the TDDFT approach yields results in excellent agreement with direct Monte Carlo simulation in cases where the exact free energy functional is available.

Formally, self-consistency can be achieved by requiring that the grand canonical potential of the system under the external field be a minimum with respect to the

average occupations, i.e., the h_i^α are such that

$$\frac{d}{d\mathbf{p}}\Omega(\mathbf{p}) = \frac{d}{d\mathbf{p}}\left[\sum_{i,\alpha}(h_i^\alpha - \mu_{\text{tot}}^\alpha)p_i^\alpha + F(\mathbf{p})\right] = 0, \tag{4.5}$$

where $\mathbf{p} = \{p_i^\alpha\}$, μ_{tot}^α is the global chemical potential of species α, and $F(\mathbf{p})$ is the free-energy functional of the system. From this last equation, it is now clear that the local fields are proportional to the local chemical potentials :

$$h_i^\alpha = \mu_{\text{tot}}^\alpha - \frac{\partial F}{\partial p_i^\alpha} = \mu_{\text{tot}}^\alpha - \mu_i^\alpha. \tag{4.6}$$

To complete the evaluation of the fields, one must specify a free-energy functional. In our case, we opted for a simple mean-field (or Bragg-Williams) approximation which, even if it usually cannot reproduce experimentally-observed phase diagrams in a quantitative manner, gives a qualitatively correct description of the phase separation process. This functional can be written :

$$\begin{aligned} F(\mathbf{p}) &= E(\mathbf{p}) - TS(\mathbf{p}) \\ &= \frac{1}{2}\sum_{i,j\in nn(i),\alpha,\beta} V_{i,j}^{\alpha,\beta} p_i^\alpha p_j^\beta + k_B T \sum_{i,\alpha} p_i^\alpha \ln p_i^\alpha, \end{aligned} \tag{4.7}$$

with $V_{i,j}^{\alpha,\beta}$ the interaction energy between atom α at site i and atom β at site j. One could also resort to the weighted density approximation — as in the original TDDFT formulation [19] — to obtain a free energy functional.

Other assumptions are required in order to obtain a tractable form for the average diffusion fluxes. First, it is assumed that, as it is typically the case for metallic alloys, configuration changes can only occur by vacancy diffusion to a nearest-neighbor site (vacancy-exchange mechanism). Second, these exchanges occur at a rate given by :

$$w_{i,j}^\alpha = \nu_0 e^{E_i^\alpha / k_B T}, \tag{4.8}$$

where E_i^α is the energy of an α-type atom at site i and ν_0 is a trial frequency. This assumes that the saddle point energy is zero in every configuration.

Combining this last result with equations 4.3 and 4.4, we obtain a very simple

form for the local master equation (Eq. 4.2) :

$$\frac{dp_i^\alpha}{dt} = \sum_{j \in nn(i)} M_{i,j}(t)(\mathcal{A}_j^\alpha(t) - \mathcal{A}_i^\alpha(t)), \tag{4.9}$$

with mobility $M_{i,j}(t) = \langle p_i^{\text{vacancy}}(t) p_j^{\text{vacancy}}(t) \rangle_t \simeq p_i^{\text{vacancy}}(t) p_j^{\text{vacancy}}(t)$ and activity $\mathcal{A}_i^\alpha(t) = e^{-h_i^\alpha(t)/k_B T}$. This equation is a generalized Fick's law where occupation probabilities diffuse from regions of high activity (and hence high chemical potential) to regions of low activity. It can be shown that this equation of motion leads to a continuous decrease of the free-energy evaluated through Eq. 4.7, and hence that a stationary state of Eq. 4.9 corresponds to a free energy minimum. Even if TDDFT is a mean-field formalism, this shows that it yields an evolution that is consistent with the equilibrium statistics specified by the free-energy functional. Further, as previously mentioned, TDDFT and Monte Carlo results were shown to be nearly identical for both equilibrium and dynamical quantities for cases where the exact energy functional is known.[37] Thus, in the present case, we cannot expect quantitative agreement with Monte Carlo simulations. However, since we are not seeking quantitative results, but rather insights into the basic physical behavior, we expect this simple approximation to be adequate. The use of higher-order approximations of the free energy will be the subject of future work.

4.2.2 TDDFT with elastic misfit

In the formalism described above, the atoms are constrained on a rigid lattice. Thus, the effect of a lattice constant misfit cannot be accounted for. One way to introduce elastic relaxation effects is to allow the interaction energies in Eq. 4.7 to depend on the positions of the atoms. For simplicity, we opted for a simple harmonic potential :

$$V_{i,j}^{\alpha,\beta} = k^{\alpha,\beta}(r_{i,j} - \sigma^{\alpha,\beta})^2 - \epsilon^{\alpha,\beta}, \tag{4.10}$$

where $r_{i,j} = |\vec{r}_i - \vec{r}_j|$. The *average* positions $\vec{r}_i$ are then obtained by requiring that they minimize Ω (or equivalently the energy in Eq. 4.7), i.e.,

$$\begin{aligned} \frac{d}{d\mathbf{r}}\Omega(\mathbf{p},\mathbf{r}) &= \frac{d}{d\mathbf{r}}\left[\sum_{i,\alpha}(h_i^\alpha - \mu_{\text{tot}}^\alpha)p_{\text{i}}^\alpha + F(\mathbf{p},\mathbf{r})\right] = 0 \\ &= \frac{d}{d\mathbf{r}}E(\mathbf{p},\mathbf{r}) = 0. \end{aligned} \tag{4.11}$$

This way, if we select different values of the lattice parameter σ for the interaction between different species (c.f. Eqns. 4.10 and 4.7), a lattice mismatch is introduced. Further, if we select different values of the stiffness k, an elastic inhomogeneity results. Likewise, the strength of the driving force for the phase separation can be tuned according to ϵ. Note that for nearest-neighbor, two-body interactions such as the ones used here, the elastic constants are always isotropic.

Concerning the accuracy of this formulation, two remarks are in order. First, this procedure completely neglects local relaxation effects, i.e., the same displacement field is used to compute, say, E_i^α and E_i^β. This somewhat overestimates the effect of the strain, since local relaxation is expected to be most effective in severely strained configurations. Second, in the present approach, elasticity is introduced at the mean-field level since atoms interact with the free-energy-minimizing displacement field, not the displacement field corresponding to a particular microscopic configuration. These two limitations are not expected to be severe in the case of a system composed of a set of almost pure inclusions embedded in an almost pure matrix (typical of the microstructures produced during phase separation processes), since every microscopic configuration which has a significant probability of being observed will have a displacement field very similar to the free-energy minimizing one. Thus, these approximations are expected to yield very good results when used in a phase separation context.

Finally, we assume that the neighbors of an atomic site do not change during the course of a simulation, i.e., elastic coherency is enforced and the contribution of plastic effects is excluded.

4.2.3 Multiscale generalization

The TDDFT model described in the first part of this section is essentially microscopic in nature since every lattice site is explicitly taken into account. This imposes severe constraints on the system sizes that can be studied. In order to alleviate this limitation, we propose a multiscale generalization of TDDFT where the number of degrees of freedom can be dynamically adjusted as the calculation proceeds. In the following, we describe first the coarse-graining procedure of the TDDFT local master-equation (Eq. 4.9), then the elastic equilibrium equation (Eq. 4.11).

4.2.3.1 Coarse-graining of the TDDFT equations

As discussed earlier, a typical microstructure observed in phase-separating systems consists of well-defined inclusions embedded in a matrix. Within each of these structures, the average occupation field varies very slowly. The only rapid changes occur close to the interphase boundaries. Thus, atomic resolution is in principle only needed close to the interfaces, while lattice sites located far from these interfaces can collectively be described using fewer degrees of freedom. To achieve this, two ingredients are required : i) a coarse-grainable representation of the average occupation field, and ii) a method to solve Eq. 4.9 in this representation.

For i), we proceed as follows. First, we select a set of atomic sites whose average occupations are representative of their neighborhoods (the procedure used to build this set will be described in Sec. 4.2.4); those sites will be referred to as *representative sites*. When needed, the average occupation of non-representative sites are obtained by a Laplace interpolation [86] defined as follows. Let $\mathbf{x}$ be a point in space; the Laplace interpolant for a general scalar function $f(\mathbf{x})$ is

$$f^l(\mathbf{x}) = \sum_{i=1}^{N_{\text{rep}}} \phi_i(\mathbf{x}) f_i, \tag{4.12}$$

where N_{rep} is the number of representative sites, f_i is the (known) value of the function f at representative site i and $\phi_i(\mathbf{x})$ is the value of the Laplace shape function of site i evaluated at $\mathbf{x}$. We now consider a Voronoï tesselation of space

using the representative site and point $\mathbf{x}$. The shape function can then be written as :

$$\phi_i(\mathbf{x}) = \frac{s_i(\mathbf{x})}{\sum_{j=1}^{N_{\text{rep}}} s_j(\mathbf{x})}, s_j(\mathbf{x}) = \frac{m(t_j(\mathbf{x}))}{d_j(\mathbf{x})}, \tag{4.13}$$

with $d_j(\mathbf{x})$ the distance between $\mathbf{x}$ and the representative site j, and $m(t_j(\mathbf{x}))$ a measure of the common facet (length in 2D and area in 3D) between the Voronoï cells of site j and of point $\mathbf{x}$; if the two cells do not share facets, $m(t_j(\mathbf{x})) = 0$. A review of the properties of this interpolant can be found in Ref. [86].

The Voronoï tesselation of space using the representative sites provides a definition of the "neighborhood" of a representative site : all lattice sites found within the Voronoï cell of a given representative site belong to its neighborhood. The last step is to reformulate Eq. 4.9 in terms of the average occupations of the neighborhoods instead of the average occupations of the lattice sites. Concerning point ii), the key is to realize that this equation is essentially a diffusion equation for the occupation probabilities, with a probability flux between adjacent sites proportional to the activity difference between the two sites. Since the total occupation probabilities are conserved, this can easily be translated into a coarse-grained representation by using the finite-volume method. The time derivative of Eq. 4.9 is then written in terms of the diffusion fluxes crossing each facet of the Voronoï cells of the representative sites; on an arbitrary grid, Eq. 4.9 becomes :

$$\frac{dp_i^\alpha}{dt} = \sum_{j \in nn(i)} M_{i,j}(t)(\mathcal{A}_j^\alpha(t) - \mathcal{A}_i^\alpha(t)) \frac{b_{i,j}}{d_{i,j} N_i}, \tag{4.14}$$

with $d_{i,j}$ the distance (in lattice constants) between representative sites i and j, N_i the number of lattice sites inside the Voronoï cell of representative site i, and $b_{i,j}$ the number of nearest-neighbor links intersected by the common facet of Voronoï cells i and j. For a rigorous derivation of such finite-volume scheme on unstructured grids, one may consult Refs. [86] and [18]. One nice feature of this coarse-graining scheme is that Eq. 4.14 reduces exactly to Eq. 4.9 as the grid is refined to the original lattice since, in this case, $d_{i,j} = 1$, $N_i = 1$ and $b_{i,j} = 1$. Thus, this formulation allows for seamless changes in the resolution of the TDDFT calculations, from the micro to the mesoscale. The only requirement is that the average occupation field varies

slowly on the scale of the distance between representative sites. Since the variations in this field are very sharp and well localized, this is not a serious limitation.

4.2.3.2 Coarse-graining of the elastic equilibrium equations

Since the activities in Eq. 4.14 also depend on the average displacement of the atoms in the neighborhood of the representative sites, the elastic equilibrium equation (Eq. 4.11) is also required to be coarse-grained. The formulation is naturally provided by the quasicontinuum method (QCM) of Tadmor and collaborators [87] (see Ref. [53] for a recent review of the method and its applications). Since its introduction, the QCM has proven to be very effective in providing a multiscale description of the micro and meso-scale elastic behavior of materials using only inter-atomic potentials as input. It was successfully applied to simulations of fracture,[52] nanoindentation,[88] and failure of carbon nanotubes under tension,[106] to name only a few examples.

We give here a rapid overview of its most important aspects. The first step is to reduce the number of degrees of freedom required to describe the displacement field. Again here, we express the average displacement field at every lattice site in terms of the average displacements of the representative sites using the Laplace interpolation scheme described above. Note that this departs from the standard QCM procedure where linear shape functions defined on triangular elements are used. In our case, it is simpler to use the same interpolation scheme for both occupations and displacements. Next, we write a coarse-grained energy functional for the complete system as a function only of the representative site displacements. For this purpose, we make use of the so-called nonlocal energy-based formulation of the QCM.[53] In this formulation, the coarse-grained energy can be written as a sum over the energy of the representative sites :

$$E^{tot,QCM} = \sum_{i=1}^{N_{\text{rep}}} N_i E_i^{int}, \tag{4.15}$$

where E_i^{int} is the energy of site i evaluated using Eqs. 4.7 and 4.10 with the Laplace-interpolated average displacements. The last step is to minimize the coarse-grained

energy with respect to the average displacements of the representative atoms. This can be carried out using any standard minimization method. In this case also, the non-local QCM formalism reduces exactly to the original microscopic model when the grid is refined to the original lattice; thus, scale-dependent effects and non-linearities are fully taken into account.

4.2.4 Choice of representative sites

In the previous two subsections, it was shown how a coarse-grainable formulation of our model can be obtained, based on the assumption that a representation of the relevant fields can be constructed from the values that these fields take on a subset of all lattice sites (the representative sites). In this section, the question of how this subset is chosen is addressed. In principle, choosing a representative set for the TDDFT equations is an easy task : atomic resolution is required only in the vicinity of the interphase boundaries, while a coarser grid can be used elsewhere. It turns out that this strategy is also appropriate for the elastic equilibrium equation of the QMC since it adequately captures the changes in elastic properties between the different phases. Further, rapid changes in the displacement field also tend to occur near the interfaces. For example, in the case of a circular inclusion in an elastically isotropic and homogeneous matrix, the radial displacement component increases linearly with the distance to the center of the inclusion until the interface is reached, where it abruptly begins to decrease.[57] While it is true that a more aggressive optimization could be achieved by choosing different sets for the TDDFT and the QCM, the performance gain would probably be more then offset by the increased complexity of the code. Thus, only a common representative set will be used here.

To facilitate both creation and management, a few constraints on the composition of the representative set are enforced. First, only four levels of coarsening are allowed ($L = 0, 1, 2, 3$); in a region of level L of a D-dimensional lattice, one out of every 2^{DL} sites is included in the representative set. Second, the representative set forms a semi-structured grid, meaning that the level-L representative set is a subset of the level-L' representative set for $L > L'$. Finally, the local coarse-

ning level is obtained from the distance d_i to the closest interphase boundary by $L = \min(\lfloor d_i/d_l \rfloor, 3)$. In the calculations presented below, we used $d_l = 7a_0$, where a_0 is the lattice parameter. The limit imposed on the number of coarsening levels ensures a smooth and rapid convergence of the TDDFT and QCM equations. (A very large difference in the volumes of the representative cells generally causes poor convergence).

Because the microstructure evolves in time, the adequacy of the representative set is checked periodically, and is automatically corrected as necessary. After corrections, the timestep is temporarily decreased to allow the solution to relax on the new sites. An example of the Voronoï cells around the representative sites for the case of a single circular inclusion within a homogeneous matrix in two dimensions is show in Fig. 4.1. One can easily appreciate the reduction in the number of degrees of freedom resulting from the multi-scale formalism presented here.

4.2.5 Implementation details

As a first implementation of this method, we chose to work in two dimensions. We examine the case of a binary alloy with vacancies (ABv alloy), but ternary alloys could just as easily be simulated. The integration of the TDDFT equations (Eq. 4.14) are carried out implicitly using the order 5 backward differentiation formulas of Gear.[24] Every implicit integration step requires the solution of a non-linear problem. This is obtained by a Newton-Krylov method [6] using the stabilized biconjugate gradient algorithm without preconditioning.[95] Since it is readily available, the exact Jacobian is used in the non-linear solution. This elaborate scheme is necessary because the TDDFT equations for our system are very stiff, so that simpler explicit methods are limited to extremely small timesteps for stability reasons. To minimize the QMC energy functional Eq. 4.15 (and hence the free energy) with respect to the site displacements, we use the conjugate-gradient algorithm [28] on the QCM forces using the exact Hessian matrix.

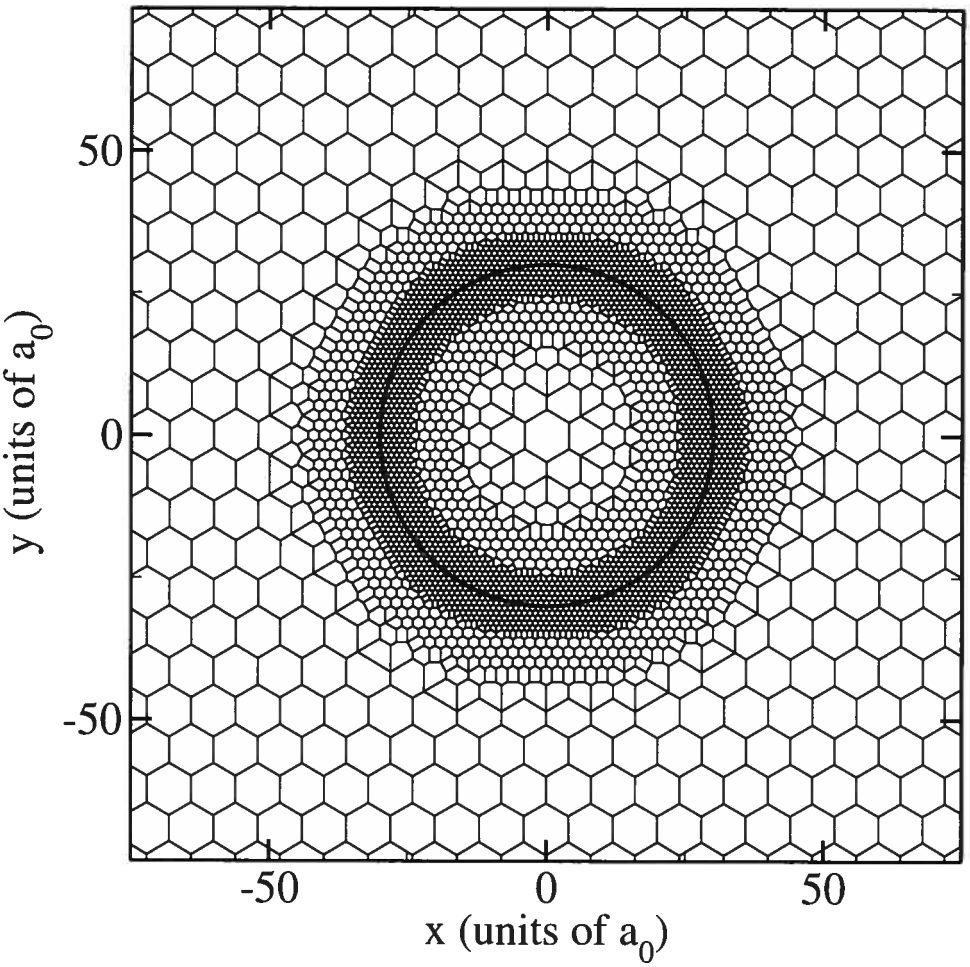

FIG. 4.1 – Voronoï cells around the representative sites for a single inclusion embedded within an otherwise homogeneous matrix in two dimensions. The contour of the inclusion is shown by the thick black line.

4.3 Results

4.3.1 Simulation setup

In the following, we present our results for the growth of isolated inclusions in elastically inhomogeneous systems with elastic misfit. In all calculations, the inclusion is rich in B-type atoms while the matrix is rich in A-type atoms. All results are reported in dimension-less, reduced units, relative to a stress-free pure A phase : lattice parameter for length (a_0), interaction energy between nearest-neighbors for energy (ϵ), and inverse trial frequency for time (τ_0). In those units, the parameters of the inter-atomic potential Eq. 4.10 were chosen to be : $\epsilon_{AA} = \epsilon_{BB} = \epsilon$,

$\epsilon_{AB} = 0.7\epsilon$ and $\sigma_{AA} = \sigma_{AB} = a_0$, $\sigma_{BB} = 1.04a_0$. The stiffnesses k are either $k_{AA} = k_{AB} = 25\epsilon/{a_0}^2$, $k_{BB} = 100\epsilon/{a_0}^2$ for hard inclusions, or $k_{BB} = k_{AB} = 25\epsilon/{a_0}^2$, $k_{AA} = 100\epsilon/{a_0}^2$ for soft inclusions. In order to clearly distinguish elastic effects from other possible contributions, we also carried out simulations for an elastically homogeneous system without elastic misfit. In this case, we use $\sigma_{BB} = a_0$ (and the stiffnesses are arbitrary since they do not enter the calculation). In all cases, the temperature is $T = 0.5\epsilon/k_B$, which is about half of the critical temperature for phase separation. At this temperature, the interface width is around one nanometer, similar to what is observed in usual experimental conditions. The vacancy concentration is taken to be 10^{-3}.

The simulation cell is an hexagon with sides of length $512a_0$. Fixed boundary conditions are applied to the QCM equations at the edges of the simulation cell. For the TDDFT equations, the average occupations at the edges are also fixed, and either open boundary conditions (the edges act as sources or drains of occupation probability) for growth simulation, or closed boundary conditions (the edges do not act as sources or drains) for relaxation simulations, are used. A small inclusion composed of B-type atoms is initially placed at the center of the cell; the initial inclusion is a circle with a radius of $10a_0$.

4.3.2 Data analysis method

The natural way to study the coarsening behavior of an inclusion is to obtain the so-called Gibbs-Thomson (GT) relation. This relation links the size of the inclusion with either its chemical potential or the solute concentration close to its interface. The coarsening behavior of a collection of inclusions of different sizes can then be inferred from the GT relation since diffusion will occur from regions of high chemical potential (or concentration) toward regions of low chemical potential (or concentration). The system under study here is a ternary mixture (ABv) and two distinct chemical potentials can be defined : μ_A and μ_B. However, the information contained in these two quantities can be summarized in the dimension-less quantity $(\mu_B - \mu_A)/k_BT = \Delta\mu/k_BT$. This can be rationalized as follows. Suppose that the activities in the matrix are given by $\mathcal{A}_m^A$ and $\mathcal{A}_m^B$, while the activities in the inclusion

are given by $\mathcal{A}_i^A$ and $\mathcal{A}_i^B$. If the inclusion is in equilibrium with the surrounding matrix, we have $\mathcal{A}_i^A = \mathcal{A}_m^A$ and $\mathcal{A}_i^B = \mathcal{A}_m^B$. If, on the other hand, the matrix is slightly supersaturated, we will have $\mathcal{A}_i^B < \mathcal{A}_m^B$ and, by Eq. 4.14, there will be an occupation probability flux of B-type atoms of magnitude proportional to $\mathcal{A}_m^B - \mathcal{A}_i^B$ toward the inclusion, i.e., the inclusion will grow. However, since the average occupation within the inclusion is a slowly varying function of the radius, the occupation probability flux of B-type atoms must be compensated by an inverse flux of A-type atoms. In this case, Eq. 4.14 implies that $\mathcal{A}_m^B - \mathcal{A}_i^B \simeq \mathcal{A}_i^A - \mathcal{A}_m^A$. From this, we can infer that the growth rate of an inclusion is proportional to $(\mathcal{A}_m^B - \mathcal{A}_m^A) - (\mathcal{A}_i^B - \mathcal{A}_i^A)$, i.e., inside a given matrix, the growth rate of an inclusion is solely a function of the difference in activity inside the inclusion. This also means that, if we now consider an ensemble of inclusions inside a given matrix, those in which $\mathcal{A}_i^B - \mathcal{A}_i^A > \mathcal{A}_m^B - \mathcal{A}_m^A$ will shrink to the benefit of those in which $\mathcal{A}_i^B - \mathcal{A}_i^A < \mathcal{A}_m^B - \mathcal{A}_m^A$. Since $\mathcal{A}^\alpha = \exp(\mu^\alpha / k_B T)$, the information about the coarsening behavior of inclusions is also contained in $\Delta\mu$. In what follows, the GT relation of $\Delta\mu$ vs r will thus be used to characterize the equilibrium behavior of inclusions.

4.3.3 Homogeneous system without elastic misfit

In order to clearly isolate elastic effects from others, we first present the results obtained with our approach for a system in which no elastic misfit is present. This will serve as a basis for comparison with elastically inhomogeneous systems. We start by discussing the equilibrium properties of the inclusions, then investigate how these are affected by growth at different rates.

4.3.3.1 Equilibrium properties

In the absence of elastic effects, the equilibrium properties of an isolated inclusion are solely a function of the curvature of the interface with the matrix. The prefered shape is a circle at high enough temperature (which is the case here) or a compact faceted shape otherwise; indeed, this is what we observe in our TDDFT simulations.

Since the chemical potential inside an inclusion is a function of interface curva-

ture, $\Delta\mu$ should follow the well known Gibbs-Thomson relation for circular inclusions :

$$\frac{\Delta\mu(R)}{k_BT} = \frac{C}{R} + \frac{\Delta\mu_\infty}{k_BT}, \tag{4.16}$$

where R is the radius, C is a constant related to the interfacial free energy, and $\Delta\mu_\infty$ is the value of $\Delta\mu$ inside an infinitely large inclusion. The results are thus best presented as a so-called Gibbs-Thomson plot, where $\Delta\mu$ is plotted against the reciprocal characteristic length of the inclusion. (In the simulation results, the characteristic length is taken to be the radius of a circle with the same area as the inclusion and will be denoted R_{eq}). The normal behavior of $\Delta\mu$ then appears as a straight line. Fig. 4.2 shows the GT relation obtained from a simulation carried out at very low supersaturation ($\Delta c^B = 1\%$, where Δc^B is the excess concentration of solute atoms in the matrix relative to the concentration at phase coexistence). The data reproduces the expected $1/R$ dependence of the chemical potentials and thus follows the GT relation.

In the next three sections, the dynamical properties of the inclusions are investigated. More specifically, we wish to assess the stability of the circular shape against growth. We also study the effect of growth on the chemical potentials of the inclusions and infer the consequences on the coarsening behavior. To address these questions, different growth rates were imposed to initially circular inclusions. The level of supersaturation of the matrix was varied from right above the spinodal limit (where new inclusions would spontaneously appear in the matrix) to the binodal limit (where the growth rate vanishes for very large inclusions), thus covering a large portion of physically possible growth rates. At the temperature where the calculations were carried out, the spinodal limit corresponds to a maximal supersaturation Δc^B of about 10%. We begin by exploring the stability of the equilibrium shape against growth and deformation.

4.3.3.2 Morphological stability

A stroboscopic view of the evolution of the inclusion is provided in Fig. 4.3 for a very high supersaturation ($\Delta c^B = 10\%$). Initially, the inclusion maintains its equilibrium circular shape. As the size increases, the inclusion adopts an increasingly

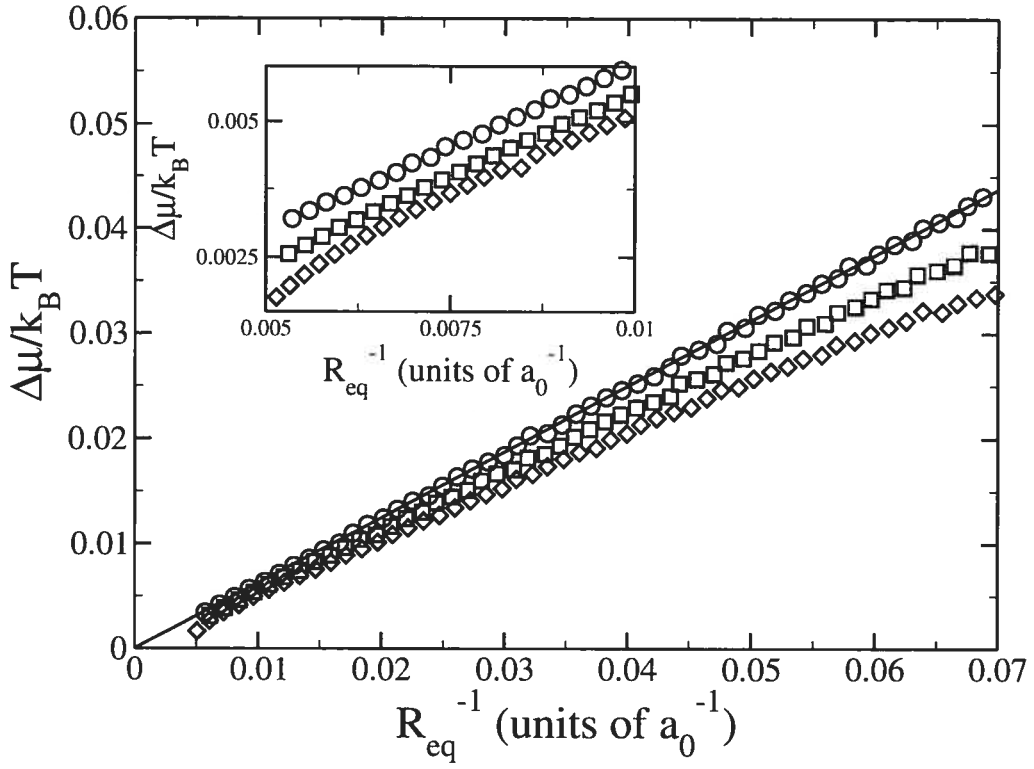

FIG. 4.2 – Dynamical Gibbs-Thomson relations for homogeneous inclusions : circles : $\Delta c^B = 1\%$ (quasi-static growth); squares : $\Delta c^B = 4\%$; diamonds : $\Delta c^B = 10\%$; continuous line : fit to Eq. 4.16 for $\Delta c^B = 1\%$.

hexagonal shape. Eventually, the "facets" of this hexagon become concave, leading to the formation of pointed tips at the vertices. Near the end of the simulation, the tips split and continue to grow while small bulges appear in their vicinity. The "facets" do not align in directions of low interface energy, so that the anisotropy of the interfacial energy (automatically present because of the underlying symetry of the lattice) is not the primary cause for the sixfold symmetry.

Growth instabilities are well known and commonly observed, both in simulations and in experiments .[7, 45, 56, 94, 103, 104] The theoretical study of this phenomena was pioneered by Mullins and Sekerka (MS),[56] who developed a model to explain shape instabilities in diffusion-controlled systems by studying the dynamics of infinitesimal perturbations around the equilibrium state. The evolution of these perturbations is governed by two opposing forces, namely capillarity, which favors the decay of the perturbations, and the so-called point effect of diffusion, which promotes their growth. The point effect is related to the bunching of isoconcen-

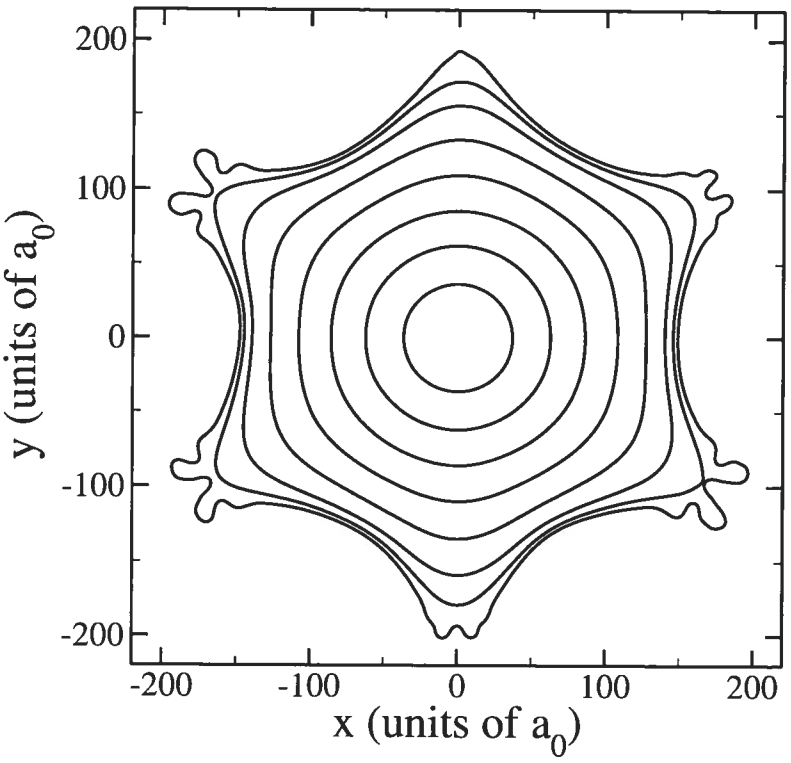

FIG. 4.3 – Evolution of a growing homogeneous inclusion for $\Delta c^B = 10\%$ over $1.5 \times 10^{12}\tau_0$.

tration lines above protuberances on a growing interface and to their rarefaction above depressions. The net result is the focusing of diffusion fluxes away from the depressions and toward the protuberances, thus increasing the amplitude of the perturbation.

In the case of a perturbed circular inclusion, the distance between the center of the inclusion and a given point on its interface with the matrix can be decomposed into a sum of contributions from different modes, i.e., $r(\theta) = R + \sum_l \delta_l \cos(l\theta + \phi_l)$, with δ_l the amplitude of mode l and ϕ_l its associated phase. MS showed that the fractional rate of increase (FRI) of the amplitude of a mode is given by :

$$\frac{\dot{\delta}_l/\delta_l}{\dot{R}/R} = (l-1)\left[1 - \frac{R_c(l)}{R}\right]\left[1 - \frac{R^*}{R}\right]^{-1}, \tag{4.17}$$

with R^* the thermodynamical critical radius of an inclusion at the imposed supersaturation and $R_c(l) = [(1/2)(l+1)(l+2)+1]R^*$ the critical radius for the amplification of mode l. [Below $R_c(l)$ mode l decays while above $R_c(l)$ it grows].

The sign of the FRI indicates whether a perturbation of the corresponding mode grows (+) or decreases (-). Further, a FRI between 0 and 1 indicates that, while the amplitude of the mode grows, it does so less rapidly than the radius of the inclusion, so that the equilibrium shape will be asymptotically restored. In constast, a FRI higher than one indicates that the relative contribution of the mode to the overall shape increases with time.

Two important conclusions can be inferred from Eq. 4.17. First, the radius at which a mode becomes unstable increases rapidly with its order. This means that only low-order modes are expected to be relevant for the range of sizes probed here. Second, the higher the order of a mode, the higher its asymptotic FRI [the FRI tends to $l-1$ for $R \gg R_c(l)$].

It is useful to recall that the MS theory is linear in that it assumes vanishingly small perturbation amplitudes, so that interactions between modes can be neglected. Thus, in order to compare the simulation results with the theory, we need to study configurations where only one mode is significantly excited. To achieve this, simulations were initialized with inclusions whose shape is perturbed by either mode 2 or mode 3 [$\delta_2(t=0)=1$ or $\delta_3(t=0)=1$]. Note that, even in this case, nonlinear effects cannot be excluded because other modes will progressively get excited during the evolution of the system. We will return to the case of the initially unperturbed inclusion below.

The FRI inferred from these simulations are reported in Fig. 4.4 for different levels of supersaturation. The agreement between the data and the predictions of the model is reasonable. The initial increase of the FRIs close to R_c and their asymptotic value are well reproduced.

However, discrepancy with the theory appears as perturbations develop further. As mentioned earlier, this is due to interactions between modes. The most important consequence is the excitation of higher-order harmonics of strongly excited modes. This can be observed in Fig. 4.5, where the FRIs of a few modes for a simulation with a strong initial perturbation of mode 3 [$\delta_3(t=0)=2a_0$] are reported. The results show that the FRI of mode 6 reaches more than twice the expected value because of interactions with mode 3. We have carried out a series

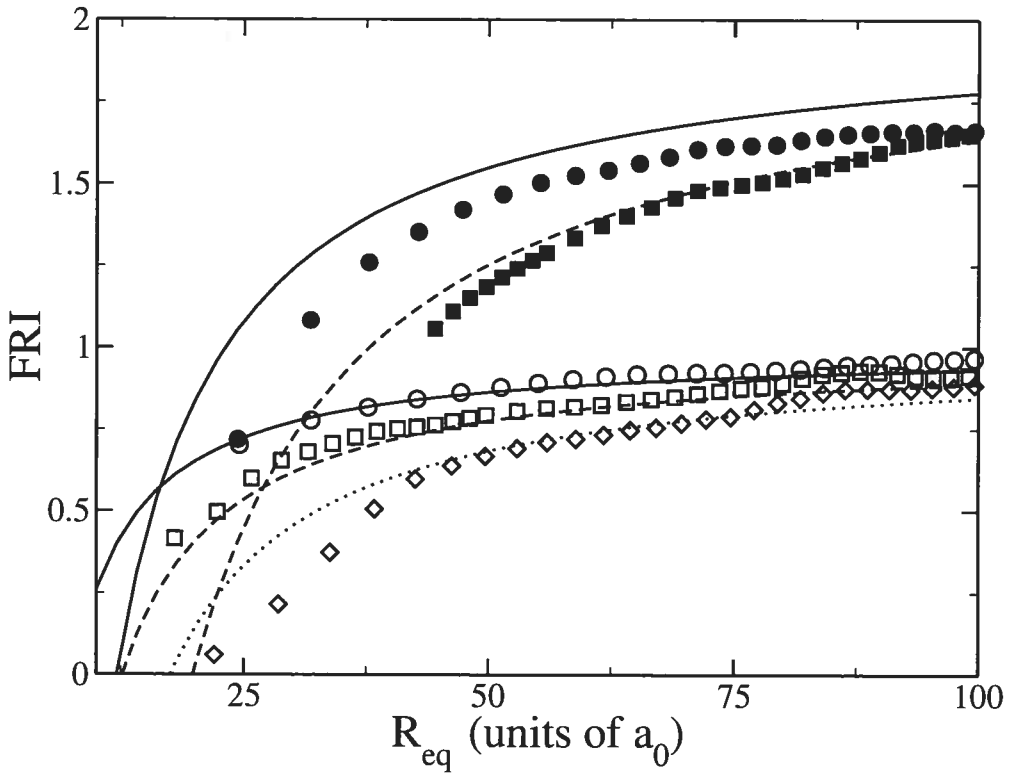

FIG. 4.4 – Fractional rate of increase of modes 2 and 3 for perturbed homogeneous inclusions : circles : $\Delta c^B = 10\%$; squares : $\Delta c^B = 7\%$; diamonds : $\Delta c^B = 3\%$; continuous lines : Eq. 4.17 with $R^* = 1.1a_0$ for $l = 2$ and $l = 3$; dashed lines : Eq. 4.17 with $R^* = 1.8a_0$ for $l = 2$ and $l = 3$; dotted line : Eq. 4.17 with $R^* = 2.5a_0$ for $l = 2$. The empty symbols correspond to $l = 2$ and the filled ones to $l = 3$.

of simulations to confirm that this excess FRI is indeed directly correlated with $\delta_3(t = 0)$. The FRIs of mode 3 and 6 then gradually decrease. Both the excitation of higher-order harmonics and the inhibition of large-amplitude modes are known consequences of nonlinearities.[7] The other commonly observed effect is the inhibition of incommensurate modes. This effect can also be observed in Fig. 4.5. In this case, the growth of mode 2 is strongly inhibited by the large amplitude of mode 3. This process is so efficient that mode 2 actually becomes stable around $R = 125a_0$ (when the FRI becomes negative).

4.3.3.3 Excitation of perturbations

Up to now, we have focused on the amplification of perturbations. Of course, they need to be created before they can be amplified. In real systems, the MS

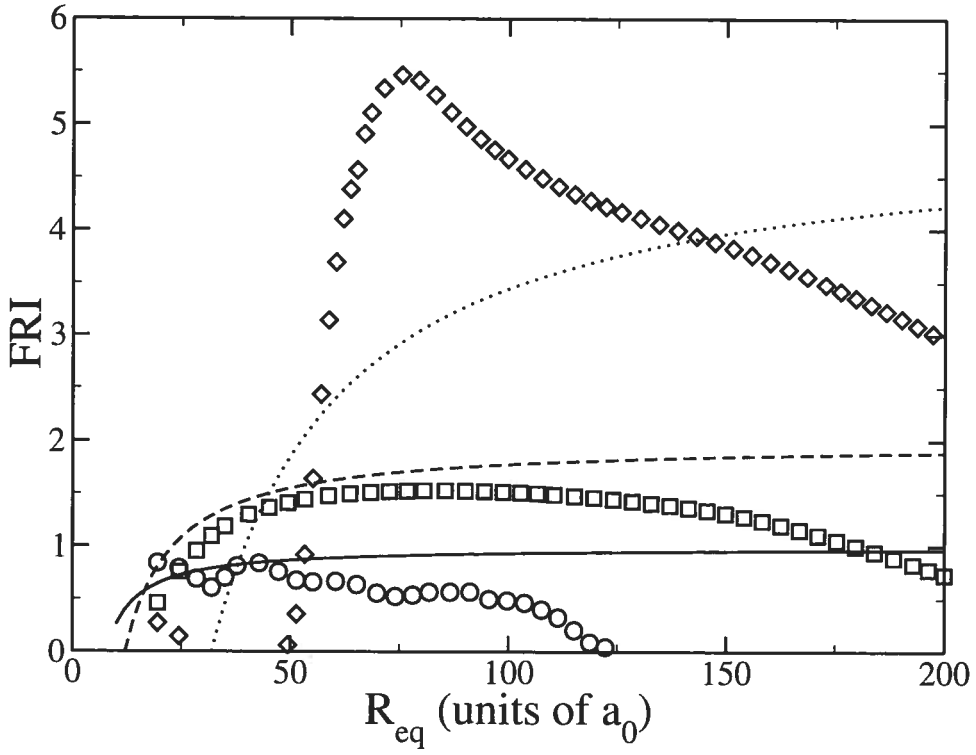

FIG. 4.5 – Fractional rate of increase for homogeneous inclusions with $\delta_3(t=0) = 2a_0$ for $\Delta c^B = 10\%$: circles : mode 2; Squares : mode 3; diamonds : mode 6; continuous line : Eq. 4.17 with $R^* = 1.1a_0$ for $l = 2$; dashed line : Eq. 4.17 with $R^* = 1.1a_0$ for $l = 3$; dotted line : Eq. 4.17 with $R^* = 1.1a_0$ for $l = 6$.

instability feeds on random thermal fluctuations while in deterministic and isotropic numerical models, the only source of instability is numerical noise (roundoff or integration errors, for example). In the present case, the microscopic resolution causes the isotropy to be broken. Indeed, the inclusion grows on a discrete lattice with sixfold rotational symmetry. This causes angular variations of various physical quantities which can couple with the inclusion shape and induce shape modulations. This phenomenon can be observed in Fig. 4.6, where the amplitude of mode 6 for an initially circular inclusion at very low supersaturation is reported. Below $R_c(6)$, the amplitude of this mode indeed exhibits an oscillatory behavior of period a_0. Note that in the range of radii of Fig. 4.6, the amplitudes of the other modes are 1 or 2 orders of magnitude below that of mode 6. Further, the phase of mode 6 relative to the underlying lattice is constant from one simulation to another, which supports the idea of an excitation through interactions with the lattice. Other

modes can then be excited either by direct coupling with mode 6 or by interaction of the slightly perturbed shape with the lattice, in addition to numerical noise. This demonstrates the power of our approach for studying phenomena that emerge from the existence of fundamental symmetries or length-scales.

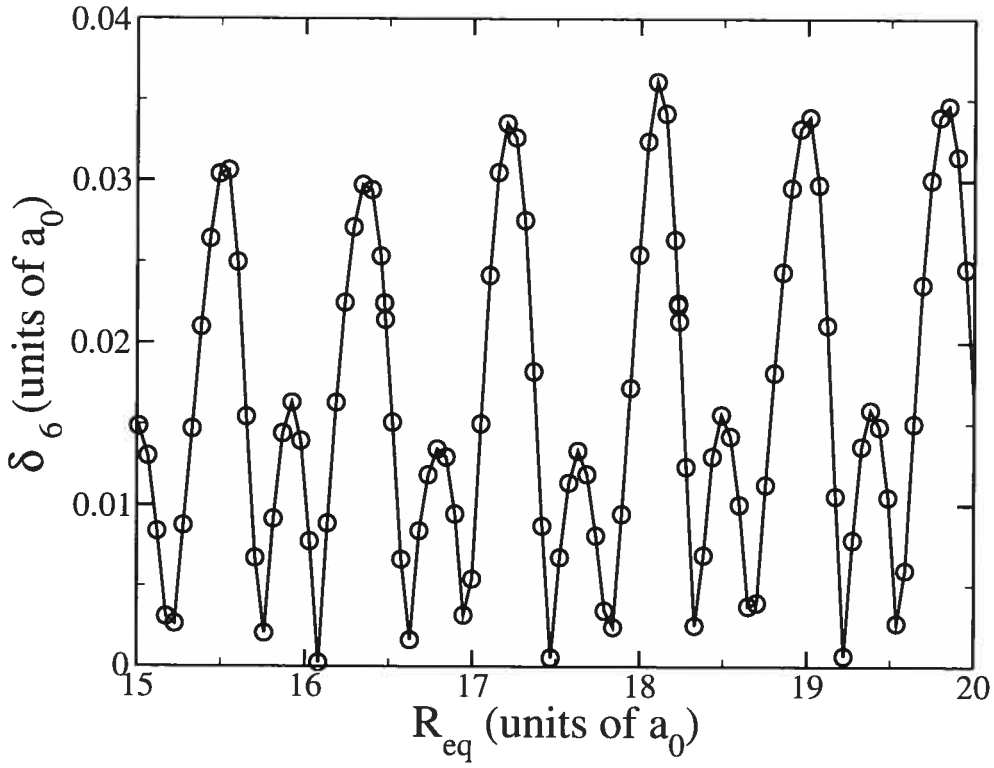

FIG. 4.6 – Amplitude of mode 6 for a homogeneous inclusion at $\Delta c^B = 0.1\%$.

The above discussion enables us to understand the evolution of initially unperturbed shapes such as that shown in Fig. 4.3. If we assume that the primary mode-excitation process is noise, the MS theory predicts that different shapes should be observed as a function of the supersaturation : low-index modes should tend to dominate at low supersaturations, while high-index modes prevail at higher supersaturation. However, this is not what we observe : mode 6 invariably emerges as the leading mode when the radius of the inclusion exceeds $R_c(6)$. Even as the supersaturation increases, higher-index modes with asymptotically larger FRIs are not able to outgrow mode 6 in the range of sizes probed here. This shows that the preferential excitation of mode 6 by the lattice is the cause of its dominance in the shape of initially circular inclusions. We also observe that the excitation of other

modes is extremely sensitive to noise : indeed, their relative contribution to the shape of the inclusion varies from one simulation to the other even for identical initial conditions (modulo the inevitable numerical roundoff errors).

Another factor related to the anisotropy of the lattice contributes to the observed dominance of mode 6 : the anisotropy of the mass transport and interface kinetics. Indeed, anisotropic kinetics are known to induce faceting [94] and the formation of corners [7, 103] and tips; it is also known to delay the well-known tip splitting instability, as clearly shown by Brush and Sekerka.[7] These results indicate that in completely isotropic systems, even very blunt tips split spontaneously, while the indroduction of kinetic anisotropy gradually stabilizes them. By comparing Fig. 4.3 with the morphologies reported in Ref. [7], it is clear that such mechanisms operate in our simulations. However, the quantitative agreement between the measured FRIs and the predictions of the isotropic MS model indicates that, at least below $R = 100a_0$ (where nonlinear effects are small), the anisotropy of the kinetic coefficients is not the dominant factor in the growth of the different modes.

These results highlight another advantage of our approach compared to MMS : the anisotropy of the kinetics and of the energetics is automatically taken into account because of the microscopic formulation of our model. This makes the task of identifying and parametrizing these anisotropies *a priori* unnecessary.

4.3.3.4 Dynamical corrections to the GT relation

Having analyzed the role of dynamical effects on the topology of the inclusions, we now turn to a discussion of their impact on the chemical potential, and hence on their coarsening behavior. Fig. 4.2 shows that finite growth rates can have a significant effect on the GT relation of the inclusions. While the general behavior is preserved, the slope of the GT curve shows a clear rate dependence. This in turn implies that the composition of the inclusion is a function of the growth rate. This dependence is a consequence of the so-called "solute trapping" effect which is also observed in such contexts as rapid solidification in alloys [4, 101] and grain coarsening in polycrystalline materials,[49] for example (see Ref. [29] for a

recent review). The solute trapping effect can be understood intuitively using a simple argument :[101] under growth conditions, a concentration gradient forms in front of the growing interface; since there is a free energy cost associated with this concentration gradient, the equilibrium partition of solute atoms across the interface can be ignored in favor of smaller gradients. By using this assumption to solve the diffusion equation for a system with an interface traveling at constant velocity, Langer and Sekerka [40] showed that the solute concentration in the growing phase should vary linearly with the interface velocity.

The topology of the inclusions also affects the GT relation through a slight downward curvature at large size. (see inset to Fig. 4.2). Clearly, this contribution could become quite significant at larger sizes and for more pronounced shape perturbations, but for the range of sizes studied here, it is very small.

While the absolute value of the dynamically-induced chemical potential shift (as measured by the distance between the quasi-static GT curve and the dynamical one) may seem important, it has to be compared to the driving force necessary to induce such a shift, i.e., for the shift to be really significant, it has to be comparable to the the driving force ($\Delta\mu/k_BT$ at the boundary of the simulation cell minus $\Delta\mu/k_BT$ in the inclusion) or else its impact on growth dynamics will be negligible. For $\Delta c^B = 10\%$, the driving force is around 0.7 while the shifts are of the order of 0.01 or smaller. Even for $\Delta c^B = 4\%$ the driving force is still large (~ 0.6). Thus, the dynamically-induced shifts are too small to significantly affect the coarsening behavior of the inclusions. For this reason, we will not try to quantify precisely the solute trapping process nor the impact of the shape perturbation on the chemical potentials in the present study.

4.3.4 Hard inclusions

4.3.4.1 Equilibrium properties

Having studied the reference homogeneous system, we now turn to the case of hard inclusions. For isotropic elasticity, Eshelby [16] showed that a circular inclusion has a lower elastic energy than an ellipse. Because, at high enough temperature, the interface-energy minimizing shape is also a circle, hard inclusions have a circular

shape independent of their size. In quasi-static growth simulations, we also observe quasi-circular shapes for all sizes investigated ($10a_0 < R < 100a_0$). However, we observe a slight departure from the circular shape through the formation of "facets". These are not facets in the strict thermodynamical sense, but shape modulations resulting from a tendency of the interface to align with atomic planes which have low interface energies. Note that this phenomena is not present in homogeneous inclusions, where the amplitude of mode 6 oscillates but does not to grow until $R_c(6)$ is exceeded (c.f. Fig. 4.6). This behavior can be explained by a strain-induced change of the orientational dependence of the interfacial free-energy. This effect, and its dynamical consequences, will be described elsewhere. The small magnitude of this (nearly rate-independent) shape variation can be appreciated from Fig. 4.7 : the amplitude of mode 6 remains below 0.5% of the radius of the inclusion in the range studied. Also, the amplitude of mode 6 is not a linear function of the radius, i.e., large inclusions are not scaled-up versions of small ones. This may be a consequence of the interface contributions to the elastic energy which are not negligible for inclusions below a few tens of nanometers.[83] This highlights another strength of our model : because of its microscopic formulation, scale-dependent effects are automatically taken into account.

In the continuum limit, the strain inside a circular inclusion is independent of its size.[57] Thus, the normal Gibbs-Thomson behavior should be observed for hard inclusions (modulo the small contributions from facet formation). This is indeed the case, as shown in Fig. 4.8 for $\Delta c^B = 1\%$ (smaller supersaturations give similar results). The effect of the elasticity is thus to modify the values of C and $\Delta\mu_\infty$, in agreement with the sharp-interface results of Thornton and collaborators.[92] In addition, the figure shows rather strong oscillations in the chemical potential, with a period of $0.866a_0$. These oscillations are related to variations in the energy required to incorporate an additional atom along the interface. Indeed, because the inclusion's shape is not perfectly isotropic, the elastic energy cost for the addition of a B atom varies as a function of position along the interface. During growth, the available sites will be filled in order of increasing energy ; since the chemical potential corresponds to the free-energy change upon adding a B atom at the

interface, it will gradually increase until new low-energy sites become available, and the cycle repeats itself. A detailed analysis of this phenomenon, and its importance for coarsening, will be reported elsewhere.[68]

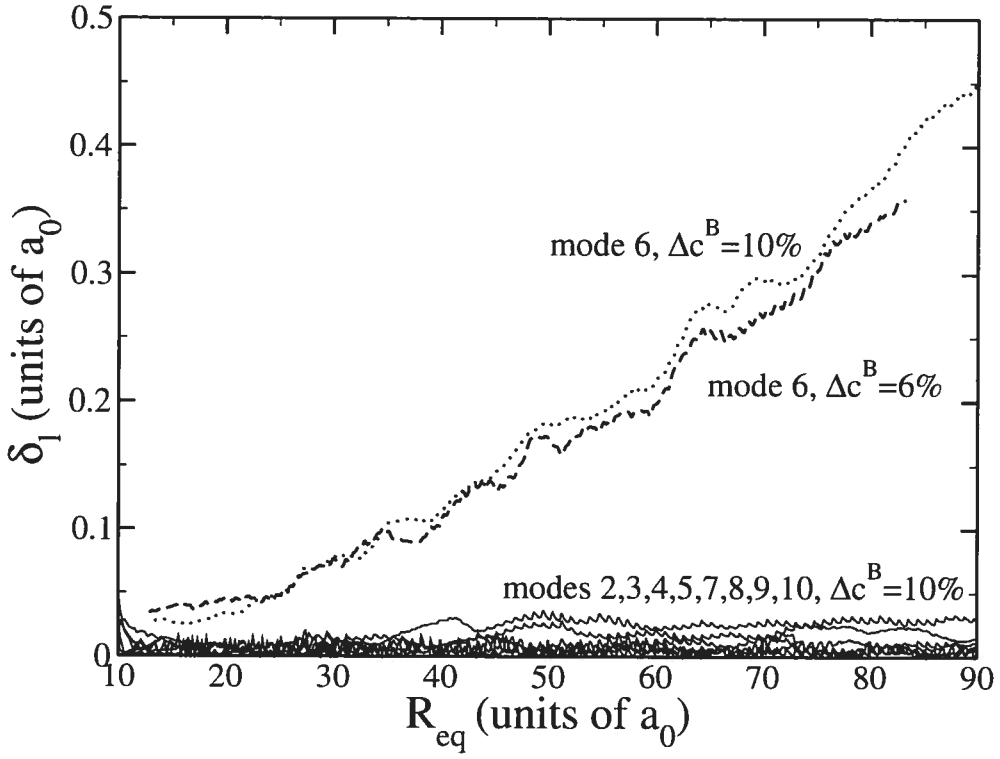

FIG. 4.7 – Amplitude of various perturbation modes as a function of size for hard growing inclusions : dotted line : mode 6 for $\Delta c^B = 10\%$; dashed line : mode 6 for $\Delta c^B = 6\%$; thin continuous lines : modes 2 to 10 excluding 6 for $\Delta c^B = 10\%$.

4.3.4.2 Morphological stability

As expected, elasticity does not induce qualitative changes in the equilibrium properties of hard inclusions compared to homogeneous inclusions. However, dynamical properties may be affected by elasticity. To clarify these matters, simulations of growth were here again carried out.

Figure 4.9 shows the evolution of the shape of a hard inclusion during growth. Compared to the homogeneous inclusion, the (quasi-)circular hard inclusion appears to be very stable : the formation of concave interfaces or tips is inhibited even at very large supersaturation. The "facets" mentioned earlier become more

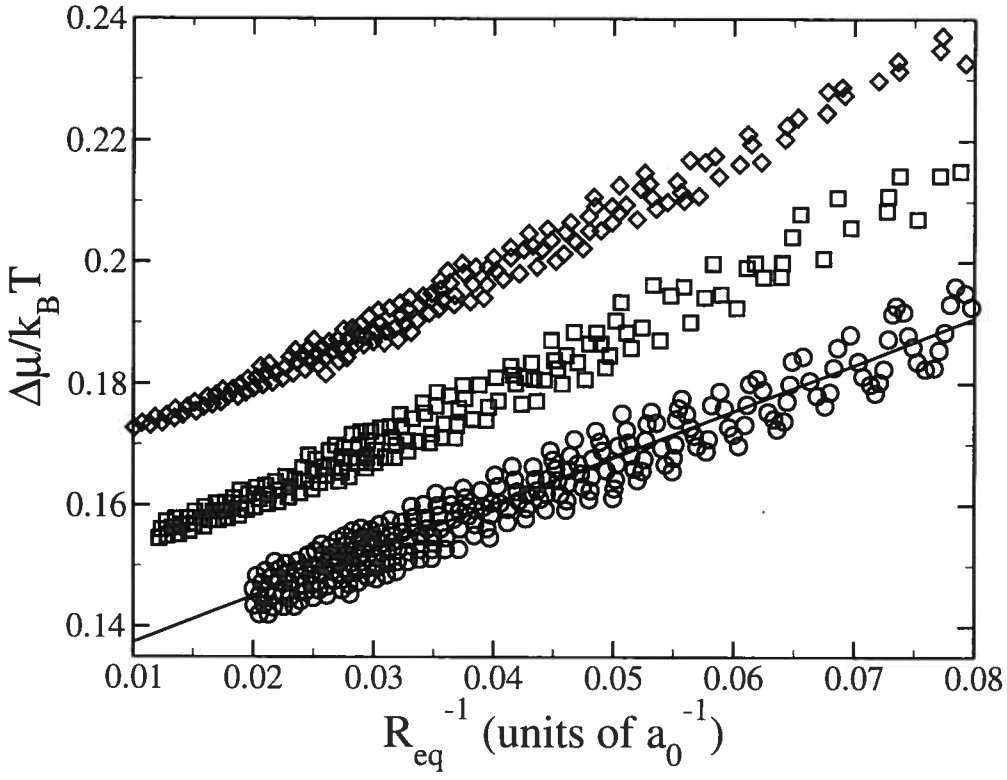

FIG. 4.8 – Dynamical Gibbs-Thomson relations for hard inclusions : circles : $\Delta c^B = 1\%$ (quasi-static growth) ; squares : $\Delta c^B = 4\%$; diamonds : $\Delta c^B = 10\%$; continuous line : fit to Eq. 4.16 for $\Delta c^B = 1\%$.

evident when comparing with a perfectly circular inclusion (dashed line). The small depressions appear when the orientation of the interface is nearly parallel to a low interface energy direction (occuring at odd multiples of $\pi/6$ in the present calculations). We may quantify these morphological changes using a modal decomposition ; the results are reported in Fig. 4.7.

We find that a perturbation along mode number 6 indeed develops as the size of the inclusion increases. The data also indicates that modes other than 6 are completely frozen for the range of sizes examined here : small variations can be observed but no amplification occurs. Since not even the low-index modes are allowed to grow (indicating high critical radii), it would be rather surprising that mode 6 could be dynamically amplified. In fact, our simulations show that the amplitude of mode 6 does not depend on supersaturation in the range probed here (see Fig. 4.7). Hence the growth of this mode is probably, rather, a manifestation of a change in the equilibrium shape of the inclusion, as mentioned above. These

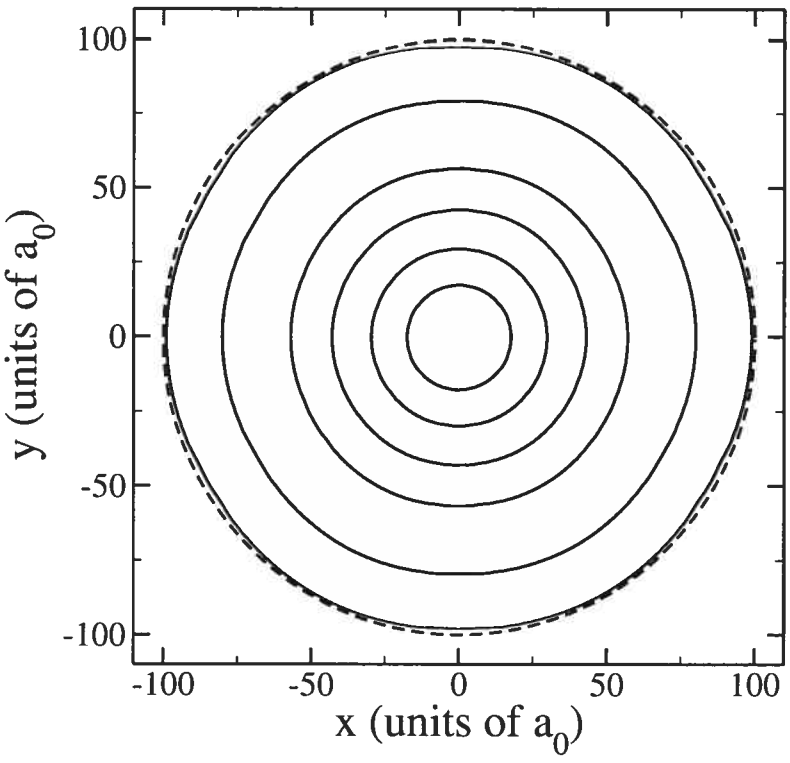

FIG. 4.9 – Evolution of a growing hard inclusion for $\Delta c^B = 10\%$ over $1 \times 10^{12}\tau_0$. The dashed line represents a perfectly circular inclusion with $R_{\text{eq}} = 100a_0$.

results indicate that elasticity leads to a very effective stabilization of circular inclusions in the size domain investigated.

This stabilization of the inclusion against perturbations was predicted by Leo and Sekerka [45] who extended the model of Mullins and Sekerka [56] to include the effects of elasticity. Qualitatively, they found that elasticity stabilizes hard inclusions by decreasing the growth rate of perturbations, by increasing the critical radius for mode amplification, and by decreasing the wavelength of the fastest growing perturbation. Quantitatively, this can be taken into account by modifying the FRI of the amplitude of perturbations compared to the elastically homogeneous case, which becomes (c.f. Eq. 4.17) :

$$\left(\frac{\dot{\delta}_l}{\delta_l}\right) / \left(\frac{\dot{R}}{R}\right) = (l-1)\left[1 - \frac{l+1}{l-1}\frac{g^{\text{el}}(l)}{2\gamma}R^*\right] \times \left[1 - \frac{R_c l}{R}\right]\left[1 - \frac{R^*}{R}\right]^{-1}, \tag{4.18}$$

where the critical radius for mode amplification is given by

$$R_c(l) = \frac{[(1/2)(l+2)(l+1)+1]R^*}{1 - \frac{l+1}{l-1}\frac{g^{\mathrm{el}}(l)}{2\gamma}R^*}, \tag{4.19}$$

with $g^{\mathrm{el}}(l)$ a factor related to the elastic properties of the material [$g^{\mathrm{el}}(l) = 0$ for homogeneous systems] and γ is the interface energy per unit length. From these equations, one can see that a positive value of $g^{\mathrm{el}}(l)$ (corresponding to hard inclusions) results in a decrease of the asymptotic FRI of every mode and an increase of the critical radius for mode amplification, $R_c(l)$, in agreement with our observations. In order to verify if our model quantitatively reproduces the predictions of Leo and Sekerka, we studied the decay of initially imposed perturbations similar to the case of homogeneous inclusions. Since the decay of perturbations is very fast for small sizes (except for low-index modes and high supersaturations), only the FRI of mode 2 at high supersaturation could be computed reliably. The results are presented in Fig. 4.10. By comparing with Fig. 4.4, one clearly observes the strong decrease of the FRI induced by elasticity, with an asymptotic value close to 0 already at a supersaturation of 7%. A reasonable fit to the data can be obtained using $g^{\mathrm{el}}(l)/2\gamma = 0.16$ and the values of R^* from homogeneous inclusions. While qualitative agreement can be claimed, it is difficult to give a quantitative assessment based only on the limited data available. Nevertheless, the general conclusions of Leo and Sekerka concerning the effect of elasticity are certainly verified.

4.3.4.3 Dynamical corrections to the GT relation

Even if dynamical effects do not induce shape changes in hard inclusions under the conditions studied here, the GT relations turn out to be strongly affected by growth, as can be appreciated from Fig. 4.8 where the GT curve is plotted for different levels of supersaturation. The results show that the normal GT behavior is observed during rapid growth. However, large shifts in the chemical potential as a function of supersaturation are measured. These are once again caused by solute trapping. The large value of these shifts compared to the homogeneous case is related to the strong coupling between strain and occupation probability fields, i.e.,

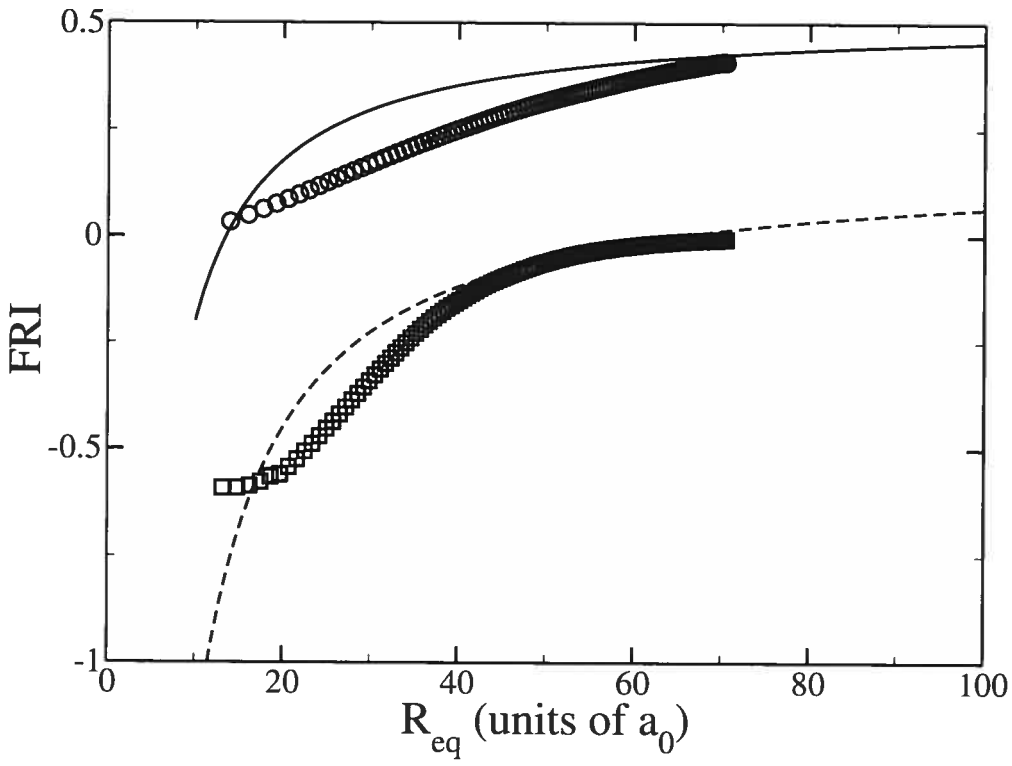

FIG. 4.10 – Fractional rate of increase of mode 2 for hard inclusions : circles : $\Delta c^B = 10\%$; squares : $\Delta c^B = 7\%$; continuous line : Eq. 4.18 with $g^{\rm el}(l)/2\gamma = 0.16$ and $R^* = 1.1a_0$; dashed line : Eq. 4.18 with $g^{\rm el}(l)/2\gamma = 0.16$ and $R^* = 1.8a_0$.

changes in the occupation probabilities induces changes in the strain field, which in turn affect the chemical potentials, causing further changes in the occupation probabilities, etc. While the shifts are larger here than in the homogeneous case, they are still small compared to the driving force (0.04 versus ~ 0.9 at $\Delta c^B = 10\%$ and 0.02 versus ~ 0.64 at $\Delta c^B = 4\%$), so, once again, the dynamical corrections are not expected to significantly affect the coarsening behavior of hard inclusions.

4.3.5 Soft inclusions

The case of soft inclusions is much more complex. Indeed, it is known since Eshelby [16] that a soft circular inclusion possesses higher elastic energy than an elliptical one. However, the interfacial component of the free energy favors the more compact circular shape. Thus, one would expect a transition from an interface-dominated regime with circular inclusions (at small sizes) to an elastic-dominated

regime with ellipsoidal inclusions (at large sizes). This transition was studied using very general symmetry considerations by Johnson *et al.* [33] who showed that, in two dimensions, a second-order transition in the aspect ratio of inclusions occurs as their size increases. In the following, the consequences of this shape transition on the equilibrium and dynamical properties of the inclusions will be explored.

4.3.5.1 Equilibrium properties

For reasons that will become clear below, growth simulations cannot be used to probe the equilibrium properties of soft inclusions. Instead, a sequence of relaxations for inclusions of different sizes with closed boundary conditions was performed. Using this method, the expected shape transition was indeed observed, as can be seen in the insets of Fig. 4.11. As predicted, there is a maximum size over which circular inclusions are not stable : they adopt instead increasingly eccentric elliptical shapes. Further, the onset of this shape transition is very abrupt, in agreement with the predictions of Johnson *et al.*.[33]

This figure also provides, through a GT plot, a quantitative view of the effect of the transition on the thermodynamic properties of the inclusions. First, the transition is clearly marked by a discontinuity in the slope at $R^{-1} = 0.59a_0^{-1}$ ($R \simeq 17a_0$). Second, the change in slope is very significant — a factor of about 2.5. This is consistent with the results of Li *et al.* [46] where the effect of the shape transition induced by anisotropic and inhomogeneous elasticity was studied. However, the magnitude of the change observed here is larger than reported in their study, probably due to the larger elastic inhomogeneity used here. The consequences of this change of slope on the coarsening behavior of a collection of soft inclusions will be discussed in Section 4.4.

4.3.5.2 Morphological stability

The presence of a shape transition during growth opens up the possibility of a complex behavior because metastable states, where both composition and shape are out of equilibrium, are now accessible. Since shape relaxation can be quite slow, the behavior of the inclusions is likely to be affected by dynamical effects over long

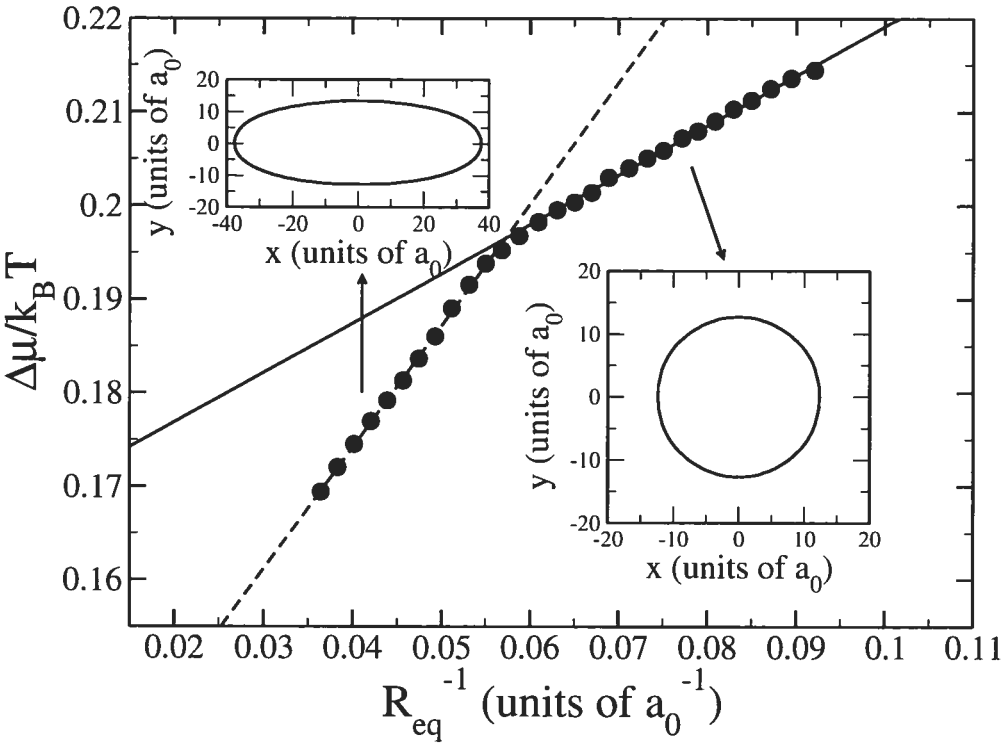

FIG. 4.11 – Equilibrium Gibbs-Thomson relation for soft inclusions. Left inset : equilibrium shape of the inclusion for $R_{eq} = 23a_0$; right inset : equilibrium shape of the inclusion for $r_{eq} = 13a_0$.

periods of time. To test this hypothesis, simulations for various growth rates were carried out.

On the basis of mere visual inspection, it is already clear that elasticity has a dramatic impact on the shape adopted by the inclusions during growth. Examples of such shapes are presented in Figs. 4.12, 4.13 and 4.14 for different values of the supersaturation. First, at very low supersaturation (0.1%), Fig. 4.12 shows that the equilibrium shape is preserved during growth : circles at small sizes, ellipses at larger sizes. In the latter regime, the major axis grows much more rapidly than the minor axis, leading to increasingly eccentric shapes. Second, for a slightly higher, but still very low supersaturation by homogeneous or hard inclusion standards (0.5%), the evolution of the system is completely different. Instead of a shape transition from circle to ellipse, a transition toward a threefold symmetric shape is observed, as shown in Fig. 4.13. Here, growth proceeds essentially from the tips of the inclusion. The important point is that this non-equilibrium shape is stable

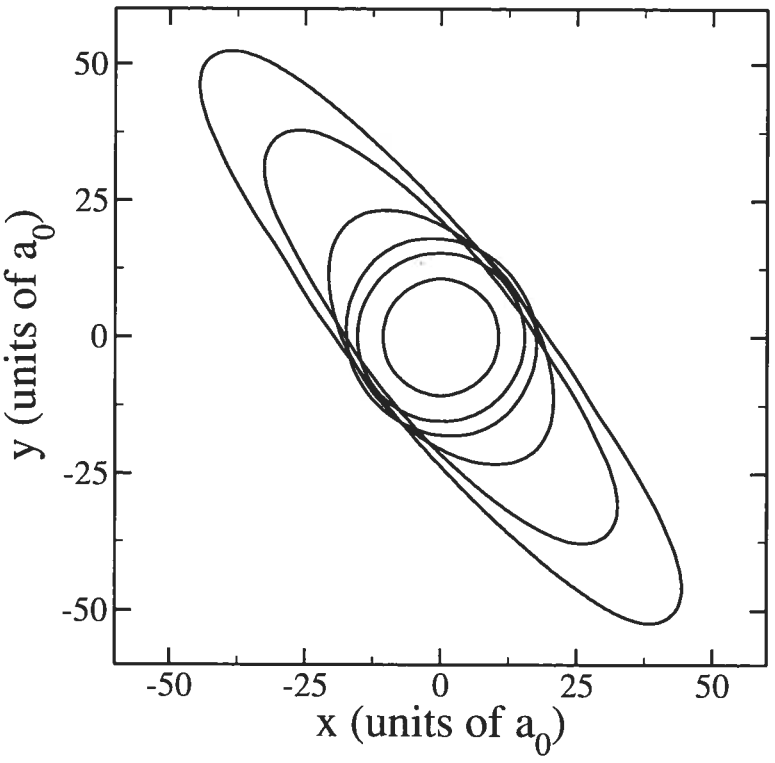

FIG. 4.12 – Evolution of a growing soft inclusion for $\Delta c^B = 0.1\%$ over $5 \times 10^{12}\tau_0$.

in time, i.e., it does not decay toward an ellipse as long as the flux is maintained. Surprisingly, only a very small supersaturation is required to achieve this. Third, for high supersaturations, Fig. 4.14 shows that sixfold symmetry is preferred. Once again, this shape is stable in time and growth occurs almost exclusively from the tips. It is interesting to note that we did not observe any tip-splitting instability in soft inclusions, unlike in the case of homogeneous inclusions, even at very high growth rates. Finally, for intermediate supersaturations, we also observed shapes with 4 or 5 tips. Note that, while there is a clear correlation between supersaturation and morphology, the relation between the two is not absolute : we observed that more than one type of inclusion may form from the same initial conditions.

The formation of shapes of increasingly higher order as supersaturation increases can be understood using the Mullins-Sekerka theory. Indeed, it predicts that the order of the fastest growing mode is proportional to $R^{*-1/2}$, and hence to the supersaturation. Thus, as the supersaturation increases, the leading mode, and therefore the shape of the inclusion, should be of increasingly higher order. For ho-

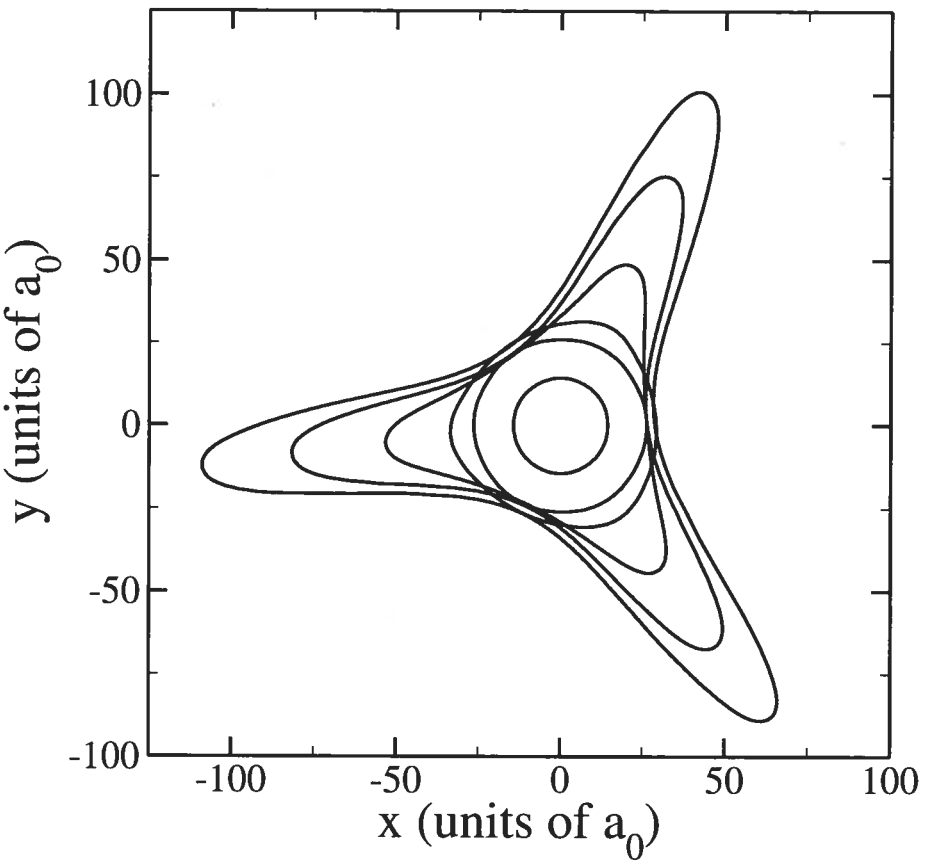

FIG. 4.13 – Evolution of a growing soft inclusion for $\Delta c^B = 0.5\%$ over $3 \times 10^{12}\tau_0$.

mogeneous inclusions, this tendency is overwhelmed by the preferential excitation of mode 6. For soft inclusions, it seems that other modes are able to overcome this disadvantage. An explanation for this will be offered later on in this section.

A quantitative appreciation of the development of the shape can be obtained from a modal analysis. This is reported in Fig. 4.15 for the system shown in Fig. 4.13. The first mode to be amplified significantly is mode 3; notice the very high rate at which it develops. Very soon after, two of its harmonics (6 and 9) are also strongly amplified through interactions with the leading mode. Concomitantly, we observe that the growth of other modes is either slowed down or reversed.

A closer look at the FRIs indicates that three regimes are in fact present. This is illustrated in Fig. 4.16 for mode 3 (similar results are obtained for other modes). The FRI initially increases rapidly to reach extremely high values — the asymptotic FRI for mode 3 is 2 in homogeneous systems (c.f. Eq. 4.17). This increase is followed

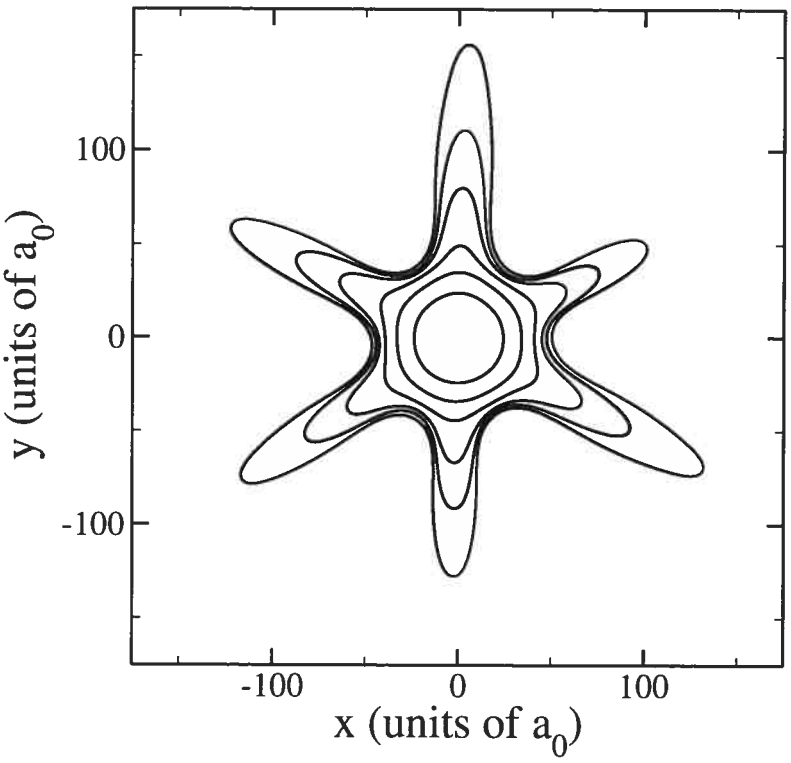

FIG. 4.14 – Evolution of a growing soft inclusion for $\Delta c^B = 10\%$ over $7 \times 10^{11} \tau_0$.

by a very rapid decrease, after which the FRI finally settles at a low value of about 1.5. The extremely high values of the FRI observed in the early stages of the simulation explain the sensitivity of the results to noise that was noted above : the least perturbation is exponentially amplified so that the balance between the different modes can easily be disrupted. These results also suggest that the rapid change of the FRI observed around $R = 30$ marks a change in perturbation growth mode. This possibility will be explored in Section 4.3.5.3.

When the amplitudes of the perturbations are sufficiently small that nonlinearities can be neglected, the behavior of the shape instability should be correctly described by the Leo-Sekerka generalization of the Mullins-Sekerka theory. In the case of soft inclusions, Eqs. 4.18 and 4.19 are still valid, but the predicted value of g^{el} is now negative. The effect of elasticity is therefore to increase the asymptotic FRIs and to decrease the critical radii compared to the homogeneous case, thus strongly favoring shape instabilities. Further, the asymptotic FRI is now proportional to R^*, so that very large values are possible even at small supersaturations.

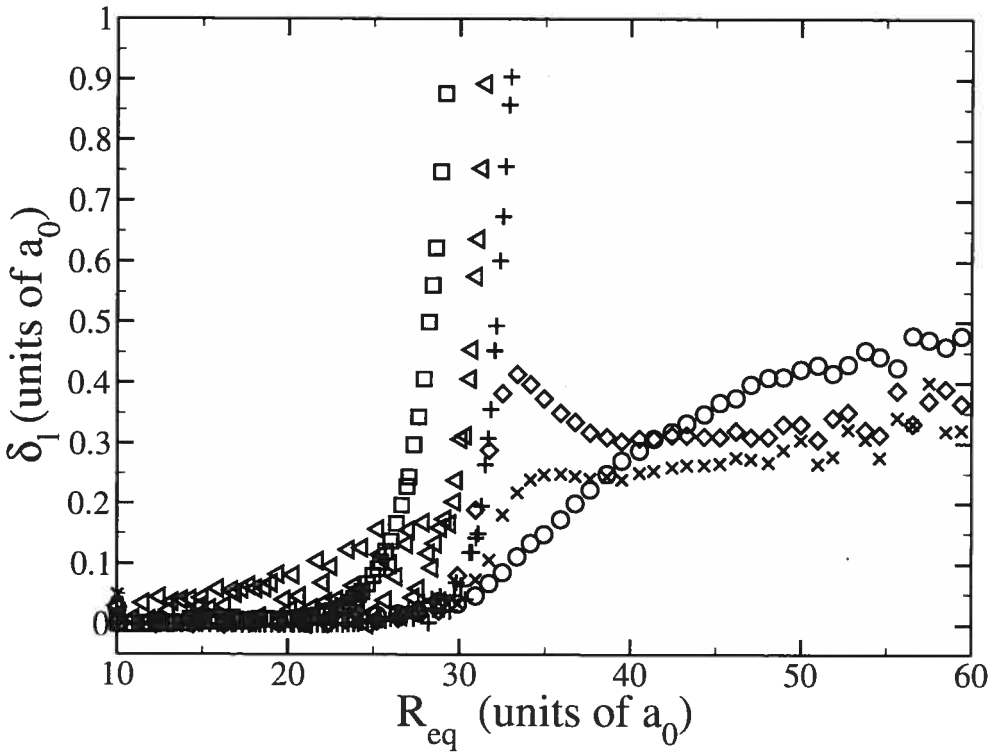

FIG. 4.15 – Amplitude of various perturbation modes as a function of inclusion size for a soft growing inclusions with $\Delta c^B = 0.5\%$: circles : mode 2; squares : mode 3; diamonds : mode 4; triangles : mode 6; $\times$: mode 7; crosses : mode 9.

This explains why the relative importance of the preferential excitation of mode 6 is now reduced : very small excitations of other modes can now be amplified very efficiently even before $R_c(6)$ is reached. In order to verify if the Leo-Sekerka theory adequately describes the shape evolution of the inclusions, growth simulations were carried out for inclusions initially perturbed by either mode 2 or 3. The FRI inferred from these simulations are reported in Figs. 4.17 and 4.18.

First, the expected increase of the FRI for mode 2 can clearly be seen in Fig. 4.17 (the asymptotic $R_{\text{eq}} \to \infty$ value of the FRI in the homogeneous case is unity for this mode, c.f. Eq. 4.17). Second, our results are in excellent agreement with the Leo-Sekerka model for $g^{\text{el}}(2)/2\gamma = -0.13$ and appropriate values of R^*. The value of $g^{\text{el}}(l)/2\gamma$ can be very precisely determined here because it fixes the radius at which the FRI for different values of R^* cross. Note that in order to get agreement with the simulations results, the theoretical FRI curves had to be shifted upward by 0.2 (see below).

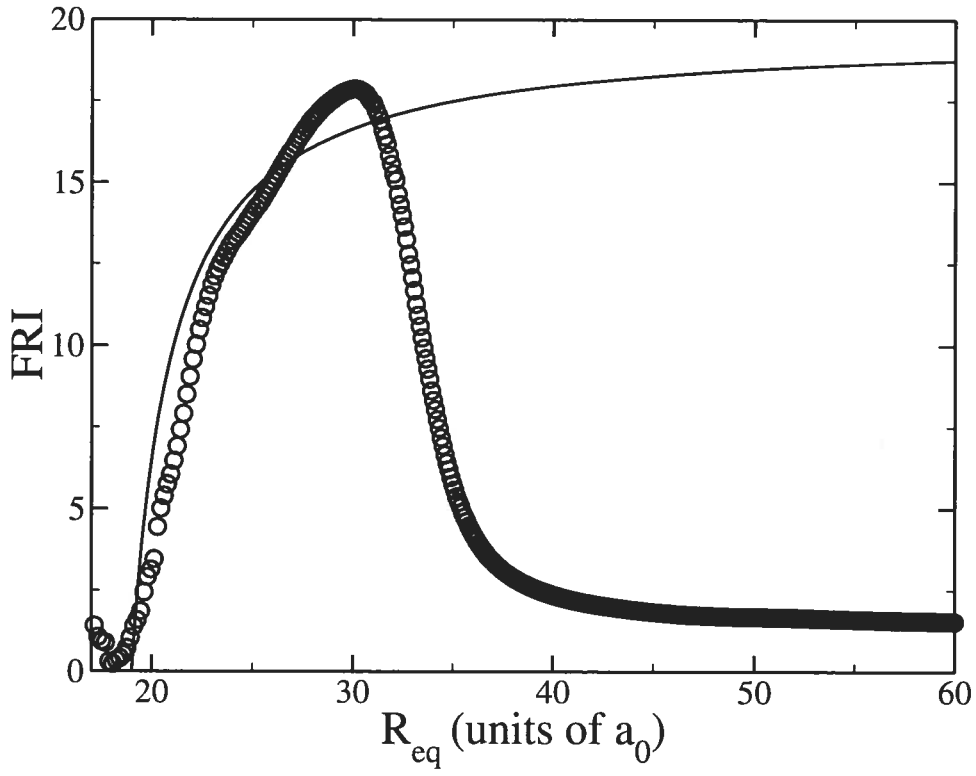

FIG. 4.16 – Fractional rate of increase of mode 3 for the soft inclusions depicted in Fig. 4.13 ($\Delta c^B = 0.5\%$) : circles : simulation results; continuous line Eq. 4.18 with $g^{\rm el}(l)/2\gamma = -0.26$ and $R^* = 17a_0$.

A similar analysis was performed for mode 3 and the results are reported in Fig. 4.18. Once again, large enhancements of the FRI (already a factor of two at small sizes and moderate supersaturation) are observed. Good agreement between simulation results and theoretical predictions is achieved with $g^{\rm el}(3)/2\gamma = -0.26$ and the values of R^* obtained from mode 2, and by shifting the theoretical curves upward by 0.2. Thus, as in the hard inclusion case, the Leo-Sekerka description of growth instabilities provides an adequate account of the simulation results for small inclusions.

The shift of the theoretical FRI curve, necessary to match the simulation data, indicates that another factor besides the Mullins-Sekerka instability contributes to the growth of shape perturbations. One possibility is that the quasi-static relaxation from a circular inclusion larger than the critical size to an elliptic inclusion involves the growth of sinusoidal perturbations, similar to those occurring via the Mullins-Sekerka mechanism, hence adding a static contribution to the FRI. In order to

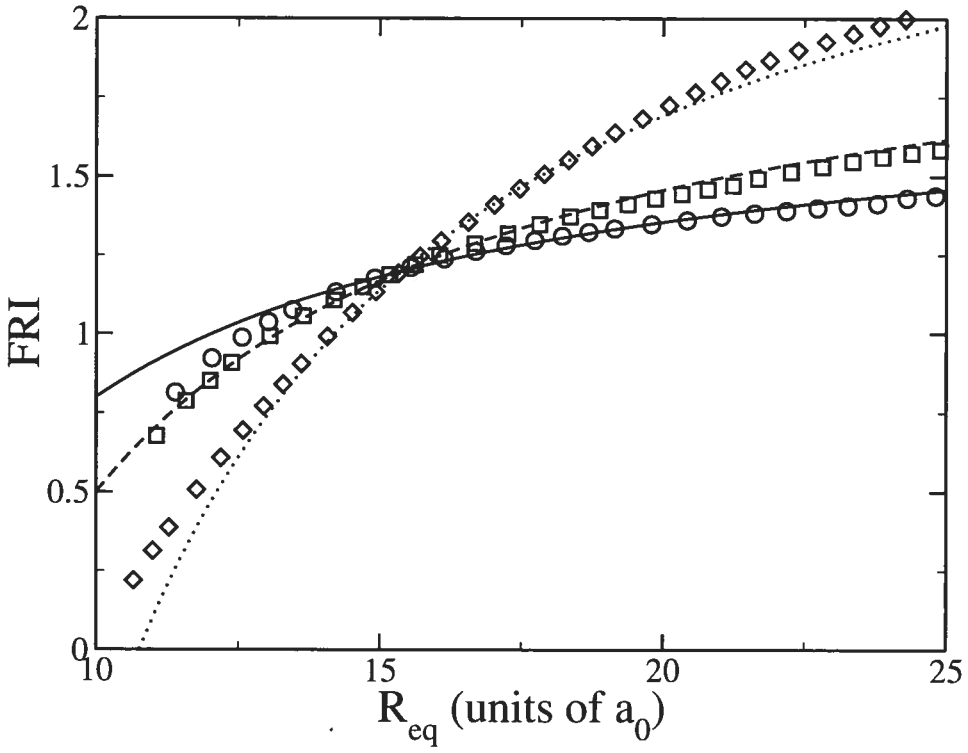

FIG. 4.17 – Fractional rate of increase of mode 2 for soft inclusions : circles : $\Delta c^B = 9\%$; squares : $\Delta c^B = 6\%$; diamonds : $\Delta c^B = 3\%$; continuous line : Eq. 4.18 with $g^{\rm el}(l)/2\gamma = -0.13$ and $R^* = 1.6a_0$; dashed line : Eq. 4.18 with $g^{\rm el}(l)/2\gamma = -0.13$ and $R^* = 2.5a_0$; dotted line : Eq. 4.18 with $g^{\rm el}(l)/2\gamma = -0.13$ and $R^* = 4.5a_0$. All lines are shifted upward by 0.2.

investigate this hypothesis, we studied the relaxation of a circular inclusion with $R = 40a_0$ (for which the equilibrium shape is an ellipse) with closed boundary conditions, i.e., without any diffusion fluxes in or out of the cell. The evolution of the shape of the inclusion and of its distance to equilibrium (as measured by the difference between its chemical potentials and those of an equilibrium inclusion of the same size) is reported in Fig. 4.19. This figure shows that the relaxation of a circular inclusion towards its equilibrium shape indeed occurs by a succession of transitions, from high to low symmetry structures, and not by a continuous and smooth deformation of the circle to an ellipse. This can be seen both in the insets, where the inclusion shape is reported, and in the main graph, where the evolution of $\Delta\mu$ is presented. Simulations show that the order of the dominant quasi-static shape perturbation increases with size, from 2 close to the equilibrium transition

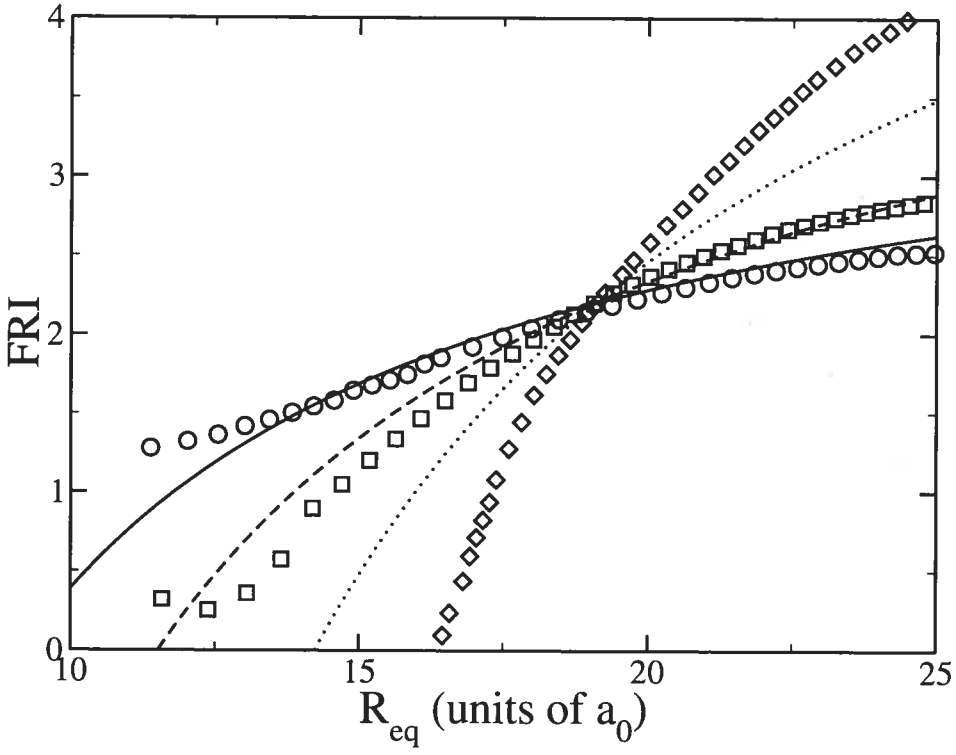

FIG. 4.18 – Fractional rate of increase of mode 3 for soft inclusions : circles : $\Delta c^B = 9\%$; squares : $\Delta c^B = 6\%$; diamonds : $\Delta c^B = 3\%$; continuous line : Eq. 4.18 with $g^{\mathrm{el}}(l)/2\gamma = -0.26$ and $R^* = 1.6a_0$; dashed line : Eq. 4.18 with $g^{\mathrm{el}}(l)/2\gamma = -0.26$ and $R^* = 2.5a_0$; dotted line : Eq. 4.18 with $g^{\mathrm{el}}(l)/2\gamma = -0.26$ and $R^* = 4.5a_0$. All lines are shifted upward by 0.2.

point to 12 for large inclusions. The quasi-static relaxation pathway thus provides an explanation for the unexpectedly large FRI and acts so as to further promote the formation of high-order symmetric shapes. Very similar relaxation patterns have been observed using conventional microscopic methods.[42, 43] This further shows that our model adequatly retains the essential physics from the discrete formulation. Note, however, that the lifetime of highly symmetry non-equilibrium shapes cannot be estimated reliably using our model since symmetry is in part broken by numerical noise and not by thermal fluctuations.

4.3.5.3 Late stages of perturbation growth

The above discussion suggests that the evolution of the shape of the inclusions should, for the most part, be governed by the Mullins-Sekerka instability. Compa-

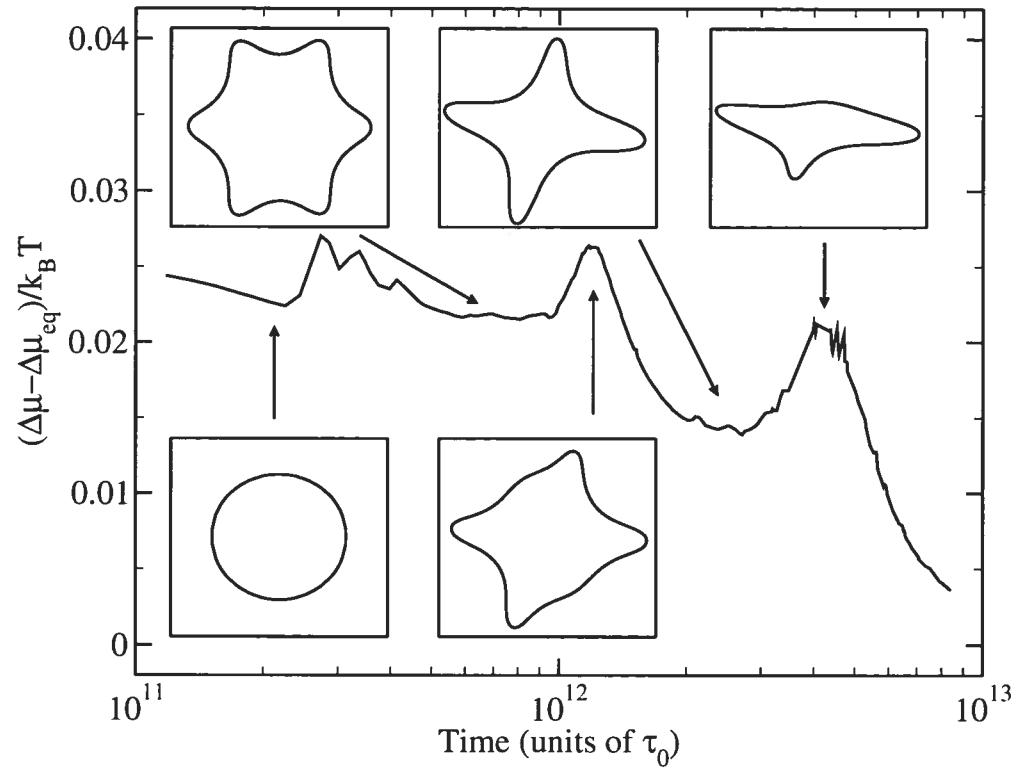

FIG. 4.19 – Relaxation of a circular inclusion with $R_{eq} = 40a_0$. Insets : shape of the inclusion at different moments during the relaxation process.

ring the predictions of the model with the evolution of mode 3 presented in Fig. 4.16, we see that good agreement is achieved here only for inclusions smaller than $R = 30a_0$. For larger sizes, the FRI sharply decreases in contradiction with the behavior predicted by this model. A possible explanation is that the Mullins-Sekerka theory breaks down because of nonlinear interactions between modes similar to that observed in Fig. 4.5. However, the amplitude of mode 3 is roughly 3% of the radius of the inclusion at $R = 30a_0$, compared with 10 to 15% in the homogeneous case, so that, while nonlinear effect are probably affecting the results, it is unlikely that they could induce change in behavior of such large extent.

The nature of the new regime can be inferred from Fig. 4.13 which shows that growth occurs exclusively at the tips in the later stage of evolution, while the regions close to the core are frozen. The signature of this regime can indeed be identified by examining the activity maps of the system during growth, an example of which is presented in Fig. 4.20 for B atoms. The data shows that the activity is relatively

uniform inside the inclusion, except at the end of the tips where minima form. Since diffusion of B atoms occurs from regions of high activity to regions of low activity, these minima yield funnels in their neighborhood, channeling solute atoms toward the tips. This channeling effect implies that regions close to the core of the inclusion receive less solute atoms, in agreement with the observations. Fig. 4.16 can thus be understood as follows : i) in the early stages of growth, perturbations grow by a Mullins-Sekerka mechanism ; ii) once small tips are formed, the channeling effect set in, causing a gradual shift toward a more directed growth mode and the inhibition of the mode instability owing to the increasingly anisotropic solute diffusion ; during this intermediate regime, the FRIs decrease ; iii) finally, at larger sizes, channeling is so efficient that few solute atoms reach the core of the inclusions, thus strongly suppressing mode instability. This also explains why tip splitting is not observed as could have been expected at an unstable interface.

Since this directed growth regime is not observed for homogeneous inclusions, it is probably a byproduct of elasticity. In order to evaluate this possibility, we carried out the elastic relaxation of a pure-B inclusion of similar shape as the inclusion shown in Fig. 4.20 within a pure-A matrix. This enables us to obtain the local elastic energies everywhere in the inclusion. These results are reported in Fig. 4.21. The similarity with Fig. 4.20 is striking : activity and elastic energy minima at the tips of the inclusion coincide, showing that the tips grow because they correspond to elastically favored regions where the strain energy is small.

4.3.5.4 Dynamical corrections to the GT relation

Having analyzed the shape evolution occurring during the growth of soft inclusions, we now turn to the study of the consequences of these morphological changes on the coarsening behavior of the inclusions.

The GT curves for the inclusions pictured in Figs. 4.12, 4.13 and 4.14 are reported in Fig. 4.22. Considering first the smallest supersaturation ($\Delta c^B = 0.1\%$), we see that $\Delta\mu/k_BT$ follows closely the equilibrium behavior at small sizes. Further, the transition toward the elliptic shape occurs near the equilibrium transition point ($R_{\text{eq}}^{-1} = 0.59a_0^{-1}$, $R_{\text{eq}} = 17a_0$). However, a small but significant deviation from

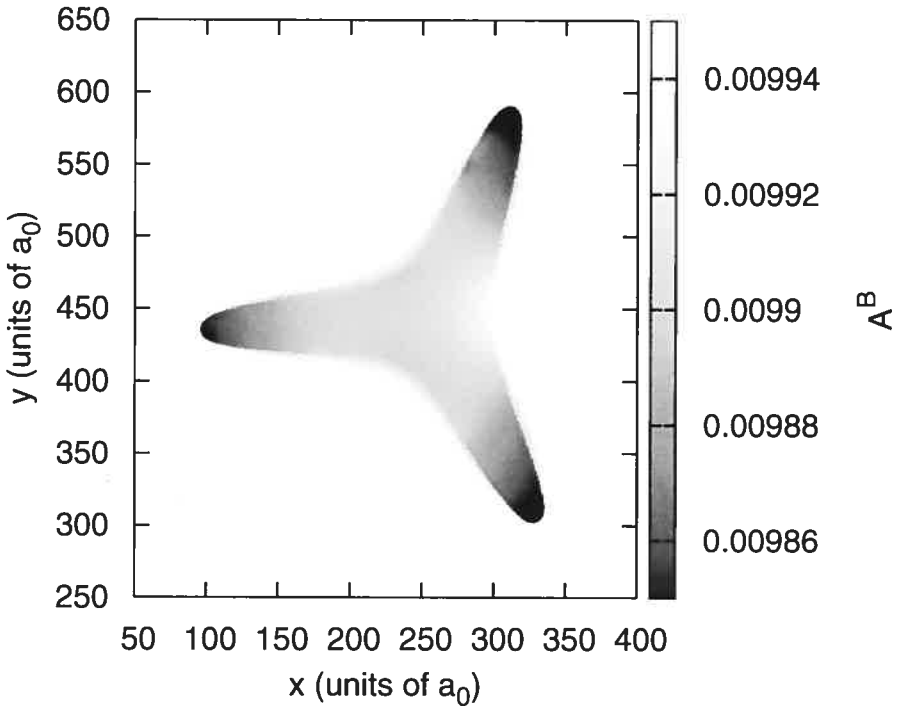

FIG. 4.20 – Activity map of B atoms for a soft inclusion for $\Delta c^B = 0.5\%$.

the equilibrium curve is observed as the size increases. This deviation does not resorb but, on the contrary, increases steadily, signaling the existence of persistent deviations from the equilibrium shape, even at this very low supersaturation.

This is further illustrated by the analysis of the GT curve of the three-branched inclusion depicted in Fig. 4.13, which corresponds to a slightly higher supersaturation ($\Delta c^B = 0.5\%$). Now the transition away from the circular shape begins at about $R^{-1} = 0.33{a_0}^{-1}$ ($R = 33a_0$). At this point, the inclusion is already strongly out of equilibrium since it followed the circular branch of the equilibrium GT relation deeply into the elliptic region. The GT curve then drops abruptly. This abrupt change corresponds to the beginning of the very fast amplification of mode 3. A similar behavior is observed for the highest supersaturation ($\Delta c^B = 10\%$) except that the shape transition now occurs at a very large radius (around $R = 50a_0$). The slope of the GT curves are also different in the large inclusion region, showing that this measurement is very sensitive to the topology of the inclusions. This dynamical

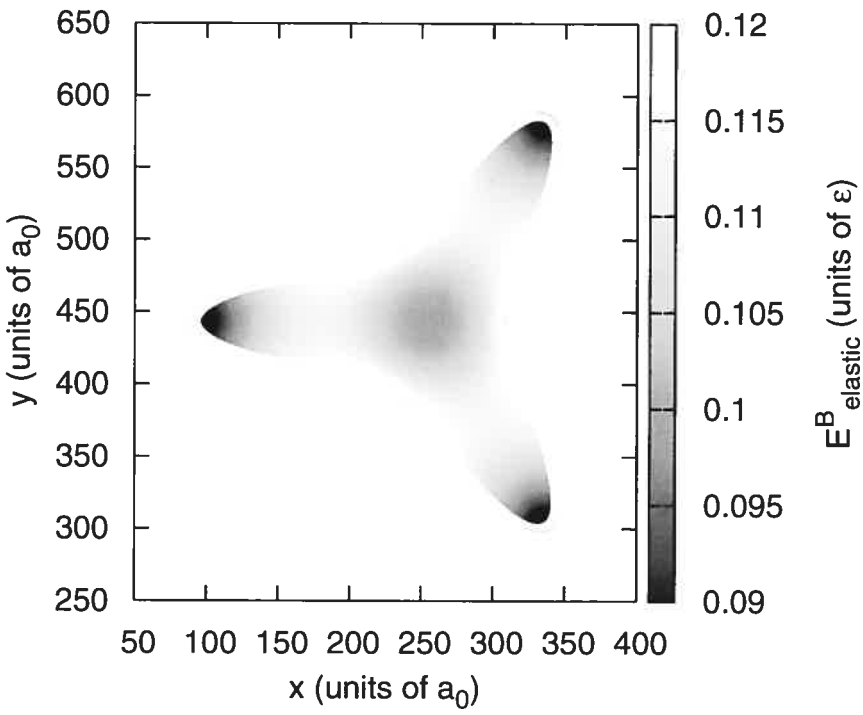

FIG. 4.21 – Elastic energy map of B atoms for a pure-B soft inclusion.

GT relation enables us to estimate the extent of the dynamical corrections on the coarsening behavior of the inclusion. The driving forces imposed by the supersaturated matrix are approximately 0.05, 0.13 and 0.67 for $\Delta c^B = 0.1\%, 0.5\%$ and 10%, respectively, compared to dynamical corrections of about $0.01 - 0.03$. These results indicate that dynamical effects can significantly alter the coarsening behavior of soft inclusions, particularly at low supersaturation.

The impact of the morphology on the growth dynamics can be quantified more precisely by taking advantage of the sensitivity of the growth process to initial conditions. Using this fact, it is possible to select the number of tips of the growing inclusion and hence to study the evolution of inclusions of different shapes in the same environment. The result of such calculation is shown in Fig. 4.23 where the evolution of the ratio of the areas of inclusions of different shapes to that of a twofold symmetric one is reported. The data shows that the difference of area between inclusions of different shapes is of the order of 10% for $\Delta c^B = 0.5\%$ in

the range of sizes probed here, in agreement with the rough estimate provided above. These effects could even be stronger for smaller supersaturations and larger inclusions, typical of the later stages of coarsening, since the FRI's will be higher in this case.

This example clearly shows that the coarsening rate of a soft inclusion is quite sensitive to its shape. Since the shape is also unstable against small changes in growth conditions, the equilibrium GT relation alone does not provide an adequate account of the growth dynamics, even in an idealized environment. Thus, in complex configurations typical of realistic microstructures, direct elastic interactions or modulations in the solute concentration field could further affect the shape of the inclusions, and hence strongly modify their growth dynamics. This will be the subject of future investigation.

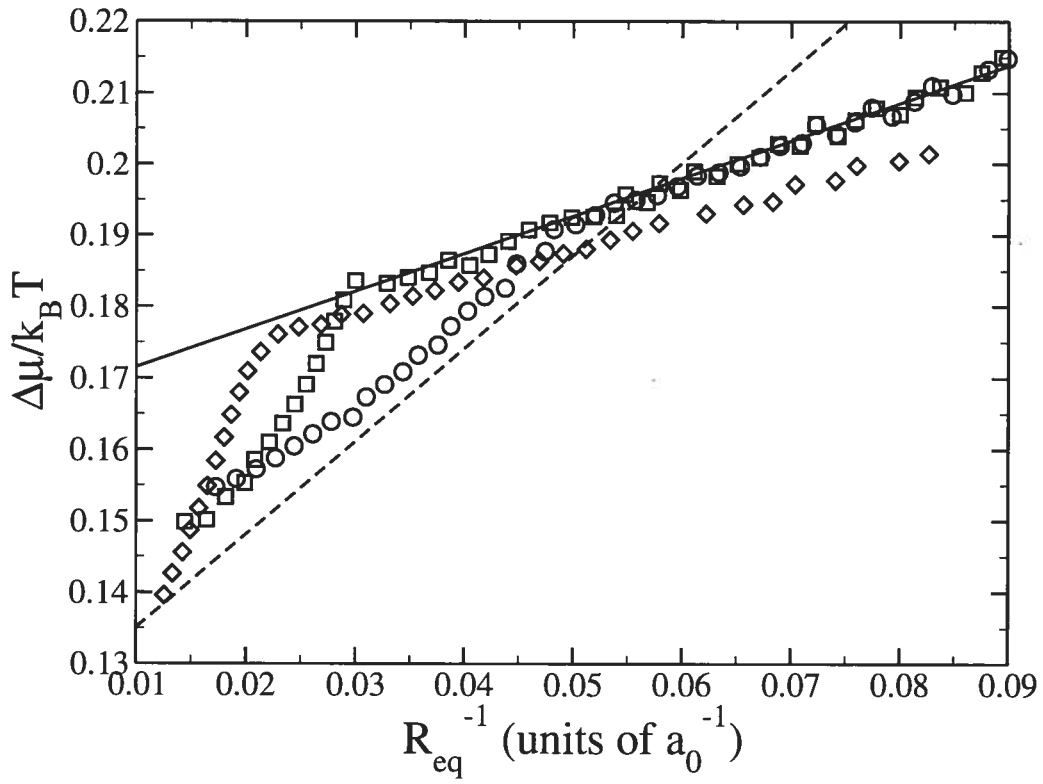

FIG. 4.22 – Dynamical Gibbs-Thomson relations for initially circular soft inclusions : circles : $\Delta c^B = 0.1\%$; squares : $\Delta c^B = 0.5\%$; diamonds : $\Delta c^B = 10\%$. The continuous and dashed lines are fits to the two sections of the equilibrium Gibbs-Thomson relation (c.f. Fig. 4.11).

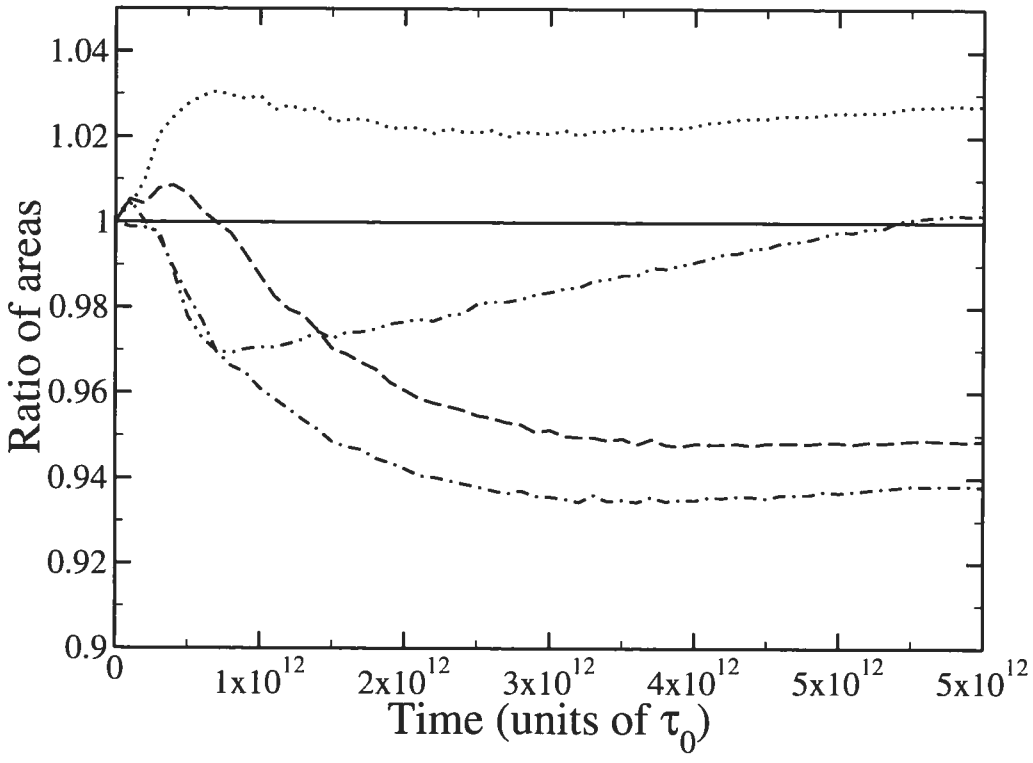

FIG. 4.23 – Ratio of the areas of inclusions of different shapes to that of a twofold symmetric inclusion for $\Delta c^B = 0.5\%$: continuous line : twofold symmetric inclusion ; dotted line : threefold symmetric inclusion ; dashed line : fourfold symmetric inclusion ; dash-dotted line : fivefold symmetric inclusion ; dash-dot-dotted line : sixfold symmetric inclusion.

4.4 Discussion

From the previous results, it is possible to infer the consequences of elasticity on the coarsening of a collection of inclusions, as long as direct elastic interactions between inclusions remain small compared to inclusion-matrix interactions. In this dilute limit (which also implies quasi-static growth), it is well known that the coarsening behavior of a collection of inclusions is adequately described by the Lifshitz-Slyozov-Wagner (LSW) model of ripening.[47] This model provides an evolution equation for the size-distribution $f(t, R)$ of a collection of inclusions interacting diffusively, of the form :

$$\frac{\partial f(t,R)}{\partial t} = -\frac{\partial}{\partial R}\left[\frac{dR}{dt} f(t,R)\right], \tag{4.20}$$

where dR/dt is the rate at which an inclusion of radius R grows. In the context of the LSW model, this rate is given by :

$$\frac{dR}{dt} \propto \frac{1}{R}[\mathcal{A}_m - \mathcal{A}_I(R)], \tag{4.21}$$

where $\mathcal{A}_m$ $[\mathcal{A}_I(R)]$ is the activity inside the matrix [inclusion]. For simplicity, we ignore the presence of vacancies in this derivation, so that a single activity can be used. In this model, the activity of the matrix is taken to be proportional to the solute supersaturation $\Delta(t)$, while the activity of the inclusion follows the Gibbs-Thomson behavior. In order to close the system of equations, we must enforce solute conservation, i.e., :

$$Q_0 = \Delta(t) + \int_0^\infty \pi R^2 f(R,t)\, dR \tag{4.22}$$

where Q_0 is the initial total supersaturation. Without loss of generality, we adopt the following convention :

$$\mathcal{A}_m(t) = \quad \Delta(t) \tag{4.23}$$

$$\mathcal{A}_i(t) = \quad (1-C)/R_t + 1/R \quad \text{if } R \leq R_t \tag{4.24}$$

$$C/R \quad \text{if } R > R_t, \tag{4.25}$$

with R_t is the radius at which the shape transition occurs and C is the Gibbs-Thomson prefactor for inclusions larger than R_t.

We numerically carried out the integration of Eq. 4.20 and computed the average inclusion size as a function of time from $f(R,t)$. The results are presented in Fig. 4.24 for values of C ranging from 1 to 5. First, for $C = 1$, corresponding to either homogeneous or hard inclusions, the usual $< R >= Kt^{1/3}$ behavior is obtained, as expected. For values of C greater than 1 (soft inclusions), two different regimes are observed. First, at low radius, the normal $< R >= Kt^{1/3}$ is seen, since in this range the Gibbs-Thomson relation is unchanged. On the other hand, for sizes much larger than R_t, a $t^{1/3}$ behavior is also observed, albeit with an increased prefactor K'. This is also expected, since most of the size distribution function is

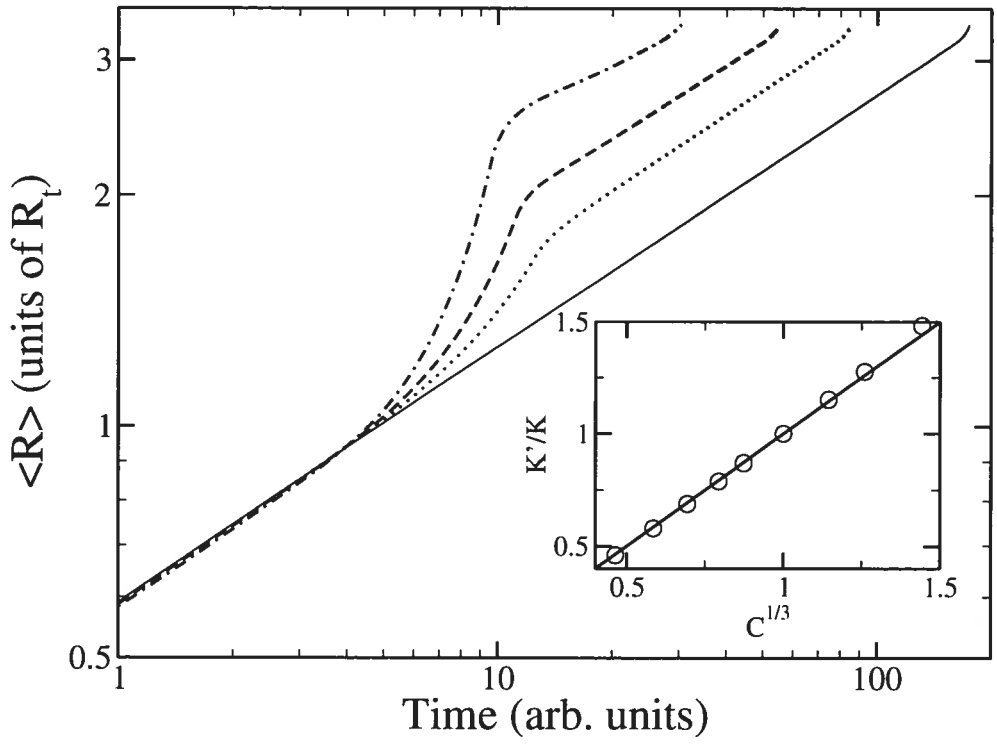

FIG. 4.24 – Time evolution of the average inclusion size for a LSW model of coarsening with different values of the parameter C (see text) : continuous line : $C = 1$; dotted line : $C = 2$; dashed line : $C = 3$; dash-dotted line : $C = 5$. Inset : dependence of the ratio of the prefactors K'/K on the value of C. Symbols : measured values; continuous line : $K'/K = C^{1/3}$.

then located in a regime where the activity is again proportional to $1/R$. These two regimes are connected by a cross-over region whose width is related to the width of $f(R,t)$. The inset of Fig. 4.24 shows that the prefactor in the large inclusion regime is given by $K'/K = C^{1/3}$. Thus, our calculations show that, at low volume fraction, elastic effects will not affect the scaling exponent of the average size versus time but instead will slightly modify the prefactor. These findings corroborate the results and analysis of Thornton *et al.* [90] concerning the coarsening behavior of a system of inclusions with homogeneous and anisotropic elasticity, where a similar shape transition is also observed.

In the above calculations, it was assumed that inclusions are in their equilibrium configuration relative to their size. However, as the volume fraction increases, larger chemical potential gradients would be allowed to form, thus increasing growth

or evaporation rates of inclusions. In this context, dynamical effects could affect the coarsening behavior in a more profound way. While homogeneous or hard inclusions were shown to be largely immune to such effects, soft inclusions are much more prone to shape transitions. These transitions in turn affect their coarsening behavior, as shown in the previous section. While, the normal LSW regime will eventually be restored as the supersaturation of the matrix decreases, the duration of the initial transient could potentially be much longer than for homogeneous or hard inclusions. On the other hand, an increase of the volume fraction will eventually lead to direct interactions between inclusions through the strain field. These interactions are known to drastically affect both the morphology of the inclusion and their coarsening rate (see Ref. [22] for a recent review). An analysis of the impact of direct interactions using the TDDFT model is underway.

Note that this analysis did not take into account the possibility of oscillations of the chemical potential as a function of size, as observed for hard inclusions in Fig. 4.8. A detailed study of the origin of these oscillations and their significance for coarsening will be presented elsewhere.[68]

4.5 Conclusion

The results of section 4.3 demonstrate that our multiscale TDDFT-based model is able to reproduce known equilibrium and dynamical properties of isolated inclusions, and to reveal new insights about the role of elasticity in their evolution. Indeed, for elastically homogeneous systems, the classical GT relation for circular inclusions is recovered. Under growth conditions, the observed shape instabilities are in quantitative agreement with the Mullins-Sekerka theory. Our model also enabled us to identify the mechanism via which certain modes are preferentially excited by the discrete atomic lattice. Departure from the predictions of the linear MS model were observed and described. Finally, the impact of the shape perturbations and of solute trapping on the chemical potentials of the inclusions were quantified and shown to be negligible in the conditions we studied.

Turning to hard inclusions, we observed that the circular shape is stable and that the form of the GT relation is not affected by elasticity, as expected. We

also observed that elasticity stabilizes hard inclusions against shape perturbations during growth, in agreement with the theory of Leo and Sekerka. The magnitude of the solute trapping correction to the chemical potential is observed to be large compared to the homogeneous case because of the coupling between the strain and concentration fields. However, this coupling proves to be too weak to significantly affect the coarsening rate of the inclusions.

Finally, for soft inclusions, we observed the transition from circular shape at small radius to elliptic shape at larger radius, and showed that the general shape of the GT curve is not affected by this transition, but that its slope changes abruptly at the transition point. Concerning dynamical properties, we observed that the shape of soft inclusions is extremely sensitive to the growth rate, even at very low supersaturation, in quantitative agreement with the model of Leo and Sekerka. Strongly out-of-equilibrium shapes are shown to initially form by a mode instability mechanism and to grow by an elastically-induced tip growing mechanism. The dynamical GT relations are shown to strongly depend on the shape adopted by the inclusions so that dynamical corrections have non-negligible effects on the growth rate of the inclusions, even at very low supersaturation.

This first application of the TDDFT framework to multiscale calculation of elastically homogeneous and inhomogeneous systems shows that the method produces results that are in good agreement with analytical models and other simulation methods concerning both equilibrium and dynamical quantities. It also serves to illustrate the advantages of the method : the only input is the potential through which atoms interact ; scale-dependent effects stemming from the existence of a fundamental length scale (the lattice parameter) are automatically taken into account and the multiscale formulation enables large systems to be treated at a fraction of the cost of Monte Carlo methods, etc. While the present formulation of TDDFT, even in its multiscale version, cannot compete with macro or mesoscopic methods to simulate large systems with complex microstructures, it has proven to be a good candidate to bridge the gap between Monte Carlo methods and phase-field models, and to allow the detailed investigation of intermediate-size systems.

4.6 Acknowledgments

The authors thank Dr. Ralf Meyer for stimulating discussions. This work has been supported by grants from the Canadian Natural Sciences and Engineering Research Council (NSERC) and Québec's *Fonds Québécois de la Recherche sur la Nature et les Technologies* (FQRNT). We are indebted to the *Réseau Québécois de Calcul Haute Performance* (RQCHP) for generous allocations of computer resources.

CHAPITRE 5

FACETTAGE CINÉTIQUE ET MÛRISSEMENT ANORMAL DANS LES SYSTÈMES MULTIPHASES ÉLASTIQUEMENT INHOMOGÈNES

Ce chapitre est constitué du premier d'une série de deux articles où, à l'aide du modèle TDDFT présenté au chapitre 4, nous étudions l'impact des contraintes élastiques d'interface sur le comportement d'inclusions isolées. Nous observons que, en fonction des paramètres décrivant l'interaction entre les différents types d'atomes, les effets élastiques peuvent modifier considérablement les énergies impliquées dans l'addition d'atomes de soluté à la surface de l'inclusion. Ces modifications sont suffisantes pour changer le mode de croissance de l'interface, de continu à couche-par-couche. Dans le cas de la croissance continue, l'inclusion conserve sa forme circulaire et son potentiel chimique est bien décrit par une relation de Gibbs-Thomson conventionnelle. Dans le cas couche-par-couche, l'inclusion subit un facettage cinétique important dû à l'apparition d'une importante barrière de nucléation d'origine élastique. En plus de modifier la forme de l'inclusion, cette barrière cause une forte oscillation dans le potentiel chimique. Nous suggérons que cette oscillation est suffisamment importante pour ralentir considérablement le mûrissement en induisant une transition entre un mode de mûrissement normal limité par la diffusion et un autre limité par la nucléation.

Ce chapitre a été soumis pour publication dans la revue *Physical Review Letters*. En tant que premier auteur de cet article, ma contribution a consisté en :

1. La création du modèle utilisé pour effectuer les calculs numériques.
2. L'implémentation des programmes informatiques nécessaires aux calculs.
3. L'exécution des calculs requis.
4. L'analyse et l'interprétation des données.
5. La rédaction de la version initiale de l'article.
6. La réalisation des modifications suggérées par le co-auteur de l'article.

Kinetic facetting and anomalous coarsening in elastically inhomogeneous multiphase systems

Danny Perez and Laurent J. Lewis

Département de physique et Regroupement Québécois sur les Matériaux de Pointe (RQMP), Université de Montréal, C. P. 6128 Succursale Centre-Ville, Montréal (Québec) H3C 3J7, Canada

With a view of finding a route toward microstructural stability in alloys, we numerically study the impact of elastic inhomogeneities on the growth of inclusions in multiphase systems. We show that growth can proceed either continuously at rough interfaces, or in a layer-by-layer fashion following an elastically-induced kinetic facetting process. In the former case, the chemical potential of the inclusions is a smooth function of size, while in the latter case, elasticity increases the barrier for nucleation of new terraces on the facets, leading to an oscillatory behavior of the chemical potential and hence a strong resistance against coarsening, opening up the possibility to stabilize the structure.

It has long been recognized that materials owe many of their physical properties to both chemical composition and microstructure. While the former is relatively easy to control experimentally, the latter is the result of a delicate balance between different competing factors. For example — as is the case in the present study — one may be concerned with the evolution of multiphase alloys where inclusions of a given phase are embedded within a matrix of different chemical composition. In this situation, the main thermodynamic driving-force is usually the capillarity-driven reduction of the interfacial free-energy ; the Lifshitz-Sloyzov-Wagner (LSW) theory of coarsening [47] then predicts the average inclusion size to increase as either $t^{1/3}$ (diffusion-limited case) or $t^{1/2}$ (attachment-detachment-limited case).

While successful in many contexts, the LSW theory only applies to capillarity-driven systems. For elastically inhomogeneous systems (the phases have different lattice and elastic constants), the contribution of the elastic energy must also be taken into account. For these materials, experiments show important deviations from the LSW predictions [22, 104], the most striking being a dramatic slowdown of the coarsening dynamics once a critical inclusion size is reached (see, e.g., Ref. [65]).

This peculiar behavior may lead to very important technological applications by improving the stability of microstructures, thus alleviating the effects of aging.

However, despite numerous theoretical efforts, the explanation of this phenomenon remains controversial. Indeed, recent phase-field calculations show, rather, a gradual decrease of the coarsening exponent as the degree of elastic inhomogeneity increases [107], casting doubts on previous reports of kinetically frozen states obtained using a similar model with approximate elastic energies [60]. Other continuous models also fail to demonstrate the occurence of stable, multi-inclusion configurations, except in cases where nearly-periodic initial conditions are imposed [35, 63, 80, 84]. This suggests that models based on a continuous, rather than atomistic, description of the microstructure fail to capture the crucial aspects of the coarsening process. It is thus possible that these limitations take root in the manner in which the interfaces are modeled (i.e., either diffuse or structureless at the atomic scale).

In this Letter we study the growth of inclusions in elastically inhomogeneous multiphase systems using a multi- (micro- to meso-) scale model we introduced recently [68]. We show that, depending on the interaction potential between different species, growth proceeds either continuously at rough interfaces, or in a layer-by-layer fashion at kinetically-facetted interfaces. Facetting results from an increase of the barrier for the nucleation of new terraces on the surface of the inclusions. This leads to strong oscillations in the chemical potential as a function of the layer filling fraction, and confers to inclusions a strong resistance against coarsening, hence providing the possibility to stabilize the microstructure, in agreement with several experimental observations.

Our model is based on the classical time-dependent density-functional theory (TDDFT), which provides a set of local master equations for the time evolution of the occupation probabilities at each lattice site in the system [74]. In our multiscale implementation, the TDDFT equations are solved on non-uniform grids that are refined to the atomic level close to the interphase boundaries — where most of the action takes place — but become coarser into the bulk. Our method relies on the Bragg-Williams free-energy functional [5] and includes the effect of elasticity

at the mean-field level; elastic energies are calculated using the non-local force-based quasicontinuum method (QCM) of Tadmor and collaborators [53]. The QCM is also used in a stand-alone fashion to carry out elastic relaxation calculations. The only input required in both methods is the interatomic potentials. A complete description of the model and demonstration of its effectiveness for the study of coarsening in elastically inhomogeneous systems can be found in Ref. [68].

We are concerned here with two-dimensional systems composed of an inclusion of B atoms coherently embedded within a matrix of A atoms. For simplicity, the atoms (which lie on a triangular lattice) are taken to interact only with their nearest neighbors through a harmonic potential with both elastic and chemical contributions, $V_{i,j}^{\alpha,\beta} = k_{\alpha,\beta}(|\mathbf{r}_{i,j}| - \sigma_{\alpha,\beta})^2 - \epsilon_{\alpha,\beta}$, where $k_{\alpha,\beta}$ are the stiffnesses, $\sigma_{\alpha,\beta}$ the equilibrium lattice constants, and $\epsilon_{\alpha,\beta}$ the chemical interaction energies between species α and β; i and j refer to lattice sites.

We consider hard inclusions ($k_{\mathrm{AA}} = 50\epsilon/\sigma^2$ and $k_{\mathrm{BB}} = 200\epsilon/\sigma^2$) with a lattice mismatch of 3% ($\sigma_{\mathrm{AA}} = \sigma$, $\sigma_{\mathrm{BB}} = 1.03\sigma$). The chemical interaction energies, $\epsilon_{\mathrm{AA}} = \epsilon_{\mathrm{BB}} = \epsilon$ and $\epsilon_{\mathrm{AB}} = 0.7\epsilon$, are typical of phase-separating systems. We examine two different sets of inter-species potentials, namely $k_{\mathrm{AB}} = 50\epsilon/\sigma^2$, $\sigma_{\mathrm{AB}} = 1.03\sigma$ (case I) and $k_{\mathrm{AB}} = 200\epsilon/\sigma^2$, $\sigma_{\mathrm{AB}} = 1.0\sigma$ (case II). Since the inclusion is much harder than the matrix, the lattice constant near the interphase boundary, σ_{ib}, will be very close to σ_{BB}. Thus, case I corresponds to a low interface misfit ($\sigma_{\mathrm{AB}} \simeq \sigma_{\mathrm{ib}}$) while case II corresponds to a high interface misfit ($\sigma_{\mathrm{AB}} < \sigma_{\mathrm{ib}}$). All calculations were carried out on an hexagonal cell of side 1024σ, large enough to eliminate finite-size effects. The temperature in the TDDFT calculations was chosen to be $T = 0.5\epsilon/k_B \simeq 0.5T_c$; all results are quoted in reduced units (ϵ for energy and σ for length). In all cases, the structures are fully relaxed.

In order to gain a qualitative understanding of the effect of elasticity on the growth of inclusions, we first carried out static QCM calculations of the elastic energy cost for substituting a B atom to an A atom at the surface of a fully relaxed, rounded hexagonal inclusion; the results are reported in Fig. 5.1. Two interesting features deserve mention : first, steps are low energy sites for the incorporation of B atoms, with a gain in energy of about 0.05ϵ in both cases; second, the change in

energy for incorporation on a terrace increases toward the step edge. Two differences between cases I and II are also worth noting : first, the incorporation energy of a B atom on a case-II terrace is about five times larger than in case I; second, the incorporation energy at a case-II step is much lower than on a terrace, while it is slightly higher in case I. Finally, as expected, the elastic incorporation energies are generally low and narrowly distributed for the low interface misfit case (I), while they are rather large and widely distributed for the high interface misfit case (II).

Important consequences follow from these simple considerations. Under growth conditions, in case I, elasticity should slightly favor the nucleation of new terraces and thus the formation of circular inclusions with rough surfaces. In constrast, in case II, the growth of existing terraces, and hence kinetic facetting [20], is strongly promoted by elasticity since incorporation on a terrace (and thus the nucleation of a new terrace) is energetically very costly. However, from a purely elastic viewpoint, the equilibrium shape is a circle : QCM calculations show indeed that a circular inclusion of radius $64a_0$ has about 1.5% lower elastic energy than an hexagon of the same area because of the large elastic energy stored in the tips. Thus, while kinetically favored, the completely facetted shape is thermodynamically disfavored.

The calculations presented above suggest that, in growth conditions, the behavior of the inclusion is strongly affected by the degree of misfit at the interface. This prediction will now be examined using our multiscale TDDFT model. More precisely, we examine in detail (i) the evolution of the shape of the inclusion during growth or evaporation; (ii) the nature of the growth process; and (iii) the behavior of the chemical potential during growth.

First, in order to assess the conclusions presented above concerning the equilibrium state of the inclusion, we carried out simulations with fixed number of A and B atoms (closed boundary conditions), starting from a circular inclusion embedded within a saturated matrix. The results are shown as dotted lines in Fig. 5.2; for both cases I and II, the circular shape is indeed stable.

The effect of growth is now studied using open boundary conditions — the system is in contact with sources of A and B atoms at fixed chemical potentials — under supersaturation conditions. The results are presented as continuous lines

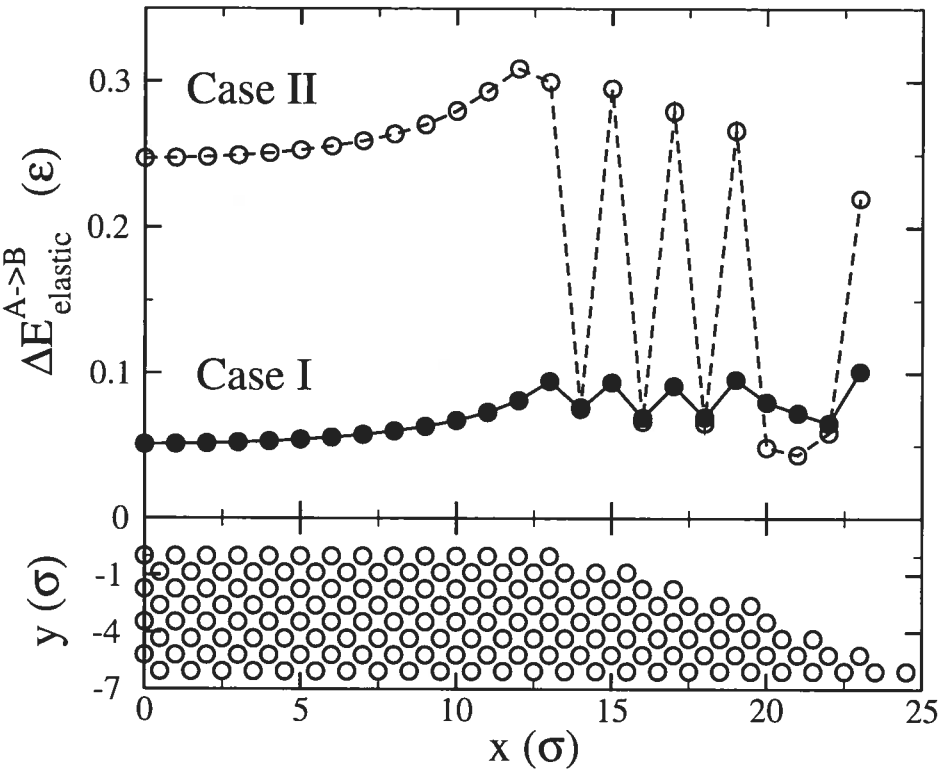

FIG. 5.1 – Upper panel : Change in elastic energy following the substitution of an A atom for a B atom at different positions along the interface of the inclusion, which has a rounded hexagonal shape (cf. lower panel; the shaded circles represent atoms in the inclusion; matrix atoms are not shown for clarity.). The parameters for the two cases are given in the text.

in Fig. 5.2; we find that, while the shape of the (initially circular) inclusion is not affected by the influx of B atoms in case I, a rounded-hexagonal profile develops in case II, in agreement with the simple energy considerations discussed above. This is further confirmed by the direct observation of the evolution in time of the profile of the inclusions, shown in panels (a) and (c) of Fig. 5.3. In case I, the circular shape is preserved [$R(\theta) = \text{cst}$ and increasing with time], while in case II facetting evidently results from the growth of small preexisting facets (centered around odd multiples of $\theta = \pi/6$ in the present case), as illustrated by the empty circles; as time increases, the shape becomes more and more closely hexagonal, fitting almost exactly the curve corresponding to a perfect hexagon (cf. open squares and full line).

The facetting process occurs because, at this supersaturation, the nucleation

of new terraces is slow compared to the growth of rough regions. Further growth proceeds layer-by-layer as will be discussed below. Note that the hexagonal shape, which results from kinetics, is preserved even if growth stops, indicating that a free-energy barrier — corresponding to the nucleation of a new terrace on a facet of the inclusion — separates the true equilibrium shape and the metastable shape which develops during growth. This effect is commonly observed in facetted systems [11, 75].

In conditions of undersaturation, now, the inclusion gradually evaporates. Because of the absence of nucleation barriers in this situation, only modest shape modulations are observed and the inclusion adopts a roughly circular shape in both cases I and II (cf. Fig. 5.2, dashed lines). The fact that different behaviors prevail under growth or evaporation further demonstrates that kinetics, and not thermodynamics, plays the leading role in case II. A more detailed study of the evolution of the shape of the inclusion during evaporation will be given elsewhere.

The evolution of the shape of the inclusion during growth provides information about growth mechanisms. Fig. 5.3(c) shows that, in case I, the interface moves at uniform speed, independent of the orientation (and thus the inclusion remains circular, as noted above) ; this is the clear signature of a continuous growth process. In contrast, in case II, growth proceeds in a layer-by-layer fashion : Fig. 5.3(b) shows that, starting with a rounded-hexagonal configuration (circles), new terraces nucleate in the center of the facets (squares), then grow (diamonds) until a new layer has formed (triangles). This behaviour is consistent with the QCM calculations. It is interesting to note that, due to the availability of low-energy sites at newly-formed steps, atoms also diffuse from the high-energy tip sites toward the new steps, leading to a transient decrease of the curvature at the tips [cf. diamonds near $\pi/3$ in Fig. 5.3(b)]. These sites eventually get filled again : the new layer is completed and the cycle repeats itself.

These differences in the growth modes have a dramatic impact on the dependence on size of the chemical potential of the inclusions. Consider case II : in order to add a B atom to an inclusion which has completely filled layers, the large elastic barrier opposing the nucleation of a new terrace (0.25ϵ; to give an idea, this is roughly half the change in chemical bonding energy for incorporating a solute B

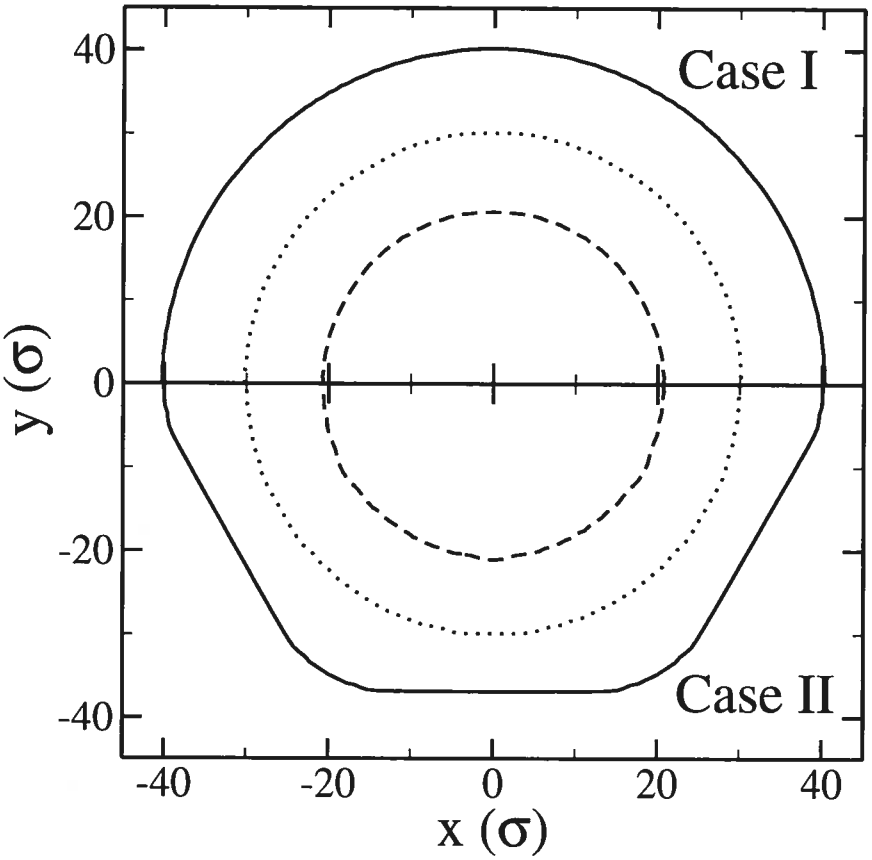

FIG. 5.2 – Shape of the inclusion for the two cases discussed in the text; dotted lines : closed boundary conditions; continuous lines : growth; dashed lines : evaporation.

atom to the interface) must be overcome. In contrast, only a modest 0.05ϵ opposes incorporation once a new terrace has formed. Thus, the chemical potential of the inclusion, $\Delta\mu_i = \mu_B - \mu_A$, should depend strongly on the state of occupation of the outermost layer. This is clearly seen in our TDDFT calculations, as demonstrated in Fig. 5.4(a). The maxima of $\Delta\mu_i$ correspond to completely filled layers, while the minima occur shortly after new terraces start to form, as expected. The increase in $\Delta\mu_i$ between the two limits reflects the increasing elastic energy associated with the growth of a terrace as the underlying step edge is approached (cf. Fig. 5.1). In contrast, for case I, Fig. 5.4(a) shows that the chemical potential difference is smooth, as low-energy steps are always available owing to the absence of a signifi-

cant elastic nucleation barrier. Thus, only small-amplitude oscillations are observed as a function of size.

These observations have important consequences for the coarsening behavior of a collection of inclusions (of average size R_{avg}). In case I, first, the behavior of $\Delta\mu_i$ is dominated by the curvature-dependent $1/R$ contribution [cf. Fig. 5.4(b)]; the normal capillarity-driven coarsening (as described by the LSW theory) should therefore prevail. Indeed, if $\Delta\mu_f$ ($\Delta\mu$ in the far-field, i.e., far from the inclusion) is larger than $\Delta\mu_i$, the inclusion will grow indefinitely; in the opposite case, the inclusion would evaporate completely. Since $\Delta\mu_f = \Delta\mu_i(R_{\text{avg}})$, those inclusions with $R < R_{\text{avg}}$ will shrink while those with $R > R_{\text{avg}}$ will grow, i.e., normal coarsening occurs.

In constrast, the oscillations of $\Delta\mu_i$ for the high interface misfit case (II) leads to an anomalous behavior whereby coarsening slows down considerably for sizes larger than a critical R_{avg}. Indeed, only for very small R_{avg} [$< 10\sigma$ in the present case; cf. Fig. 5.4(b)] is $\Delta\mu_f$ large enough to overcome the chemical potential barrier for growth of large inclusions, so that coarsening proceeds normally. For larger R_{avg}, inclusions will grow or shrink by only a fraction of a layer before achieving metastable equilibrium with the environment. Due to the abundance of metastable states provided by the rugged chemical potential landscape, the growth of inclusions rapidly becomes an activated process : nucleation of new terraces must rely on thermal fluctuations instead of the thermodynamic driving force provided by the ambiant supersaturation. Upon entering this nucleation-limited regime, coarsening drastically slows down, or even virtually stops on experimental timescales, as shown by Rohrer and collaborators [76].

In conclusion, we have shown that, as a function of the degree of elastic misfit at interphase boundaries, the growth of inclusions in an elastically-inhomogeneous multiphase system proceeds either continuously at rough interfaces or in a layer-by-layer manner following kinetic facetting. In the latter case, the elastic contributions to the nucleation barrier for new terraces induce strong oscillations in the chemical potential of the inclusions as a function of their size. This behavior causes a transition from a normal capillarity-driven coarsening at small sizes to a

nucleation-limited regime at larger sizes, thus efficiently impeding the coarsening of the microstructure.

The present work clearly demonstrates that an atomistic description of the interfaces is crucial for properly capturing the relevant aspects of the growth dynamics. While it allowed us to identify a simple and robust mechanism for the coarsening slowdown, a complete study requires the effect of elastic interactions between inclusions to be included, as it is experimentally established that the volume fraction of inclusions also affects the coarsening behavior [65] ; such a study in currently under way.

This work has been supported by grants from the Natural Sciences and Engineering Research Council of Canada (NSERC) and the *Fonds Québécois de la Recherche sur la Nature et les Technologies* (FQRNT). We are indebted to the *Réseau Québécois de Calcul de Haute Performance* (RQCHP) for generous allocations of computer resources.

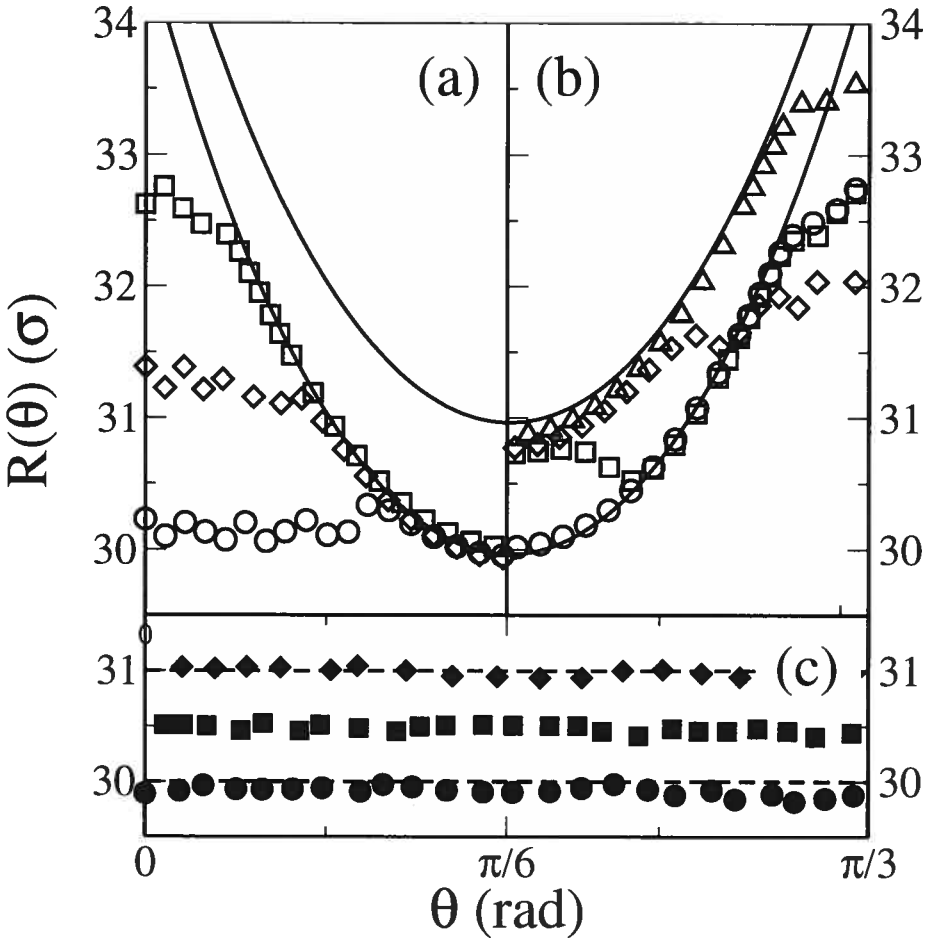

FIG. 5.3 – Angular dependence of the radius $R(\theta)$ of an inclusion at different times under growth conditions : (a) evolution of an initially circular inclusion (empty circles) toward a rounded-hexagonal shape (empty square) in case II; (b) layer-by-layer growth of an initially rounded-hexagonal inclusion in case II (empty circles), and then, in order of increasing time, empty squares, diamonds and triangles; (c) growth of an initially-circular inclusion in case I — filled circles, squares and diamonds in order of increasing time. The lines show the expected dependance for a perfect hexagon (continuous lines, one-layer size difference) and a perfect circle (dashed lines, one-layer size differences).

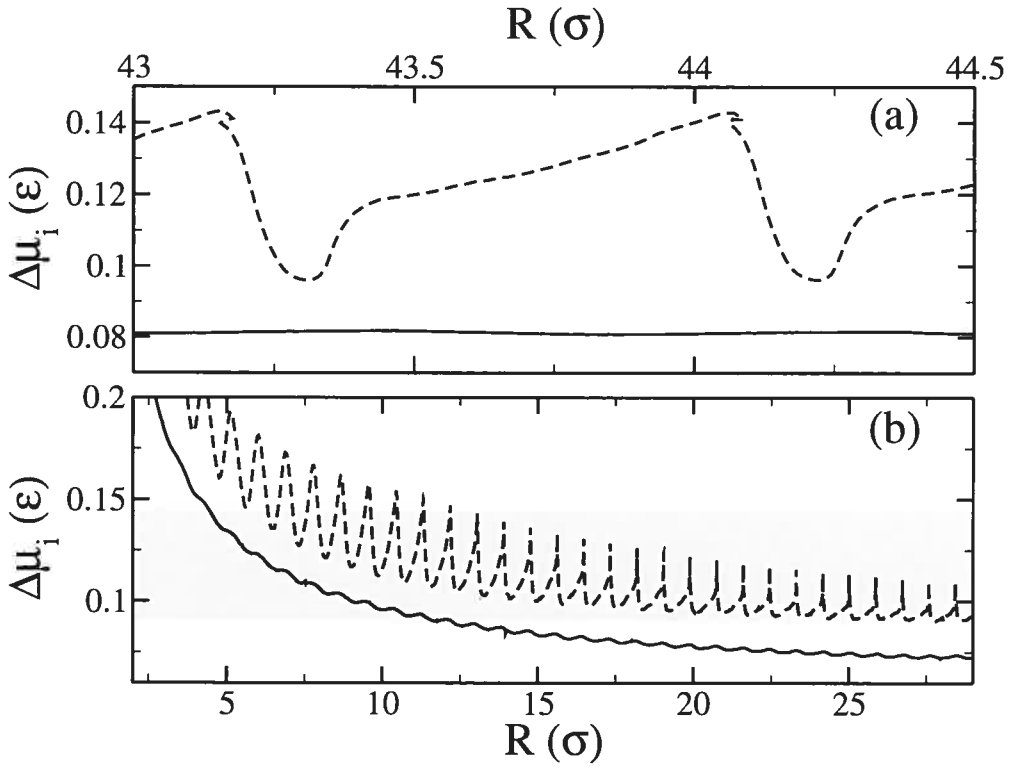

FIG. 5.4 – Chemical potential difference between species B and species A ($\Delta\mu_i$) as a function of the size of the inclusion; (a) : $\Delta\mu_i$ during growth; (b) : $\Delta\mu_i$ during evaporation. Continuous lines : case I; dashed lines : case II. The shaded region in panel (b) represents the range of oscillation of $\Delta\mu_i$ in panel (a).

CHAPITRE 6

PROPRIÉTÉS DES INTERFACES ET STABILISATION MICROSTRUCTURALE DANS LES SYSTÈMES MULTIPHASES ÉLASTIQUEMENT INHOMOGÈNES

Ce chapitre est composé d'un deuxième article traitant de l'importance des effets élastiques d'interface. Nous procédons maintenant à une analyse systématique des effets mis en évidence au chapitre 5. À l'aide de la QCM, nous étudions la variation des énergies d'addition d'atomes de soluté à l'interface de l'inclusion en fonction des paramètres du potentiel interatomique et déduisons l'impact de ces variations sur la forme et le potentiel chimique des inclusions. À cet effet, nous démontrons qu'une vaste gamme de comportements est possible : l'élasticité peut autant favoriser que défavoriser le facettage cinétique ; dans le premier cas, on observe aussi bien des mécanismes d'auto-limitation que d'auto-amplification. Ces prédictions sont ensuite confirmées à l'aide de la TDDFT. Les simulations permettent aussi de mettre en évidence que le phénomène d'oscillation du potentiel chimique est très général. En effet, en plus du mécanisme identifié au chapitre 5, nos calculs indiquent que les oscillations surviennent aussi suite à la modulation de la forme des inclusions durant la croissance. Par contre, pour de faibles désaccords d'interface, le comportement du potential chimique est très semblable à celui d'une inclusion élastiquement homogène.

À l'aide d'une généralisation du modèle LSW, nous étudions ensuite l'impact des oscillations sur le mûrissement. Les résultats montrent que les oscillations n'affectent pas le déroulement de la phase initiale du mûrissement, qui reste bien décrite par l'exposant classique de $1/3$. Par contre, une décroissance rapide de l'exposant de mûrissement est observé pour des temps plus longs, menant même à la stabilisation complète de la microstructure. De plus, cette stabilisation s'accompagne d'un élargissement de la fonction de distribution en taille.

Ce chapitre est soumis pour publication dans la revue *Physical Review E*. En tant que premier auteur de cet article, ma contribution à consisté en :

1. La création du modèle utilisé pour effectuer les calculs numériques.
2. L'implémentation des programmes informatiques nécessaires aux calculs.
3. L'exécution des calculs requis.
4. L'analyse et l'interprétation des données.
5. La rédaction de la version initiale de l'article.
6. La réalisation des modifications suggérées par le co-auteur de l'article.

Interface properties and microstructural stabilization in elastically inhomogeneous multiphase systems

Danny Perez and Laurent J. Lewis

Département de physique et Regroupement Québécois sur les Matériaux de Pointe (RQMP), Université de Montréal, C. P. 6128 Succursale Centre-Ville, Montréal (Québec) H3C 3J7, Canada

Using a multiscale model based on the classical time-dependent density-functional theory we recently introduced, we numerically study the impact of elastic inhomogeneities on the growth of isolated inclusions in multiphase alloys. We demonstrate that the coupling between the overall interface structure (as determined by the shape of the inclusions) and the local, atomic-scale structure can be very large, and is able to significantly affect the behavior of inclusions during growth. Elasticity is shown to have a strong influence on the local energetics at interfaces, leading to shape modulations and kinetic faceting. Morphological and energetic changes induce oscillations in the chemical potential of the inclusions, opening the way to the stabilization of multi-inclusion microstructures, consistent with experiment. We demonstrate that the interface elastic misfit is a key parameter for controlling the strength of elastic effects.

6.1 Introduction

Many properties of materials strongly depend on their atomic- and meso-scale structure, like, e.g., optical absorption and emission [23, 82], electrical and thermal conductivity [93], yield strength [72], hardness [51], etc. The design and optimization of high-performance materials thus require their microstructural state to be precisely controlled. However, unlike the chemical composition, the microstructure is difficult to monitor because it results from a delicate competition between many thermodynamical and kinetic processes. Further, it is usually unstable as it continuously evolves through various processes such as diffusion, nucleation, evaporation, etc. Consequently, it is important to understand the energetics of the microstructural state, but also how it evolves in time. The ultimate goal is to gain absolute control

over the formation of the microstructure and, once formed, ensure that it is stable in time.

Because they spontaneously form from supersaturated mixtures, multi-phase microstructures are ubiquitous in materials science. Discovering strategies for stabilizing them would open the way to important technological applications. As an illustration, it is well known that hardness can be greatly increased by embedding small coherent precipitates (inclusions) within the bulk material [51]. Precipitate hardening occurs because the inclusions are able to pin down dislocations, thereby reducing their mobility. This process, however, is quite sensitive to the size and distribution of the inclusions. The inclusion-matrix interface, for example, usually becomes incoherent for large inclusions, leading to a decrease of the pinning efficiency. The spatial distribution of inclusions must also be such that they can stop most dislocations.

Solid-state multiphase microstructural states are usually not stable because they contain a lot of interfaces. In fact, it was shown by Lifshitz, Slyozov and Wagner (LSW) [47, 99] that if the dynamics results solely from the capillarity-driven reduction of the interfacial free-energy, large inclusions tend to grow at the expense of smaller ones — a process called "coarsening" —, leading to an increase of the average inclusion size either as $t^{1/3}$ in the diffusion-limited case, or $t^{1/2}$ in the attachment-limited case. Ultimately, a microstructure evolving according to the LSW model will consist of a single inclusion. The LSW behavior has been observed in a wide range of multiphase materials in various experimental conditions and geometries, and can therefore be regarded as *normal* coarsening. Returning to the example above, the evolution of the microstructure would lead to a decrease of the hardness of the material resulting from an increase of the size of the inclusions and a concomitant decrease of their number.

Identifying routes to microstructural stabilization in multiphase systems is the purpose of the present study. In order to achieve this goal, it is reasonable to consider systems for which one of the assumptions underlying the LSW theory is violated, viz. (i) the capillarity approximation is valid i.e., the chemical potential of an inclusion is proportional to the curvature of its interface; (ii) the dynamics is

strictly capillarity-driven; and (iii) the volume fraction of inclusions is vanishingly small. It is implicit in assumption (ii) that the contribution of the interface to the free energy is large compared to other contributions. It should thus be possible to achieve stabilization by introducing competing terms in the free energy. Since the lattice constants within the inclusions and the matrix are in general different, elastic interactions are an obvious candidate for this purpose. In fact, it is well known that elasticity drastically affects both the morphology and the kinetics of multi-phase systems [22]. The effects on morphology range from spontaneous symmetry breaking of the shape of inclusions [50] and the formation of spatial correlations with regards to both shape and position [8, 25, 104], to the inversion of the roles of the matrix and the inclusions at high volume fractions [44, 61]. Concerning kinetics, the range of possible behaviors is also large, and both acceleration [8] and (more often) slowdown [8, 13, 25, 41, 54, 55, 65, 105] of the coarsening kinetics have been observed. In fact, complete stabilization has even been reported in some cases. For example, in Ni-Cu-Si alloys [13, 55, 105], the evolution initially proceeds normally (i.e., *à la* LSW), but completely stops (or slows down considerably) once a critical average inclusion size ($\sim$ 10 to 20 nm) is reached; other examples include Ti-Mo [41], Ni-Al-To [8], and Ni-Al-Ti [25] alloys. Further, the slowdown process is accompanied by either an increase [8, 25] or a reduction [55] of the width of the distribution of the sizes of the inclusions. In spite of the diversity of behaviors observed, the systems share a common feature : they all possess a large degree of elastic inhomogeneity, i.e., large difference between the elastic constants in the different phases [65]. As a last point, it is also found that coarsening in these materials depends on the volume fraction of the inclusions [55], indicating a violation of assumption (iii). On the other hand, the anisotropy of the elastic constants, while strongly affecting the shape and the distribution of the inclusions, do not appear to influence the coarsening behavior significantly [90, 92].

This anomalous behavior — slowdown of the coarsening kinetics — is sometime viewed as a manifestation of *inverse coarsening*, whereby small inclusions grow at the expense of larger ones. The occurrence of this phenomenon was predicted several years ago [3, 15, 32] on the basis of Eshelby's formula for the interaction energy

between two spherical inclusions [17]. Eshelby showed that this energy is minimum for soft inclusions if the two have identical sizes. Elastic interactions could thus, in principle, counteract the normal capillarity-driven coarsening process, as suggested above. However, this interpretation suffers from three flaws. First, the formula is only valid for spherical inclusions while it is known that the interaction energy is very sensitive to the shape of the inclusions [62]; numerical simulations where constraints on the shape of the inclusions had been lifted have indeed shown that, while *transient* inverse coarsening is often observed [35, 63, 80, 84], complete stabilization is not expected except when quasi-periodic initial conditions are imposed [80, 84]. Second, anomalous coarsening is also observed in systems where the inclusions are harder than the matrix [65], while Eshelby's formula predicts that elasticity should enhance coarsening in this case. Third, inverse coarsening implies a narrowing of the inclusion size distribution, but widening is also observed. Thus, while some observations are consistent with the inverse coarsening theory, the latter evidently cannot account for the whole variety of behaviors observed.

It has recently become possible to carry out large-scale simulations of complex microstructures using phase-field methods. Using such an approach, Onuki and collaborators [60, 61] suggested that stabilization was in fact a robust process occurring even in complex microstructures. Their results indicated that coarsening would initially proceed normally, and that a transition to a frozen state would take place suddenly, without the occurrence of inverse coarsening. These conclusions have however been questioned by Chen *et al.* who, using a more precise approach for elastic energy calculations [30], did not observe stabilization but, rather, coarsening with a reduced exponent [107]. This exponent was shown to decrease rather slowly, from 0.33 in homogeneous systems to 0.26 for systems with a threefold misfit in shear moduli.

Based on the previous (conflicting) observations, one can conclude that some important physical processes are not properly taken into account in present models. One may speculate that these have to do with the way interfaces are handled, as the studies of coarsening mentioned above implicitly assume that the capillarity approximation (i) is valid. Indeed, the vast majority of models used to study this

problem rely on either a sharp-interface [35, 46, 80, 84, 90, 91] or a phase-field formulation [10, 60, 61, 63, 107], where the interphase boundaries are treated as structureless or smooth on the scale of the lattice constant, respectively (exceptions include Refs. [21, 26, 42, 48]). In these models, the physical properties of the inclusions are thus continuous functions of shape and size. Since we are concerned with inclusions having radii in the nanometer range and interfaces that are sharp on the nanometer scale [89], the validity of this approximation is not guaranteed. Further, anisotropies in either thermodynamic or kinetic quantities, introduced by the underlying lattice structure, can strongly affect the dynamical behavior of inclusions [7, 94, 103]. Finally, it is well known (particularly in the crystal growth community [58]) that the atomic-scale structure of the interfaces can have a dramatic impact on the way solids grow (e.g., continuous vs. layer-by-layer), and hence on growth kinetics. For example, coarsening in faceted systems strongly differs from that when the interfaces are rough [75]. An assessment of the validity of assumption (i), and of the consequences of it being violated, could help resolve some of the discrepancies between theory and experiment.

This is what we propose to do in the present article. Following up on previous work where strong interfacial elasticity effects were reported [66], we demonstrate that the interplay between elastic inhomogeneity and atomic-scale interface structure profoundly affects the coarsening behavior of the inclusions. We show that elasticity-induced variations of the attachment energy of solute atoms at different sites at the surface of the inclusions lead to modulations in their shape during growth and, consequently, oscillations in their chemical potential. We show also that the energetics of the sites available for the incorporation of new atoms around the inclusions changes rapidly during growth, increasing the amplitude of the chemical potential variations. Our study establishes that the elastic mismatch at the interface is the primary factor controlling the strength of these effects. We demonstrate, finally, that proper consideration of the atomic structure of the interfaces can account for some of the "peculiar" aspects of coarsening mentioned earlier.

6.2 Model

Since atomic-scale resolution is necessary at interphase boundaries, a simulation method based on a microscopic description of the dynamics is required. To this effect, we recently proposed a multiscale model [68] based on the time-dependent density functional theory (TDDFT) for classical lattice systems developed by Reinel, Fisher and collaborators [19, 37, 74]. Since a complete description of TDDFT can be found in Ref. [19], and of our particular implementation in Ref. [68] (where we also demonstrate that it can successfully describe elastically inhomogeneous multiphase systems), we only give here, for completeness, a rapid overview of the methodology.

The basic assumption behind TDDFT is that, in typical conditions of microstructural evolution, the only relevant dynamical variables are the site occupation probabilities $p_i^\alpha(t) = \langle n_i^\alpha \rangle_t$ — the probability that lattice site i be occupied by a type-α atom at time t —, where n_i^α is the number of type-α atoms at site i (either 0 or 1) and $\langle\rangle_t$ represents the non-equilibrium ensemble average at time t. Implicit in this assumption is that the system can, $\forall t$, be considered to be in *local* equilibrium *relative to the instantaneous values of the p's.* A set of reduced equations for the dynamics of the system can then be obtained in terms of the $\{p_i^\alpha(t)\}$ alone. (Other methods based on similar assumptions are described in Refs. [9, 70])

These equations can be derived starting from a microscopic master equation for the probability $P(\mathbf{n}, t)$ to find the system in configuration $\mathbf{n} = \{n_i^\alpha\}$ at time t :

$$\frac{dP(\mathbf{n},t)}{dt} = \frac{1}{2}\sum_{i,j\in nn(i)} [w_{i,j}(\tilde{\mathbf{n}})P(\tilde{\mathbf{n}},t) - w_{i,j}(\mathbf{n})P(\mathbf{n},t)]. \tag{6.1}$$

Here, it is assumed that a configuration evolves in time through successive exchanges of nearest-neighbors particles [$nn(i)$ denotes the set of nearest-neighbors of site i]. These exchanges proceed at rate $w_{i,j}(\mathbf{n})$; $\tilde{\mathbf{n}}$ represents a configuration which differs from $\mathbf{n}$ only by the exchange of the occupations of sites i and j.

This equation can be formally written in terms of the $\{p_i^\alpha(t)\}$ as :

$$\frac{dp_i^\alpha}{dt} = \sum_{j \in nn(i),\beta} \langle J_{i,j}^{\beta,\alpha} \rangle_t - \langle J_{i,j}^{\alpha,\beta} \rangle_t, \tag{6.2}$$

with the diffusion fluxes defined as :

$$J_{i,j}^{\beta,\alpha}(\mathbf{n}) = n_i^\beta n_j^\alpha w_{i,j}(\mathbf{n}). \tag{6.3}$$

Eq. 6.2 is the basic equation of TDDFT; the problem is now to compute the non-equilibrium averages. Since a direct calculation of $P(\mathbf{n}, t)$ is prohibitive, one must resort to the aforementioned local equilibrium approximation, i.e., $P(\mathbf{n}, t) \simeq P^{\text{loc}}(\mathbf{n}, t)$ with :

$$P^{\text{loc}}(\mathbf{n}, t) = \frac{1}{Z(t)} \exp\left\{ -\frac{1}{k_B T} \left[H(\mathbf{n}) + \sum_{i,\alpha} h_i^\alpha n_i^\alpha \right] \right\}, \tag{6.4}$$

where H is the Hamiltonian of the system, h_i^α is an external, site- and species-dependent field, and $Z(t)$ is such that $\sum_{\mathbf{n}} P^{\text{loc}}(\mathbf{n}, t) = 1$. The value of the external field is obtained by requiring self-consistency between $P^{\text{loc}}(\mathbf{n}, t)$ and the $\{p_i^\alpha(t)\}$.

Formally, self-consistency is achieved by requiring the grand canonical potential of the system under the external field to be stationary with respect to the average occupations, i.e., the h_i^α are such that :

$$\frac{d}{d\mathbf{p}} \Omega(\mathbf{p}) = \frac{d}{d\mathbf{p}} \left[\sum_{i,\alpha} (h_i^\alpha - \mu_{\text{tot}}^\alpha) p_i^\alpha + F(\mathbf{p}) \right] = 0, \tag{6.5}$$

where $\mathbf{p} = \{p_i^\alpha\}$, μ_{tot}^α is the global chemical potential of species α, and $F(\mathbf{p})$ is the free-energy (in terms of the $\{p_i^\alpha\}$). From this last equation, it is now clear that the local fields are proportional to the local chemical potentials :

$$h_i^\alpha = \mu_{\text{tot}}^\alpha - \frac{\partial F}{\partial p_i^\alpha} = \mu_{\text{tot}}^\alpha - \mu_i^\alpha. \tag{6.6}$$

To complete the evaluation of Eq. 6.2, a free-energy functional $F(\mathbf{p})$ must be specified; we resort to a simple Bragg-Williams mean-field approximation of the

form :

$$\begin{aligned} F(\mathbf{p}) &= E(\mathbf{p}) - TS(\mathbf{p}) \\ &= \frac{1}{2} \sum_{i,j \in nn(i),\alpha,\beta} V_{i,j}^{\alpha,\beta} p_i^\alpha p_j^\beta + k_B T \sum_{i,\alpha} p_i^\alpha \ln p_i^\alpha, \end{aligned} \tag{6.7}$$

with $V_{i,j}^{\alpha,\beta}$ the interaction energy between atom α at site i and atom β at site j. Quantitative agreement with a direct Monte Carlo solution of Eq. 6.1 cannot be assumed with such a functional, but a qualitatively correct description of the behavior of the different phases is expected.

By also assuming that microscopic configurations change only by vacancy diffusion to a nearest-neighbor site at a rate given by

$$w_{i,j}^\alpha = \nu_0 e^{E_i^\alpha / k_B T}, \tag{6.8}$$

where E_i^α is the energy of an α-type atom at site i and ν_0 is a trial frequency, a tractable form for Eq. 6.2 is obtained, namely :

$$\frac{dp_i^\alpha}{dt} = \sum_{j \in nn(i)} M_{i,j}(t)[\mathcal{A}_j^\alpha(t) - \mathcal{A}_i^\alpha(t)], \tag{6.9}$$

with mobility $M_{i,j}(t) = \langle p_i^{\text{vacancy}}(t) p_j^{\text{vacancy}}(t) \rangle_t \simeq p_i^{\text{vacancy}}(t) p_j^{\text{vacancy}}(t)$ and activity $\mathcal{A}_i^\alpha(t) = e^{-h_i^\alpha(t)/k_B T}$. This equation is a generalized Fick's law where occupation probabilities diffuse from regions of high activity (and hence high chemical potential) to regions of low activity.

The effect of elasticity is introduced through a dependence of the free-energy, Eq. 6.7, on the positions of the atoms. At the mean-field level, the free-energy becomes a function of the *average* position of the atom at each lattice site. These positions are obtained by requiring that they minimize the grand-potential, i.e.,

$$\frac{d}{d\mathbf{r}} \Omega(\mathbf{p}, \mathbf{r}) = \frac{d}{d\mathbf{r}} \left[\sum_{i,\alpha} (h_i^\alpha - \mu_{\text{tot}}^\alpha) p_{\text{l}}^\alpha + F(\mathbf{p}, \mathbf{r}) \right] = 0, \tag{6.10}$$

or, equivalently, that :

$$\frac{d}{d\mathbf{r}} E(\mathbf{p}, \mathbf{r}) = 0. \tag{6.11}$$

Here we use a simple harmonic potential to model the elastic interactions between atoms :

$$V_{i,j}^{\alpha,\beta} = k^{\alpha,\beta}(r_{i,j} - \sigma^{\alpha,\beta})^2 - \epsilon^{\alpha,\beta}, \tag{6.12}$$

where $r_{i,j} = |\vec{r}_i - \vec{r}_j|$.

As a final point, we note that coherency is assumed at all times, i.e., the neighbors of an atomic site do not change during the course of a simulation; plasticity effects are thus excluded.

Up to this point, the formalism has been strictly microscopic, each lattice site being explicitly taken into account. This is clearly not suited to the study of large systems consisting of hundreds of thousands or even millions of atoms. However, the variables of interest in the TDDFT calculation — the average occupations and the average positions — vary slowly away from interphase boundaries. Microscopic resolution is thus only needed close to the interfaces, while other regions can be described using fewer degrees of freedom. Exploiting this fact, we proposed a multiscale TDDFT formulation where Eqns. 6.2 and 6.11 are solved on non-uniform grids using an unstructured finite-volume formulation [18, 86] and the quasicontinuum method (QCM) [87], respectively. The QCM relies on a coarse-grainable representation of the displacement field and of the elastic energy to bridge the gap between the micro- and the meso-scale; a recent review of the method and applications can be found in Ref. [53]. In the present study, the QCM is also used in a stand-alone fashion for carrying out elastic energy calculations.

6.3 Computational details

6.3.1 Simulation Setup and Parameters

In the calculations reported below, we consider a two-dimensional binary alloy with vacancies (ABv); more precisely, we study the evolution of B-rich inclusions embedded within an A-rich matrix, where the dynamics is governed by the migration of vacancies (i.e., the exchange of atoms with vacancies). The simulation

cell is an hexagon with sides of length $1536a_0$ containing about 14 millions sites; the underlying lattice is triangular. Fixed boundary conditions are applied to the elastic equilibrium equations (Eq. 6.11) and grand-canonical boundary conditions (fixed chemical potential at the edges of the cell) are applied to Eq. 6.2. In all cases, the temperature is $T = 0.5\epsilon/k_B$, which is about half of the critical temperature for phase separation; at this temperature the width of the interface is around 1 nm, a typical value in usual experimental conditions. The vacancy concentration is taken to be 10^{-3}. All results will be given in dimensionless, reduced units relative to a stress-free pure A phase (cf. Eq. 6.12) : lattice parameter for length (σ) and interaction energy between nearest-neighbors for energy (ϵ).

Five distinct cases have been studied, each corresponding to a different set of elastic stiffnesses and lattice parameters, as listed in Table 6.1 : homogeneous inclusions (no elastic misfit), hard inclusions with low interface misfit (HI-LM), hard inclusions with high interface misfit (HI-HM), soft inclusions with low interface misfit (SI-LM), and finally soft inclusions with high interface misfit (SI-HM). An inclusion is hard (soft) if $k_{BB} > (<)\ k_{AA}$. The degree of interface misfit qualitatively refers to the difference between σ_{AB} and the typical lattice parameter in the interface region. Since hard inclusions tend to impose their lattice constant to the surrounding matrix, a low interface misfit corresponds to an interface bond length close to that in the inclusion, i.e., $\sigma_{AB} = \sigma_{BB}$ while a high misfit corresponds to $\sigma_{AB} = \sigma_{AA}$. For soft inclusions, the two situations are inverted. Other parameters of the potential are $\epsilon_{AA} = \epsilon_{BB} = \epsilon$ and $\epsilon_{AB} = 0.7\epsilon$.

The above choice of parameters will enable us to clearly isolate the effects of "bulk" elasticity (controlled by the values of k_{AA}, k_{BB}, σ_{AA}, and σ_{BB}) from those arising from "interface" elasticity (determined by k_{AB} and σ_{AB}).

6.3.2 Method of analysis

In elastically homogeneous systems, the energetics of atoms at interphase boundaries depends only on the nature of neighbouring atoms; sites with identical local configurations are therefore equivalent. However, when elastic inhomogeneities are introduced, the problem becomes non-local owing to the long range character of

Type	k_{AA}	k_{AB}	k_{BB}	σ_{AA}	σ_{AB}	σ_{BB}
Homogeneous	0	0	0	1.00	1.00	1.00
HI-LM	50	50	150	1.00	1.03	1.03
HI-HM	50	50	150	1.00	1.00	1.03
SI-LM	50	50	10	1.00	1.00	1.03
SI-HM	50	50	10	1.00	1.03	1.03

TAB. 6.1 – Values of the stiffnesses k_{XY} and lattice constants σ_{XY} for the various types of inclusions considered in the present work. Stiffnesses are in units of ϵ/σ^2 and lattice constants in units of σ.

elastic interactions. We have recently shown that the non-locality induces significant changes in the shape, growth mode, and coarsening behavior of inclusions by promoting or impeding the attachment of solute atoms at different sites along the interface [66]. A similar, more exhaustive analysis is reported in the present article; in particular, we demonstrate that a remarkably rich variety of behaviors emerges from the presence of elasticity at interphase boundaries, and that these strongly affect the coarsening process of a collection of inclusions.

Since the growth of inclusions in multi-phase systems physically occurs through the substitution of a matrix atom (A) by a solute atom (B) at the interphase boundary, it is essential to understand first how elasticity affects this basic process. The first part of our analysis will thus be concerned with the interplay between the local (atomic-scale) and the global (overall shape) elastic effects upon the addition of solute atoms at different sites along the surface of the inclusions; these calculations were carried out within the QCM through sequences of elastic relaxations.

In order to obtain information on the behavior of both faceted and rough regions of the surface, a rounded-hexagonal inclusion with a maximum radius of 70σ was chosen as model system; this is illustrated in Fig. 6.1(a). Anticipating our results, we note that this configuration is typical of those observed in growth conditions. Due to its symmetric shape, only a small portion of the interface [shown in Fig. 6.1(b)] needs to be monitored; this contains half the long terrace composing a (10) facet (centered at $\pi/6$), in addition to a rough region containing many small terraces. The elastic *addition* or *substitution* energy $\Delta E^{A\to B}_{\text{elastic}}$, i.e., the change in elastic energy resulting from the exchange of an A atom with a B atom at the

surface of the inclusion, will be computed for every site along the interface shown in Fig. 6.1(b). The energies for *sequential filling* (lateral growth) of terraces on the facet were also computed, in both forward (from the center of the terrace toward the step edge) and backward (from the step edge toward the center of the terrace) directions.

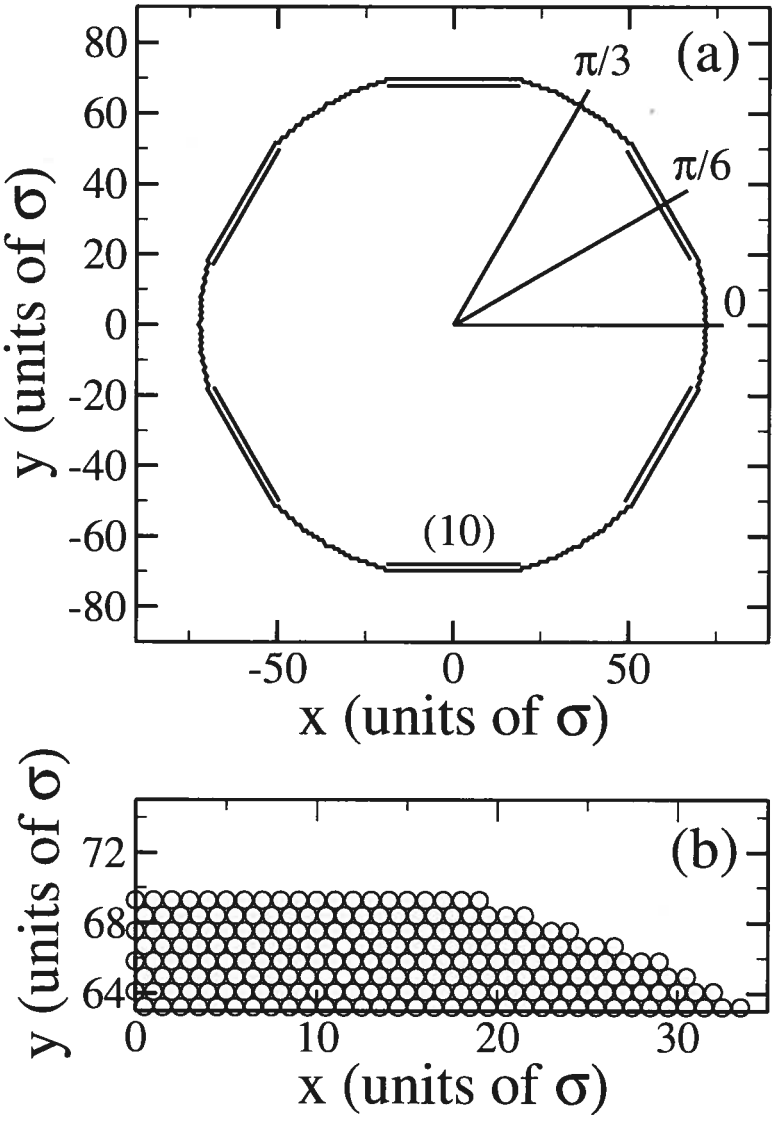

FIG. 6.1 – Model inclusion used in the calculation of substitution elastic energies. (a) General shape of the inclusion; double lines indicate (10) facets; the angular convention used is also shown. (b) Atomic-scale structure of the interface; grey circles correspond to atoms within the inclusion (type B); matrix atoms (type A) are not shown for clarity.

The second part of our analysis will deal with the consequences of elasticity, as

determined by the QCM calculations, on the coarsening dynamics of a collection of inclusions; these calculations were performed using the multi-scale TDDFT model described in Section 6.2. More specifically, we investigate how $\Delta E_{\text{elastic}}^{A\to B}$ affects the shape of the inclusions, their growth and their chemical potentials. Growth and evaporation were studied using the TDDFT in the grand-canonical ensemble, i.e., with the boundary of the simulation cell acting as constant source or drain of chemical potential. Typically, undersaturations or supersaturations below 0.2% are used in the present study. In all cases, circular inclusions with radius $R = 40\sigma$ were used as the initial configuration. Since the model system studied here is basically a substitutional alloy (notwithstanding the very small vacancy concentration), the inclusions will be characterized by the value of $\Delta\mu_i = \mu_B - \mu_A$, where μ_A and μ_B are the chemical potentials of species A and B inside the (B-rich) inclusions, respectively.

We conclude this section with some remarks on terminology. We frequently refer here to "facets", even if, strictly speaking, these do not exist (in the thermodynamical sense) for 1D interfaces; a more rigorous term would be "quasi-facets". In the same spirit, "layer-by-layer" growth strictly occurs only when partial layers behave as a low-dimensional undercritical phase, also rigorously impossible on a 1D interface, even if the filling fraction vs. μ curves can be extremely sharp [58]; here we use "layer-by-layer" in a weaker sense to describe growth by successive addition of laterally-growing layers.

6.4 Results

6.4.1 Elastically homogeneous systems

The properties of inclusions (e.g., the interfacial free energy) are affected by the atomic-scale structure along the surface even in absence of elastic misfits. Also, the shape can be modulated by kinetic factors; for example, growth modifies the local curvature of the surface through Mullins-Sekerka shape instabilities [45, 56], or its profile through solute trapping [29, 40]. These effects usually become significant only for relatively large growth rates. Others, such as kinetic faceting [20, 102], can affect slowly moving interfaces; this takes place when faceted orientations grow

more slowly than rough orientations, so that fast orientations gradually grow out of existence. This typically occurs at low to moderate growth rates because it requires the chemical potential difference between step sites and terrace sites to be significant compared to the driving force. Conversely, inclusions that suffered evaporation (or dissolution) are more rounded. Since we are mostly concerned with coarsening in the dilute limit here, only low growth rates will be investigated; for larger driving forces, see Ref. [68].

As there is no coupling between the local and the global interface structure in misfit-free systems, the results in this section will serve as a reference for clearly separating elastic effects from other, purely chemical, contributions. Without elastic misfits, elastic substitution energies vanish, and we therefore directly proceed with the TDDFT results.

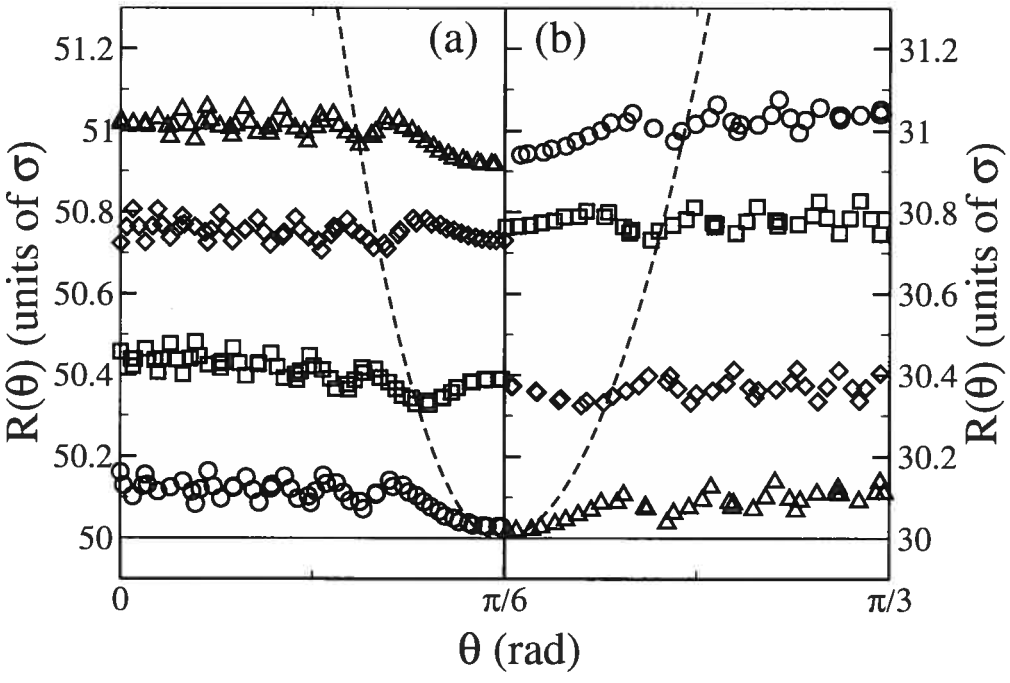

FIG. 6.2 – Angular dependence of the radius $R(\theta)$ of a homogeneous inclusion at different times (a) under growth and (b) under evaporation. θ is defined in Fig. 6.1; $\pi/6$ corresponds to the center of a (10) facet. Symbols appear in order of increasing time : circles, squares, diamonds, and triangles. The dashed and continuous lines show the expected dependence for a perfect hexagon and a perfect circle, respectively. The initial state of the inclusion is a circle of radius $R = 40\sigma$.

We investigate first the effect of growth and evaporation. During growth, as can be seen in Fig. 6.2(a), the shape of the inclusion (initially circular) remains essentially unchanged (cf. continuous line), indicating that thermodynamic or kinetic faceting are relatively unimportant at this temperature and for this growth rate. Yet, small modulations in the shape of the inclusion are visible near $\theta = \pi/6$, corresponding to the low-energy (10) plane of the triangular lattice (cf. Fig. 6.1). This behaviour is the consequence of orientational variations in the interfacial free energy and hence, the concavity of $R(\theta)$ near $\pi/6$ is the signature of a weak faceting tendency in regions of the surface close to (10) orientations. During growth, the inclusion oscillates between this weakly faceted state and a nearly circular one *as a function of the filling fraction of the interface layer.* A similar behavior is observed for evaporation, Fig. 6.2(b), supporting the thermodynamic (as opposed to kinetic) origin of the modulations. The importance of this natural tendency to form partially-faceted shapes will be demonstrated below. In contrast, away from $\pi/6$ (i.e., in rough regions), $R(\theta)$ increases continuously without deformation as growth proceeds.

Since the chemical potential of an elastically homogeneous inclusion is a function of the curvature of its surface, variations in the latter will affect the former : even a weak tendency to facet changes the average number of A–B bonds per interface atom, and hence the chemical potential of the inclusion. As shown in Fig. 6.3, oscillations in $\Delta\mu_i$ are indeed observed, superimposed on the usual capillarity $1/R_{\text{eq}}$ dependence. The minima correspond to a perfect circular shape while the maxima correspond to a partially-faceted shape. As expected, the period of the oscillations [cf. Figs. 6.3(b) and (c)] is precisely the distance between neighboring (10) atomic layers, that is $\sqrt{3}\sigma/2 = 0.866\sigma$.

The effect of the shape modulations of an inclusion on $\Delta\mu_i$ can be parametrized using a few simple hypothesis. First, if we assume the inclusion to possess a partially-faceted (rounded-hexagonal) shape similar to that shown in Fig. 6.1, we

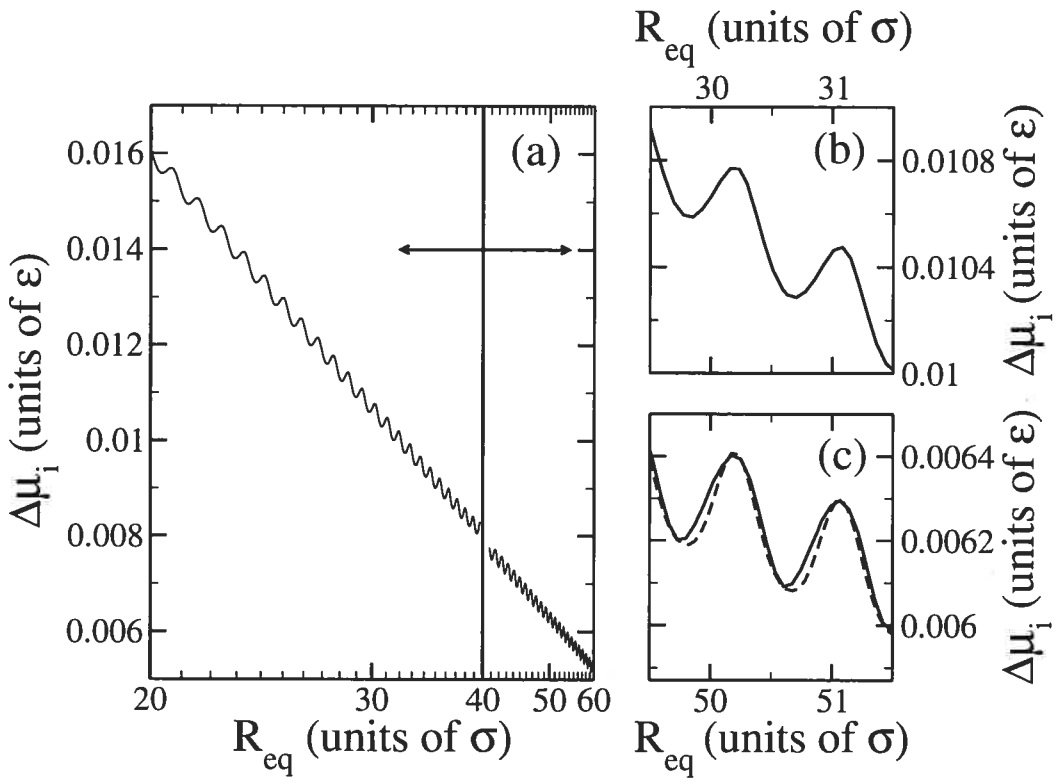

FIG. 6.3 – (a) Chemical potential difference $\Delta\mu_i = \mu_B - \mu_A$ between species B and species A as a function of the size of a homogeneous inclusion during evaporation for $R_{\rm eq} < 40\sigma$ (left-pointing arrow), and during growth for $R_{\rm eq} > 40\sigma$ (right-pointing arrow). (b) and (c) Close-up views near $R_{\rm eq} = 30\sigma$ and $R_{\rm eq} = 50\sigma$, respectively. The dashed line corresponds to the prediction of Eq. 6.14.

can write

$$R_{\rm rh}(\theta) = \begin{array}{ll} \frac{\sqrt{3}R_0}{\sin(\theta)+\sqrt{3}\cos(\theta)} & \text{if } |\theta - \frac{\pi}{6}| < \theta_f \\ \frac{\sqrt{3}R_0}{\sin(\theta_f+\frac{\pi}{6})+\sqrt{3}\cos(\theta_f+\frac{\pi}{6})} & \text{if } |\theta - \frac{\pi}{6}| > \theta_f. \end{array} \tag{6.13}$$

The facets are oriented along the (10) direction and occupy an angular spread $2\theta_f$ ($\theta_f = 0$ for a circular inclusion and $\pi/6$ for an hexagonal inclusion). Here, $0 < \theta < \pi/3$; values of $R_{\rm rh}$ for θ outside this range are obtained by evaluating the expression at $\theta' =$ mod $(\theta, \pi/3)$. Second, the chemical potential of a partially-faceted inclusion may be written

$$\Delta\mu_i(R_{\rm eq}, \theta_f) = \left\{C + D[\mathrm{exc}(\theta_f) - \mathrm{exc}(0)]\right\}/R_{\rm eq} + \Delta\mu_i^{\infty}, \tag{6.14}$$

where C and D are constants related to the interface free-energy, $\mathrm{exc}(\theta_f)$ is such that the excess number of A–B bonds per interface atom for a shape given by Eq. 6.13 is $\mathrm{exc}(\theta_f)/R_{\mathrm{eq}}$ (obtained numerically), and $\Delta\mu_i^{\infty}$ is the value of $\Delta\mu_i$ at thermodynamic coexistence (i.e., between macroscopic phases) ; C, D, and $\Delta\mu_i^{\infty}$ are treated as adjustable parameters. Third, and finally, we assume that the inclusion oscillates between two states characterized by two angles, $\theta_f^{\max}$ and $\theta_f^{\min}$ with a period of $\sqrt{3}\sigma/2$ (see above) :

$$\theta_f(R_{\mathrm{eq}}) = \theta_f^{\min} + (\theta_f^{\max} - \theta_f^{\min})[\frac{\sin(4\pi R_{\mathrm{eq}}/\sqrt{3} + \phi) + 1}{2}]. \qquad (6.15)$$

Thus, $\theta_f^{\min}$ measures the stable departure from the circular shape (for example, in the event of facetting), while $(\theta_f^{\max} - \theta_f^{\min})$ represents the amplitude of the change in shape in the course of adding (removing) a complete new layer to (from) the inclusion.

The values of C, D and $\Delta\mu_{\infty}$ are obtained by fitting the calculated $\Delta\mu_i$ to Eq. 6.14, while $\theta_f^{\min}$ $\theta_f^{\max}$ are obtained by fitting to Eq. 6.13. From the data of Fig. 6.3, we find $\theta_f^{\min} = 0$ and $\theta_f^{\max} = 0.07$. Note that these values are valid for all sizes, and for both growth and evaporation. As shown in Fig. 6.3(c), the agreement between the model and the data is excellent. From now on, the value of D obtained here (5.25) will be kept constant when fitting other $\Delta\mu_i(R_{\mathrm{eq}})$ curves to Eq. 6.14. This will serve as an estimate of the contribution of shape modulations to $\Delta\mu_i$.

Three important consequences can be inferred from the fact that the circular shape is maintained during growth : (i) the interface free-energy is nearly isotropic at the temperature considered ; (ii) the kinetic coefficient (related to the growth speed of different orientations of the interface) is isotropic at this temperature and supersaturation ; and (iii) shape instabilities are absent for the growth rate considered. Departures from these characteristics will thus be attributed to elasticity.

6.4.2 Energetics of inhomogeneous inclusions

Before repeating the previous analysis on misfitted inclusions, we discuss their energetics in order to assess whether interfacially-induced shape modifications are

favored or impeded by elasticity. These calculations, carried out within the QCM, also provide an estimate of the elastic energies involved.

It is known since Eshelby that, within linear elasticity, hard inclusions have minimum elastic energy when circular and soft inclusions when plate-like (very elliptic) [16]. This is verified in our QCM calculations, as shown in Fig. 6.4(a) : The transition to an elliptic shape increases the elastic energy of the HI by about 3% ($\sim 0.07\epsilon$ per B atom), while the elastic energy of the elliptic SI drops by about 2.5% relative to that of the circle ($\sim 0.02\epsilon$ per B atom). In order to assess the cost of faceting, we also considered hexagonal inclusions : the elastic energy increases by 1.5% upon faceting for the HI, while it decreases by roughly the same amount for the SI. Thus, from the energetics point of view, elasticity either promotes (SI) or limits (HI) faceting. However, since the bulk of the excess elastic energy is stored in the tips of the hexagon, *partial* faceting incurs a relatively low cost in energy. As a final point, it is is interesting to note that the relative elastic energies of the different inclusions depend on size, especially at small sizes. This is a manifestation of interface contributions to the elastic energy, which are ignored in conventional linear-elasticity calculations [83].

Of course, the (chemical) interfacial energy also contributes to determining the equilibrium shape of the inclusions. Using linear elasticity and an interface energy which is isotropic (i.e., does not depend on orientation), Johnson *et al.* [33] have shown that, in two dimensions, the equilibrium shape of the HI is circular for all sizes, while it changes from circular to elliptic (through a second-order transition) with increasing size in the SI. This behavior can also be infered from our QCM calculations, as demonstrated in Fig. 6.4(b) which shows the size dependence of the total (elastic plus interfacial) energy. At $T = 0$, the interfacial energy is here given by the number of A–B bonds times $\epsilon_{AA} + \epsilon_{BB} - 2\epsilon_{AB} = 0.3\epsilon$. As can be seen in Fig. 6.4(b), the elliptic HI is energetically disfavored for all sizes. For the SI, the ellipse initially possesses higher energy than the circle, due to its larger circumference ; as size increases, the gain in interfacial energy is eventually offset by the decrease of the elastic energy. This behaviour was shown earlier to be correctly described by our TDDFT model [68]. Note that the cross-over occurs around $R =$

100σ ; this is above the maximum size considered in the TDDFT calculations (70σ), and we can therefore be confident that the equilibrium shape of all our inclusions is a circle. Finally, owing to the small cost in interfacial energy they incur, faceted inclusions can be energetically advantageous over circular ones. This is the case for both SI and HI, as shown in Fig. 6.4(b). As the area/perimeter ratio increases, the faceted HI energy eventually increases above that of the circular HI. In contrast, since the elastic energy of the faceted SI is lower than of the circular SI, the former possesses a lower total energy over the whole range of sizes considered here. Of course, this analysis is only valid a $T = 0$; as shown in the previous section, finite-temperature entropic contributions offset this energy advantage at $T = 0.5\epsilon/k_B$.

6.4.3 Hard inclusions

6.4.3.1 Hard inclusions with low interface misfit (HI-LM)

We undertake now a systematic investigation of the interplay between elasticity, interface structure, and chemical potential in the different types of inclusions, starting with the case of a HI-LM. We begin by examining the elastic contribution to the energy required for substituting a B atom for an A atom at various sites along the surface of the inclusion. The results, presented in Fig. 6.5, show that $\Delta E^{A\to B}_{\text{elastic}}$ depends sensitively on both the local state of the interface (local atomic configuration) and the overall shape of the inclusion. To illustrate this, consider for example the faceted region : while every site along the terrace has the same local neighborhood, $\Delta E^{A\to B}_{\text{elastic}}$ nevertheless varies strongly with position, from 0.045ϵ at the center of the facet (indicated by label A) to 0.085ϵ at the edge (B). We note, in passing, that this is not significantly different from the $\Delta E^{A\to B}_{\text{elastic}}$ for sequential filling of the terrace — which proceeds by substitution at a step instead of directly on the terrace — from either the center or the edge. In the rough region, elasticity slightly favors substitution at steps (0.065ϵ — C) over edges (0.085ϵ — D), and $\Delta E^{A\to B}_{\text{elastic}}$ is generally larger than on the facet.

This "landscape of addition energies" leads to a slight increase of the stability of terraces on facets in comparison to the misfit-free case. From Fig. 6.5 we see that the change in elastic energy for evaporating an atom at a step in the rough region

is about -0.07ϵ (C), while it ranges between -0.05 and -0.065ϵ at a step on a facet which is sufficiently far from the edge of the terrace (cf. curve for forward sequential filling). Terraces on facets therefore tend to be stabilized by elasticity, the more so that they are shorter (since the energy gain in evaporating a B atom is lowest in the middle of the facet).

From the point of view of kinetics, the preferential attachment of B atoms at steps (C) vs. edges (D) in the rough regions slightly promotes the lateral growth of terraces, leading to the expansion of pre-existing facets. This process is however self-limiting since the longer the terrace, the larger $\Delta E^{A\to B}_{\text{elastic}}$ at the steps (cf. dashed line in Fig. 6.5). This is related to the increase of elastic energy upon faceting, as reported in Section 6.4.2. Thus, we would expect the inclusions to gradually adopt a rounded-hexagonal shape. On the other hand, the low values of $\Delta E^{A\to B}_{\text{elastic}}$ on long terraces have the opposite effect, viz. favoring the nucleation and growth of new terraces (preferably from the center of facets). The inclusion's evolution dynamics will result from a balance between these two competing factors.

Consistent with these observations, the TDDFT simulations reveal that elastic contributions to the shape of the inclusion during growth or evaporation are small; this is clearly seen in Fig. 6.6 (HI-LM), as well as Fig. 6.7. Growth and evaporation behave in qualitatively the same way as in the misfit-free case, i.e., continuously, except for small modulations around $\theta = \pi/6$ (Fig. 6.7). Quantitatively, the shape modulations are slightly more pronouced : fitting to Eq. 6.13 for $R_{\text{eq}} = 50\sigma$ yields $[\theta_f^{\min}, \theta_f^{\max}] = [0, 0.11]$ here, vs. $[0, 0.07]$ in the misfit-free case. This is consistent with the discussion above concerning the stabilization of terraces on facets. Similar results are obtained in evaporation. Modest kinetic faceting is also observed upon growth, $\theta_f^{\min}$ increasing to 0.03 at $R_{\text{eq}} = 70\sigma$.

The stabilization of facets can also be inferred from the behaviour of the chemical potential of the inclusion, shown in Fig. 6.8 : the amplitude of the oscillations of $\Delta\mu_i$ is here three-fold enhanced compared to the homogeneous case. The excellent agreement with the predictions of Eq. 6.14 [cf. Fig. 6.8(c)] confirms that this enhancement is essentially due to the increase of $\theta_f^{\max}$.

6.4.3.2 Hard inclusions with high interface misfit (HI-HM)

We turn now to the HI-HM case ; because of the large interface misfit, the effects of elasticity are evidently expected to be more important. The elastic substitution energies, presented in Fig. 6.9, indeed show an increase in both magnitude and sensitivity to the local and the global interface structure as compared to the HI-LM case.

A first noteworthy feature of the substitution energy landscape is the very large values of $\Delta E^{A\to B}_{\text{elastic}}$ on the facets, which range from 0.125ϵ at the center (A) to 0.18ϵ at the edge (B) — two or three times the barrier for addition at steps in the rough region, 0.065ϵ (C). However, the nucleation of a new terrace on a facet causes $\Delta E^{A\to B}_{\text{elastic}}$ to decrease drastically : the energies for sequentially filling a facet (either from the center or from the edge — cf. dashed and dotted lines in Fig. 6.9) drop to about 0.05ϵ once a first B atom has attached, i.e., *below* the value for steps in rough regions (C). Thus, elasticity opposes a strong barrier to the nucleation of new terraces on facets, but not against their growth once they have started to form. In rough regions, the larger misfit causes an increase of $\Delta E^{A\to B}_{\text{elastic}}$ at step edges to about 0.14ϵ (D), while substitution at steps remains essentially the same as in the low-misfit case, $\sim 0.065\epsilon$ (C).

Similar to the HI-LM case, elasticity affects the shape of inclusions by stabilizing terraces on facets : the gain in elastic energy for evaporating an atom is indeed lower from a step on a facet (dotted line) than from a step in the rough region (C). In contrast with the HI-LM case, however, the distribution of $\Delta E^{A\to B}_{\text{elastic}}$ strongly promotes kinetic faceting. Indeed, in addition to the strong bias in favor of the attachment of B atoms at steps in the rough region, which drives the lateral growth of existing terraces, elasticity opposes a large barrier to the nucleation of new terraces on pre-existing facets as noted above, further limiting the growth along these orientations. Thus, rather than competing as in the HI-LM case, these two factors combine now to favor the growth of existing facets. However, as discussed earlier, given the rapid increase of $\Delta E^{A\to B}_{\text{elastic}}$ near the edges of the facets (B), faceting is self-limiting. In addition, the structure of $\Delta E^{A\to B}_{\text{elastic}}$ induces a transition from continuous to lateral layer-by-layer growth on the facets : the nucleation of new

terraces preferentially occurs at the center of facets (A) where the substitution energy is smallest; subsequent growth proceeds by sequential filling of the facet, as discussed above.

Enhanced faceting is indeed observed in the TDDFT simulations. Very sharp facets form near $\theta = \pi/6$, as shown in Fig. 6.10 (cf. circles and dashed line) as well as Fig 6.6. Further, the layer-by-layer growth mode anticipated above is also observed : the nucleation of a new layer (squares to diamonds) occurs from the center of an initially clean facet (circles) and is followed by lateral growth (diamonds to triangles). During the first part of the process, the rough region (near $\theta = 0$) does not grow appreciably, as it is more advantageous for B atoms to attach at the steps of the newly-formed terrace (near $\theta = \pi/6$). As the latter develops, substitution energies at its steps increases to the point that further growth is gradually outpaced by the growth of rough regions (diamonds to triangles). By then, a complete layer has formed and the cycle repeats itself.

The stabilization of facets also occurs during evaporation. Indeed, the terrace on the facet is the last section of the layer to evaporate; faceting is however less important than during growth. From a fit to Eq. 6.13, one obtains the following parameters for the facets : $[\theta_f^{\min}, \theta_f^{\max}] = [0.01, 0.15]$, $[0.01, 0.18]$, and $[0.11, 0.18]$ for $R_{\text{eq}} \approx 30\sigma$, 50σ, and 70σ, respectively.

The steady increase of $\theta_f^{\min}$ shows that the kinetics strongly contributes to faceting : the high barrier for addition on a clean facet efficiently opposes growth along the corresponding orientation [viz. (10)] compared to that in rough regions. This leads to the development of an increasingly faceted shape.

As shown in Fig. 6.11, the large modulations in the shape of the inclusion we have just described have a profound effect on the size dependence of $\Delta\mu_i$, which now exhibits very large oscillations during both growth and evaporation. Upon comparing with the predictions of Eq. 6.14 [cf. Fig. 6.11(c)], we find however that the oscillations are too large to be accounted for by shape modulations alone. Thus, another process is at play, which can in fact be inferred from the behavior of $\Delta E_{\text{elastic}}^{A \to B}$ (Fig. 6.9) as follows : For partially-faceted shapes (corresponding to maxima of $\Delta\mu_i$), low-energy sites are not available for the addition of B atoms

because of the high cost of $A \rightarrow B$ substitution on top of a facet. Since $\Delta\mu_i$ is the average increase of the free energy for such substitution processes at the interface, high values of $\Delta E_{\text{elastic}}^{A\rightarrow B}$ translate into high values of $\Delta\mu_i$. However, as soon as the nucleation of a new terrace occurs, low-energy sites become available for other B atoms to attach, causing a drop in $\Delta\mu_i$, in addition to that caused by the shape change. Note that this was not observed in the HI-LM case because $\Delta E_{\text{elastic}}^{B\rightarrow A}$ does not change significantly following the nucleation of new terraces on facets, and because the substitution energies are much smaller in this case.

It can also be appreciated from Figs. 6.11 (b) and (c) that the profile of $\Delta\mu_i$ differs quite a bit from the simple model of Eq. 6.13. This is a consequence of the peculiar growth behavior of HI-HM : the transition from maxima (clean facets) to minima (nucleation of new terraces on facets) occurs in a very small interval of R_{eq} because the rough regions do not change appreciably during the transition (cf. Fig. 6.10), in contrast to either the misfit-free or the HI-LM case. Once the (fast) formation or evaporation of small terraces on facets is completed, the evolution of the rough regions proceeds more uniformly, leading to smoother variations of $\Delta\mu_i$ with R_{eq}.

6.4.3.3 Summary of results for hard inclusions

The previous two sections demonstrate that elastic inhomogeneities strongly affect the growth of inclusions. They also highlight the important role played by interfacial elasticity — recall that in both low- and high-misfit cases, the "bulk" elastic properties of inclusions and matrix are the same, while they differ at the interface. At low misfit, the inclusions behave in much the same way as in the homogeneous case. At large misfit, however, the energetics of the addition of solute atoms is significantly modified, with two important consequences : (i) (efficient) kinetic faceting is triggered and gradually pushes the inclusion away from equilibrium; (ii) strong oscillations of the chemical potential develop as a function of the filling fraction of the outer layer (in agreement with our previous results [66]). We stress again here that a proper account of these effects requires an atomic-scale description of the interfaces; this is further warranted by the demonstration of the

very strong dependence of the local energetics on both local and global interface structure.

6.4.4 Soft inclusions

6.4.4.1 Soft inclusions with low interface misfit (SI-LM)

We now turn to soft inclusions, beginning with the SI-LM case. Given the low misfit, and the low elastic energy stored in soft inclusions, the influence of elasticity on interface properties is expected to be very small. This is in fact confirmed by the elastic substitution energies shown in Fig. 6.12 : $\Delta E^{A\to B}_{\text{elastic}} \sim 0.02\epsilon$, compared to $0.05 - 0.09$ for HI-LM and $0.05 - 0.18$ for HI-HM. Even more significant is the fact that $\Delta E^{A\to B}_{\text{elastic}}$ is almost independent of position along the interface, the variations being $\sim 0.005\epsilon$; we therefore do not expect growth to depend strongly on orientation. In fact, substitution on a facet is totally independent of position, except in the case of sequential filling where $\Delta E^{A\to B}_{\text{elastic}}$ decreases abruptly at the edge of the terrace (B). Further, only small energy differences are found between steps and step edges in the rough region. Consequently, the behavior of SI-LM should be quite similar to that of a misfit-free inclusion, except perhaps for a small kinetic faceting tendency arising from the fact that barriers for addition on facets (either on a clean facet or at the steps of a terrace on a facet) are slightly larger than in the rough region.

The TDDFT calculations, presented in Figs. 6.6 and 6.13, confirm that the shape of the inclusions during growth and evaporation is essentially unaffected by the small elasticity (compare with Fig. 6.2). From a fit of $R(\theta)$ to Eq. 6.13, we obtain $[\theta_f^{\min}, \theta_f^{\max}] = [0, 0.08]$ for both $R_{\text{eq}} \sim 30\sigma$ and $R_{\text{eq}} \sim 50\sigma$, very close to the misfit-free values ($[0, 0.07]$). Yet, a small kinetic contribution can be detected during growth, as $\theta_f^{\min}$ increases to 0.03 when $R_{\text{eq}} \sim 70\sigma$. Note that the inclusion does not spontaneously adopt a faceted shape even if the calculations reported in Section 6.4.2 indicate that this would lower the total elastic energy. In fact, we observe that the inclusion relaxes to the circular shape even if its initial shape is hexagonal. This shows that entropic effects are strong enough to compensate the energetic advantage of the hexagonal shape at the temperature used.

As shown in Fig. 6.14, the chemical potential of the inclusion is not significantly affected by the small shape modulations, the latter being nearly identical to that of the misfit-free inclusion. Finally, comparison with Eq. 6.13 confirms that variations of the chemical potential are essentially caused by shape modulations during growth [see Fig.6.14(c)].

6.4.4.2 Soft inclusions with high interface misfit (SI-HM)

We conclude our study of the different types of inclusions with the SI-HM case. The substitution energies are presented in Fig. 6.15. The misfit is sufficiently large that the elastic energies now depend in a significant manner on the local and global interface structures. In particular, the addition energy clearly decreases as the edge of the terrace (B) is approached. However, sequential filling of the facet from either side strongly modifies this behavior : upon filling from the edge (dotted line in Fig. 6.15), $\Delta E^{A\to B}_{\text{elastic}}$ jumps from ~ 0 to $\sim 0.02\epsilon$ upon the addition of a single B atom, then slightly increases toward the center of the facet. Likewise, upon filling from the center (dashed line), $\Delta E^{A\to B}_{\text{elastic}}$ forms a little cusp following the addition of the first atom, then gradually decreases toward the edge. Finally, in the rough region, $\Delta E^{A\to B}_{\text{elastic}}$ behaves in much the same way as for hard inclusions : substitution at steps ($\sim 0.02\epsilon$ — C) is favored over substitution at step edges ($\sim 0.03\epsilon$ — D). Note that the addition energies for sequential filling are slightly larger on facets than in rough regions.

As discussed previously, the behavior of $\Delta E^{A\to B}_{\text{elastic}}$ in the rough region favors the lateral growth of existing terraces. Further, the (slightly) larger values of the addition energies on terraces also favor faceting, as in the HI-HM case. However, unlike hard inclusions, self-limitation of the faceting process is absent; on the contrary, faceting is self-promoting here, as $\Delta E^{A\to B}_{\text{elastic}}$ decreases toward the edge of the facet. This is in agreement with the results of Section 6.4.2 showing a decrease of the elastic energy upon faceting. Thus, thermodynamics and kinetics concur to promote faceting in the present situation.

TDDFT simulations confirm that faceting is significant in this case, as can be seen in Fig. 6.6 and, more quantitatively, in Fig. 6.16 : near $\theta = \pi/6$, $R(\theta)$ closely

follows the curve corresponding to a perfect facet. Further, deviations from the circular shape are now generalized as $R(\theta)$ remains concave down to $\theta = 0$ (recall that $R(\theta) = \text{cst.}$ for a circular inclusion). In fact, deviations are so important that $R(\theta)$ can no longer be separated into a facet and a rough region during growth. As in the HI-HM case, the addition of a new layer is initiated from the center of the facets (squares). The new terrace grows by sequential filling (diamonds); once the latter reaches its final size (triangles), addition continues in the rough region. Fig. 6.16 also reveals that evaporation behaves very differently, faceting being now much less important [notice the difference in scale between panels (a) and (b)]. A quantitative analysis of the angular size of the facets during growth gives $[\theta_f^{\min}, \theta_f^{\max}] = [0.07, 0.21]$ for $R_{\text{eq}} \approx 50\sigma$, reaching $[0.21, 0.24]$ for $R_{\text{eq}} \approx 70\sigma$. In contrast, during evaporation, θ_f ranges between 0 and 0.12, providing further evidence for an important kinetic component to faceting.

As in previous cases, oscillations in the shape of the inclusion show up in the behavior of $\Delta\mu_i$, presented in Fig. 6.16. The impact of kinetic faceting can also be observed in this figure, the amplitude of the oscillations in $\Delta\mu_i$ increasing with size. Comparison with Eq. 6.14 indicates that these oscillations are essentially due to shape modulations. This result is not surprising given the relatively small values of $\Delta E_{\text{elastic}}^{A\to B}$, and the weaker dependence on the interface state compared to HI-HM.

6.4.4.3 Summary of results for soft inclusions

Given the low elastic energies involved in the relaxation of soft inclusions compared to hard ones, only small deviations from the homogeneous case were expected. This is indeed the situation for low-misfit inclusions, which essentially behave as misfit-free (homogeneous) inclusions. However, upon increasing the interface misfit, strong kinetic faceting develops which induces large oscillations in the chemical potential as a function of increasing size. This once again results from changes in the distribution of elastic substitution energies because of the coupling between local and global interface structure. Note that the magnitude of the elastic substitution energies are quite small here compared to the HI-HM case; still, faceting is much more efficient. This underscores the importance of the self-limitation of kinetic fa-

ceting in HI-HM and of self-promotion in SI-LM. These results also demonstrate that small variations in the local energetics of the interface can affect the general behavior during growth, hence the importance of explicitly considering atomic-level elastic contributions.

6.5 Discussion

Our QCM and TDDFT calculations unambiguously establish the crucial importance of an atomic-scale description of the interface for reproducing the wide variety of possible behaviors induced by interface elasticity. We have shown that the chemical potential is strongly affected by modulations of the shape of the inclusions as well as by the energetics of the interface sites available for incorporating solute B atoms. Our calculations also show that chemical potentials which continuously and monotonously decrease with increasing inclusion size are the exception and not the rule as far as inhomogeneous elasticity is concerned. This implies that assumption (i) of the LSW model — the validity of the capillarity approximation, i.e., the chemical potential of an inclusion is proportional to the curvature of its interface — is violated, and hence normal coarsening, $\langle R \rangle \propto t^{1/3}$, does not necessarily take place.

In order to understand the consequences of the chemical potential oscillations on the coarsening behavior of a dilute assembly of inclusions, we have constructed and numerically solved a generalized LSW model which, as with the original LSW model [47], provides an equation of motion for the evolution of the size distribution $f(t, R)$ of the assembly :

$$\frac{\partial f(t,R)}{\partial t} = -\frac{\partial}{\partial R}\left[\frac{dR}{dt} f(t,R)\right], \tag{6.16}$$

where dR/dt is the rate at which an inclusion of radius R grows. By analogy with Eq. 6.9, one gets :

$$\frac{dR}{dt} \propto \frac{1}{R}[\mathcal{A}_m - \mathcal{A}_I(R)], \tag{6.17}$$

where $\mathcal{A}_m$ and $\mathcal{A}_I(R)$ are the activities within the matrix and inclusion, respectively ; for simplicity, the vacancies are ignored. The activity of the matrix is taken

to be proportional to the solute supersaturation $\Delta(t)$, while the activity of the inclusion follows a modified Gibbs-Thomson behavior :

$$\mathcal{A}_m(t) = \Delta(t) \tag{6.18}$$

$$\mathcal{A}_i(t) = C_1/R + C_2[\cos(4\pi R/\sqrt{3}) + 1]/2 \tag{6.19}$$

with C_1 and C_2 arbitrary constants; note that setting $C_2 = 0$ recovers the original LSW model. In order to close the system of equations, we must enforce conservation of solute atoms :

$$Q_0 = \Delta(t) + \int_0^\infty \pi R^2 f(R,t)\, dR, \tag{6.20}$$

where Q_0 is the initial, total supersaturation.

In what follows, we set $C_1 = 0.00025\sigma^{-1}$ and vary the value of C_2 between 0 and $3\text{x}10^{-6}$; $f(0,R)$ is (arbitrarily) taken to be constant between $R = 13\sigma$ and 21σ and zero elsewhere. The average inclusion size (obtained by numerically integrating Eq. 6.16) is presented in Fig. 6.18. This figure shows that the chemical potential oscillations (or equivalently, the activity oscillations, Eq. 6.19) do not affect the early stages of coarsening, which exhibits the normal LSW behavior (dashed line). However, when the amplitude of the oscillations (as determined by C_2) gets sufficiently large, coarsening is completely inhibited in later stages : after a transient period where the growth exponent gradually decreases, the system becomes kinetically frozen and the size distribution function ceases to evolve. The stabilization of the average inclusion size is not caused by some sort of inverse coarsening, which would imply gradual narrowing of the size distribution. In fact, the opposite is true : the distribution widens with time, as shown in Fig. 6.19 for $C_2 = 3\text{x}10^{-6}$. For $\langle R \rangle \leq 30\sigma$, the size distribution is little affected by the oscillations in the chemical potential, as it is close to the predictions of the classical LSW model (dashed line). However, as time runs (and $\langle R \rangle$ gets larger), the small R section of $f(R,t)$ rapidly becomes frozen, while the large R maximum moves toward larger values, causing the formation of a gradually widening bimodal distribution. The large size peak gradually decays, leaving a long tail in its wake, until coarsening completely stops.

This behavior can be understood in terms of the growth rate of the inclusions dR/dt, Eq. 6.17; the results for this quantity are presented in Fig. 6.20. The main consequences of the oscillations is that dR/dt possesses multiple zeroes, in contrast to the pure-capillarity case which has only one zero at any given time. This difference is of great significance because it implies that a finite fraction of the inclusions can simultaneously be in equilibrium at the same supersaturation, while this fraction is vanishingly small for smooth chemical potentials. For small average size $\langle R \rangle$ (cf. $\langle R \rangle = 30\sigma$ in Fig. 6.20), equilibrium ($dR/dt = 0$) is only possible over a rather small range of sizes (roughly between $R = 22\sigma$ and $R = 28\sigma$), so that the effect on the overall dynamics of the system is limited and coarsening proceeds normally. For larger average inclusion size (cf. $\langle R \rangle = 58\sigma$ in Fig. 6.20), the range of possible equilibrium states expands (to $R = 40\sigma$–75σ), causing a gradual freezing of the distribution function. In fact, only the two extremes of the distribution (in regions where the growth rate does not cross the equilibrium $dR/dt = 0$ line) are able to evolve, causing the formation of a bimodal distribution and, subsequently, of a large size tail. Eventually, the whole distribution function is located in regions where equilibrium with the matrix is possible, causing the coarsening to completely stop.

These results demonstrate, again, that the oscillations of the chemical potential during growth significantly affect the coarsening behavior of the inclusions, and can even lead to a complete stabilization of the microstructure without appealing to inverse coarsening. Indeed, a rapid decrease of the coarsening exponent from $1/3$ at early times to 0 at later times is observed. The oscillations can also strongly modify the size distribution of the inclusions through the formation of a large size tail.

The $\langle R \rangle$ vs. t curves presented in Fig. 6.18 are in striking agreement with the behaviour observed in such elastically inhomogeneous alloys as Ni-Cu-Si and Ti-Mo [65]. In these systems, coarsening initially proceeds according to the LSW theory with a growth exponent of $1/3$, then abruptly stops. We note that, in contrast to this, recent large-scale phase-field simulations have predicted that coarsening proceeds with a reduced, but constant, exponent in elastically inhomogeneous systems

[107]. In view of the agreement of our findings with experiment, we may conclude that the physical process responsible for microstructural stabilization in elastically inhomogeneous alloys is not properly included in phase-field models; our calculations indicate that the "missing link" is interface, atomic-scale elasticity. In addition, the oscillations in the chemical potential very likely explain the widening of the size distribution function observed during slow coarsening in some alloys [8, 25, 77], as discussed above.

It must nevertheless be mentioned that the present analysis suffers from two limitations. First, coarsening is assumed to arise strictly from the thermodynamic driving force $\mathcal{A}_m - \mathcal{A}_I(R)$. In real materials, thermal fluctuations enhance coarsening by helping the system to escape from long-lived metastable states even if the thermodynamic driving force alone is insufficient for this. For example, the nucleation of new terraces onto a facet of an HI-HM would abruptly decrease the chemical potential of an inclusion, allowing it to grow further. What was identified as a transition from a coarsening state to a frozen state in the present model is in fact a transition from diffusion-limited coarsening to nucleation-limited coarsening. For small nucleation barriers, thermal fluctuations enable coarsening to continue, albeit at a very small rate, while as shown by Rohrer and collaborators [76], higher barriers (compared to $k_B T$) virtually stop coarsening on experimental timescales. Second, it is known from experiment that the volume fraction of the inclusions affects coarsening in elastically inhomogeneous systems [54, 65]; this is not taken into account here. Thus, the slowdown of the kinetics is most likely not the result of interface effects alone. The impact of direct interactions between inclusions through the long-ranged strain field will be the subject of future investigations.

An aspect that has not been considered here it that metallic alloys are generally elastically anisotropic, implying the presence of "soft" orientations along which inclusions have a tendency to align. Consequently, inclusions usually adopt a cuboid shape with well-defined facets. Interface elasticity could thus be even more important in elastically anisotropic systems since, with large facets, the spectrum of addition energies is likely to become very wide, leading to larger oscillations of the chemical potential and hence larger impact on coarsening.

6.6 Conclusion

We have studied the role of interfacial elastic effects on the behavior of inhomogeneous inclusions under growth or evaporation conditions. This was achieved by decoupling the effect of "bulk" misfit from the effect of "interface" misfit through independent variations of the intra- and inter-specie terms of the interatomic potential. While it is already well known that strong inhomogeneities are able to considerably modify the coarsening behavior of the inclusions, our results show that the level of interface misfit is also crucially important : at low interface misfit, the behavior of isolated inclusions is similar to that of elastically homogeneous inclusions but a high interface misfit induces very strong coupling between the global shape of the inclusions and its structure on a local, atomic scale. This alters the energetics of the interface by favoring incorporation of solute atoms at certain specific sites. In turn, the new energy landscape modifies the morphology of the inclusions during growth, and hence the chemical potential of the inclusions. Oscillations of the chemical potential following the addition or subtraction of a new layer around the inclusion are shown to be commonplace in elastically inhomogeneous systems at high interface misfit. Using a modified LSW model, we have shown that, in presence of these oscillations, coarsening initially proceeds normally (with a $1/3$ exponent) but eventually stops completely, leading to stabilization of the microstructure. The results are in good qualitative agreement with the experimental studies of some inhomogeneous alloys [54, 65]. These results stress the need for an atomistic treatment of the interfaces in elastically inhomogeneous systems in order to unravel the wide range of possible growth behaviors, each having distinct kinetic properties.

This work has been supported by grants from the Natural Sciences and Engineering Research Council of Canada (NSERC) and the *Fonds Québécois de la Recherche sur la Nature et les Technologies* (FQRNT). We are indebted to the *Réseau Québécois de Calcul de Haute Performance* (RQCHP) for generous allocations of computer resources.

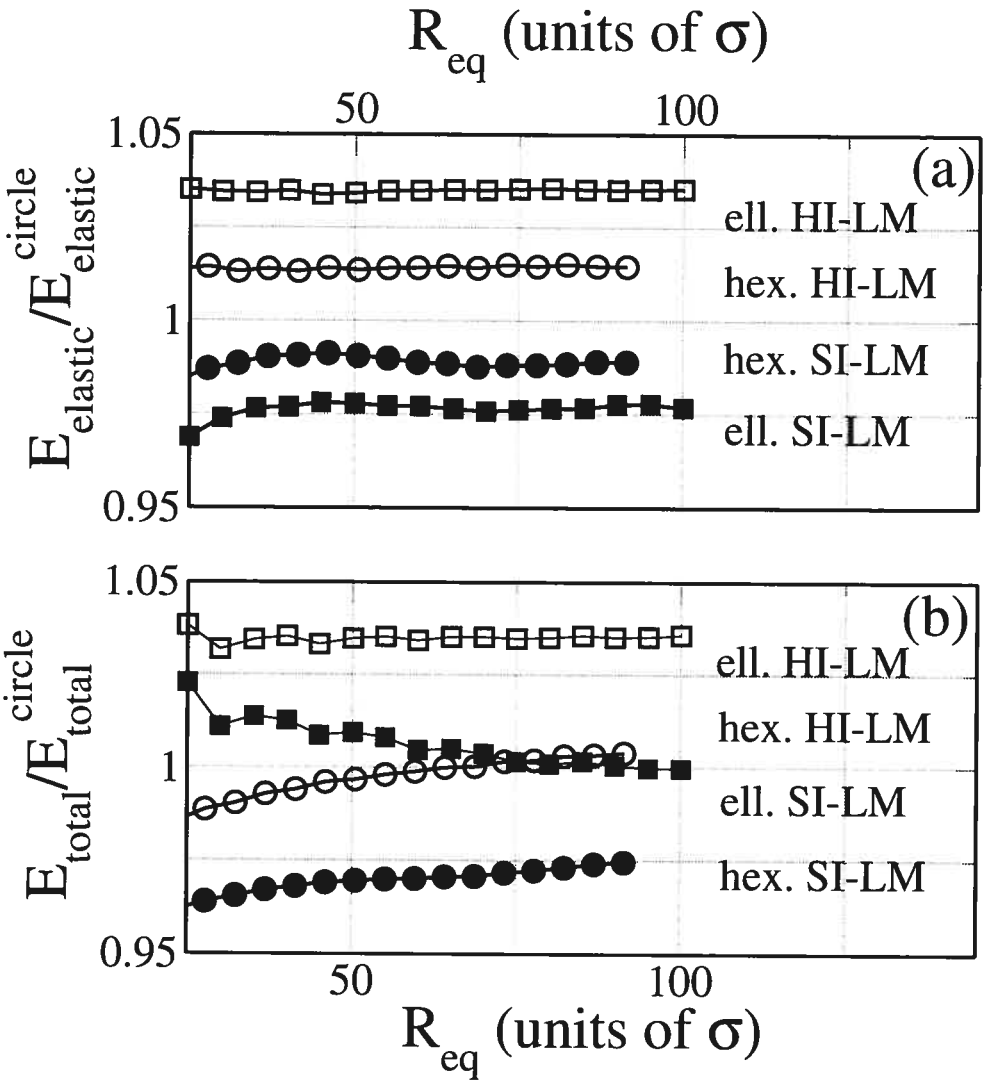

FIG. 6.4 – Energies of various types of inclusions (as indicated) relative to that of a circular inclusion as a function of equivalent radius (i.e., the radius of the circle having identical area) : (a) elastic energies; (b) total energies. The elliptic inclusions have an eccentricity of 0.75.

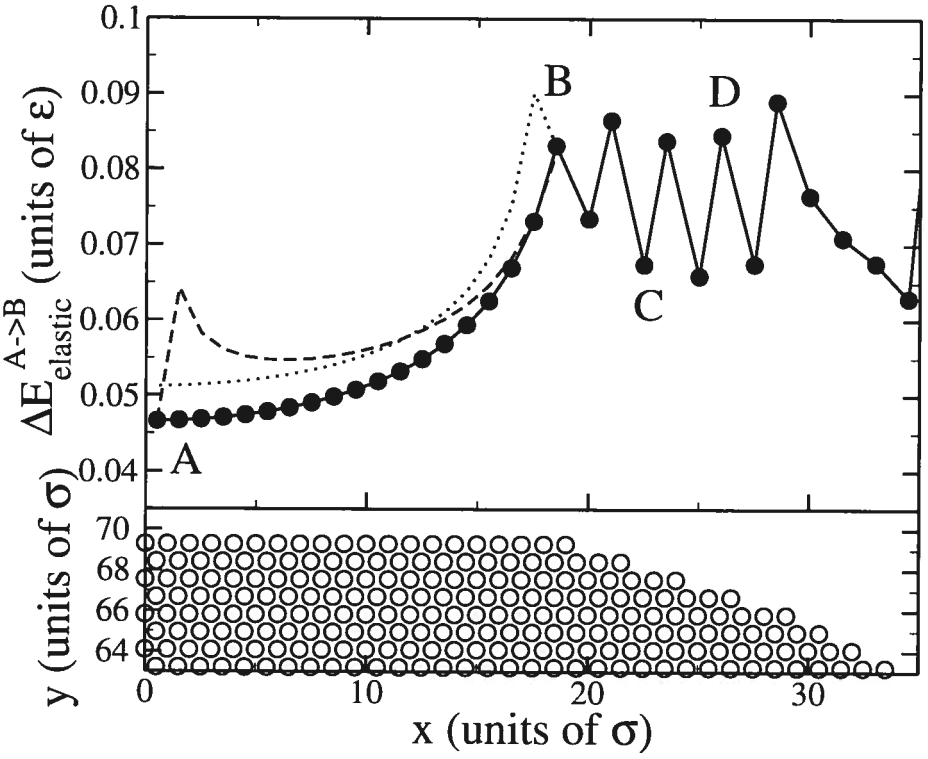

FIG. 6.5 – Change in elastic energy following the substitution of an A atom for a B atom at different positions along the interface of an HI-LM inclusion (filled circles and continuous line) ; the dashed and dotted lines correspond to forward and backward sequential filling, respectively. Capital letters refer to the various sites along the interface discussed in the text ; A : center of the facet ; B : edge of the facet ; C : step ; D : step edge. The bottom panel is the same as Fig. 6.1(b).

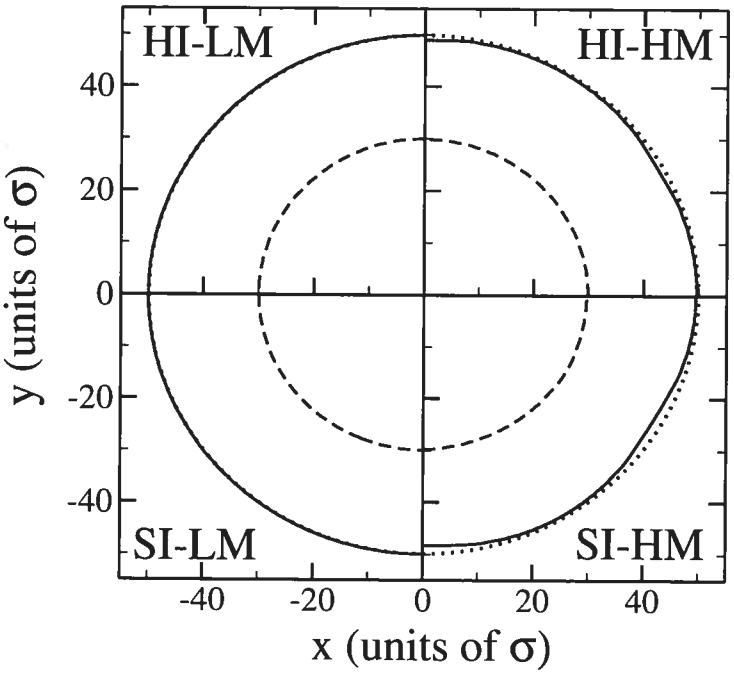

FIG. 6.6 – Shapes of the four types of misfitted inclusions during growth (continuous line) and evaporation (dashed line); the dotted line is a circle of radius $R = 50\sigma$ that serves as a reference.

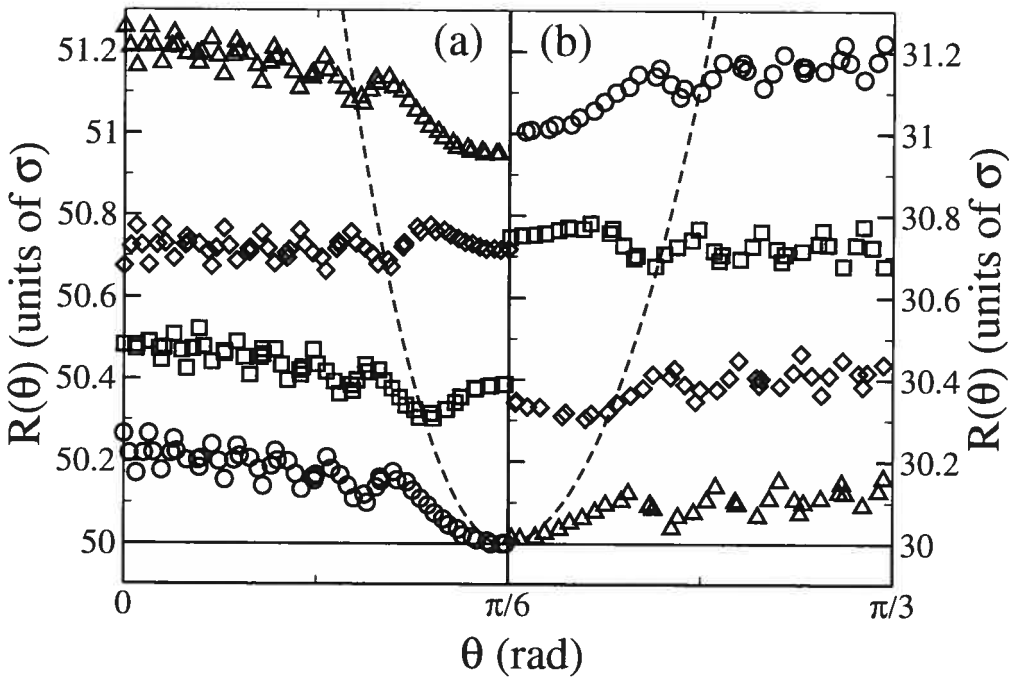

FIG. 6.7 – Same as Fig. 6.2 for the HI-LM case.

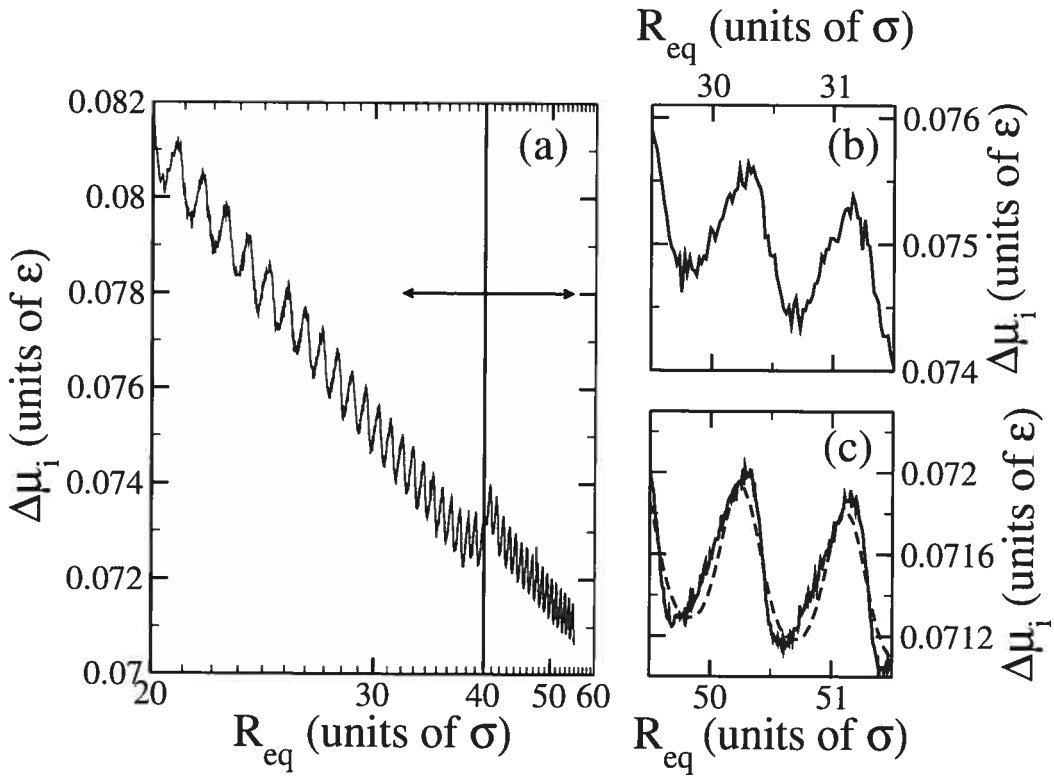

FIG. 6.8 – Same as Fig. 6.3 for the HL-LM case.

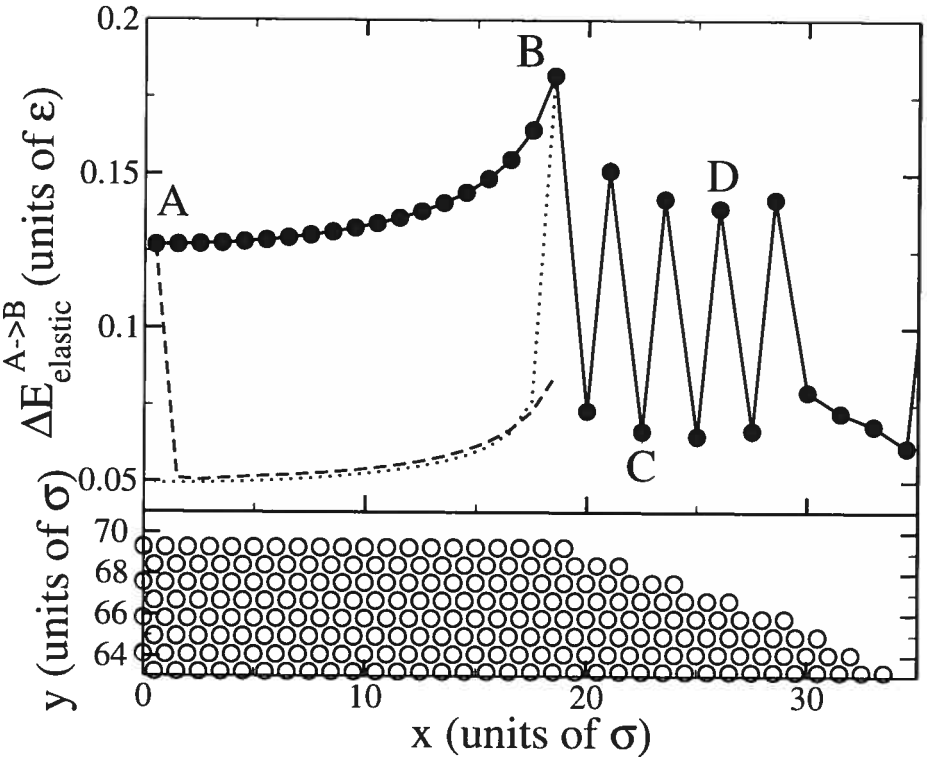

FIG. 6.9 – Same as Fig. 6.5 for the HI-HM case.

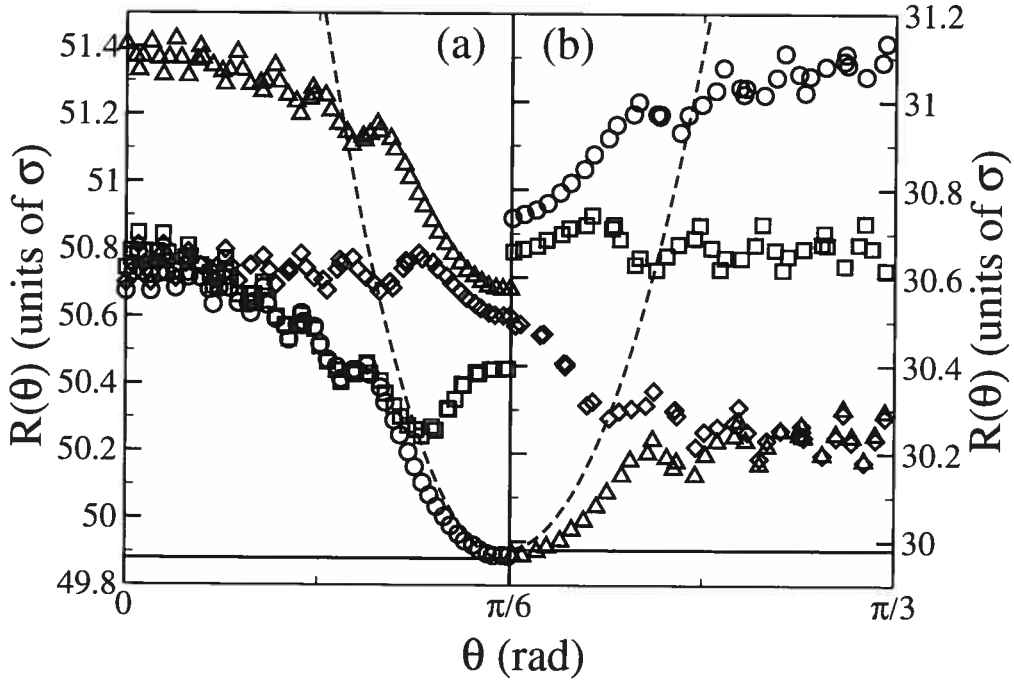

FIG. 6.10 – Same as Fig. 6.2 for the HI-HM case.

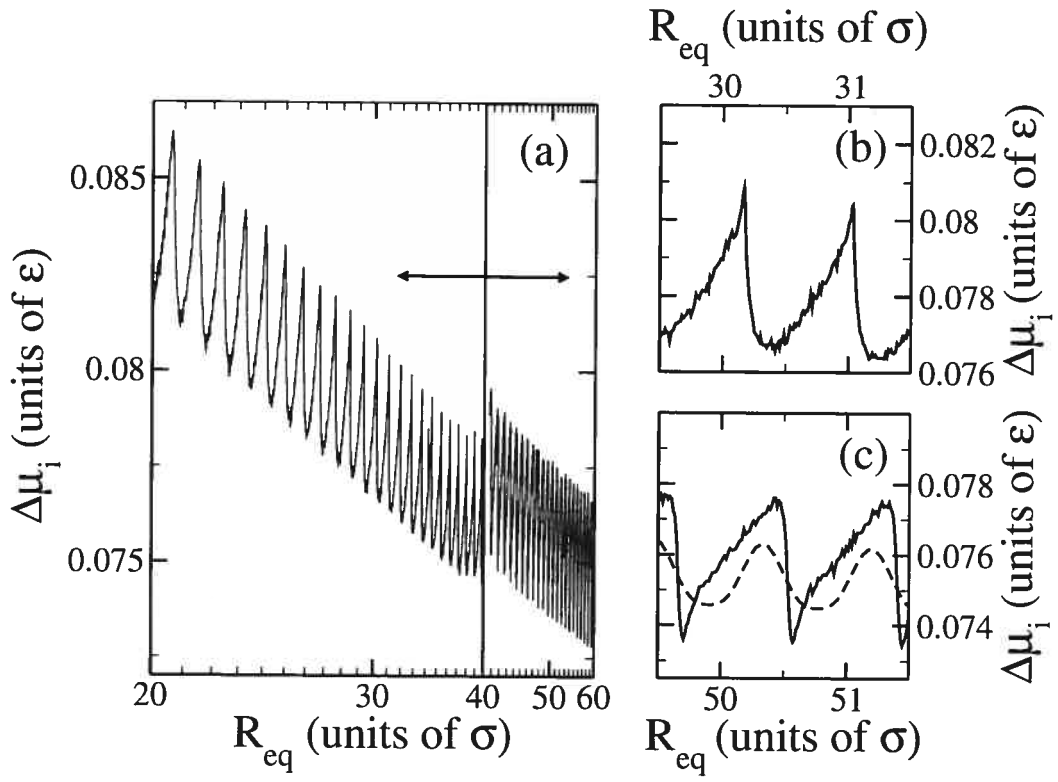

FIG. 6.11 – Same as Fig. 6.3 for the HI-HM case.

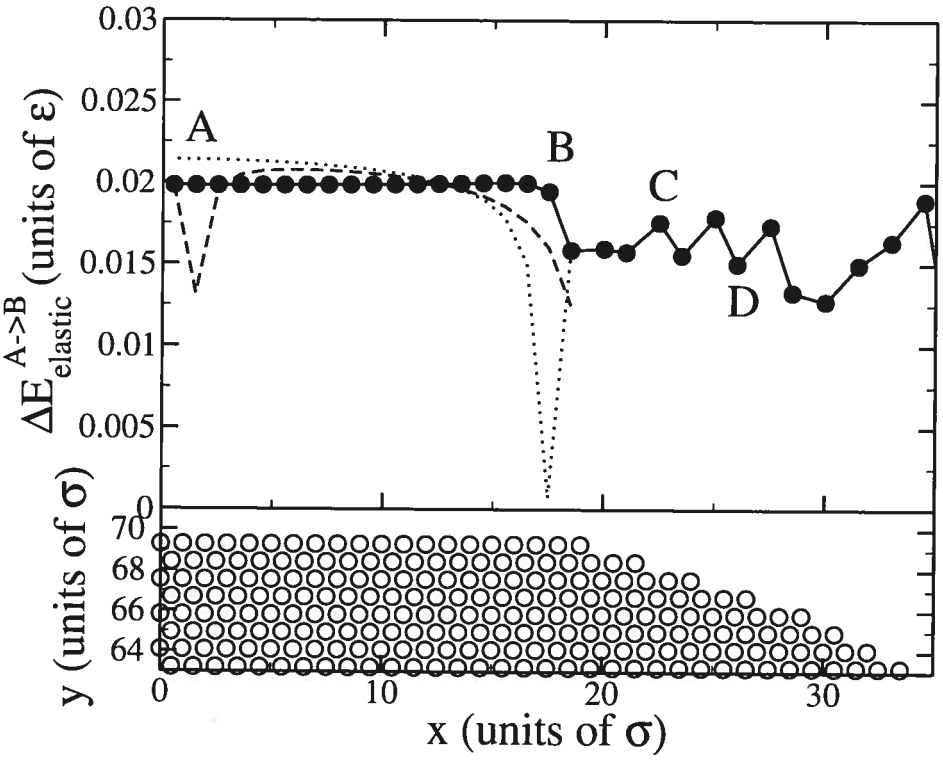

FIG. 6.12 – Same as Fig. 6.5 for the SI-LM case.

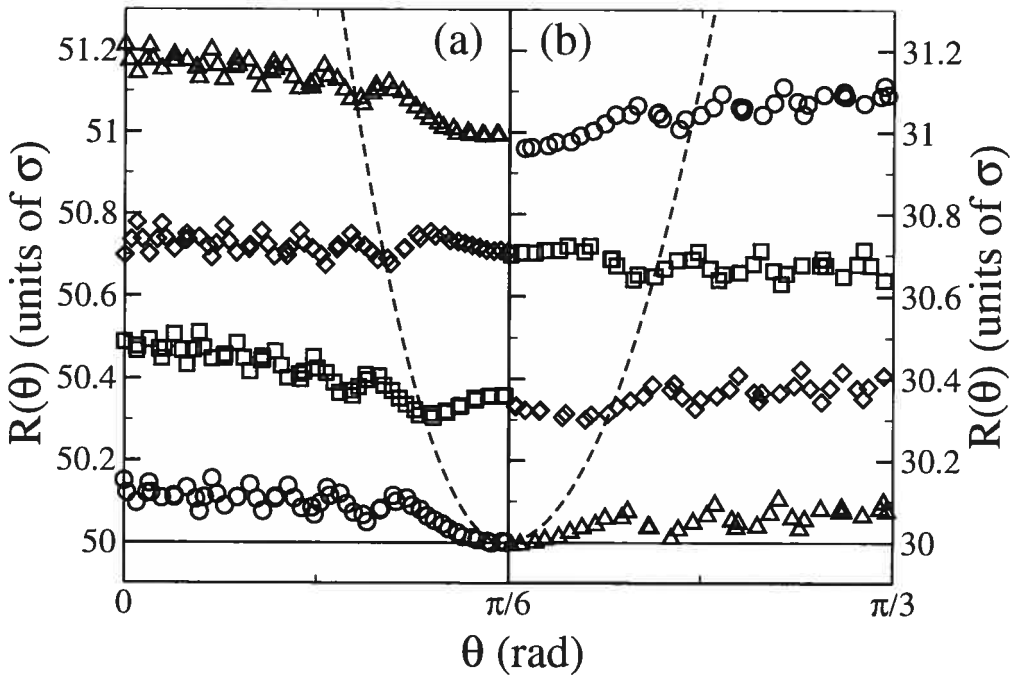

FIG. 6.13 – Same as Fig. 6.2 for the SI-LM case.

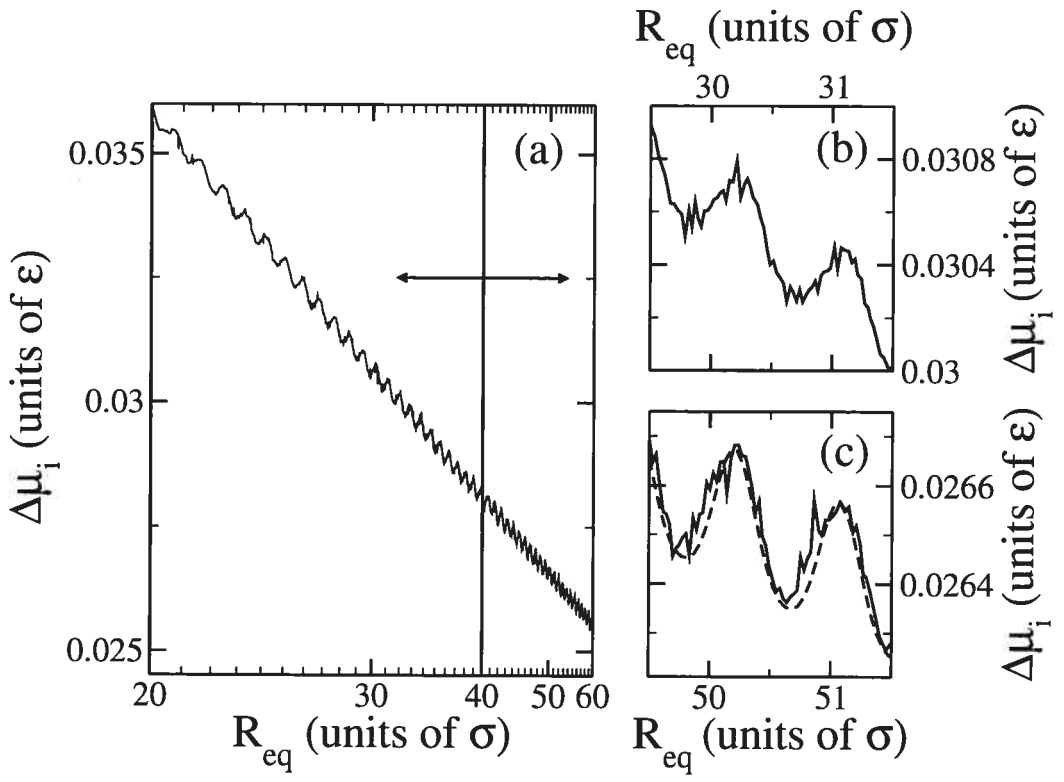

FIG. 6.14 – Same as Fig. 6.3 for the SI-LM case.

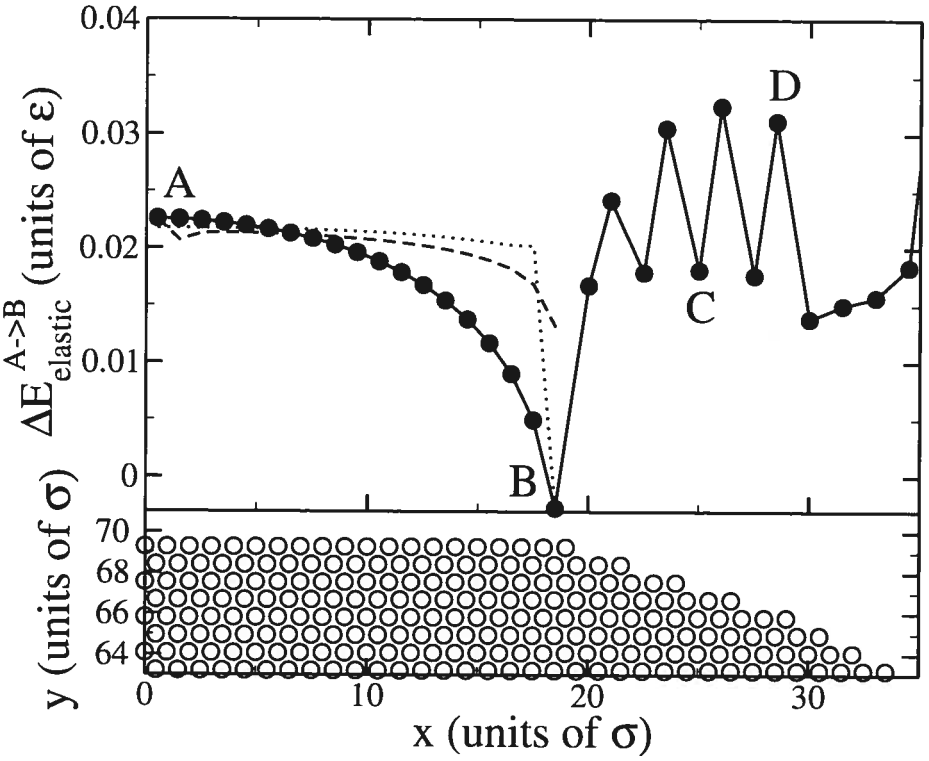

FIG. 6.15 – Same as Fig. 6.5 for the SI-HM case.

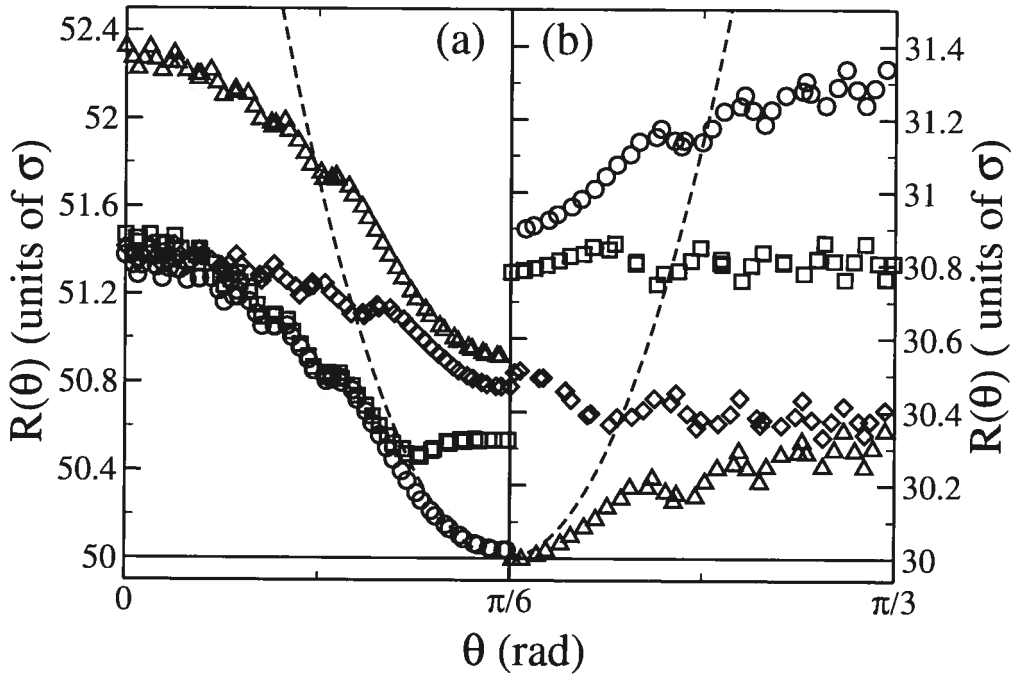

FIG. 6.16 – Same as Fig. 6.2 for the SI-HM case.

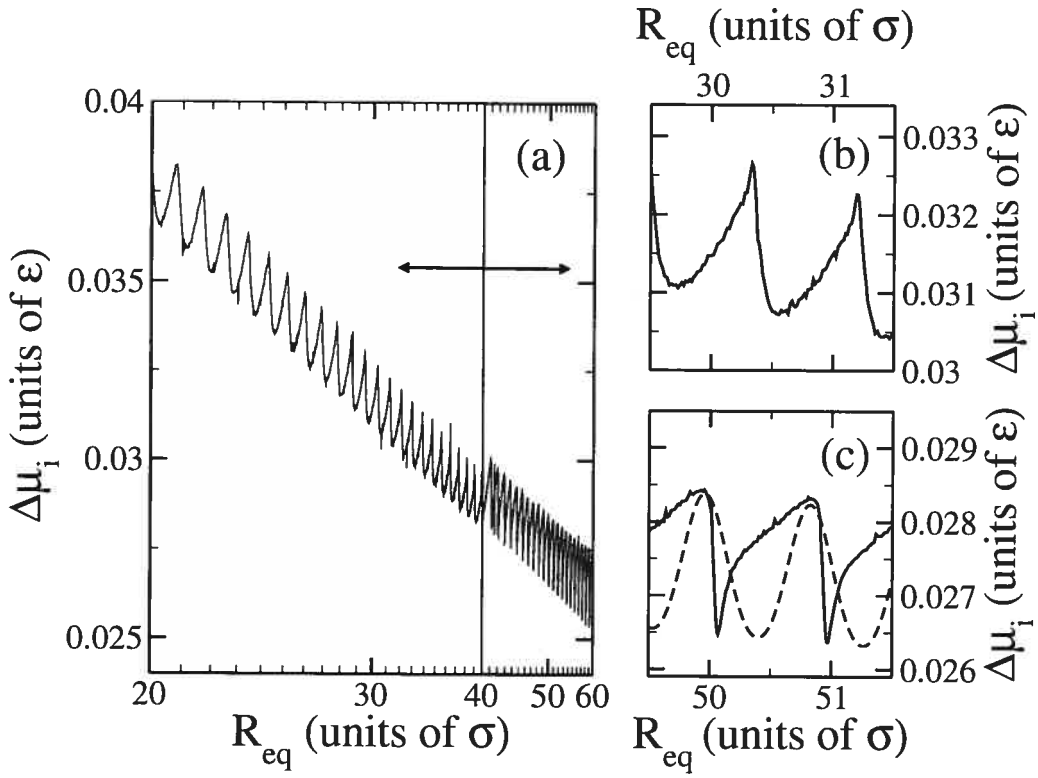

FIG. 6.17 – Same as Fig. 6.3 for the SI-HM case.

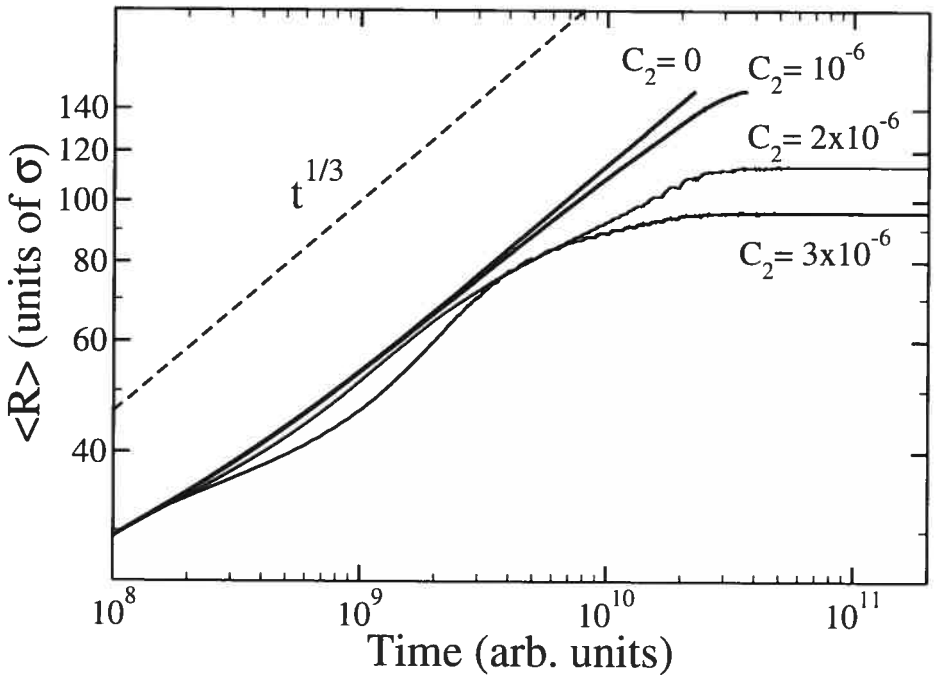

FIG. 6.18 – Average inclusion size for different values of the parameter C_2 as obtained using the modified LSW model (see text for details).

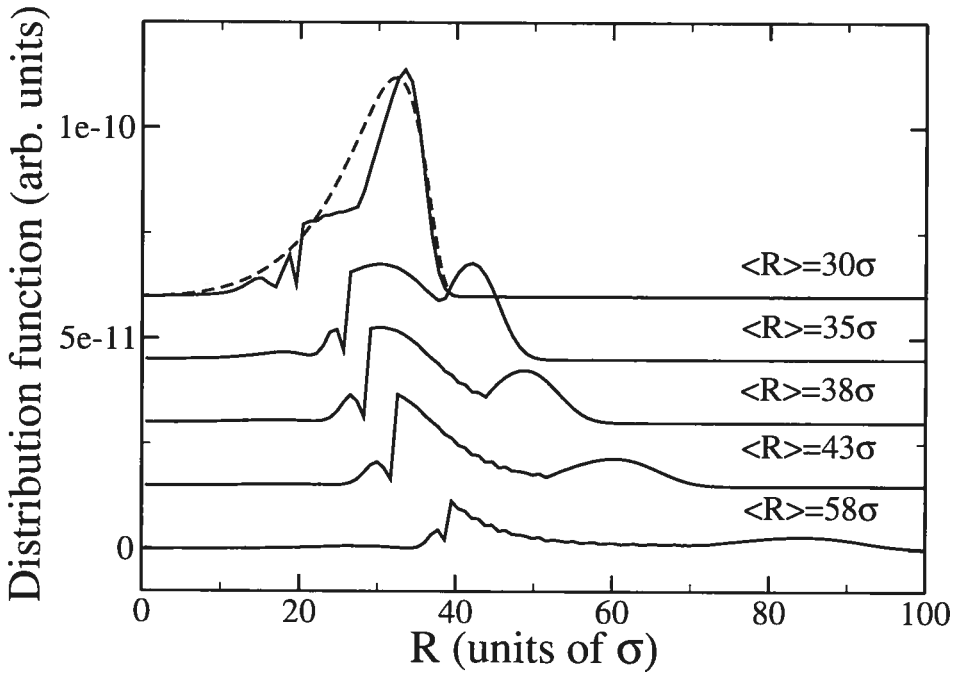

FIG. 6.19 – Size distribution function $f(t, R)$ at various average size (and thus time) for $C_1 = 0.00025\sigma^{-1}$ and $C_2 = 3\text{x}10^{-6}$. The dashed line is the LSW result ($C_2 = 0$) ; the different curves have been shifted for clarity.

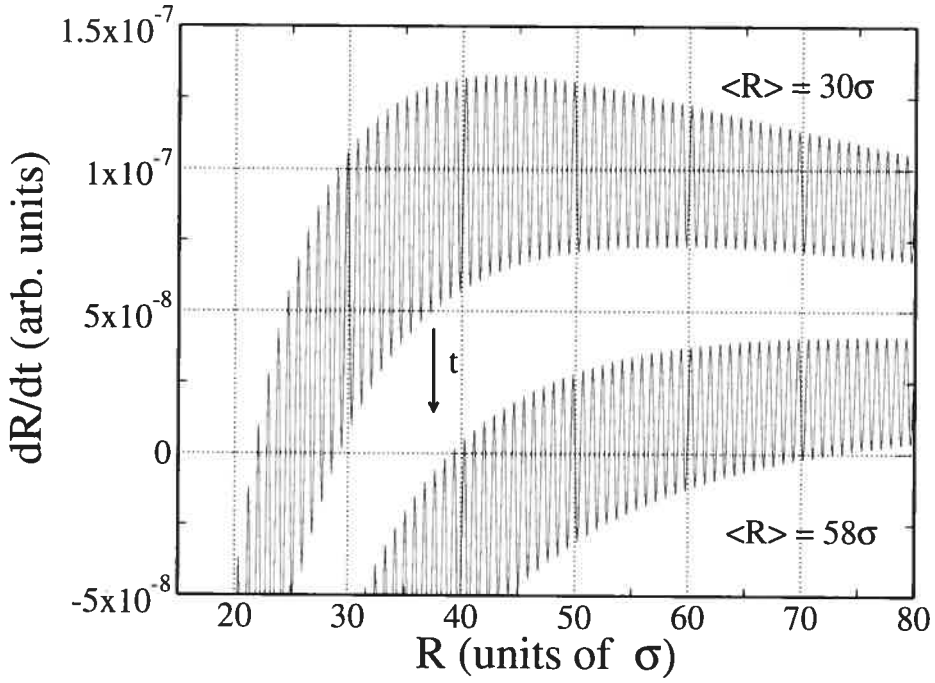

FIG. 6.20 – Growth rate dR/dt (Eq.6.17) at two values of the average size for $C_1 = 0.00025\sigma^{-1}$ and $C_2 = 3\text{x}10^{-6}$; the increase in the average size is a measure of time since the system is in a coarsening mode.

CHAPITRE 7

EFFET DES INTERACTIONS ÉLASTIQUES SUR LE MÛRISSEMENT DES SYSTÈMES MULTIPHASES ÉLASTIQUEMENT INHOMOGÈNES

Ce chapitre est composé du quatrième et dernier article composant le corps de cette thèse. Après avoir abondamment étudié l'effet de l'interaction élastique entre la matrice et les inclusions (cf. chapitres 4 à 6), nous nous attardons finalement au rôle des interactions élastiques entre inclusions. Cet aspect est important car la déformation de la matrice due à la présence d'une inclusion s'atténue très lentement (comme $1/r$). Une inclusion peut donc ressentir la présence d'une deuxième inclusion même si cette dernière est très distante. De plus, comme nous l'avons vu au chapitre 2, les expériences montrent que le mûrissement des alliages élastiquement inhomogènes est sensible à la fraction volumique d'inclusions. On se doit donc de considérer cet aspect pour obtenir un tableau complet du comportement de ces alliages. De plus, on a traditionnellement imputé aux interactions inter-inclusion la capacité de causer le *mûrissement inverse*, i.e., la croissance des petites inclusions au détriment des grosses. Ce processus pourrait hypothétiquement mener à la stabilisation de microstructures composées d'inclusions de tailles égales. Par contre, comme nous le verrons, la justification usuelle de ce phénomène ne repose pas sur une base théorique très solide. Ce chapitre sera donc aussi l'occasion de revisiter cette question quelque peu polémique.

Dans ce qui suit, nous démontrons que la réaction d'une inclusion à la présence d'une voisine est fortement dépendante de l'environnement. En effet, nous observons que la présence d'une seule autre inclusion n'affecte pratiquement en rien le mûrissement, même si la distance les séparant est très petite. Nous montrons que ceci est dû au fait que les inclusions possèdent la capacité de changer de forme pour limiter l'impact énergétique de l'interaction. Par contre, si le voisinage contient plusieurs autres inclusions, la relaxation par changement de forme n'est plus efficace. L'impact sur le potentiel chimique (et donc sur le mûrissement) augmente alors

de manière drastique, d'autant plus que la fraction volumique d'inclusions dans le voisinage est grande. Nous montrons que ces corrections au potentiel chimique peuvent être suffisamment importantes pour induire une transition entre un mûrissement normal (plus gros = plus stable) et un mûrissement anormal (plus petite fraction volumique = plus stable). Nous démontrons explicitement notre prédiction en donnant un exemple de mûrissement inverse dans un environnement confiné.

Dans la deuxième partie du chapitre, nous montrons que les effets d'interface discutés aux chapitres précédents restent importants même en présence d'interactions élastiques. À cet effet, nous présentons un exemple de stabilisation d'un système de deux inclusions de tailles inégales.

Finalement, nous proposons une généralisation du modèle LSW prenant en compte à la fois les effets interfaciaux et les effets des interactions. Nous montrons que ce modèle simple est en mesure de reproduire la vaste gamme des anomalies du mûrissement signalées au chapitre 2.

Ce chapitre est soumis pour publication dans la revue *Physical Review E*. En tant que premier auteur de cet article, ma contribution à consisté en :

1. La création du modèle utilisé pour effectuer les calculs numériques.
2. L'implémentation des programmes informatiques nécessaires aux calculs.
3. L'exécution des calculs requis.
4. L'analyse et l'interprétation des données.
5. La rédaction de la version initiale de l'article.
6. La réalisation des modifications suggérées par le co-auteur de l'article.

Effect of elastic interactions on coarsening in elastically inhomogeneous multiphase systems

Danny Perez and Laurent J. Lewis

Département de physique et Regroupement Québécois sur les Matériaux de Pointe (RQMP), Université de Montréal, C. P. 6128 Succursale Centre-Ville, Montréal (Québec) H3C 3J7, Canada

We investigate the effect of interactions between inclusions on the coarsening behaviour of elastically inhomogeneous multiphase systems using a recently introduced two-dimensional multiscale model based on the classical time-dependent density-functional theory. We show that spontaneous shape changes are very efficient in limiting the impact of the interactions on the chemical potential of inclusions. For this reason, the interactions between isolated pairs of inclusions are unable to significantly affect coarsening. At higher volume fraction, the efficiency of shape changes drops and major shifts of the chemical potential are observed; these are shown to be strong enough to counteract capillarity. For example, we show that sufficient confinement by neighboring inclusions causes inverse coarsening and we provide illustrations of this. We also examine the effect of interface elasticity in presence of interactions. We demonstrate that elasticity induces kinetic faceting and gives rise to oscillations in the chemical potential of the inclusions. This is shown to lead to the stabilization of microstructures composed of inclusions of various sizes. Finally, we propose a simple modified Lifshitz-Slyozov-Wagner model for assessing the effect of interactions on coarsening. The results are shown to be in excellent agreement with experiment.

7.1 Introduction

It is well known that the macroscopic properties of materials depend strongly on their chemical composition. It is perhaps less appreciated that their macro-scale behavior is also directly related to the microstructure. Indeed, nearly all properties of materials — optical [23, 82], electrical [93] and, of course, mechanical [51, 72] — are affected by micro- and even meso-scale morphological features. Control over the microstructure is thus essential to exploiting the full potential of materials. However, over sufficiently long periods of time, microstructural evolution may lead

to the degradation of the performance of materials, a phenomenon known as aging. Reliable models of microstructural evolution are thus required in order to fully optimize materials with respect to specific applications.

The canonical model for microstructural evolution ("coarsening") in multiphase systems is that of Lifshitz and Slyozov [47], and Wagner [99] (LSW). It describes the evolution of a collection of spherical domains interacting diffusively under the following assumptions : (i) the capillarity approximation is valid ; (ii) the dynamics is exclusively capillarity-driven ; and (iii) the density of inclusions is vanishingly small (dilute limit). Within the limits of these assumptions, it was shown that coarsening proceeds through the growth of large inclusions at the expense of small ones so that the average size of the inclusions $\langle R \rangle$ increases as $t^{1/3}$ (in the diffusion-limited regime). This behavior — also known as Ostwald ripening [64] or *normal* coarsening — has been observed in a wide range of phases, materials and geometries. It eventually leads to complete phase separation with only one domain remaining ; from a technological perspective, this is a rather unpleasant state of affairs.

Fortunately, it is known that microstructures do not always evolve according to the LSW theory. The possibility of controling microstructural evolution opens the door to a wealth of interesting applications ; stabilizing the microstructure is itself of great importance as it could help extend the lifetime of materials, perhaps considerably. In the present investigation, we are concerned with a particular class of materials exhibiting *abnormal* microstructural evolution, viz. elastically inhomogeneous multiphase alloys, where the microstructure is composed of inclusions (or precipitates) of a given material embedded within a matrix made out of a different material. A multiphase alloy is said to be elastically inhomogeneous if the elastic constants of the matrix and of the inclusions are different. Since such microstructure naturally forms from supersaturated solid solutions, multiphase alloys are commonplace in materials science.

The kinetics of microstructural evolution is known to be strongly affected by elastic effects. Slowdown relative to the LSW behavior, or even complete stabilization, has been reported in such materials as Ni-Cu-Si [65], Ti-Mo [41], Ni-Al-Ti [25], Ni-Al-Mo [8], etc. In some cases, slowing down is preceded by a normal coarsening

phase [25, 41, 65]. Variations of the coarsening exponent or of the asymptotic average inclusion size as a function of the volume fraction of inclusions have been frequently reported [54, 65]. Also, the morphology of the microstructures exhibits features that are not explained by the standard theory. For example, elasticity is known to induce shape transition in inclusions [8, 50] as well as spatial correlations in both shape and position [8, 25, 104]; further, the size distribution is strongly affected as both widening [8, 25, 77] and narrowing [54] have been reported. It is generally accepted that these deviations from the LSW behavior stem from the fact that the relaxation of the elastic energy (originating either from inclusion-matrix or inclusion-inclusion interactions) competes with the decrease of the interfacial energy, hence violating assumption (ii) of the model. While the nature of the root cause is identified, the mechanisms leading to such strong changes in kinetics are still subject to debate.

The objectives of the present work are threefold. First, we revisit the problem of interacting inclusions using a two-dimensional multiscale model we introduced recently [68]. We describe changes in the morphology of the inclusions arising from interactions, but we are mainly concerned with modifications to the thermodynamic force which drives coarsening, obtained by measuring the chemical potential shifts induced by elastic interactions in either binary systems or periodic arrays of inclusions. We show that, in two-inclusion systems, spontaneous shape changes are extremely efficient in attenuating the effects of interactions, leading to small chemical potential shifts even at very short range. If, however, the inclusions are organized in a periodic fashion, thus reducing the efficiency of shape changes, very large shifts — proportional to the volume fraction of inclusions— are measured. We demonstrate that these elastic corrections are sufficient to significantly alter the coarsening behavior. Second, following up on our previous work [66, 67], we study the effect of interface elasticity on the coarsening behavior of systems of *interacting* inclusions. We show that high interface elastic misfits increase the efficiency of kinetic faceting, hence modifying the behavior of inclusions during growth.The misfits also induce oscillations in the chemical potentials; these oscillation are able to stabilize systems of inclusions of different sizes, even in presence of elastic interactions. A stable system of two inclusions is presented to illustrate this point.

Third, and finally, using the results of the simulations, we formulate a simple model for the effect of elasticity on coarsening. The model is able to reproduce the essential characteristics of the experimental observations mentioned above. Based on these results, we propose that widening of the distribution of inclusions is related to strong interface misfits while narrowing is a consequence of inverse coarsening. We also show that inverse coarsening occurs in simple systems if the confining effect of the environment is taken into account.

7.2 Theoretical Background

From a theoretical point of view, the study of interactions in elastically inhomogeneous systems dates back to Eshelby [17], who first obtained an expression for the interaction energy between two spherical inclusions with radii R_1 and R_2, respectively, embedded in a matrix and separated by a distance D :

$$E_{\text{int}} = \frac{8\pi}{81}\left(\frac{1+\nu}{1-\nu}\right)^2 [q]^2[G] \left[\frac{R_1^6 R_2^3}{(D^2-R_2^2)^3} + \frac{R_2^6 R_1^3}{(D^2-R_1^2)^3}\right], \tag{7.1}$$

where ν is the Poisson ratio, $[q]$ is the lattice misfit between the two phases, and $[G]$ is the difference in shear moduli between the inclusions and the matrix. This equation is valid to first order in $[G]$, and thus for small inhomogeneities. Eshelby's formula has frequently been employed to discuss the effect of interactions on both the morphology and the kinetics of inhomogeneous systems. For example, concerning the morphology, the interactions are predicted to be repulsive or attractive for hard or soft inclusions, respectively, and should thus lead to positional correlations between inclusions [85, 97], in agreement with experimental observations. The formula also suggests that coarsening kinetics would be strongly affected by elasticity. For example, for a fixed total inclusion volume, E_{int} is minimal for $R_1 = R_2$ if the inclusions are soft ($[G] < 0$). The interaction energy is thus expected to counteract the normal capillarity-driven tendency for the larger inclusion to grow at the expense of the smaller one, giving rise to *inverse coarsening* where the small inclusion

grows until it reaches the size of the large one [31]. In contrast, for hard inclusions, the interaction energy is minimum when the size of the small inclusion vanishes. In this case, elastic interactions promote coarsening. In fact, it was shown by Enomoto and Kawasaki [15] — also assuming spherical inclusions — that for soft inclusions, the average inclusion size initially increases as $t^{1/3}$, but later completely stops because of inverse coarsening; for hard inclusions, the normal regime is followed by an acceleration of coarsening with $\langle R \rangle \propto t^{1/2}$. These authors have also predicted a narrowing (widening) of the size distribution function for soft (hard) inclusions because of the decreased (increased) growth rate of large inclusions relative to the homogeneous case.

While of appealing simplicity, a description of coarsening based on Eshelby's formula is unable to account for the wide variety of behaviors observed. For example, slowing down has been reported in systems of hard inclusions as well [65]. Also, widening of the distribution function can occur concomitantly with slowing down [8, 25]. Such disagreements between theory and experiment may stem from two causes. First, energetics alone is not sufficient to determine the dynamics of systems driven by diffusion since the existence of an energy minimum does not ensure that it can be reached dynamically. Second, the validity of Eshelby's formula (Eq. 7.1) is not always guaranteed : strictly speaking, it is only correct for spherical inclusions while it is known that elastic interactions strongly affect the shape of inclusions. In fact, it was demonstrated by Onuki and Nishimori [62] that two interacting circular inclusions adjust their shapes such as to cancel the anisotropic components of the strain field. This process was shown to be very efficient in reducing the interaction energy; the effect of interactions on coarsening is thus probably much lower than could have been expected from Eshelby's formula. The robustness of inverse coarsening as a possible pathway to stabilization is hence also questioned.

The relevance of this observation was confirmed in subsequent simulations where constraints on the shape of the inclusions were lifted. For homogeneous but anisotropic elasticity, simulations of microstructures composed of a few inclusions showed that, while *transient* inverse coarsening is common, it does not persist long enough to lead to complete stabilization of the structure [84]. For elastically inhomoge-

neous systems, however, a two-inclusion configuration can minimize the energy [81], suggesting that stabilization through inverse coarsening can indeed occur. However, under diffusive dynamics, complete stabilization was not observed except for highly-symmetric initial conditions [80].

In spite of these observations, the stabilization of complex microstructures was reported by Onuki and Nishimori [60]. Their simulations showed an initial, normal coarsening stage, followed by a transition to a frozen state, suggesting that stabilization does not necessarily involve inverse coarsening and that it might in fact be a very robust process occurring even in complex geometries. Concerns on the validity of these results were however raised by Chen and collaborators who, using an improved formalism for the calculation of the elastic energy [30], did not observe stabilization but, instead, a gradual (and rather slow) decrease of the coarsening exponent, from $1/3$ in homogeneous systems to about $1/4$ for a threefold difference in shear moduli between the two phases [107]. Other large-scale simulations also showed important reductions of the coarsening rate, but the effect on the coarsening exponents could not be inferred precisely [63].

The origin of the transition from normal coarsening to a stable (or slowly evolving) state observed in experiment [8, 25, 41, 54, 65] is thus still subject to debate. Further, the role of inverse coarsening in the anomalous behavior of elastically inhomogeneous systems remains unclear since it is seldom observed in simulations. However, as mentioned earlier, some alloys show a narrowing of the size distribution in the slow regime, strongly suggesting that inverse coarsening does occur in certain conditions. Finally, it remains to be understood why slowing down of coarsening is sometimes associated with narrowing a of the size distribution function, and sometimes with widening.

7.3 Model and computational details

As mentioned earlier, we are interested in both bulk and interface elastic contributions. A proper treatment of these requires an atomic-scale description of the interphase boundaries. In the present investigation, this is achieved using a multiscale model we recently proposed [68], which is based on the time-dependent density-

functional-theory (TDDFT) for classical lattice systems developed by Reinel, Fisher and collaborators [19, 37, 74]. The TDDFT provides a system of master equations for the evolution of the occupation probabilities of each site on the lattice. In our particular implementation, the TDDFT equations are solved using a multi-scale framework where the resolution of the calculation varies from fully-resolved at the atomic-scale near interphase boundaries, to coarse-grained within the bulk phases. This enables us to treat large systems at a reasonnable computational cost. Further, our implementation also includes the effect of elasticity using the quasicontinuum method of Tadmor and collaborators [53, 87]. A complete description of the model can be found in Ref. [68], and an outline is given in Ref. [67].

In this work, we consider a two-dimensional binary alloy with vacancies (ABv) and use the TDDFT to model the evolution in time of inclusions composed of a B-rich phase embedded within an A-rich matrix. The atoms are assumed to interact with their first-neighbors through a harmonic potential of the form :

$$V_{i,j}^{\alpha,\beta} = k^{\alpha,\beta}(r_{i,j} - \sigma^{\alpha,\beta})^2 - \epsilon^{\alpha,\beta}, \tag{7.2}$$

where $r_{i,j} = |\vec{r}_i - \vec{r}_j|$; i, j refer to lattice sites and α, β to atomic species. The underlying lattice is triangular. All results will be expressed in dimensionless, reduced units relative to a stress-free pure A phase : lattice parameter for length (σ), interaction energy between nearest-neighbors for energy (ϵ), and inverse trial frequency (τ_0) for time. In all cases, the temperature is $T = 0.5\epsilon/k_B$ (about half of the critical temperature for phase separation) and the vacancy concentration is 10^{-3}.

The lattice mismatch between the two phases is fixed to 3%. Four different combinations of elastic stiffnesses and lattice parameters are considered, as listed in Table 7.1, namely : hard inclusions with low interface misfit (HI-LM), hard inclusions with high interface misfit (HI-HM), soft inclusions with low interface misfit (SI-LM), and soft inclusions with high interface misfit (SI-HM). An inclusion is hard (soft) if $k_{BB} > (<)\ k_{AA}$. The interface misfit qualifies the difference between σ_{AB} and the typical lattice constant near the interfaces. Since a hard inclusion tends to impose its lattice constant to nearby matrix material, a low misfit corresponds to

Type	k_{AA}	k_{AB}	k_{BB}	σ_{AA}	σ_{AB}	σ_{BB}
HI-LM	50	50	150	1.00	1.03	1.03
HI-HM	50	50	150	1.00	1.00	1.03
SI-LM	50	50	10	1.00	1.00	1.03
SI-HM	50	50	10	1.00	1.03	1.03

TAB. 7.1 – Values of the stiffnesses k_{XY} and lattice constants σ_{XY} for the various types of inclusions considered in the present work. Stiffnesses are in units of ϵ/σ^2 and lattice constants in units of σ.

$\sigma_{AB} = \sigma_{BB}$ while a high misfit corresponds to $\sigma_{AB} = \sigma_{AA}$. For soft inclusions, the opposite is true. Other parameters of the potential are $\epsilon_{AA} = \epsilon_{BB} = \epsilon$, $\epsilon_{AB} = 0.7\epsilon$.

The present study is based on two main types of simulations. First, we consider systems of two initially-circular inclusions of radii $R = 60\sigma$ and $R = 30\sigma$, respectively. In this case, calculations are carried out within an hexagonal cell of side 1536σ with closed boundary conditions (no flux in or out of the cell) for the TDDFT (diffusion) equations, and zero-displacement boundary conditions for the elastic equilibrium equations. Such a large cell size is required to eliminate finite-size effects. Second, we consider periodic arrays of inclusions. The simulation cell in this case is a parallelogram with a single inclusion placed at its center. Interactions between inclusions are introduced through periodic boundary conditions on the elastic equilibrium equation. When needed, growth is activated by imposing a constant chemical potential along the edge of an hexagon centered on the inclusion. Using this technique, *all* inclusions of the periodic array grow simultaneously.

7.4 Results

In order to isolate the effects of bulk elasticity from those related to interfaces, we examine first the case of hard inclusions with low misfit (HI-LM), then move on to study soft inclusions with low misfit (SI-LM); the peculiar behavior arising from large interface misfits will be discussed in section 7.4.3.

7.4.1 Interaction between hard inclusions

7.4.1.1 Two-inclusion systems

We consider first a system of two inclusions placed at the center of a very large cell. An example of the evolution of such a system is presented in Fig. 7.1. As soon as time starts running, the "inner" surfaces (between the two inclusions) strongly repel each other, leading to an elongation in the direction perpendicular to the axis joining the two inclusions. Such conformational changes have been predicted by Johnson *et al.* [34] and subsequently observed in numerous simulations [35, 61]. They can in fact be expected on the basis of Eshelby's formula since the interaction energy between two HI is repulsive. As mentioned earlier, it was shown by Onuki and Nishimori [62] that shape changes occur so as to cancel the anisotropic components of the strain field within the inclusions. Note however that the inclusions as a whole do not move away from each other (the outer edges do not move during the simulation, cf. Fig. 7.1), as observed when a circular shape is imposed [3, 97]. We will return to this point below.

Morphological modifications can be quantified using a normal-mode analysis where the angular dependence of the radii of the inclusions is decomposed into a sum of cosines, viz. $R(\theta) = R_0 + \sum_l \delta_l \cos(l\theta + \phi_l)$. In the present case, the leading contribution comes from mode $l = 2$ since this corresponds to a uniaxial elongation. Fig. 7.2 clearly shows the rapid development of the elongated shape, particularly so for the small inclusion ($R \leq 30$) where the modulation reaches about 25% of the initial radius (R_0) at small inter-inclusion distance D, compared to roughly 5% for the large inclusion ($R \geq 60$).

These shape changes do not occur following the condensation or evaporation of solute atoms, as the sizes of the inclusions are approximately constant until maximum deformation is reached (cf. Fig. 7.2). At this point, however, solute atoms start to diffuse from the small inclusion toward the large one, i.e., coarsening begins ; we note that inverse coarsening was never observed in such configurations, even for smaller differences in the size of the two inclusions. Growth and evaporation are strongly anisotropic : the exchange of mass occurs almost exclusively at the inner surfaces, leaving the outer ones practically unaffected. As coarsening proceeds, the

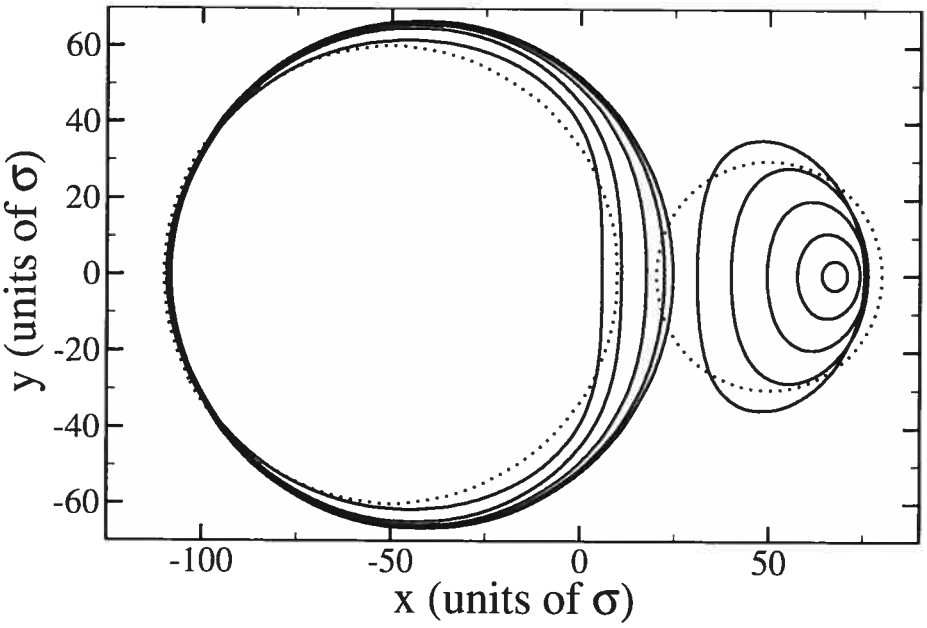

FIG. 7.1 – Evolution in time of two HI-LM initially separated by $D = 100\sigma$ during coarsening. The dotted line represents the initial configuration.

inclusions become increasingly circular ($\delta_2 \to 0$) — the large one because the strain field of the small one gradually gets weaker compared to its own, and the small one because of the increasing importance of capillarity (which favors a circular shape) as size decreases. The anisotropic character of the flow of solute atoms also favors the gradual return of the large inclusion to its equilibrium shape.

While the amplitude of the shape changes gives an indication of the strength of elastic interactions, it cannot be used directly to predict the effect on coarsening. Indeed, large variations in the shape imply extensive *relaxation* in response to an initially strong interaction, but the interactions are not necessarily strong once relaxation is completed. To obtain information about coarsening, one must measure changes in the thermodynamic force which drives diffusion, given here by the difference in chemical potentials $\Delta\mu_i^1 - \Delta\mu_i^2$, with $\Delta\mu_i^k = \mu_B - \mu_A$ within inclusion k. The evolution of $\Delta\mu_i$ for each of the two inclusions is presented in Fig. 7.3 for two different separations D; for reference, $\Delta\mu_i$ for an isolated inclusion (continuous

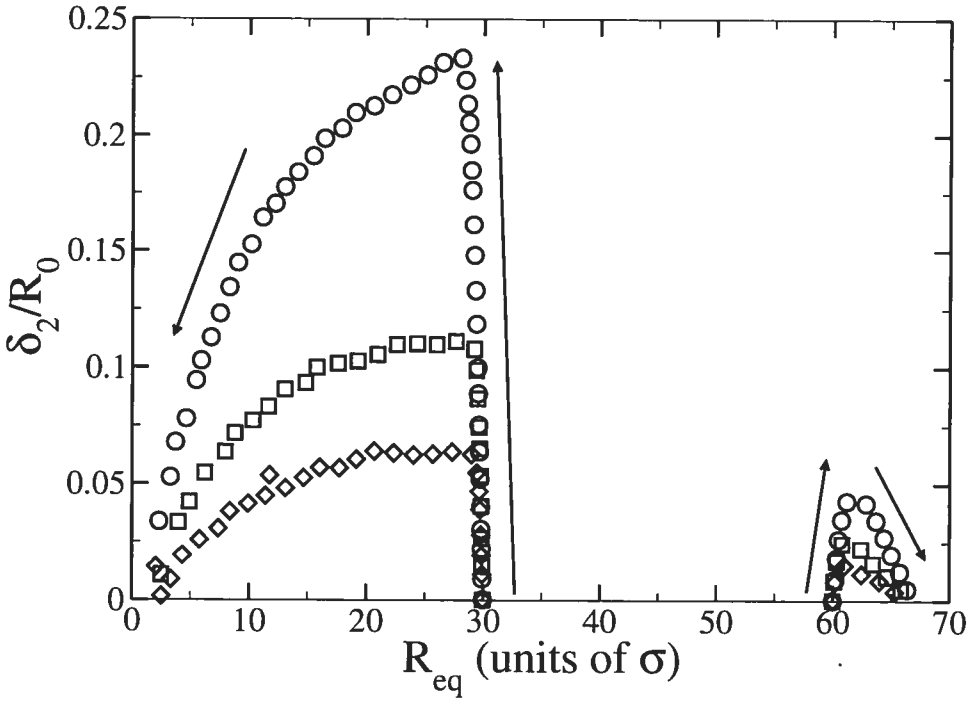

FIG. 7.2 – Relative amplitude of mode 2 for different distances D between two HI-LM with initial radii of 30 and 60σ, respectively : circles : $D = 100\sigma$ (cf. Fig. 7.1) ; squares : $D = 150\sigma$; diamonds : $D = 200\sigma$. Arrows indicate the flow of time.

line ; fit to the data of Ref. [67]) is also plotted. As expected, when the distance between the inclusions is large (e.g., $D = 300\sigma$), the interactions do not significantly affect $\Delta\mu_i$ and the two inclusions behave as if they were isolated ; in this case, elasticity evidently does not affect the coarsening behavior of the system in any significant manner. However, as the distance decreases, the repulsive character of the interactions manifests itself, essentially through an upward shift of $\Delta\mu_i$; note that the shift mostly concerns the small inclusion ($R \leq 30$), leaving the large one ($R \geq 60$) almost unaffected. This anisotropy results in an increased driving force for coarsening ($\Delta\mu_i^1 - \Delta\mu_i^2$ increases), hence accelerated coarsening compared to the elastically homogeneous case. The magnitude of the shift is however relatively small compared to the variations due to size changes, even at very small D. Further, as shown in the inset to Fig. 7.3, the shift (as obtained by fitting the different $\Delta\mu_i$ curves to a smooth function of $1/R_{\text{eq}}$) decreases rapidly with increasing distance ($\sim D^{-2.22}$). This points to the high efficiency of shape changes in lowering

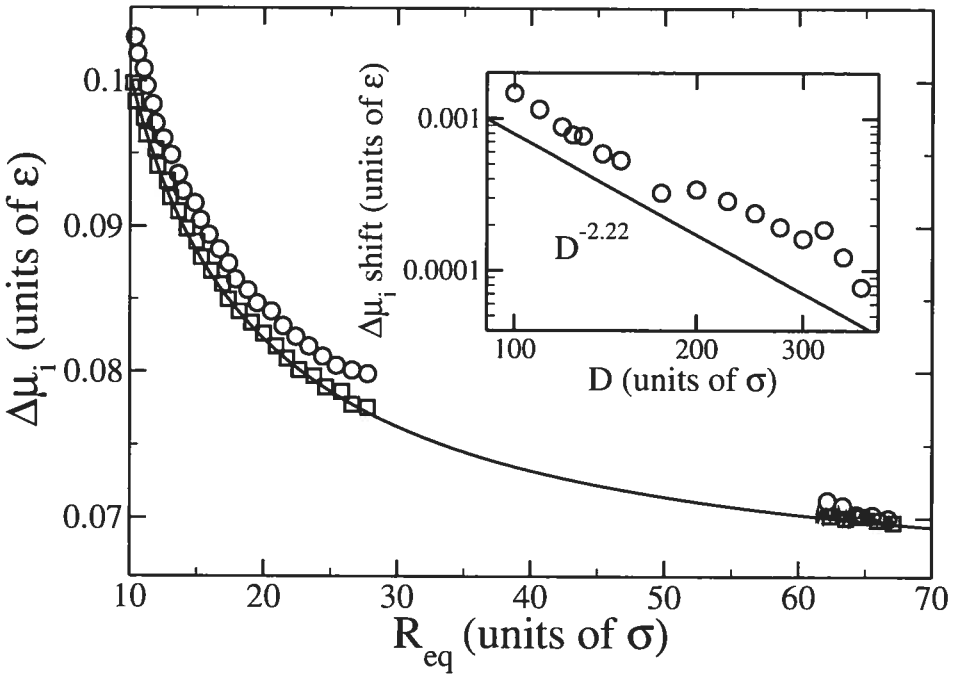

FIG. 7.3 – Chemical potential difference $\Delta\mu_i$ between species B and species A as a function of size for two HI-LM with initial radii of 30 and 60σ, respectively : circles : $D = 100\sigma$; squares : $D = 300\sigma$; continuous line : $\Delta\mu_i$ for an isolated inclusion. Inset : shift in $\Delta\mu_i$ in the small inclusion as a function of D.

the interaction energy, and therefore minimizing the effect on coarsening.

7.4.1.2 Periodic arrays of inclusions

If shape changes are efficient in limiting the impact of pair interactions on coarsening, the behavior of microstructures containing a large density (volume fraction) of inclusions cannot be inferred from the study of simple configurations composed of only a few inclusions. In denser arrangements, the efficiency of the relaxation process is likely to decrease sharply because of the more stringent constraints imposed by many-body effects. Since a direct simulation of large multi-inclusion systems would be computationally prohibitive within the present TDDFT framework, we instead use periodic arrays of inclusions as model systems.

In a first series of simulations, we imposed conditions of growth in order to study the effect of increasing volume fraction. The evolution of the morphology

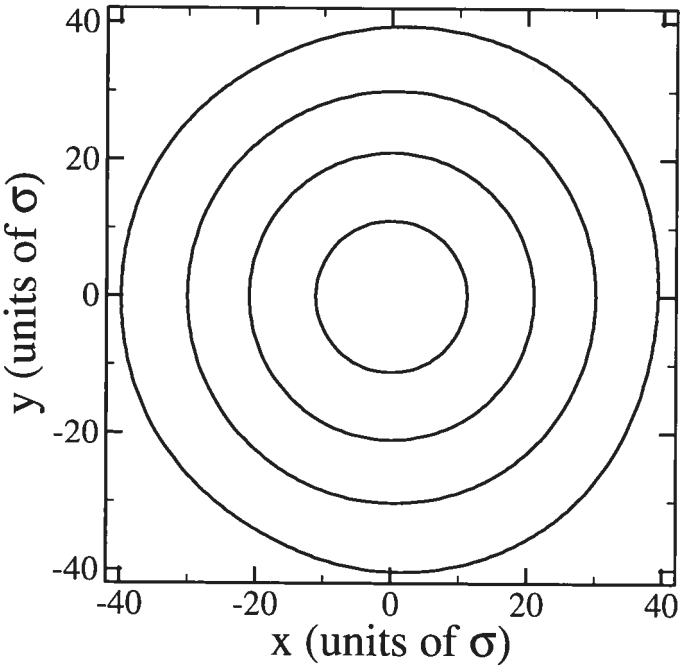

FIG. 7.4 – Growth of a HI-LM belonging to an array of period 160σ.

of an inclusion so obtained is shown in Fig. 7.4; here, the period of the array is 160σ. The inclusion is found to remain essentially circular during growth, except near the end of the process where deformations develop, which are however quite small in comparison to those observed in the two-inclusion system (cf. Fig. 7.1). Constraints forced upon the inclusion by the complex environment therefore prove to be very strong, as expected.

While the impact of inclusion-inclusion interactions on morphology is relatively minor, the opposite is true for the chemical potential. The effect is in fact so strong that, as shown in Fig. 7.5, $\Delta\mu_i$ is completely dominated by elasticity by the time the volume fraction reaches about 5% (which occurs near $R_{\text{eq}} = 15\sigma$ in the present geometry). Indeed, at this point, $\Delta\mu_i$ starts to *increase* with R_{eq}, while capillarity prescribes a $1/R_{\text{eq}}$ decay [continuous line in Fig. 7.5(a)]. Upon varying the separation D, we find that $\Delta\mu_i$ can be decomposed into the usual capillarity term plus a shift due to elastic interactions whose magnitude is controlled by the volume fraction; the latter is plotted in Fig. 7.5(b). The shift is initially a (roughly)

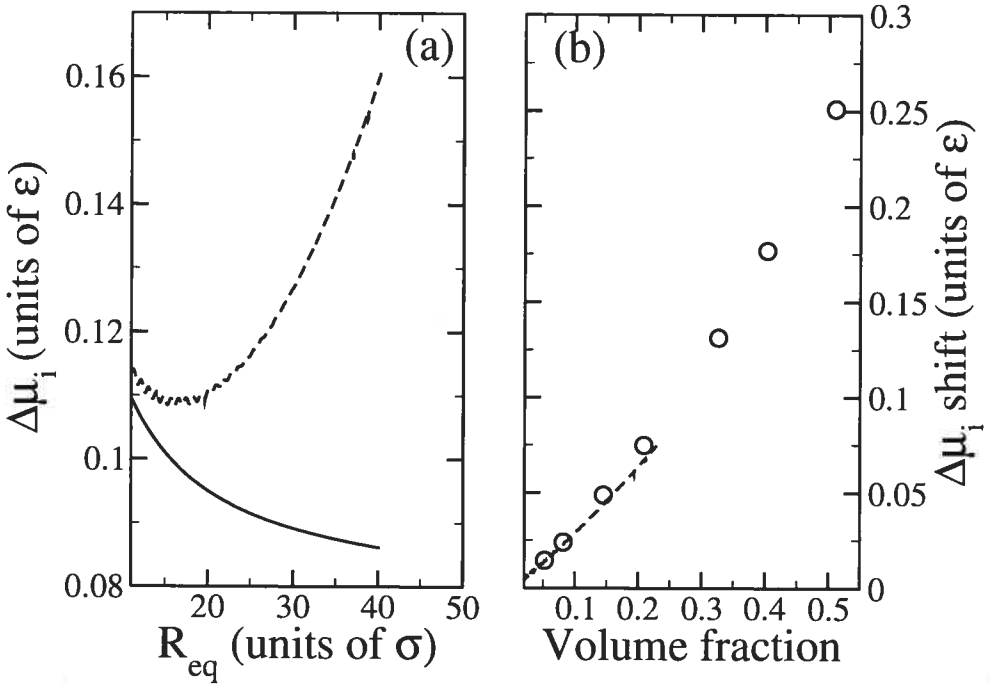

FIG. 7.5 – Chemical potential difference $\Delta\mu_i$ (dashed lines) between species B and species A for an array of HI-LM of period 160σ. (a) $\Delta\mu_i$ as a function of size; the continuous line is for an isolated HI-LM and shows the normal capillarity-driven shift. (b) Shift in $\Delta\mu_i$ as a function of the volume fraction of the inclusions; the circles show the results for a periodic array of HI-LM following static relaxation; see text for details.

linear function of the volume fraction. Note that a linear variation with volume fraction is equivalent to a D^{-2} dependence with respect to inter-inclusion distance, not too far from the $D^{-2.22}$ variation observed for pair interactions. However, as can be appreciated by comparing Figs. 7.5(b) and 7.3(inset), typical shifts here are one or two orders of magnitude larger than in the two-inclusion system.

For high volume fractions, the above method cannot be used because the presence of a source of solute atoms close to the inclusion could lead to artificial effects. In this regime, we use instead a sequence of relaxations with periodic boundary conditions on the TDDFT equations, keeping the inclusion size fixed at $R = 30\sigma$ and varying the size of the simulation cell. The results are presented as circles in Fig. 7.3(b). At low volume fraction, the measured shifts agree well with those obtained in the growth simulations, indicating that the elastic contribution indeed de-

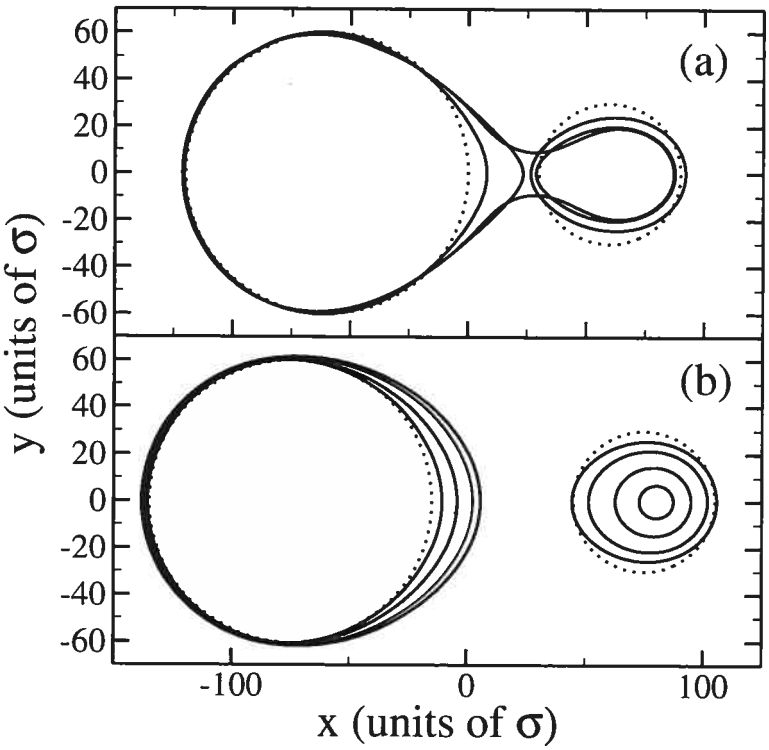

FIG. 7.6 – Evolution in time of two SI-LM during coarsening : for inter-inclusion distance (a) $D = 120\sigma$ and (b) : $D = 150\sigma$.

couples from the capillarity contribution. At higher volume fraction, non-linearities appear, further increasing the elastic shift. Note that for a volume fraction of 0.5, the shift amounts to $\sim 300\%$ of the value of $\Delta\mu_i$ for an isolated inclusion.

7.4.2 Interaction between soft inclusions

7.4.2.1 Two-inclusion systems

From Eshelby's formula, Eq. 7.1, we expect soft inclusions to exhibit a very different behavior than hard inclusions since the interaction is now attractive. Further, as shown by Johnson [34], the local growth rate should be larger along the alignment axis than across, leading to the elongation of the inclusions along this axis. This is observed in our TDDFT simulations, as shown in Fig. 7.6. The inclusions gradually adopt an egg-like shape, pointing towards one another, typical of interacting soft inclusions [35]. Our calculations reveal that shape changes occur rapidly for the small inclusion, but more slowly for the large one; also, as shown

in Fig. 7.7, deformations occur at nearly-constant size for the small inclusion, but develop concomitantly with growth for the large inclusion.

As coarsening proceeds, there are two possible outcomes : either the inclusions merge [cf. Fig. 7.6(a)] or the large inclusion grows at the expense of the small one [cf. Fig. 7.6(b)]. In the first situation, coalescence follows from the formation of a sharp tip on the inner surface of the large inclusion, which rapidly grows toward the small inclusion until the two merge. Soft inclusion are well known for their tendency to coalesce with their neighbors [44] and, as a result, the softer phase often assumes the role of the matrix, even at very low volume fraction [107]. This process is particularly efficient because a local elastic energy minimum (and hence a local chemical potential minimum) forms at sharp interface features such as tips [68]. Note that merging does not result from the displacement of the inclusions but, rather, from shape changes and directional growth. In the second situation, coarsening occurs diffusively : the small inclusion gradually evaporates and solute atoms diffuse toward the large one. In this process, the small inclusion returns to a circular shape while the large one becomes increasingly elliptic because of the anisotropic solute supply (cf. Fig. 7.7) ; the elongation is very large compared to the HI case. Only when the small inclusion has completely evaporated does relaxation toward a circular shape begins.

The lack of a significant spontaneous reorganization of the large inclusion in the present (soft) case, as compared to the hard case, can be explained by the relatively small amplitude of the elastic perturbations caused by the small inclusion (which has $k_{BB} = 10\epsilon/\sigma^2$ vs $150\epsilon/\sigma^2$ for hard inclusions), while the capillary forces (which favor a circular shape) are roughly equal. The relatively small driving force pulling the large inclusion back to equilibrium can also be attributed to elasticity. Indeed, it is known that the elastic energy of an isolated soft inclusion is minimized for an ellipse instead of a circle, whereas the circle is preferred for a hard inclusion [16]. Thus, while both capillarity and elasticity favor the circle for hard inclusions, they compete in the case of soft inclusions, leading to a slower relaxation process. The formation of such long-lived, out-of-equilibrium shapes in growth conditions has been observed in our previous TDDFT calculation [68].

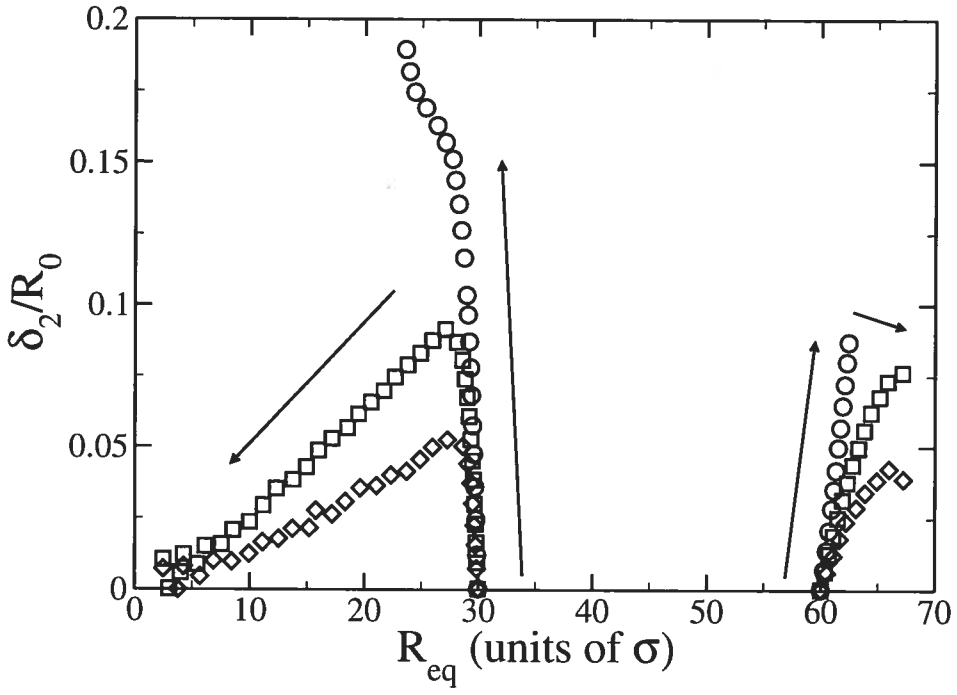

FIG. 7.7 – Relative amplitude of mode 2 for different distances D between two SI-LM with initial radii of 30 and 60σ, respectively : circles : $D = 120\sigma$ [cf. Fig. 7.6(a)] ; squares : $D = 150\sigma$ [cf. Fig. 7.6(b)] ; diamonds : $D = 200\sigma$. Arrows indicate the flow of time.

Even if the deformations of the two inclusions are now of comparable magnitude, the variations of the chemical potentials $\Delta\mu_i$ are still largely restricted to the small inclusion, as shown in Fig. 7.8. These results indicate that elastic corrections are very small for the large inclusion, even at small D. For the small inclusion, however, $\Delta\mu_i$ shifts slightly downward relative to the isolated inclusion (continuous line), in qualitative agreement with Eshelby's formula. As shown in the inset to Fig. 7.8, the magnitude of this shift decreases extremely rapidly with increasing distance, roughly as $D^{-4.65}$. It must be concluded that elastic interactions have a stabilizing effect only at very short separations, since the driving force for coarsening decreases with increasing interaction. Also, the shifts in $\Delta\mu_i$ are not primarily caused by changes in the shape of the inclusion but, rather, by the strain which is present within the inclusions.

For the parameters used here, inverse coarsening — which requires $\Delta\mu_i$ to be

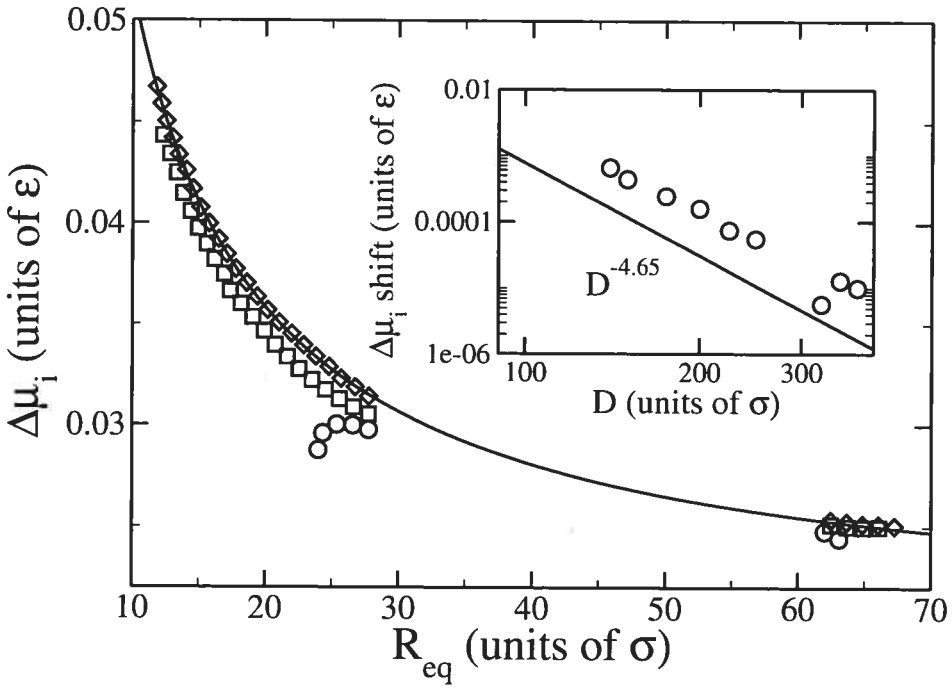

FIG. 7.8 – Chemical potential difference $\Delta\mu_i$ between species B and species A as a function of size for two SI-LM with initial radii of 30 and 60σ, respectively : circles : $D = 120\sigma$; squares : $D = 150\sigma$; diamonds : $D = 300\sigma$; continuous line : $\Delta\mu_i$ for an isolated inclusion. Inset : shift in $\Delta\mu_i$ in the small inclusion as a function of D.

lower in the small inclusion than in the large one — is unlikely, as a very small size difference is required for the elastically-induced shift to counterbalance the capillarity $1/R_{\text{eq}}$ term. But since the chemical potential shifts in the two inclusions have to be equal at equal sizes (by symmetry), the shift of the small inclusion decreases as its size increases relative to the large one. One can also obtain a sharp drop of $\Delta\mu_i$ in the smallest inclusion by decreasing D (cf. circles in Fig. 7.8) ; this route however leads to coalescence, as we have seen above.

7.4.2.2 Periodic arrays of inclusions

We now turn to periodic systems of soft inclusions, first investigating the dependence on volume fraction ; to this effect, we impose growth on an array of inclusions with lattice constant fixed to 160σ. Here again, as shown in Fig. 7.9, the effect of interactions on the shape of the inclusions is very modest — compare to the two-

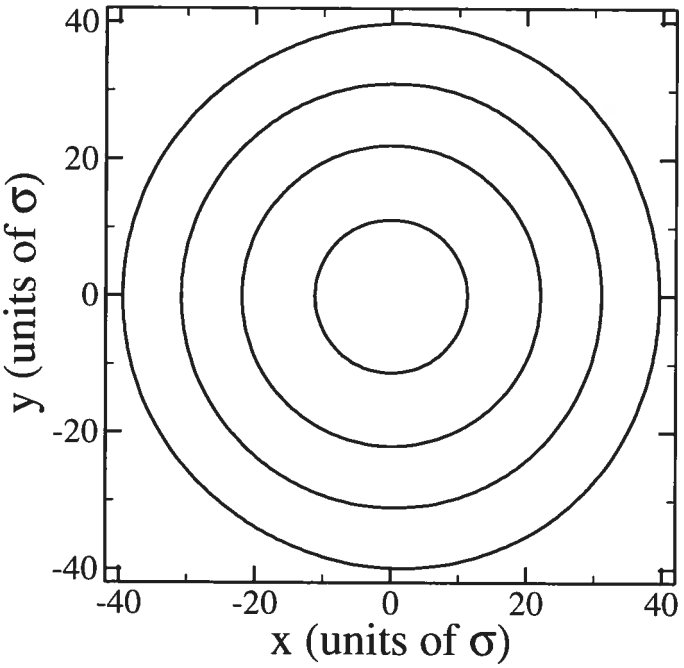

FIG. 7.9 – Growth of a SI-LM belonging to an array of period 160σ.

inclusion system, Fig. 7.6. As in the case of hard inclusions, the presence of many neighboring inclusions efficiently impedes relaxation through shape changes.

Because of the limited efficiency of relaxation, the effect of interactions on the coarsening behavior increases considerably. Surprisingly, the sign of the chemical potential shift is also affected : as shown in Fig. 7.10, interactions now cause an *increase* of $\Delta\mu_i$ compared to isolated inclusions, even at small sizes (low volume fraction), while it was found to *decrease* in the two-inclusion system (cf. Fig. 7.8). Because of the lower elastic energies involved, the shifts in $\Delta\mu_i$ are however much more modest than for hard inclusions, reaching about 10% for a volume fraction of 0.35 [cf. Fig. 7.10(b)]. Further, the results at high volume fraction (obtained as discussed in Section 7.4.1.2) indicate that the rate of increase of the shift decreases at higher volume fraction. Note however that the impact of interactions is still at least one order of magnitude larger in periodic systems than in two-inclusion systems. In the present case, these modest corrections are sufficient to counterbalance the $1/R_{\rm eq}$ capillarity term for $R_{\rm eq} > 50\sigma$ (the dashed line in Fig. 7.10(a) stops to

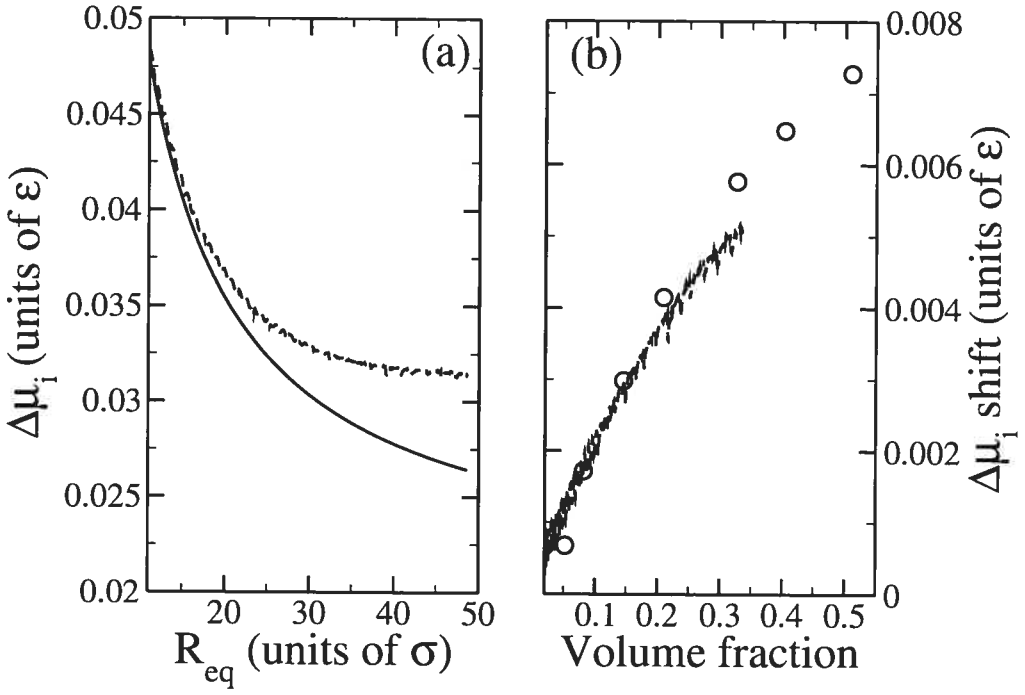

FIG. 7.10 – Chemical potential difference $\Delta\mu_i$ (dashed lines) between species B and species A for an array of SI-LM of period 160σ. (a) $\Delta\mu_i$ as a function of size; the continuous line is for an isolated HI-LM. (b) Shift in $\Delta\mu_i$ as a function of the volume fraction of the inclusions; the circles show the results for a periodic array of SI-LM following static relaxation; see text for details.

decrease with increasing R_{eq}). Finally, as is the case for hard inclusions, the shift in $\Delta\mu_i$ initially increases roughly linearly with volume fraction, indicating a D^{-2} dependence on inter-inclusion separation. This is much faster than the -4.65 exponent for the two-inclusion system, further demonstrating the efficiency of shape relaxation in limiting the effect of interactions on coarsening.

7.4.3 The role of interface misfit

Having discussed the impact of bulk elasticity, we now turn to the specific role of interface misfits in systems of inclusions. This follows-up on recent work where we demonstrated the importance of these misfits on the evolution of isolated inclusions in elastically inhomogeneous systems [66, 67].

We examine first the impact of elastically-induced kinetic faceting on coarse-

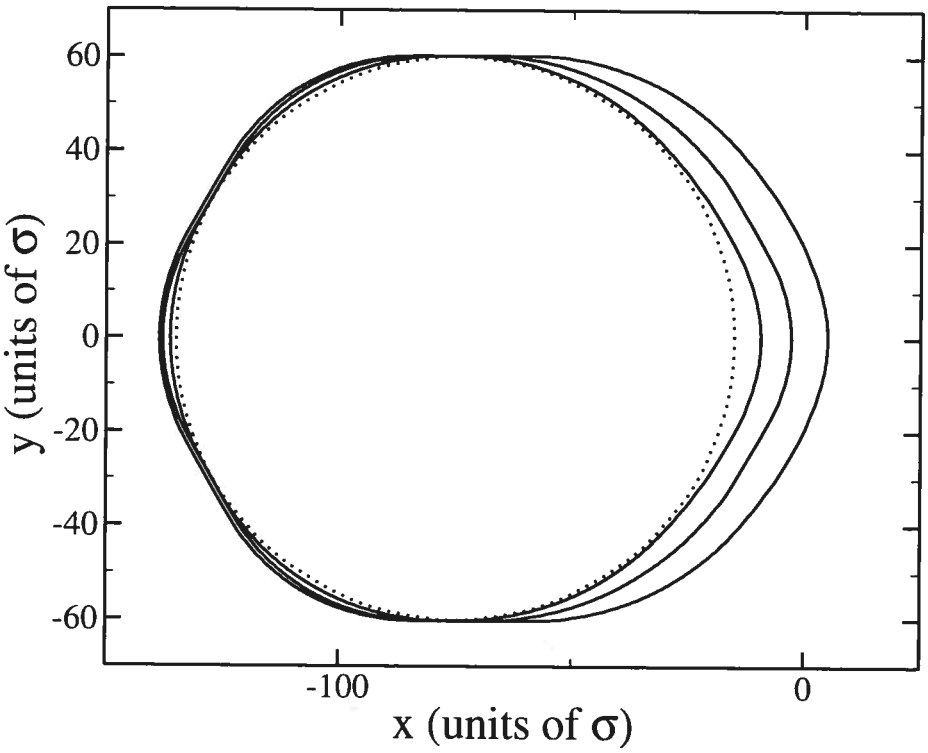

FIG. 7.11 – Evolution in time of a large SI-HM initially separated by $D = 150\sigma$ from a small inclusion (located on the right; not shown) during coarsening. The dotted line represents the initial configuration.

ning. From a mesoscopic point of view, kinetic faceting results from the difference in growth speeds between different interfacial orientations [102]. During growth, the contribution of slow orientations (usually low-energy facets) to the shape of the inclusion increases, as fast orientations rapidly "grow out" of existence [94]. From a microscopic perspective, kinetic faceting occurs when the growth of pre-existing terraces outpaces the nucleation of new terraces [58]. Conversely, upon evaporation, the slow orientations gradually disappear [94]. We have shown, using TDDFT, that elasticity can intensify kinetic faceting through either the imposition of a barrier to the nucleation of new terraces, or the increase of the relative stability of steps compared to other sites at the surface [66, 67].

An example of kinetic faceting is given in Fig. 7.11 for two SI-HM with $D = 150\sigma$; only the large inclusion is displayed since kinetic faceting does not affect the small one (which lies on the right). The figure clearly shows the rapid formation of facets along the low-energy (10) orientations of the triangular lattice. Subsequent

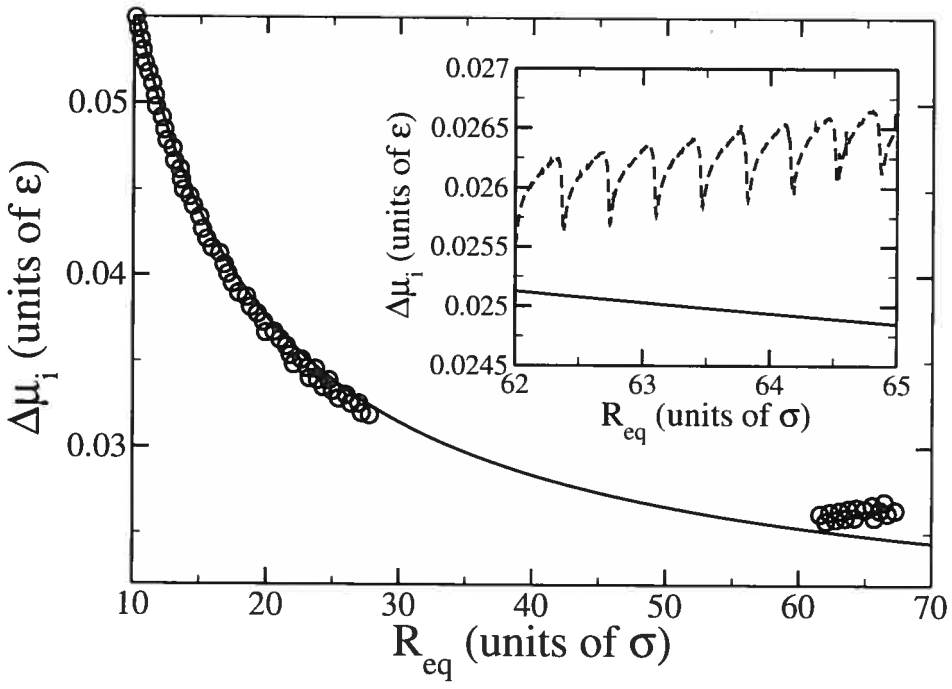

FIG. 7.12 – Chemical potential difference $\Delta\mu_i$ between species B and species A as a function of size for two SI-HM with initial radii of 30 and 60σ, respectively, $D = 150\sigma$ apart. The inset is an enlarged view of $\Delta\mu_i$ for the large inclusion. The continuous lines give the behaviour for an isolated inclusion.

growth occurs by the successive addition of atomic layers on the facets facing the small inclusion; this gradually leads to the growth of the two facets parallel to the x axis, while other facets retain their original orientation and length. This behaviour is to be contrasted with that for the SI-LM case, Fig. 7.6(b), where the large inclusion adopts a smooth, facet-free shape which becomes increasingly elongated during growth.

Such morphological changes have consequences on the chemical potential of the inclusions; as shown in Fig. 7.12, $\Delta\mu_i$ actually increases in the large inclusion as growth proceeds, gradually pushing it away from the equilibrium curve. This is to be contrasted with the low-misfit case (cf. Fig. 7.8), where kinetic faceting does not occur and the large inclusion closely follows the expected behavior. These results clearly demonstrate that, while $\Delta\mu_i$ is relatively unaffected by morphological modifications involving changes in the local curvature (cf. Section 7.4.2), it is very

sensitive to changes in the nature (i.e., rough vs. faceted) of some regions of the interface. In contrast, the small inclusion remains free of facets and closely mimics the SI-LM behavior during coarsening.

Kinetic faceting affects coarsening because it allows inclusions to follow different $\Delta\mu_i(R_{\rm eq})$ curves upon growth or evaporation. In the present case, this results in a slowdown of coarsening since faceting of the large inclusion causes an increase of $\Delta\mu_i$ and hence a decrease in the driving force for diffusion. Notice that the magnitude of changes in $\Delta\mu_i$ due to kinetic faceting is relatively small compared to shifts due to elastic interactions in dense systems (cf. Fig. 7.10) Kinetic faceting could nevertheless become important in the later stages of coarsening when the size of the inclusions gets large (and hence the differences in $\Delta\mu_i$ get small) or when neighboring inclusions have similar sizes.

The importance of kinetic faceting on coarsening is however difficult to assess precisely because its occurrence makes the instantaneous state of inclusions history-dependent. Indeed, partially-faceted shapes can be very stable since large barriers may separate them from their equilibrium configuration [75]; the state of an inclusion at any given time is thus a function of the duration and intensity of previous growth and evaporation episodes. Adding to the difficulty is the fact that the faceting efficiency is strongly rate-dependent. On the one hand, if growth is too slow, thermal fluctuations are able to restore the equilibrium shape of the inclusion — even in presence of kinetic biases — and faceting will not occur. On the other hand, if growth is too fast, the differences in chemical potential between different atomic states of the interface become insignificant compared to the driving force so that *kinetic roughening* occurs instead [58]. Since the effects due to faceting are relatively small compared to those due to elasticity, we will not attempt to quantify further their impact.

The discrete nature of growth through successive additions of atomic layers also manifests itself in oscillations of $\Delta\mu_i$, as shown in the inset to Fig. 7.12 where maxima correspond to completely filled layers and minima to newly nucleated terraces. Oscillations occur because of modulations in the shape of the inclusions or changes in the energetics of interface sites available for addition (of solute atoms) or

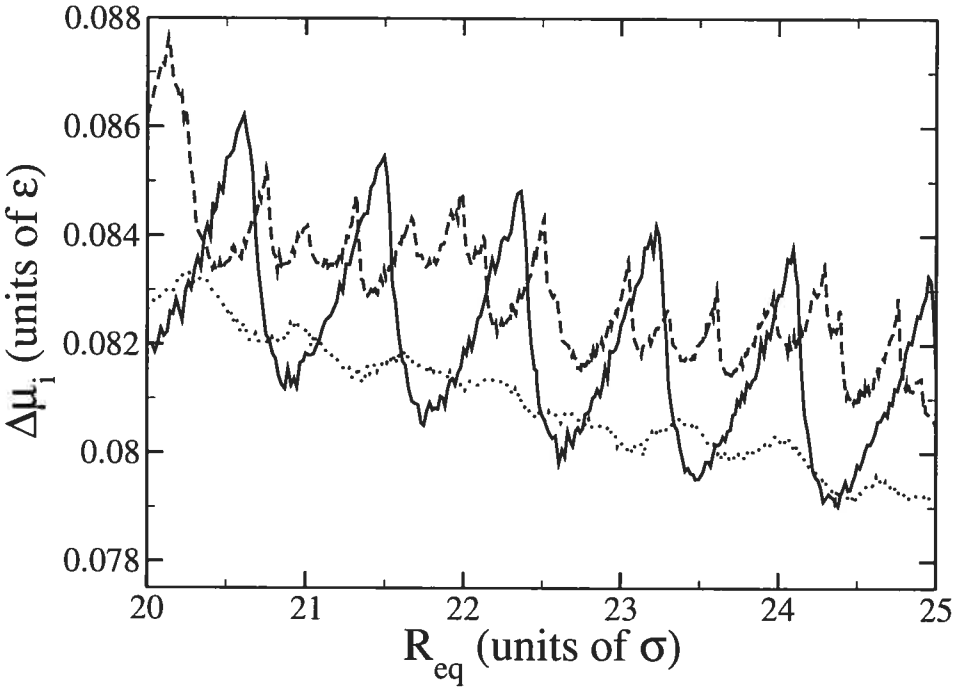

FIG. 7.13 – Chemical potential difference $\Delta\mu_i$ between species B and species A as a function of size for two HI-HM with $D = 150\sigma$ (dashed line), two HI-LM with $D = 150\sigma$ (dotted line) and an isolated HI-HM (continuous line).

evaporation [67]. These oscillations are significant because they provide a pathway to the stabilization of microstructures. Indeed, oscillations act as chemical potential barriers hampering coarsening; while such barriers can be overcome by thermal fluctuations, they still slow down coarsening considerably by pushing the system away from a thermodynamically-driven coarsening regime to a nucleation-driven regime [76].

Oscillations were observed in all the dilute elastically inhomogeneous systems we examined, and found to be strongest when the interface misfit is large [67]. Systems where interactions are important are no exception, as can be seen in Fig. 7.13. The oscillations in $\Delta\mu_i$ are in fact much larger for interacting HI-HM (dashed line) than for interacting HI-LM (dotted line). Comparison between the interacting HI-HM and the isolated HI-HM however indicates a significant decrease of the amplitude in presence of interactions. This can be explained by the reduced symmetry of the interacting system : because of the anisotropy of the strain field and of the supply of

solute atoms, equivalent interfacial orientations in different regions of the inclusion grow at different speeds, leading to a de-synchronization of the processes which cause oscillations in the chemical potential. In contrast, for a highly-symmetric inclusion with an isotropic supply of solute atoms, these processes (e.g. the nucleation of new atomic layers) occur completely in phase. These arguments also explain the lack of regularity in the behavior of $\Delta\mu_i$ for interacting inclusions compared to the regular oscillations (of period $\sqrt{3}\sigma/2$ — see Ref. [67]) for isolated inclusions. Note that when growth occurs in a layer-by-layer fashion, as is the case for the large SI-HM depicted in Fig. 7.11, oscillations can still be mostly regular, even in presence of interactions (cf. Fig. 7.12).

Despite their reduced amplitude, oscillations can still strongly hamper coarsening. Indeed, in a two-inclusion situation, if the intervals of $\Delta\mu_i$ swept the different inclusions overlap, i.e., $[\Delta\mu_i^{1,\min}, \Delta\mu_i^{1,\max}] \cup [\Delta\mu_i^{2,\min}, \Delta\mu_i^{2,\max}] \neq \varnothing$, a large number of metastable configurations become accessible. In contrast, in the purely capillarity-controlled case, the monotonous behavior of the chemical potential inexorably leads to a final state composed of a single inclusion. An example of such a metastable configuration is shown in Fig. 7.14 for a two HI-HM system with initial sizes 40σ and 30σ : after a brief transient period, growth and evaporation cease and the configuration stabilizes. Such situations are extremely easy to obtain at high interface misfits : they appear as soon as the difference in $\Delta\mu_i$ between the inclusions and the amplitudes of the oscillations are comparable. Note that these configurations are not true equilibrium states because $\Delta\mu_i$ still decreases *on average* with increasing size (cf. Fig. 7.13). Thus, thermal fluctuations could overcome the chemical potential barrier imposed by oscillations, enabling coarsening to proceed further. However, since the chemical potential landscape is very rugged, a large number of crossings are required before the thermodynamic force can freely drive diffusion again. Short-period oscillations of the chemical potential thus provide a very robust mechanism leading to stabilization of microstructures, even in presence of interactions.

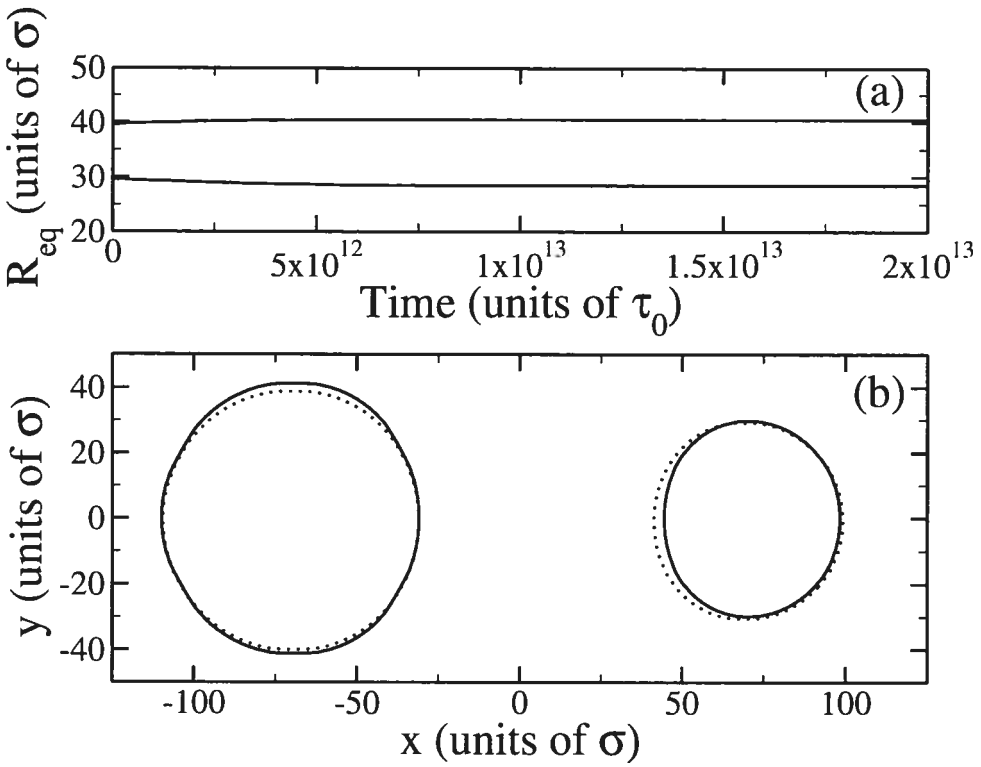

FIG. 7.14 – Coarsening of two HI-HM with initial radii of 30 and 40σ, respectively, separated by $D = 140\sigma$: (a) time evolution of the equivalent radii of the inclusions ; (b) initial (dotted lines) and metastable (continuous lines) shape of the inclusions.

7.5 Discussion

7.5.1 Interactions and confinement

Our results emphasize the highly nonlinear character of elastic interactions between inclusions in multiphase alloys. Indeed, the response of an inclusion to the presence of a neighboring inclusion was found to depend strongly on the local environment or, more precisely, on the strength of constraints imposed by the local environment. If there is a single neighbor, for example, the constraints impeding elastic relaxation are small. In this case, as shown in Sections 7.4.1.1 and 7.4.2.1, substantial shape changes take place and chemical potential shifts of at most a few percent (relative to isolated inclusions) can be expected, even for very small separations. The calculated shifts are in qualitative agreement with the predictions of Eshelby's formula : interactions cause stabilization of soft inclusions and destabilization of hard inclusions. However, the magnitude of the corrections to the

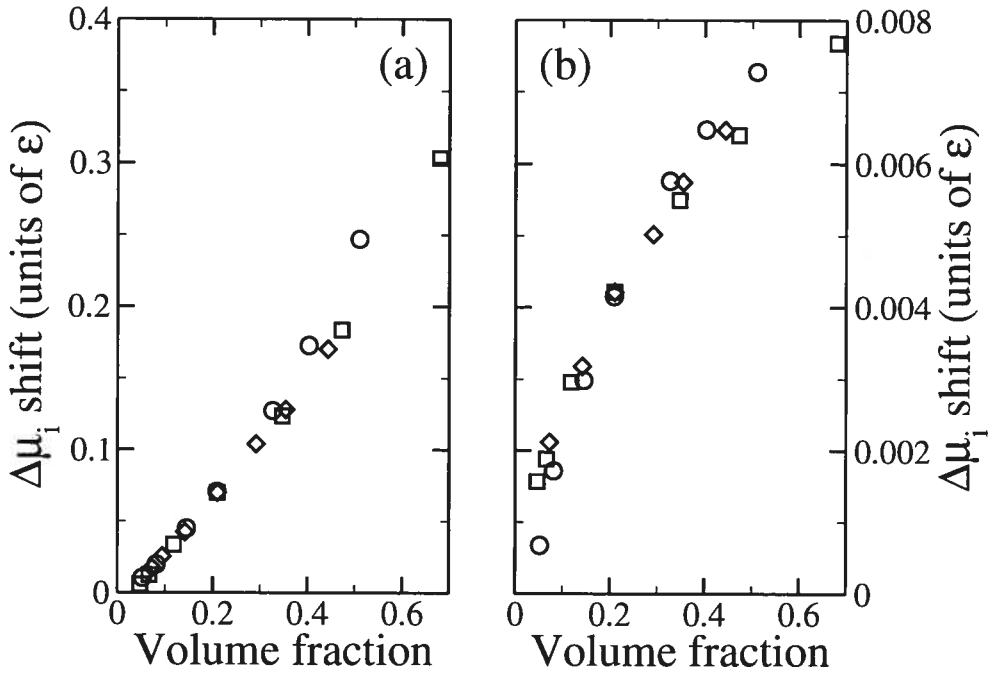

FIG. 7.15 – Chemical potential shifts $\Delta\mu_i$ for (a) HI-LM and (b) SI-LM in different situations of confinement; circles : periodic array of inclusions; squares : single inclusion in a regular-hexagon cell; diamonds : single inclusion in a hexagonal cell of varying aspect ratio (see text for details).

capillarity-driven behavior is so small that it is unlikely that coarsening could be significantly affected.

In the case where there are many neighbouring inclusions, now, relaxation by shape changes becomes inefficient because of the severe constraints imposed by the environment. As discussed in Sections 7.4.1.2 and 7.4.2.2, the effect on the chemical potential is one or two orders of magnitude larger than in the two-inclusion case. For both SI and HI, the interactions were found to *increase* the chemical potential, hence counteracting the normal $1/R_{\rm eq}$ dependence of $\Delta\mu_i$. Further, the shifts were shown to be additive constants proportional to the volume fraction [cf. Figs 7.5(b) and 7.10(b)].

These results suggest a simple model for the effect of interactions on the chemical potential shift of an inclusion, based on the following observation : neighboring inclusions may be viewed as obstacles impeding the relaxation of the internal

strain energy of a given inclusion. Consider a single inclusion in an infinite two-dimensional matrix; the displacement field decays as $1/r$. Adding a second inclusion forces the displacement (or at least some of its components) to vanish somewhere along the line joining the two inclusions. Since there is still plenty of room in which to relax the excess elastic energy, shape changes are able to efficiently modify the strain field in order to make use of this free volume; impact on the chemical potential is therefore small. For a periodic array of inclusions, now, the displacement field is constrained in every direction, thus reducing considerably the volume available for the inclusion to relax its strain energy. In this case, a significant portion of the elastic energy remains stored within the inclusion, causing a strong increase of its chemical potential.

In order to test the validity of this simple model, we carried out a series of simulations where the available volume is controlled using finite-size cells. Zero-displacement boundary conditions were imposed on the elastic equilibrium equation while closed boundary conditions were used for the TDDFT equation. The simulation cell is either a regular hexagon with all sides varying between 40 and 152σ, or an hexagon with 4 sides of length 72σ and two others of length varying between 40 and 152σ. The angle between adjacent edges of the cells is set to $2\pi/3$. A single circular inclusion with $R_{\text{eq}} = 30\sigma$ is placed at the center of each cell. The results of these calculations are reported in Fig. 7.15, together with those for a periodic array of inclusions (circles). From the finite-cell, regular-hexagon data (squares), we see that the effect of physically restricting the volume available for relaxation is indeed very similar to that resulting from the presence of other inclusions (circles). This agreement is not a fortuitous consequence of the high symmetry of the systems : for the irregular-hexagonal cells (diamonds), we find that inclusions are able to modify their shapes in order to make use of the strongly asymmetric distribution of free volume, similar to what is observed for binary systems of inclusions. The end result is then the same as if confinement was isotropic, as far as coarsening is concerned. Of course, it is not as easy to define the "volume available for relaxation" in non-symmetric systems; we will return to this point below.

This model helps understand why long-lasting inverse coarsening is usually not

observed in simple microstructures composed of only a few inclusions. In such a case, confinement is poor since very large volumes are available to relax the elastic energy ; elastic corrections are thus small and normal coarsening eventually prevails. In contrast, as the volume fraction increases, coarsening gradually shifts from "larger is more stable" to "larger free volume is more stable" since elastic contributions to the chemical potential are proportional to the local volume fraction ; this transition is clearly visible in Fig. 7.5, suggesting that inverse coarsening should be observed in a confined environment.

To test this hypothesis we studied the evolution of a two-HI-LM system in an hexagonal cell with two sides of length 256σ (along the axis joining the two inclusions) and four sides of length 128σ ; we used closed boundary conditions for the TDDFT equations and zero-displacement boundary conditions for the elastic equilibrium equations. This finite cell emulates the confining effect of the environment. The initially-circular inclusions had radii of 30σ and 40σ, respectively, and were 100σ apart, corresponding to an average volume fraction of ~ 0.1. The evolution of the system is presented in Fig. 7.16 ; as expected, the effect of confinement is strong : diffusion now carries solute atoms from the large to the small inclusion, i.e., inverse coarsening takes place. Diffusion however stops before the inclusions reach a common size, demonstrating the existence of other stable states besides the symmetric one. From Fig. 7.16(b), one also finds that, in contrast to the unconfined case, inclusions move during the simulation. Thus, under strong confinement, displacement of the inclusions and inverse coarsening are important for relaxing the strain energy ; under weak confinement, this proceeds through shape changes alone. Note that inverse coarsening and motion of the inclusion are processes taking place on very long timescales ($10^{12} - 10^{13}\tau_0$) compared to shape changes ($10^{11}\tau_0$).

Inverse coarsening is found to be an extremely robust process in confined environments : in the system described above, it occurs for inclusions as small as 20σ ; normal coarsening is only restored at smaller size. The final state however depends on the sizes of the inclusions and the distance between them, and both symmetric and asymmetric configurations are observed.

These results have important consequences regarding the volume available to

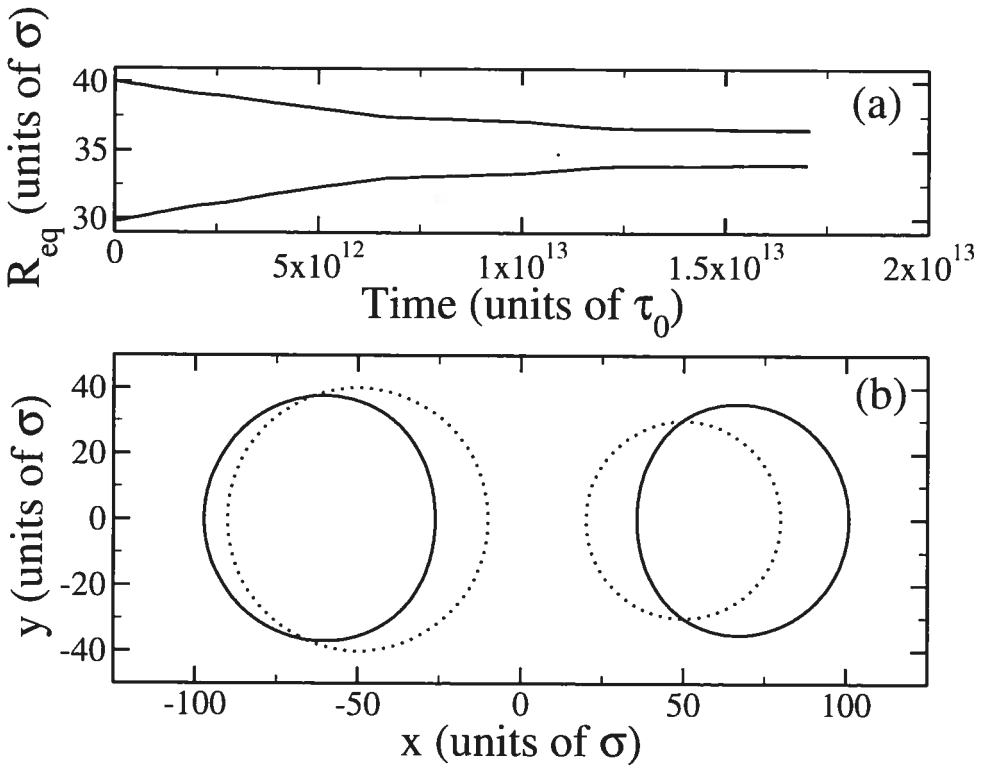

FIG. 7.16 – Evolution of two HI-LM with initial radii of 30 and 40σ, respectively, separated by $D = 140\sigma$: (a) time evolution of the equivalent radii of the inclusions; (b) initial (dotted lines) and metastable (continuous lines) shape of the inclusions.

each inclusion for relaxing its strain energy. In the system above, the cell may be partitioned into two "zones of influence", one for each inclusion. The occurrence of inverse coarsening means that the effect of confinement is stronger on the large inclusion than on the small one or, equivalently, that the effective volume fraction around the large inclusion is larger than around the small one. This in turn implies that, in presence of confinement, *the influence volume of an inclusion grows more slowly than its own volume.* This is an extremely significant result since it implies that elasticity will eventually hamper the growth of larger-than-average inclusions.

7.5.2 Interactions and coarsening

We now investigate the consequences of these observations on the the coarsening behavior of multi-inclusions systems. To this effect, we propose a simple LSW-type model modified to take the effect of elastic interactions into account; the LSW

equations are solved numerically to yield the time-evolution of the distribution in size of the inclusions. A similar model is described in detail in Ref. [67]. The only input needed is the relation between the activity (or, equivalently, $\Delta\mu_i$) and the size of an inclusion. The activity results from two contributions : one from capillarity, which decays as $1/R$, and one from elasticity, which we take to be linearly proportional to the local volume fraction (cf. Fig. 7.15) :

$$\mathcal{A}_i(t) = C_1/R + C_2 V_f^l(R,t), \tag{7.3}$$

where C_1 is a parameter related to the interface free energy, C_2 describes the strength of elastic interactions; $V_f^l(R) = \pi R^2/V_i(R,t)$ is the local volume fraction around an inclusion of size R, related to the influence volume $V_i(R,t)$ available to an inclusion, which we propose is proportional to its real volume to some power γ, $V_i(R,t) = N(t)[\pi R^2]^\gamma$, with $N(t)$ a time-dependent normalization factor ensuring that the sum of the V_i's is constant. As mentioned above, the existence of inverse coarsening in a confined geometry implies $\gamma < 1$; analysis of our simulation results indicates that $0.4 < \gamma < 0.6$; in what follows, we set $\gamma = 0.5$. This choice is not critical, as we found no qualitative differences in the results for values of γ between 0 and 1. This is also true of the other parameters of the model, which only affect the length and time scales of the problem; we set $C_1 = 0.00025\sigma^{-1}$ and $C_2 = 10^{-4}$.

Of course, this model can only give a rather crude description of the real coarsening dynamics. The LSW model is formally correct only in the limit $V_f \to 0$. It is known that increasing the volume fraction leads to wider and more symmetric distribution functions than predicted by LSW, but that the coarsening exponent is not significantly altered [96]. Also, elastically-induced correlations could modify the coarsening behavior; this possibility is not considered in LSW-type models because the inclusions are assumed to interact with the environment in a mean-field way. Thus, our model cannot be expected to yield quantitative results, but it should capture the essentials of elastic inhomogeneity.

The dependence on time of the average inclusion size $\langle R \rangle$ for different volume fractions V_f obtained within this model are presented in Fig. 7.17. We note first that in the dilute limit ($V_f \to 0$), coarsening is "normal", well described by a single

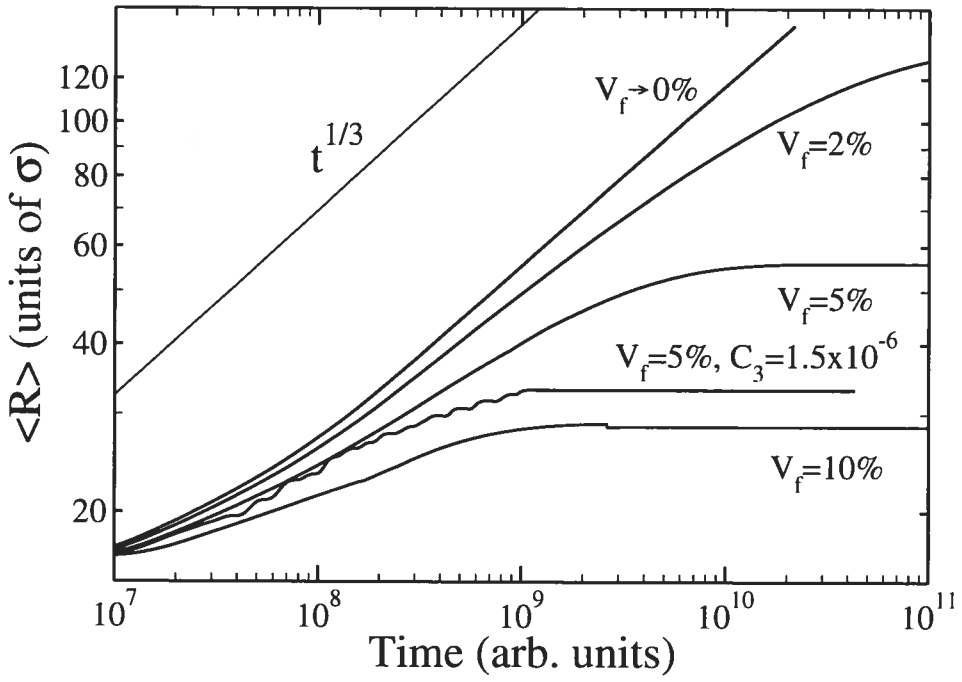

FIG. 7.17 – Average inclusion size $\langle R \rangle$ for different volume fractions V_f obtained using a modified LSW model (see text for details); unless otherwise specified, $C_1 = 0.00025\sigma^{-1}$, $C_2 = 1\text{x}10^{-4}$, and $C_3 = 0$.

exponent $1/3$ as predicted by the LSW theory. In contrast, at finite volume fraction, significant departures from the normal behaviour are observed, and coarsening is found to proceed in three distinct phases. First, after an initial transient period, a power-law dependence with an exponent somewhat smaller than $1/3$ is observed, and the higher the volume fraction, the smaller the exponent, which gradually decreases (intermediate phase), and finally reaches 0 (third phase) — the system stabilizes and coarsening apparently stops; this occurs at increasingly small average size as the volume fraction increases. Inverse coarsening sets in once $\langle R \rangle$ reaches its maximum value. This can indeed be seen from the size distribution function, shown in Fig. 7.18 : at finite volume fraction (dashed line), the distribution gradually gets narrower (compare with the continuous curve for $V_f \to 0$), converging to a delta function at later times. Such a behaviour signals the growth of small inclusions at the expense of larger ones, i.e., inverse coarsening.

In spite of its crude nature, our model is in remarkably good qualitative agree-

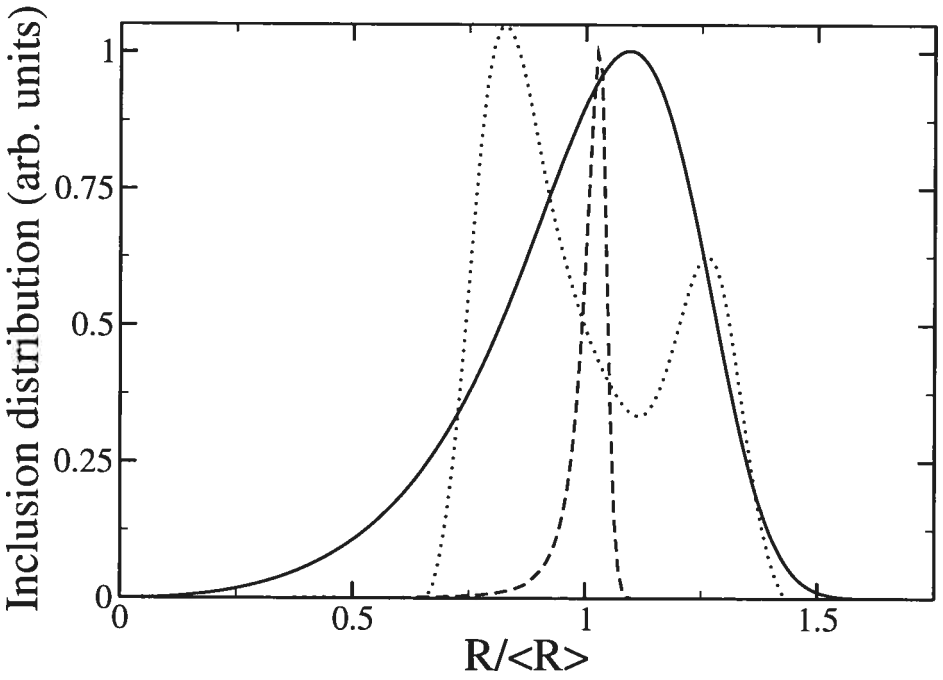

FIG. 7.18 – Size distribution function for different values of the parameters of the modified LSW model, Eqs. 7.3 and 7.4. Continuous line : $\langle R \rangle = 92\sigma$ with $V_f \to 0\%$, $C_3 = 0$; dashed line : $\langle R \rangle = 55\sigma$ with $V_f = 5\%$, $C_3 = 0$; dotted line : $\langle R \rangle = 33\sigma$ with $V_f = 5\%$, $C_3 = 1.5\text{x}10^{-6}$.

ment with experiment. Stabilization has indeed been observed over long timescales in a wide range of inhomogeneous alloys [65]. Also, as expected, the maximum average size decreases with increasing volume fraction when stabilization occurs [65]. Finally, on small and intermediate timescales, a gradual decrease of the coarsening exponent with increasing volume fraction is observed, in agreement with experimental results [54]. Our simple model thus captures the essential physics of coarsening in elastically inhomogeneous systems.

Within LSW-type models, the existence of an asymptotic distribution function which is non-zero at a given finite R implies that the activity function possesses a minimum at this value of R. Indeed, any monotonously decreasing activity function leads to a distribution such that $\langle R \rangle \to \infty$. Elastic inhomogeneities yield such a minimum through the size-dependent chemical potential shifts which penalize large inclusions. While the narrowing of the distribution function observed in some

alloys during the stable or very-slowly coarsening stage [54] (third stage of the present model) is consistent with the presence of a single minimum, widening — also observed in some cases [8, 25, 77] — requires many. As demonstrated in Section 7.4.3, chemical potential oscillations caused by interface misfits provide a mechanism for the existence of such a rugged landscape, enabling microstructures composed of inclusions of various sizes to become (meta-)stable against coarsening. These oscillations can be accounted for by adding a term in Eq. 7.3, which we now write :

$$\mathcal{A}_i(t) = C_1/R + C_2 V_f^l(R,t) + C_3[\cos(4\pi R/\sqrt{3}) + 1]/2. \tag{7.4}$$

Since the results are not affected by the period of the oscillations we use, for simplicity, the value appropriate for isolated inclusions, viz. $\sqrt{3}/2\sigma$; we set $C_3 = 1.5\text{x}10^{-6}$.

We previously demonstrated that oscillations alone, i.e., without elastic effects ($C_2 = 0$), are able to induce a transition from a normal coarsening state to a frozen state (with the present choice of parameters, this occurs at $\langle R \rangle \simeq 140\sigma$ [67]) and that slowing down is accompanied by the formation of a long tail at large sizes in the distribution function. If contributions from both oscillations and elastic interactions ($C_2 \neq 0$, $C_3 \neq 0$) are included, now, the evolution of the microstructure is not modified dramatically. As shown in Fig. 7.17 for a volume fraction of 5%, the main differences are a decrease of the maximum $\langle R \rangle$, a slight decrease of the coarsening exponent in the first phase, and a reduction of the duration of the intermediate regime. In contrast, the size distribution is significantly affected. As illustrated in Fig. 7.18 (dotted line), it stabilizes with a finite width — wider than the normal LSW distribution — in agreement with the above discussion. Also, the formation of a long tail is avoided because elasticity prohibits the growth of very large inclusions. Note that while widening is a robust feature of the model, the precise shape of the distribution function is quite sensitive to the amplitude of the oscillations.

These results demonstrate that the oscillations in the chemical potential induced by the interface misfits are able to stabilize microstructures containing inclusions of various sizes, even in presence of interactions. The oscillations are also able to

prevent inverse coarsening and hence account for the widening of the distribution function observed in some alloys [8, 25, 77]. Finally, the model suggest that interface misfits strongly contribute to the slowing down of coarsening in cases where it initially occurs with an exponent close to 1/3 but then abruptly stops [65], since, as our model indicates, an exponent of 1/3 is associated with small bulk elastic effects. In this case, however, slowing down is expected to be very gradual (cf. Fig. 7.17 at low volume fraction) ; in contrast, the transition from normal coarsening to frozen state is possible in presence of large interface misfits [67]. In this case, bulk elasticity would only assist the transition by slowing down the growth of large inclusions, thus making the transition sharper.

As a final point, it must be mentioned that another mechanism besides oscillations may cause the stabilization of distribution functions of finite width : the ruggedness of the activity could indeed originate from local variations of the environment of the inclusions, an effect not taken into account in the present model. This would require some sort of self-organization of the influence volumes, as simple random fluctuations eventually lead to a mono-disperse distribution of inclusion sizes in absence of chemical potential oscillations. This problem will be the subject of further work. The fact that significant inverse coarsening was never observed in large-scale simulations [60, 63, 107] may indicate that such self-organization processes do occur. It may also be simply due to limitations in time of the simulations, as inverse coarsening only becomes significant in the very late stages of microstructural evolution, once the average inclusion size has reached its final value. Before this stage is reached, elasticity is only expected to slow down the growth of large inclusions in comparison to the homogeneous case.

7.6 Conclusion

We have investigated the role of interactions between inclusions on the coarsening dynamics of elastically inhomogeneous alloys. From our study of binary systems, we found that shape changes are the main process by which strain energy relaxes. The latter was found to be so efficient that coarsening is not significantly affected by interactions. However, we have also found that the efficiency of the me-

chanism drops for denser arrangements of inclusions, leading to corrections proportional to the local volume fraction. In this case, the effect of elasticity on coarsening increases by one or two orders of magnitude so that these corrections are sufficient to counteract the usual capillarity-dominated behavior. In contrast to what would be expected from Eshelby's formula, the effect of interactions is qualitatively the same if both hard and soft inclusions are organized in dense arrangements.

In the second part of this study, we examined the impact of interface elasticity on coarsening. Interactions were shown to modify very little the role of interface misfit in comparison to the dilute limit [67] : interface elasticity induces kinetic faceting or oscillations in the chemical potential of the inclusions. Both processes were shown to be able to significantly affect the coarsening behavior. In particular, oscillations were shown to stabilize microstructures containing inclusions of unequal sizes, without the need for some other stabilizing process like inverse coarsening. An example of interface-stabilized system of inclusions was given.

In the last part, finally, we showed that the effect of interactions on the chemical potential of inclusions is akin to the effect of confinement by cells of finite volumes. On the basis of this observation, we explained why dense arrangements of inclusions are required for inverse coarsening to take place; an example was presented. Finally, we proposed a modified LSW model to account for the effect of elasticity (both bulk and interface contributions) on coarsening. The predictions of the model were shown to be in excellent agreement with the experimental observations : in bulk-elasticity-dominated systems, coarsening initially proceeds with a reduced exponent but gradually reaches a stable state through inverse coarsening; in interface-elasticity-dominated cases, transitions from a normal coarsening state with exponent $1/3$ to a stable state take place, and final inclusion distribution functions of finite widths are observed.

This work demonstrates that elasticity provides two distinct pathways for controlling the morphology and coarsening kinetics of multiphase microstructures : the traditional route involving inter-inclusion interactions, and a novel route relying on interface effects. It should be possible to use this dichotomy to further enhance our control over microstructures. Indeed, on the one hand, interface elasticity

provides an unselective stabilization process that can operate nearly irrespective of the morphological features of the microstructures. On the other hand, our results suggest that inter-inclusion interactions can only stabilize monodisperse microstructures; however, they can also induce shape changes and movement of inclusions. Careful balancing of these two factors could thus enable precise tuning of the microstructural properties, as hinted by the wide range of behaviors observed in real materials where these two factors simultaneously operate. However, understanding of the forces involved in microstructural evolution will not be complete until the impact of correlations between inclusions is understood : since both inverse coarsening and inclusion migration operate at high volume fraction, complex correlations, not taken into account here, could form and affect both kinetic and morphological features of the system. This will be the subject of future investigation.

This work has been supported by grants from the Natural Sciences and Engineering Research Council of Canada (NSERC) and the *Fonds Québécois de la Recherche sur la Nature et les Technologies* (FQRNT). We are indebted to the *Réseau Québécois de Calcul de Haute Performance* (RQCHP) for generous allocations of computer resources.

CHAPITRE 8

DISCUSSION ET SYNTHÈSE

À la lumière des résultats des simulations TDDFT présentés aux chapitres 4 à 7, il est maintenant possible de brosser un tableau plus général du comportement des alliages multiphases élastiquement inhomogènes lors de leur mûrissement. Pour ce faire, nous reviendrons sur chacune des questions posées en début de thèse (cf. chapitre 3), lesquelles ont fait office de fil conducteur tout au long de ce travail.

Premièrement, nous avons exploré la validité de l'équation de Gibbs-Thomson (GT), reliant le potentiel chimique d'une inclusion à sa taille. Cette relation est primordiale pour bien comprendre le mûrissement puisqu'elle dicte le taux auquel les échanges avec la matrice s'effectuent. Au chapitre 4, nous avons montré que la forme générale de la relation de GT décrit correctement le comportement d'inclusions isolées, sauf lorsqu'une transition spontanée dans la forme survient, comme dans le cas des inclusions molles. Dans ce cas, on observe un changement dans le préfacteur du terme de courbure de part et d'autre de la transition. Les résultats montrent cependant que le potentiel chimique ne varie pas nécessairement de manière monotone avec la taille en présence d'élasticité. On reviendra sur ce point, qui s'est avéré très important, plus bas.

Toujours au chapitre 4, nous nous sommes attardés à l'effet sur le mûrissement de la transition de forme observée pour les inclusions molles. À l'aide d'un modèle LSW modifié, nous avons montré que le mûrissement comporte alors deux régimes distincts, un pour une taille moyenne inférieure à la taille critique de la transition de forme, et un pour une taille moyenne supérieure à ce seuil. Ces deux régimes sont décrits par un même exposant $1/3$, mais possèdent des préfacteurs différents. Dans le cas traité ici, le changement de préfacteur cause une accélération du mûrissement. La stabilisation de la microstructure n'est donc pas liée aux transitions de forme. Ces résultats sont similaires à ceux obtenus par Thornton *et al.* [92] pour des transitions induites par l'anisotropie élastique.

Dans le but de comprendre les propriétés dynamiques des inclusions, nous avons

ensuite étudié l'effet de la croissance (cf. chapitre 4). Nous avons montré que le piégeage de soluté (*solute trapping*) est un mécanisme commun, observé dans tous les types d'inclusions enchassées dans une matrice sursaturée. Cependant, bien que ce phénomène puisse être amplifié par l'inhomogénéité élastique, nos calculs indiquent que son impact sur le mûrissement est marginal. Une autre conséquence de l'afflux rapide de soluté est que la forme d'équilibre des inclusions peut devenir instable. Notre analyse montre que le modèle de Leo et Sekerka [45] décrit de manière adéquate les propriétés de stabilité des inclusions inhomogènes dans la limite des faibles déformations. Par contre, pour les inclusions molles, l'instabilité de mode est éventuellement remplacée par une instabilité de croissance de pointes qui éloigne de manière durable les inclusions de leur état d'équilibre, même pour de faibles sursaturations. L'impact de ces changements de forme sur le potentiel chimique et sur le mûrissement s'est avéré significatif. Par contre, même dans ce cas, les effets observés ne sont pas en mesure d'affecter le mûrissement au point de causer la stabilisation observée expérimentalement.

La question de l'effet des contraintes élastiques à l'interface a ensuite été traitée aux chapitres 5 et 6. Nous avons montré que les effets d'interface, ignorés jusqu'à maintenant dans les autres études sur le sujet, peuvent affecter de manière très importante le mûrissement. En effet, nous avons observé que l'élasticité, due à sa longue portée, est en mesure de coupler la structure globale de l'interface (la forme générale de l'inclusion) avec sa structure locale (la structure à l'échelle atomique). Ce couplage influence la forme des inclusions durant la croissance ou l'évaporation en favorisant certains types de sites à l'interface. Ces changements peuvent être durables [comme dans le cas du facettage cinétique (*kinetic faceting*)] ou temporaires (comme dans le cas des oscillations de forme). Nous avons observé que les modulations de la forme et les changements dans l'énergie des sites disponibles pour l'addition d'atomes de soluté peuvent induire de fortes oscillations du potentiel chimique des inclusions. À l'aide d'un deuxième modèle LSW convenablement modifié, nous avons montré que ces oscillations peuvent mener à une stabilisation complète de la microstructure après une période initiale de mûrissement normal, en accord avec les résultats expérimentaux obtenus sur certains alliages inhomogènes.

Les oscillations peuvent aussi expliquer l'élargissement des fonctions de distribution en taille des inclusions. Nous avons finalement établi que l'intensité de ces effets est contrôlée en grande partie par le désaccord d'interface (*interface misfit*).

Finalement, au chapitre 7, nous avons exploré l'effet de l'interaction élastique entre les inclusions, un facteur très important pour comprendre le mûrissement à haute fraction volumique. Nous avons montré que les inclusions réagissent fortement à la présence d'autres inclusions dans leur voisinage, principalement par le biais de changements de forme. Ces changements ont pour effet de minimiser dramatiquement l'impact de l'interaction sur le mûrissement. En effet, pour un système binaire d'inclusions isolées, les changements de forme sont si efficaces que le potentiel chimique des inclusions est affecté d'au plus quelques pourcents par la présence d'un voisin, même quand la séparation entre les deux inclusions est extrêmement faible. Par contre, pour des systèmes d'inclusions plus denses, l'efficacité des changements de forme diminue fortement et l'impact sur le potentiel chimique augmente d'un ou deux ordres de grandeur. Nous avons déterminé que ces contributions élastiques au potentiel chimique sont proportionnelles à la fraction volumique locale. Pour des fractions volumiques suffisamment importantes, ces contributions peuvent dominer complètement le comportement de la relation de Gibbs-Thomson, induisant une transition entre un mode de mûrissement "plus gros = plus stable" vers un mode "plus petite fraction volumique = plus stable". La pertinence de cette transition a été démontrée de manière éclatante par l'observation de mûrissement inverse dans un système confiné de deux inclusions. Ce mécanisme procure une deuxième voie pour atteindre la stabilisation de la microstructure. Par la même occasion, nous avons démontré que la translation des inclusions devient un mécanisme efficace de relaxation des contraintes élastiques à haute fraction volumique.

Nous avons aussi étudié l'effet des contraintes d'interface sur le mûrissement d'inclusions en interaction. Nous avons démontré explicitement que les oscillations du potentiel chimique causées par les effets d'interface sont en mesure de stabiliser des microstructures composées d'inclusions de tailles différentes, même en présence d'interactions. Finalement, à l'aide d'un troisième modèle de type LSW, modifié pour tenir compte autant des effets d'interface que des interactions entre

inclusions, nous avons obtenu un excellent accord qualitatif avec l'expérience en reproduisant la diminution graduelle de l'exposant dans le régime de mûrissement et de la taille moyenne maximale des inclusions dans le régime stabilisé lorsque s'accroît la fraction volumique. De plus, nous observons la diminution de la largeur de la distribution des inclusions lorsque les effets d'interaction dominent et son augmentation lorsque les effets d'interfaces contrôlent la dynamique.

Ces résultats permettent d'expliquer l'essentiel des anomalies du mûrissement présentées au chapitre 2. En effet, nos calculs suggèrent que la diminution graduelle de l'exposant de mûrissement dans la phase initiale de l'évolution de la microstructure est liée aux interactions élastiques qui augmentent de manière importante le potentiel chimique des inclusions de grande taille limitant ainsi leur croissance, en accord autant avec la variation de cet exposant selon la fraction volumique observée expérimentalement [54] qu'avec les simulations de type "phase-field" les plus récentes [107]. La variation de la taille moyenne maximale des inclusions avec la fraction volumique [65] ainsi que la diminution de la largeur de la distribution en taille [54] seraient aussi causées par ces interactions. Par contre, dans les alliages où le mûrissement se déroule initialement avec un exposant près de $1/3$, les effets d'interface seraient les principaux responsables de l'arrêt éventuel du mûrissement en induisant une transition entre un mode de mûrissement limité par la diffusion et un mode de mûrissement limité par la nucléation. L'élargissement de la fonction de distribution en taille [25] serait aussi lié à ce type d'effets. Puisqu'en général les deux facteurs sont en compétition, on peut facilement expliquer la vaste gamme de comportements décrits au chapitre 2.

CONCLUSION

Cette thèse apporte trois contributions principales à la connaissance : une, de nature méthodologique, liée aux méthodes de modélisation numérique et deux, de nature physique, liée à la compréhension des mécanismes en jeu lors du mûrissement dans les alliages élastiquement inhomogènes.

Concernant l'aspect méthodologique, nos travaux ont démontré l'utilité de la TDDFT lorsqu'appliquée à la simulation de l'évolution microstructurale, en mettant en évidence ses forces comparativement aux techniques conventionnelles. En effet, en conjonction avec notre implémentation multi-échelle, la méthode conserve les principaux avantages des méthodes Monte Carlo (faible nombre de paramètres, formulation en terme des mécanismes physiques fondamentaux, résolution à l'échelle atomique). Elle profite aussi de ceux associés aux méthodes macro ou mésoscopiques (représentation en terme de variables continues, grandes échelles de temps et d'espace, facilité d'imposition de conditions aux frontières variées). De plus, la méthode offre un formalisme unifié prenant en considération différents processus physiques se déroulant sur de vastes gammes d'échelles de temps et d'espace. Sans cette flexibilité, il aurait, par exemple, été impossible de corréler de manière convaincante les changements dans la structure microscopique de l'interface dus aux contraintes élastiques et leur impact à long terme sur le mûrissement de systèmes d'inclusions.

Cet avantage de notre méthode a en fait permis la seconde contribution, celle-là au niveau de la compréhension de la physique du mûrissement. En effet, nos travaux ont demontré que l'élasticité induit un couplage très fort entre l'échelle microscopique, à laquelle se déroulent les événements individuels de condensation et d'évaporation d'atomes de soluté sur les inclusions, et l'échelle mésoscopique, où se déroulent les changements microstructuraux impliquant plusieurs inclusions. Dans le cas présent, il s'avère que ce couplage est en mesure d'affecter le mûrissement au point de pouvoir stabiliser complètement la microstructure. Cette possibilité avait été négligée jusqu'à maintenant, peut-être simplement en raison des limitations propres aux modèles précédents, qui oeuvraient chacun à leur échelle respective. Cette constatation renforce d'autant plus l'idée que des approches novatrices sont

requises lorsqu'on s'attaque à des problèmes qui ont subi, avec un certain succès, l'épreuve du temps.

La troisième contribution concerne le rôle du mûrissement inverse. En effet, nous avons pu confirmer que ce dernier est bel et bien un mécanisme général et robuste lorsque le confinement offert par les inclusions voisines est suffisamment important. Cette observation permet de relier la stabilisation au mûrissement inverse à haute fraction volumique. Notre travail permet aussi de montrer qu'il est parfois préférable d'utiliser des systèmes modèles simples au lieu de s'attaquer directement à des microstructures complexes, puisque dans ce cas, le mûrissement inverse n'est attendu que dans la phase finale de l'évolution du système.

Bien que ces contributions soient significatives, elles prennent la forme d'un socle sur lequel on pourra éventuellement construire une compréhension globale des propriétés des systèmes élastiquement inhomogènes plutôt que celle d'un ouvrage complet et auto-portant. En effet, deux points importants restent à explorer. Premièrement, une étude systématique de l'importance des corrélations dans ce type de microstructure s'impose. En effet, nous avons vu, au chapitre 7, que les inclusions sont à la fois flexibles et mobiles. Elles sont donc en mesure de s'adapter à leur environnement de manière active. Il se peut que cette capacité mène à l'apparition de corrélations dont l'effet n'a pas été considéré ici. Une deuxième avenue à explorer est l'effet de l'anisotropie élastique. En plus d'intensifier les corrélations spatiales entre inclusions, ce qui faciliterait l'étude du point précédent, l'anisotropie favorise les formes facettées. Tel que mentionné au chapitre 6, ceci pourrait accroître l'importance du mode de croissance couche-par-couche et, par conséquent, le rôle des barrières de nucléation de terrasses et les variations spatiales de l'énergie d'addition de soluté, augmentant d'autant l'amplitude des oscillations de potentiel chimique et l'impact sur le mûrissement.

Finalement, on se doit de souligner que, dans sa forme actuelle, notre modèle possède un pouvoir prédictif limité. Premièrement, on ne peut prétendre à de réelles prédictions quantitatives en se basant uniquement sur des fonctionnelles d'énergie libre de type champ moyen comme celle utilisée ici. Bien qu'adéquat pour l'identification des mécanismes physiques de base régissant le mûrissement des systèmes

multi-phases, ce type de fonctionnelle commet une erreur significative sur l'estimation de la force motrice entraînant la séparation de phase et ne peut être utilisé pour décrire des systèmes ordonnés, comme les inclusions γ' fréquemment observées dans les alliages de nickel. L'avenir de la TDDFT dépendra de la possibilité de développer des fonctionnelles améliorées prenant en compte les corrélations. Des pistes de solutions pour accomplir cet objectif sont présentées à l'annexe V. Deuxièmement, l'imposition de la cohérence élastique limite le domaine d'applicabilité du modèle aux contraintes plutôt modestes. De plus, il est difficile d'identifier clairement la limite de ce domaine. Il serait donc des plus intéressant de généraliser le modèle pour inclure des effets de plasticité, comme la possibilité de décrire des interfaces au niveau variable de cohérence ou encore de permettre l'émission et la propagation de dislocations. Les spectre des applications possibles s'élargirait alors considerablement. Par exemple, on pourrait étudier l'effet de la perte de cohérence sur le mûrissement ou encore sur l'efficacité du piégeage des dislocations par les inclusions. Pour ce faire, il faudrait mettre au point un modèle de diffusion généralisé, valide quelle que soit la configuration atomique locale. On devrait aussi abandonner le potentiel harmonique en faveur d'un potentiel plus réaliste pour décrire les interactions interatomiques.

BIBLIOGRAPHIE

[1] http ://www.msm.cam.ac.uk/phase-trans/2002/zhang.html.

[2] http ://www.msm.cam.ac.uk/utc/projects/.

[3] T. A. Abinandanan and W. C. Johnson. Coarsening of elastically interacting coherent particles — II. Simulations of preferential coarsening and particle migrations. *Acta Metallurgica et Materialia*, 41(1) :27–39, 1992.

[4] M.J. Aziz, J. Y. Tsao, M. O. Thomson, P. S. Peercy, and C. W. White. Solute trapping : Comparison of theory with experiment. *Physical Review Letters*, 57(23) :2489–2492, 1986.

[5] W. L. Bragg and E. J. Williams. *Proceedings of the Royal Society (London)*, A 145 :699, 1934.

[6] P. N. Brown and Y. Saad. Hybrid Krylov methods for nonlinear systems of equations. *SIAM Journal on Statistical and Scientific Computing*, 11(3) :450–481, 1990.

[7] L. N. Brush and R. F. Sekerka. A numerical study of two-dimensional crystal growth forms in the presence of anisotropic growth kinetics. *Journal of Crystal Growth*, 96 :419–441, 1989.

[8] H. A. Calderon, G. Kostorz, Y. Y. Qu, H. J. Dorantes, J. J. Cruz, and J. G. Cabanas-Moreno. Coarsening kinetics of coherent precipitates in Ni-Al-Mo and Fe-Ni-Al alloys. *Materials Science and Engineering*, A238 :13–22, 1997.

[9] L. Q. Chen. Kinetics of ordering and spinodal decomposition in the pair approximation. *Physical Review B*, 58(9) :5266–5274, 1998.

[10] L. Q. Chen. Phase-field models for microstructure evolution. *Annual Review of Mateials Research*, 32 :113–140, 2002.

[11] N. Combe, P. Jensen, and A. Pimpinelli. Changing shapes in the nanoworld. *Physical Review Letters*, 81(1) :110–113, 2000.

[12] J. W. D. Connolly and A. R. Williams. Density-functional theory applied to phase transformations in transition-metal alloys. *Physical Review B*, 27(8) :5169–5172, 1983.

[13] M. Doi, T. Miyazaki, and T. Wakatsuki. The effect of elastic interaction energy on the morphology of γ' precipitates in nickel-based alloys. *Materials Science and Engineering*, 67(2) :247–253, 1989.

[14] S. C. Eisenstat and H. F. Walker. Globally convergent inexact Newton method. *SIAM Journal on Optimization*, 4 :392–422, 1994.

[15] Y. Enomoto and K. Kawasaki. Computer simulation of ostward ripening with elastic field interactions. *Acta Metallurgica*, 37(5) :1399–1406, 1989.

[16] J. D. Eshelby. The determination of the elastic field of an ellipsoidal inclusion, and related problems. *Proceedings of the Royal Society A*, 241 :376–396, 1957.

[17] J. D. Eshelby. On the elastic interaction between inclusions. *Acta Metallurgica*, 14 :1306–1309, 1966.

[18] R. Eymard, T. Gallouët, and R. Herbin. A cell-centered finite-volume approximation for anisotropic diffusion operators on unstructured meshes in any space dimension. *IMA Journal of Numerical Analysis*, 2005.

[19] H. P. Fischer, J. Reinhard, W. Dieterich, J. F. Gouyet, P. Maass, A. Majhofer, and D. Reinel. Time-dependent density functional theory and the kinetics of lattice gas in systems in contact with a wall. *Journal of Chemical Physics*, 108(7) :3028–3037, 1998.

[20] F. C. Frank. *Growth and Perfection of Crystals.* Wiley, New York, 1958.

[21] P. Fratzl and O. Penrose. Ising model for phase separation in alloys with anisotropic elastic interaction–I. Theory. *Acta Metallurgica et Materialia*, 43(8) :2921–2930, 1995.

[22] P. Fratzl, O. Penrose, and J. L. Lebowitz. Modeling of phase separation in alloys with coherent elastic misfit. *Journal of Statistical Physics*, 95(5/6) :1429–1503, 1999.

[23] J. C. Maxwell Garnett. *Philos. Trans. R. Soc. London A*, 203 :385, 1904.

[24] C. W. Gear. The automatic integration of stiff ordinary differential equations. In *Proceedings IFIP 68*, pages 187–193. North-Holland, Amsterdam, 1968.

[25] A. Ges, O. Fornaro, and H. Palacio. Long term coarsening of γ' precipitates in a Ni-base superalloy. *Journal of Materials Science*, 32 :3687–3691, 1997.

[26] H. Gupta, R. Winkamer, P. Fratzl, and J. L. Lebowitz. Microscopic computer simulations of directional coarsening in face-centered cubic alloys. *Acta Materialia*, 49 :53–63, 2001.

[27] E. O. Hall. *Proceedings of the Physical Society of London*, B64 :747, 1951.

[28] M. R. Hestenes and E. Stiefel. Methods of conjugate gradients for solving linear systems. *Journal of Research of the National Bureau of Standards*, 49 :409–436, 1952.

[29] M. Hillert. Solute drag, solute trapping and diffusional dissipation of Gibbs energy. *Acta Materialia*, 47(18) :4481–4505, 1999.

[30] S. Y. Hu and L. Q. Chen. A phase-field model for evolving microstructures with strong elastic inhomogeneity. *Acta Materialia*, 49 :1879–1890, 2001.

[31] W. C. Johnson. On the elastic stabilization of precipitates against coarsening under applied load. *Acta Metallurgica*, 32(3) :465–475, 1984.

[32] W. C. Johnson, T. A. Abinandanan, and P. W. Voorhees. The coarsening kinetics of two misfitting particles in an anisotropic crystal. *Acta Metallurgica et Materialia*, 38(7) :1349–1367, 1990.

[33] W. C. Johnson and J. W. Cahn. Elastically induced shape bifurcations of inclusions. *Acta Metallurgica*, 32(11) :1925–1933, 1984.

[34] W. C. Johnson, P. W. Voorhees, and D. E. Zupon. The effect of elastic stress on the kinetics of ostwald ripening : The two-particle problem. *Metallurgical Transactions A*, 20A :1175–1189, 1989.

[35] H.J. Jou, P. H. Leo, and J. S. Lowengrub. Microstructural evolution in inhomogeneous elastic media. *Journal of Computational Physics*, 131 :109–148, 1997.

[36] B. P. Kashyap and K. Tangri. On the Hall-Petch relationship and substructural evolution in type 316L stainless steel. *Acta Metallurgica et Materialia*, 43(11) :3971–3981, 1995.

[37] M. Kessler, W. Dieterich, H. L. Frisch, J. F. Gouyet, and P. Maass. Kinetic in one-dimensional lattice gas and ising models from time-dependent density-functional theory. *Physical Review E*, 65 :066112, 2002.

[38] R. Kikuchi. A theory of cooperative phenomena. *Physical Review*, 81(6) :988, Mar 1951.

[39] R. Kikuchi. Superposition approximation and natural iteration calculation in cluster-variation method. *Journal of Chemical Physics*, 60(3) :1071–1080, 1973.

[40] J. S. Langer and R. F. Sekerka. Theory of departure from local equilibrium at the interface of two-phase diffusion couple. *Acta Metallurgica*, 23 :1225–1237, 1975.

[41] F. Langmayr, P. Fratzl, G. Vogl, and W. Miekeley. Crossover from ω-phase to α-phase precipitation in bcc Ti-Mo. *Physical Review B*, 49 :11759, 1994.

[42] J. K. Lee. Coherency strain analyses via a discrete atom method. *Scripta Metallurgica et Materialia*, 32(4) :564, 1994.

[43] J. K. Lee. Elastic stress and microstructural evolution. *Materials Transactions, JIM*, 39(1) :114–132, 1998.

[44] P. H. Leo, J. S. Lowengrub, and H. J. Jou. A diffuse interface model for microstructural evolution in elastically stressed solids. *Acta Materialia*, 46(6) :2113–2130, 1997.

[45] P. H. Leo and R. F. Sekerka. The effect of elastic fields on the morphological stability of a precipitate grown from solid solution. *Acta Metallurgica*, 37(12) :3139–3149, 1989.

[46] X. Li, K. Thornton, Q. Nie, P. W. Voorhees, and J. S. Lowengrub. Two- and three-dimensional equilibrium morphology of a misfitting particle and the Gibbs-Thomson effect. *Acta Materialia*, 52 :5829–5843, 2004.

[47] I. M. Lifshitz and V. V. Slyozov. The kinetics of precipitation from supersaturated solid solutions. *Journal of Physics and Chemistry of Solids*, 19(1-2) :35–50, 1961.

[48] J. M. Liu. Dynamics of phase separation in alloys with internal elastic energy : a Monte Carlo approach. *Materials Letters*, 28 :189–195, 1996.

[49] K. Lücke and K. Deter. A quantitative theory of grain-boundary motion and recrystallization in metals in the presence of impurities. *Acta Metallurgica*, 5 :628–637, 1957.

[50] A. Maheshwari and A. J. Ardell. Morphological evolution of coherent misfitting precipitates in anisotropic elastic media. *Physical Review Letters*, 70 :2305, 1993.

[51] P. D. Merica. The age-hardening of metals. *Trans. Am. Inst. Min. Metall. Eng.*, 99 :13–54, 1932.

[52] R. Miller, E. B. Tadmor, R. Phillips, and M. Ortiz. Quasicontinuum simulation of fracture at the atomic scale. *Modelling and Simulation in Materials Science and Engineering*, 6 :607–638, 1998.

[53] R. E. Miller and E. B. Tadmor. The quasicontinuum method : Overview, applications and current directions. *Journal of Computer-Aided Materials Design*, 9 :203–239, 2002.

[54] T. Miyazaki. The role of elastic strain energy on two-phase microstructures. In D.E. Laughlin W.C. Johnson, J.M. Howe and W.A. Soffa, editors, *Solid-Solid Phase Transformations*. The Minerals, Metals and Materials Society, 1994.

[55] T. Miyazaki and M. Doi. *Materials Science and Engineering*, A110 :175, 1989.

[56] W. W. Mullins and R. F. Sekerka. Morphological stability of a particle growing by diffusion or heat flow. *Journal of Applied Physics*, 34(2) :323–329, 1963.

[57] T. Mura. *Micromechanics of Defects in Solids, 2nd edition*. Kluwer Academic, 1987.

[58] B. Mutaftschiev. *The Atomistic Nature of Crystal Growth*. Springer series in materials science, 2001.

[59] M. Nemoto, W. H. Tian, and T. Sano. Coherent precipitation strengthening by/in $L1_2$-ordered phases. *Journal de Physique III*, 1 :1099–1117, 1991.

[60] A. Onuki and A. Furukawa. Phase transitions of binary alloys with elastic inhomogeneity. *Physical Review Letters*, 86(3) :452–455, 2001.

[61] A. Onuki and H. Nishimori. Anomalously slow domain growth due to a modulus inhomogeneity in phase-separating alloys. *Physical Review B*, 43 :13649, 1991.

[62] A. Onuki and H. Nishimori. On eshelby's elastic interaction in two-phase solids. *Journal of the Physical Society of Japan*, 60(1) :1–4, 1991.

[63] D. Orlikowski, C. Sagui, A. Somoza, and C. Roland. Large-scale simulations of phase separation of elastically coherent binary alloy systems. *Physical Review B*, 59(13) :8646–8659, 1999.

[64] W. Ostwald. Studien uber die bildung und umwandlung fester korper. *Z. Phys. Chem*, 22 :289, 1897.

[65] O. Paris, F. Langmayr, G. Vogl, and P. Fratzl. A possible criterion for slowing down of precipitate coarsening due to elastic misfit interactions. *Z. Metallkd.*, 86 :860–863, 1995.

[66] D. Perez and L. J. Lewis. *submitted*, 2006.

[67] D. Perez and L. J. Lewis. *submitted*, 2006.

[68] D. Perez and L. J. Lewis. Multiscale model for microstructure evolution in multiphase materials : application to the growth of isolated inclusions in elastically homogeneous and inhomogeneous systems. *Physical Review E*, accepted for publication, 2006.

[69] N. J. Petch. *J. Iron Steel Inst.*, 174 :25, 1953.

[70] M. Plapp and J.F. Gouyet. Interface dynamics in a mean-field lattice gas model : Solute trapping, kinetic coefficient and interface mobility. *Physical Review E*, 55(5) :5321–5337, 1997.

[71] W. H. Press, S. A. Teukolsky, W. T. Vetterling, and B. P. Flannery. *Numerical Recipes in C : The Art of Scientific Computing, Second Edition.* Cambridge University Press, Cambridge, 1988.

[72] A. Chennakesava Reddy and S. Sundar Rajan. Influence of ageing, inclusions and voids on ductile fracture mechanism in commercial Al-alloys. *Bull. Mater. Sci.*, 28(1) :75–79, 2005.

[73] L. E. Reichl. *A Modern Course in Statistical Physics.* Wiley-Interscience, New York, 1998.

[74] D. Reinel and W. Dieterich. Time-dependent density functional theory in lattice gas problems. *Journal of Chemical Physics*, 104(7) :5234–5239, 1996.

[75] G. S. Rohrer, C. Lane Rohrer, and W. W. Mullins. Nucleation energy barriers for volume-conserving shape changes of crystal with nonequilibrium morphologies. *Journal of the American Ceramic Society*, 84(9) :2099–2104, 2001.

[76] G. S. Rohrer, C. Lane Rohrer, and W. W. Mullins. Coarsening of faceted crystals. *Journal of the American Ceramic Society*, 85(3) :675–682, 2002.

[77] H. J. Ryu, S. H. Hong, J. Weber, and J. H. Tundermann. Effect of elastic interaction energy on coarsening of γ' precipitates in mechanically alloyed ODS Ni-base superalloy. *Journal of Materials Science*, 34 :329–336, 1999.

[78] Y. Saad. *Iterative Methods for Sparse Linear Systems, 2dn ed.* SIAM, Philadelphia, 2003.

[79] I. Schmidt. The equilibrium shape of an elastically inhomogeneous inclusion. *Journal of the Mechanics and Physics of Solids*, 45(9) :1521–1549, 1997.

[80] I. Schmidt. Microstructural evolution in two-phase solids : morphological stability of near-periodic particle arrangements. *Computational Materials Sciencs*, 22 :333–344, 2001.

[81] I. Schmidt, R. Mueller, and D. Gross. The effect of elastic inhomogeneity on equilibrium and stability of a two particle morphology. *Mechanics of Materials*, 30 :181–196, 1998.

[82] S. Schmitt-Rink, D. S. Chemla, and D. A. B. Miller. Linear and nonlinear optical properties of semiconductor quantum wells. *Advances in Physics*, 38(2) :89–188, 1988.

[83] P. Sharma and S. Ganti. Size-dependent eshelby's tensor for embedded nano-inclusions incorporating surface/interface energies. *Journal of Applied Mechanics*, 71 :663–671, 2004.

[84] C. H. Su and P. W. Voorhees. The dynamics of precipitate evolution in elastically stressed solids — I. Inverse coarsening. *Acta Materialia*, 44(5) :1987–1999, 1995.

[85] C. H. Su and P. W. Voorhees. The dynamics of precipitate evolution in elastically stressed solids — II. Particle alignement. *Acta Materialia*, 44 :2001, 1996.

[86] N. Sukumar. Voronoi cell finite-difference method for the diffusion operator on arbitrary unstructured grids. *International Journal For Numerical Methods in Engineering*, 57 :1–34, 2003.

[87] E. B. Tadmor, R. Phillips, and M. Ortiz. Mixed atomistic and continuum models of deformation in solids. *Langmuir*, 12 :4529–4534, 1996.

[88] E.B. Tadmor, R. Miller, R. Phillips, and M. Ortiz. Nanoindentation and incipient plasticity. *Journal of Materials Research,*, 14 :2233–2250, 1999.

[89] K. Thornton, J. Agren, and P. W. Voorhees. Modelling the evolution of phase boundaries in solids at the meso- and nano-scales. *Acta Materialia*, 51 :5675–5710, 2003.

[90] K. Thornton, N. Akaiwa, and P. W. Voorhees. Dynamics of late-stage phase separation in crystalline solids. *Physical Review Letters*, 86(7) :1259–1262, 2001.

[91] K. Thornton, N. Akaiwa, and P. W. Voorhees. Large-scale simulations of ostwald ripening in elastically stressed solids : I. Development of microstructures. *Acta Materialia*, 52 :1353–1364, 2004.

[92] K. Thornton, N. Akaiwa, and P. W. Voorhees. Large-scale simulations of ostwald ripening in elastically stressed solids : II. Coarsening kinetics and particle size distribution. *Acta Materialia*, 52 :1365–1378, 2004.

[93] S. Torquato, S. Hyun, and A. Donev. Multifunctional composites : Optimizing microstructures for simultaneous transport of heat and electricity. *Physical Review Letters*, 89(26) :266601, 2002.

[94] T. Uehara and R. F. Sekerka. Phase field simulations of faceted growth for strong anisotropy of kinetic coefficient. *Journal of Crystal Growth*, 254 :251–261, 2003.

[95] H. A. van der Vorst. Bi-CGSTAB : a fast and smoothly converging variant of Bi-CG for the solution of nonsymetric linear systems. *SIAM Journal on Statistical and Scientific Computing*, 13 :631–644, 1992.

[96] P. W. Voorhees. The theory of ostwald ripening. *Journal of Statistical Physics*, 32(1/2) :231–252, 1985.

[97] P. W. Voorhees and W. C. Johnson. Development of spatial correlations during diffusional late-stage phase transformation in stressed solids. *Physical Review Letters*, 61(19) :2225–2228, 1988.

[98] P. W. Voorhees, G. B. McFadden, and G. B. Johnson. On the morphological development of second-phase particles in coherently stressed solids. *Acta Metallurgica et Materialia*, 40(11) :2979–2992, 1992.

[99] C. Wagner. *Z. Elektrochem*, 65 :581, 1961.

[100] Y. Wang and A. G. Khachaturyan. Shape instability during precipitate growth in coherent solids. *Acta Metallurgica et Materialia*, 43(5) :1837–1857, 1995.

[101] A. A. Wheeler, W. J. Boettinger, and G. B. McFadden. Phase-field model of solute trapping during solidification. *Physical Review E*, 47(3) :1893–1909, 1993.

[102] G. Wulff. *Z. Kristallogr.*, 34 :449, 1901.

[103] E. Yokoyama and R. F. Sekerka. A numerical study of the combined effect of anisotropic surface tension and interface kinetics on pattern formation during the growth of two-dimensional crystals. *Journal of Crystal Growth*, 125 :389–403, 1992.

[104] Y. S. Yoo, D. Y. Yoon, and M. F. Henry. The effect of elastic misfit strain on the morphological evolution of γ'-precipitates in a model Ni-base superalloy. *Metals and Materials*, 1(1) :47–61, 1995.

[105] S. Yoshida, M. Fukaya, and T. Miyazaki. *J. Japan Inst. Metals*, 51 :18, 1987.

[106] P. Zhang, Y. Huang, H. Gao, and K. C. Hwang. Fracture nucleation in single-wall carbon nanotubes under tension : A continuum analysis incorporating interatomic potentials. *Journal of Applied Mechanics*, 69 :454–458, 2002.

[107] J. Zhu, L. Q. Chen, and J. Shen. Morphological evolution during phase separation and coarsening with strong inhomogeneous elasticity. *Modelling and Simulation in Materials Science and Engineering*, 9 :499–511, 2001.

Annexe I

Déroulement d'un calcul TDDFT multi-échelle

Bien que les origines physiques et les équations principales du modèle multi-échelle développé dans le cadre de cette thèse aient été exposées au chapitre 4, nous avons été plutôt avares de détails sur l'implémentation pratique de celui-ci sous forme d'un programme informatique. Cette lacune sera corrigée dans la présente annexe, qui résume les grandes lignes de la procédure de simulation, ainsi que dans les annexes suivantes où seront analysées en détail chacune des étapes déterminantes du calcul.

Nous débutons donc par une présentation générale du déroulement d'une simulation. Ce dernier est illustré à la figure I.1. La simulation débute par une phase d'initialisation répondant à deux objectifs principaux, soient : 1) obtenir les valeurs des paramètres du modèle et 2) créer une représentation de l'état initial de la microstructure. La première partie consiste essentiellement en la lecture des fichiers de configuration, alors que la deuxième consiste en la création de la cellule de calcul, en la spécification des conditions aux frontières à appliquer aux limites de cette cellule, en la spécification du champ de concentration initial et, finalement, au choix des sites représentatifs (*representative sites*) requis pour représenter ce champ. La procédure utilisée pour réaliser cette dernière étape est décrite au chapitre 4.

Une fois l'initialisation terminée, on peut procéder au calcul de l'évolution de la microstructure. Cette dernière est effectuée de manière incrémentielle à l'aide d'une boucle d'intégration. Cette boucle débute par une étape d'interpolation qui permet d'obtenir la valeur des variables d'intérêt (essentiellement les déplacements et les probabilités d'occupation) en des positions où ne se trouvent aucun site représentatif. Ceci est nécessaire autant pour le calcul des activités locales que pour celui des forces élastiques. Cette tâche est effectuée à l'aide d'une procédure dite sans-maillage (*meshless*) basée sur l'analyse des voisins naturels (*natural neighbors analysis*). La description de cette procédure fera l'objet de l'annexe II.

Ensuite, on incrémente la variable de temps d'une quantité dt et on calcule le

changement subi par les probabilités d'occupation durant cet intervalle de temps. Ceci est effectué à l'aide de la version multi-échelle des équations de la TDDFT. Cette étape cruciale est décrite en détail à l'annexe III. Puisque les probabilités d'occupation des sites représentatifs ont été modifiées, on doit répéter l'étape d'interpolation effectuée au début de la boucle d'intégration avant de solutioner les équations de l'équilibre élastique à l'aide de la QCM. Cette dernière étape a pour objectif de déterminer les nouveaux déplacements moyens de manière cohérente avec les probabilités d'occupation. La méthode utilisée pour accomplir cette tâche fera l'objet de l'annexe IV.

Finalement, on doit s'assurer que l'ensemble des sites représentatifs courant est toujours en mesure de représenter de manière adéquate les champs de probabilités d'occupation et de déplacement. Au besoin, on ajoute ou on supprime des sites selon la procédure décrite au chapitre 4.

Les étapes contenues dans la boucle d'intégration sont répétées aussi souvent que nécessaire jusqu'à ce qu'un temps maximal $t_{\max}$ prescrit à l'avance soit atteint, ou que toute autre critère pertinent soit rempli.

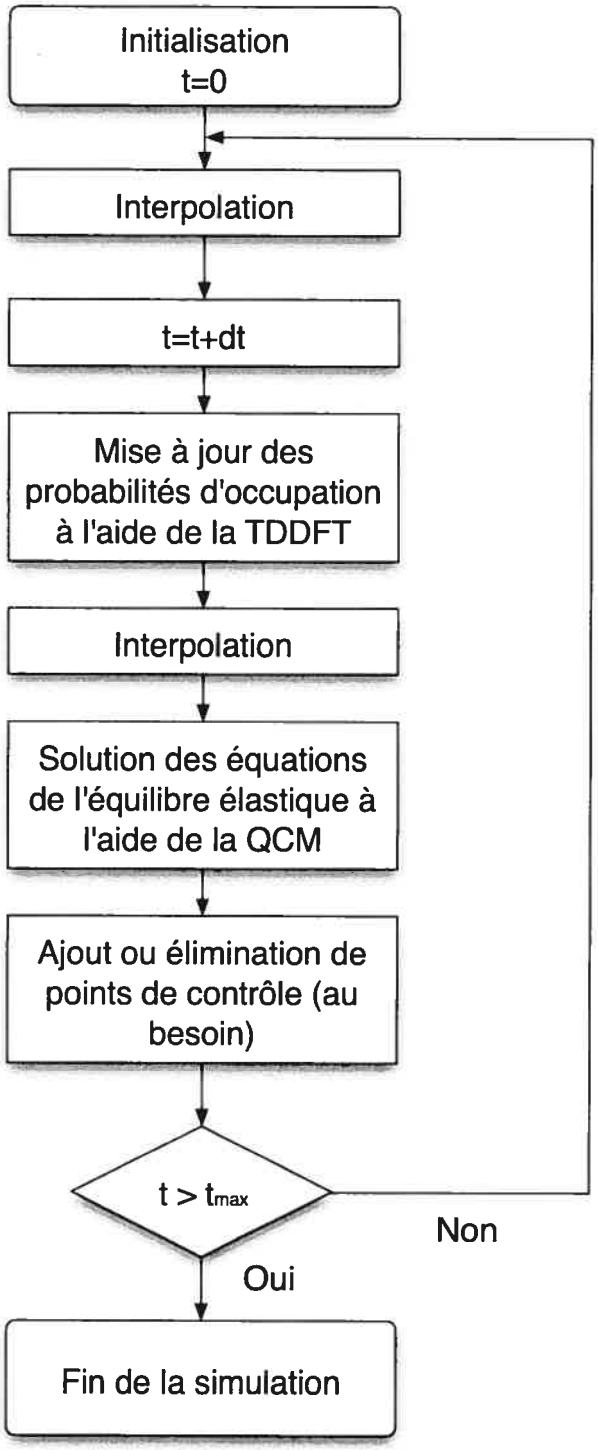

FIG. I.1 – Représentation schématique du déroulement d'une simulation TDDFT multi-échelle.

Annexe II

Interpolation des quantités physiques à partir des sites représentatifs

L'efficacité de toute méthode multi-échelle repose sur la possibilité de représenter de manière adéquate le système d'intérêt en utilisant un nombre restreint de degrés de liberté. Le choix de ces degrés de liberté ainsi que de la représentation du système en fonction de l'état de ces derniers sont donc deux étapes cruciales dans la mise au point de modèles numériques. Dans le cas qui nous occupe ici, l'objectif est de décrire l'état *global* de la microstructure en utilisant uniquement des variables *locales* définies sur un sous-ensemble de tous les sites de notre réseau. Les sites sur lesquels sont définis ces variables locales sont appelés sites représentatifs. Il s'agit donc *d'interpoler* la valeur d'une fonction à un point donné à partir de celles définies aux sites représentatifs.

D'un point de vue mathématique, le problème se résume à identifier un ensemble de fonctions de base $\phi_i(\mathbf{x})$ avec lesquelles il est possible d'approximer une fonction scalaire $f(\mathbf{x})$ à partir des valeurs u_i que prend cette fonction sur un ensemble de n points $\mathbf{x_i}$ (les sites représentatifs), i.e., nous cherchons des $\phi_i(\mathbf{x})$ tels que

$$f(\mathbf{x}) \simeq f^l(\mathbf{x}) = \sum_{i=1}^{n} f_i \phi_i(\mathbf{x}). \tag{II.1}$$

De plus, la méthode retenue doit répondre à un certain nombre de critères dans le but de faciliter la création et la mise à jour de l'ensemble des sites représentatifs :

1. La méthode doit être simple.
2. La méthode doit être robuste.
3. La méthode doit pouvoir s'accommoder d'une distribution fortement non-uniforme de sites représentatifs.
4. La méthode ne doit pas contraindre le choix des sites représentatifs en imposant une certaine symétrie dans leur distribution ou en dictant leur espacement.
5. Les fonctions $\phi_i(\mathbf{x})$ doivent avoir un support compact.

Puisque nous voulions faciliter le plus possible la gestion des sites représentatifs, nous avons décidé de nous tourner vers une méthode dite "sans-maillage" (*meshless*). L'avantage de ce type de méthode est qu'il ne requiert pas la spécification de relations entre les sites, contrairement aux méthodes basées sur des triangulations. L'ajout ou la suppression de sites représentatifs est donc extrêmement aisé. De plus, nous voulions une méthode qui n'impose pas de régularité dans la disposition des sites. Un choix logique dans ce cas est d'utiliser une méthode de type "voisins naturels" (*natural neighbors*) puisque ces méthodes prennent automatiquement en compte la densité et la position des sites représentatifs lors de l'interpolation. Notre choix final s'est donc porté sur la méthode d'interpolation de Laplace. Les propriétés de cette technique, présentée brièvement au chapitre 4, seront maintenant explorées plus en détail.

La méthode de Laplace est basée sur la tesselation de l'espace en polygones de Voronoï (ou en volumes de Voronoï en trois dimensions). Nous rappelons que le polygone de Voronoï associé à un site k, faisant partie d'un ensemble de sites $\{j\}$, contient tous les points de l'espace plus rapprochés du site k que de n'importe quel autre site dans $\{j\}$. Supposons qu'une telle tesselation soit construite en utilisant les sites représentatifs $\mathbf{x_i}$ et le point $\mathbf{x}$ auquel on désire approximer notre fonction f. Un exemple d'une telle configuration est illustré à la figure II.1. Les fonctions de base de Laplace sont alors définies comme :

$$\phi_i(\mathbf{x}) = \frac{s_i(\mathbf{x})}{\sum_{j=1}^{n} s_j(\mathbf{x})}, s_j(\mathbf{x}) = \frac{m(t_j(\mathbf{x}))}{d_j(\mathbf{x})}, \tag{II.2}$$

avec $d_j(\mathbf{x})$ la distance entre $\mathbf{x}$ et le site représentatif j et $m(t_j(\mathbf{x}))$ une mesure (longueur en 2D et aire en 3D) de la facette commune entre les polygones de Voronoï du site j et du point $\mathbf{x}$. Si les deux polygones ne possèdent pas de facette commune, alors $m(t_j(\mathbf{x})) = 0$. Nous voyons maintenant clairement le sens de l'expression "voisins naturels" : un site et un point sont des voisins naturels si et seulement si leurs polygones de Voronoï partagent une facette.

Les fonctions de base de Laplace présentent toute une gamme de propriétés très intéressantes, notamment :

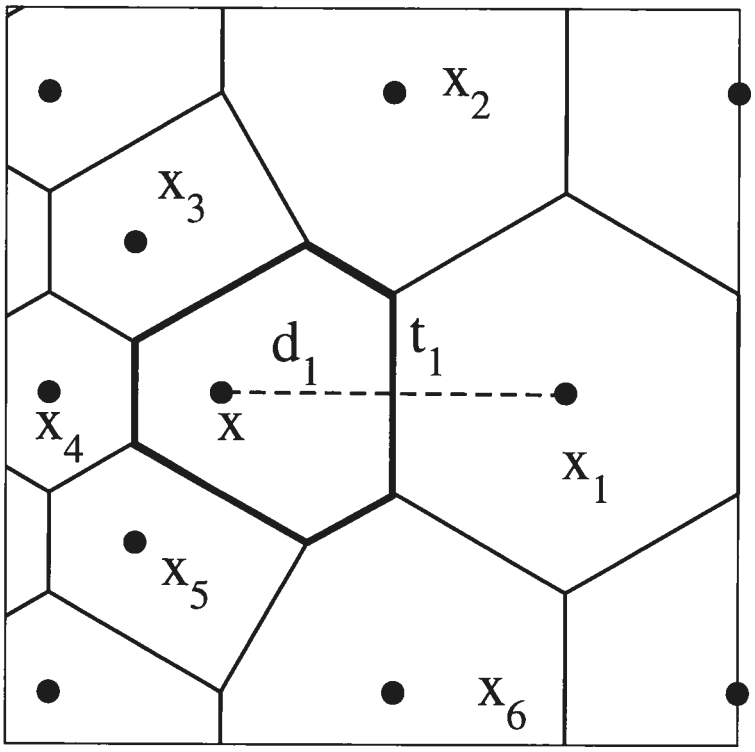

FIG. II.1 – Représentation schématique de l'interpolation de Laplace.

1. Il n'y a aucun paramètre libre dans la formulation des fonctions de base.
2. Le formalisme peut traiter n'importe quelle distribution de sites représentatifs.
3. Les fonctions de base forment une base linéairement complète :

$$\mathbf{x} = \sum_{i=1}^{n} \phi_i(\mathbf{x})\mathbf{x_i}. \tag{II.3}$$

4. Les fonctions de base possèdent un support compact car elles sont non-nulles uniquement dans leur voisinage naturel. Ceci facilite beaucoup la solution nu-

mérique de systèmes d'équations impliquant les valeurs interpolées en rendant le problème local et donc les matrices jacobiennes éparses.

Une fois les fonctions de base $\phi_i(\mathbf{x})$ obtenues, la valeur de la fonction $f^l(\mathbf{x})$ peut être calculée à partir de l'équation II.1. Tel que mentionné plus tôt, nous utilisons cette technique à chaque fois que la valeur de la probabilité d'occupation ou du déplacement est requise sur un site non-représentatif. Cette technique d'interpolation nous permet donc de reconstruire l'état microscopique du système en utilisant un nombre restreint de degrés de liberté.

Bien qu'appropriée pour l'usage que nous en faisons ici, l'interpolation de Laplace souffre de quelques inconvénients. Premièrement, comme avec toutes les méthodes sans-maillage, il est difficile d'imposer des conditions aux frontières essentielles (contraintes sur la valeur de la fonction ou de sa dérivée) sur les fonctions interpolées. Deuxièmement, il n'existe pas de méthode efficace pour intégrer les fonctions interpolées avec une grande précision à faible coût numérique. L'interpolation de Laplace est donc plus appropriée lorsque utilisée en conjonction avec des méthodes de collocation.

Annexe III

Évolution des probabilités d'occupation à l'aide de la TDDFT

Une fois la représentation du système obtenue à l'aide des sites représentatifs et de la méthode d'interpolation décrite à l'annexe II, nous pouvons nous attaquer à la question cruciale de l'évolution de cette représentation en fonction du temps. Dans la présente annexe, nous nous limiterons aux équations de la TDDFT ; le cas des équations de l'équilibre élastique sera traité à l'annexe IV. Le problème se pose en deux temps : premièrement, nous devons obtenir un système d'équations décrivant l'évolution des probabilités d'occupation des sites représentatifs, alors que la formulation standard de la TDDFT n'offre la solution que lorsque tous les sites du réseau sont représentatifs et, deuxièmement, nous devons établir la procédure optimale pour intégrer ce système d'équations.

III.1 Formulation multi-échelle de la TDDFT

Tel que démontré au chapitre 4, dans le cas où tous les sites du réseau sont considérés comme représentatifs, les équations de la TDDFT sont de la forme :

$$\frac{dp_i^\alpha}{dt} = \sum_{j \in nn(i)} M_{i,j}(t)[\mathcal{A}_j^\alpha(t) - \mathcal{A}_i^\alpha(t)], \tag{III.1}$$

avec une mobilité $M_{i,j(t)} = \langle p_i^{\text{vacancy}}(t) p_j^{\text{vacancy}}(t) \rangle_t \simeq p_i^{\text{vacancy}}(t) p_j^{\text{vacancy}}(t)$ et des activités $\mathcal{A}_i^\alpha(t) = e^{\mu_i^\alpha(t)/k_B T}$. La sommation dans l'équation précédente est effectuée sur tous les premiers voisins du site i. Cette équation stipule que le flux de probabilité entre les sites i et j est proportionnel à la différence d'activité entre ces sites. Notons que le flux de probabilité du site i vers le site j est égal en valeur absolue mais de signe opposé au flux de probabilité du site j vers le site i. On a donc conservation des probabilités totales.

Dans le cadre de la formulation multi-échelle, le problème se pose comme suit : obtenir une équation pour le changement moyen de probabilité d'occupation dans les régions associées à chacun des sites représentatifs. Pour atteindre cet objectif,

nous devons d'abord définir ce que nous entendons par "régions". Puisque nous avons insisté pour ne pas imposer de contraintes au choix des sites représentatifs, il n'est pas possible de partitionner l'espace en régions associées à chacun des sites représentatifs de manière régulière. Par contre, nous avons décrit à l'annexe II une méthode permettant de réaliser une telle partition de manière robuste pour une distribution quelconque de sites représentatifs : la tesselation de Voronoï. Dans ce cadre, la région d'un site représentatif donné contient l'ensemble des sites du réseau situé à l'intérieur du polygone de Voronoï de ce site représentatif. Il suffit maintenant de dériver une expression des flux de probabilité entrant dans chaque région ou en sortant pour obtenir un équivalent multi-échelle à l'équation III.1.

Encore une fois, le concept de voisinage naturel intervient de manière déterminante. En effet, étant donné la définition de la région associée à chaque site représentatif, deux régions ne peuvent échanger de flux de probabilité que si elles partagent une facette commune, i.e., deux sites représentatifs n'échangent des flux de probabilité que si ces derniers sont des voisins naturels. La valeur de ces flux peut être obtenue de manière intuitive. Premièrement, d'après l'équation III.1, le flux total entre deux régions doit être proportionnel à la différence d'activité entre les deux sites représentatifs concernés. Par contre, pour une différence d'activité donnée, le flux devrait être inversement proportionnel à la distance entre les sites représentatifs puisque l'efficacité de la diffusion devrait être proportionnelle au *gradient d'activité*. Finalement, le flux total traversant une facette devrait être proportionnel à une certaine mesure de cette facette. Dans notre cadre discret, la mesure appropriée est le nombre de canaux de diffusion traversant la facette, i.e., le nombre de trajectoires entre sites voisins qui intersectent la facette. À partir de ces arguments, on obtient l'équation recherchée :

$$\frac{dp_i^\alpha}{dt} = \sum_{j \in nn(i)} M_{i,j}(t)[\mathcal{A}_j^\alpha(t) - \mathcal{A}_i^\alpha(t)]\frac{b_{i,j}}{d_{i,j}N_i}, \tag{III.2}$$

où $b_{i,j}$ est le nombre de canaux de diffusion traversant la facette entre les sites représentatifs i et j, $d_{i,j}$ est la distance entre les sites représentatifs i et j (mesurée en paramètres de maille) et N_i est le nombre de sites du réseau qui se trouvent

à l'intérieur du polygone de Voronoï du site i. Si tous les sites du réseau sont considérés comme représentatifs, on a $d_{i,j} = 1, N_i = 1, b_{i,j} = 1$, et on retrouve exactement l'équation standard de la TDDFT (Éq. III.1).

Cette équation, obtenue ici de manière intuitive, peut en fait être dérivée de manière rigoureuse à l'aide de la méthode des volumes finis, appliquée à la diffusion sur des grilles non-structurées. Pour les détails mathématiques, le lecteur intéressé peut consulter les références [18, 86].

III.2 Intégration des équations de la TDDFT

Maintenant que le système d'équations différentielles correspondant à la formulation multi-échelle de la TDDFT est disponible, nous devons déterminer la méthode optimale pour le résoudre. Dans l'intérêt de la concision, nous utiliserons, dans ce qui suit, une forme compacte du système d'équations formé à l'aide de la relation III.2. Sous forme vectorielle, cette équation prend la forme :

$$\dot{\mathbf{p}} = f(\mathbf{p}) \tag{III.3}$$

où $\mathbf{p} = \{p_i^\alpha\}$ est un vecteur contenant l'ensemble des probabilités d'occupation des sites représentatifs.

L'intégration de ce système d'équation s'est avérée beaucoup plus coriace que prévu. En effet, nous nous sommes rapidement rendu compte que les méthodes usuelles était intolérablement inefficaces pour résoudre ce problème. Par exemple, en utilisant la méthode de Euler-avant

$$\mathbf{p}(t + dt) = \mathbf{p}(t) + f(\mathbf{p}(t))dt, \tag{III.4}$$

l'intégration devenait instable alors que les composantes maximales de $f(\mathbf{p})dt$ atteignaient à peine 10^{-6}, ce qui implique environ un million de pas pour qu'un site passe de l'état $p_i^A \simeq 1, p_i^B \simeq 0$ à l'état $p_i^A \simeq 0, p_i^B \simeq 1$! La situation est semblable pour toutes les autres méthodes explicites testées (Runge-Kutta, Adam-Bashford, etc.). Ceci est un symptôme connu d'un système d'équations rigide (*stiff*). Les systèmes rigides sont caractérisés par un vaste éventail d'échelles de temps carac-

téristiques. Le problème provient du fait que les méthodes explicites (qui utilisent seulement l'état passé du système pour extrapoler son état futur) sont limitées par les échelles de temps longues au chapitre de la précision mais par les échelles de temps courtes au niveau de la stabilité, ce qui fait en sorte que même des solutions en apparence très lisses à l'échelle de dt deviennent instables.

III.2.1 Intégration implicite

Le remède à ce problème consiste à utiliser des méthodes dites implicites. Le prototype de cette classe de méthode est la méthode de Euler-arrière :

$$\mathbf{p}(t+dt) = \mathbf{p}(t) + f(\mathbf{p}(t+dt))dt. \tag{III.5}$$

Cette dernière possède l'avantage considérable d'être *inconditionnellement stable*, peu importe le pas de temps dt. Par contre, elle possède aussi l'inconvénient considérable de demander la solution d'un système d'équations non-linéaires à chaque pas de temps ! Cette demande complexifie de manière importante l'implémentation de la méthode. C'est par contre le prix à payer pour atteindre une efficacité raisonnable.

III.2.2 Solution du problème non-linéaire : Méthode de Newton

Pour résoudre l'équation III.5 on a recours à une variante de la méthode de Newton où le système d'équations non-linéaires est résolu itérativement à l'aide d'une version linéarisée du problème. En effet, au premier ordre, on a :

$$f(\mathbf{p}(t+dt)) = f(\mathbf{p}(t)) + \bar{J}(\mathbf{p}(t)) \cdot [\mathbf{p}(t+dt) - \mathbf{p}(t)] + O([\mathbf{p}(t+dt) - \mathbf{p}(t)]^2), \tag{III.6}$$

avec $\bar{J}$ la matrice Jacobienne telle que :

$$\bar{J}(\mathbf{p})|_{i,j} \equiv \frac{\partial f_i(\mathbf{p})}{\partial \mathbf{p}_j}. \tag{III.7}$$

À l'itération m de la méthode de Newton, la solution approximative $\mathbf{p}^{m+1}(t+dt)$

est donnée par :

$$\mathbf{p}^{m+1}(t+dt) = \mathbf{p}(t) + f(\mathbf{p}^m(t+dt))dt + \bar{J}(\mathbf{p}^m(t+dt)) \cdot [\mathbf{p}^{m+1}(t+dt) - \mathbf{p}^m(t+dr)]. \tag{III.8}$$

Quand la convergence sera atteinte, on aura $\mathbf{p}^{m+1}(t+dt) = \mathbf{p}^m(t+dt)$, et l'équation précédente devient équivalente à l'équation III.5.

En pratique, on résout plutôt l'équation sous la forme suivante :

$$[1 - \bar{J}(\mathbf{p}^m(t+dt))dt] \cdot [\mathbf{p}^{m+1}(t+dt) - \mathbf{p}^m(t+dt)] = \mathbf{p}(t) - \mathbf{p}^m(t+dt) + f(\mathbf{p}^m(t+dt))dt. \tag{III.9}$$

Cette dernière équation n'est en fait qu'un simple système linéaire du type $\bar{A}\mathbf{x} = \mathbf{b}$.

L'intégration par la méthode de Euler-arrière se déroule donc de la manière suivante :

1. On estime $\mathbf{p}^0(t+dt)$ à l'aide d'un prédicteur.
2. On résout pour $[\mathbf{p}^{m+1}(t+dt) - \mathbf{p}^m(t+dt)]$ à l'aide de l'équation III.9.
3. Si $||[\mathbf{p}^{m+1}(t+dt) - \mathbf{p}^m(t+dt)]||$ est plus petit qu'un certain seuil, la convergence est atteinte et on a $\mathbf{p}(t+dt) = \mathbf{p}^{m+1}(t+dt)$. Sinon, on incrémente m et on retourne à l'étape 2.

On ne saurait sous-estimer l'importance de l'étape 1 ci-haut. En effet, comme la méthode de Newton repose sur la linéarisation d'un problème non-linéaire, il faut que l'approximation soit suffisamment bonne pour ne pas compromettre la convergence. Dans notre implémentation, le prédicteur utilise une extrapolation polynomiale d'ordre 5 construite à partir de l'histoire récente de $\mathbf{p}(t)$. De plus, nous utilisons une stratégie dite de convergence globale pour assurer que la solution approximative $\mathbf{p}^m(t+dt)$ s'améliore à chaque itération. Une description plus complète de cette stratégie peut être obtenue en consultant la référence [14].

III.2.3 Améliorer la précision : Algorithmes multi-pas

Dans le but de rendre la plus limpide possible la discussion précédente, nous avons présenté une dérivation basée sur la méthode de Euler. Cependant, bien que

d'une robustesse inégalée, cette méthode possède une précision qui laisse quelque peu à désirer. En effet, l'équation III.5 montre que la méthode de Euler approxime la fonction $f(\mathbf{p})$ comme une constante sur l'intervalle $[t, t+dt]$; une erreur est donc commise si $\mathbf{p}(t)$ n'est pas linéaire. On peut améliorer la situation en approximant plutôt $f(\mathbf{p})$ par un polynôme d'ordre supérieur à 1. On a alors :

$$\begin{aligned}\mathbf{p}(t+dt) &= \mathbf{p}(t) + dt[\alpha_0 f(\mathbf{p}(t+dt)) + \alpha_1 f(\mathbf{p}(t)) \\ &\quad +\alpha_2 f(\mathbf{p}(t-dt)) + ... + \alpha_l f(\mathbf{p}(t-(l-1)dt))] \qquad \text{(III.10)}\end{aligned}$$

où $\alpha_0 = 0$ indique une méthode explicite. En décomposant les $f(\mathbf{p})$ à l'aide de la méthode des différences finies, on obtient une formulation équivalente en terme des $\mathbf{p}$, i.e.,

$$\begin{aligned}\mathbf{p}(t+dt) &= \mathbf{p}(t) + dt[\beta_0 \mathbf{p}(t+dt) + \beta_1 \mathbf{p}(t) \\ &\quad +\beta_2 \mathbf{p}(t-dt) + ... + \beta_l \mathbf{p}(t-(l-1)dt)]. \qquad \text{(III.11)}\end{aligned}$$

Cette dernière équation est la formulation générale d'une méthode multi-pas (*multistep*), les méthodes particulières correspondant à différents choix des coéfficients β. Dans le cadre de notre implémentation de la TDDFT, nous utilisons une variante spécialement conçue pour posséder une stabilité accrue, la méthode BDF (*Backward Differentiation Formula*) d'ordre 5 développée par Gear [24]. Ce choix particulier correspond à $\beta_0 = 60/137, \beta_1 = 300/137, \beta_2 = -300/137, \beta_3 = 200/137, \beta_4 = -75/137$ et $\beta_5 = 12/137$. Notons qu'au point de vue de l'implémentation, une méthode multi-pas se traite de manière identique à la méthode de Euler ; on se contente simplement d'ajouter les termes appropriés au côté droit de l'équation III.9. Il faut cependant aussi prévoir du stockage supplémentaire puisque l'état du système à plusieurs temps précédents est requis. La gestion du pas de temps est aussi plus complexe avec les algorithmes multi-pas, mais cela pose un problème essentiellement technique.

III.2.4 Solution du problème linéaire : Méthode de Krylov

Nous avons vu que la méthode de Newton réduit la solution d'un système d'équations non-linéaires à une séquence de problèmes linéaires, rendant ainsi le problème plus facilement soluble. Par contre, nous n'avons pas explicité la manière de résoudre ce problème simplifié. En effet, la solution de gros problèmes linéaires (nous avons typiquement de l'ordre de 10^6 degrés de liberté dans un calcul TDDFT) reste un défi de taille puisque les méthodes directes pour résoudre un système de N équations requièrent un nombre d'opérations proportionnel à N^3, ce qui rend leur utilisation impossible ici. Par contre, tel que mentionné à l'annexe II, les fonctions de base de Laplace utilisées pour représenter le champ de concentration possèdent un support fini. Ceci implique que la matrice Jacobienne $\bar{J}$ introduite plus haut est fortement éparse (contient une proportion très faible d'éléments non-nuls). En effet, l'activité dans une région ne peut être affectée que par les probabilités d'occupation dans le voisinage naturel de cette région. À partir de l'équation III.2, on voit que cela implique que le flux de diffusion entre deux régions ne peut être affecté que par les probabilités d'occupation des sites représentatifs situés dans les voisinages naturels de ces deux sites, ou, autrement dit, un élément i, j du Jacobien n'est non-nul que si i et j possèdent un voisin naturel commun. Une colonne du Jacobien ne contiendra donc en moyenne que quelques dizaines d'éléments non-nuls sur un total de quelques centaines de milliers. Dans ce cas, il existe une classe de méthodes qui permet de tirer profit de cette propriété pour solutionner approximativement le système d'équations en utilisant seulement de l'ordre de N opérations. Ces dernières sont connues sous le vocable de méthodes de Krylov.

Les méthodes de Krylov forment un cas particulier des méthodes dites projectives où la solution approximative $\mathbf{x}_m$ d'un système linéaire $\bar{A}\mathbf{x} = \mathbf{b}$ est obtenue à l'intérieur d'un sous-espace $\mathcal{K}_m$ de dimension m en imposant la condition de Petrov-Galerkin :

$$\mathbf{b} - \bar{A}\mathbf{x}_m \perp \mathcal{L}_m, \tag{III.12}$$

où $\mathcal{L}_m$ est un autre sous-espace de dimension m. Dans le cadre des méthodes de

Krylov, le sous-espace $\mathcal{K}_m$ utilisé est le sous-espace de Krylov :

$$\mathcal{K}_m(\bar{A}, \mathbf{v}_1) = span\{\mathbf{v}_1, \bar{A}\mathbf{v}_1, \bar{A}^2\mathbf{v}_1, ..., \bar{A}^{m-1}\mathbf{v}_1\} \tag{III.13}$$

alors que différents choix du sous-espace $\mathcal{L}_m$ correspondent aux différents algorithmes de cette classe de méthodes. Pour intégrer les équations de la TDDFT, nous avons recours à un algorithme du type gradient biconjugué, approprié aux matrices $\bar{A}$ non-symétriques. Dans ce cas, on a

$$\mathcal{L}_m(\bar{A}^T, \mathbf{w}_1) = span\{\mathbf{w}_1, \bar{A}^T\mathbf{w}_1, (\bar{A}^T)^2\mathbf{w}_1, ..., (\bar{A}^T)^{m-1}\mathbf{w}_1\}. \tag{III.14}$$

On utilise habituellement $\mathbf{v}_1 = \mathbf{r}_0/|\mathbf{r}_0|$, le résidu initial $\mathbf{r}_0 = \bar{A}\mathbf{x}_0 - \mathbf{b}$ étant donné une solution approximative $\mathbf{x}_0$, et $\mathbf{w}_1$ quelconque mais tel que $\mathbf{w}_1 \cdot \mathbf{v}_1 \neq 0$. Pour un énoncé détaillé de l'algorithme numérique utilisé, ainsi que pour une introduction générale aux méthodes de Krylov, on peut consulter Saad [78].

Les méthodes de Krylov possèdent deux avantages de taille : premièrement, elles sont économes en opérations mathématiques, ne requiérant que des produits matrice-vecteur [$O(N)$ pour des matrices éparses] et des produits scalaires [$O(N)$] ; deuxièmement, bien que formellement exactes seulement pour $m = N$, elle procurent des solutions de très bonne qualité pour m relativement petit ($m \sim 100$). Puisque les algorithmes d'intégration sont de toute manière approximatifs, il est inutile de solutioner les problèmes linéaires avec une précision supérieure à celle de ces derniers. La combinaison des méthodes de Newton et de Krylov offre donc un outil extrêmement puissant pour l'intégration de systèmes d'équations différentielles de très grande taille. Il faut par contre souligner que les méthodes de Newton-Krylov ne se laissent pas dominer facilement. En effet, étant donné leur caractère itératif, elles souffrent fréquemment de problèmes de convergence qui ne se règlent qu'au prix de longues heures d'essais et erreurs. Il faut donc s'armer de patience avant de s'attaquer à leur implémentation. Tout compte fait, le jeu en vaut la chandelle !

Annexe IV

Solution multi-échelle des équations de l'équilibre élastique à l'aide de la QCM

Étant donné le rôle primordial des effets élastiques dans notre étude, il est essentiel de recourir à une méthode fiable, mais flexible, pour résoudre les équations de l'équilibre élastique. En guise de rappel, il s'agit de résoudre l'équation

$$\frac{d}{d\mathbf{r}}E(\mathbf{p},\mathbf{r}) = 0 \tag{IV.1}$$

où l'énergie totale du système E se décompose en une somme sur tous les sites du réseau :

$$E(\mathbf{p},\mathbf{r}) = \sum_{i}^{N_{tot}} E_i(\mathbf{p},\mathbf{r}) = \frac{1}{2}\sum_{i,j\in nn(i),\alpha,\beta} V_{i,j}^{\alpha,\beta}(r_{i,j})p_i^{\alpha}p_j^{\beta} \tag{IV.2}$$

avec, dans notre cas,

$$V_{i,j}^{\alpha,\beta}(r_{i,j}) = k^{\alpha,\beta}(r_{i,j} - \sigma^{\alpha,\beta})^2 - \epsilon^{\alpha,\beta}. \tag{IV.3}$$

Cependant, la résolution directe, à l'aide de la statique moléculaire, par exemple, est hors de question puisque la cellule de simulation peut contenir des millions de sites de réseau.

Afin de s'intégrer facilement dans notre approche TDDFT multi-échelle, les méthodes candidates doivent impérativement :

1. Admettre une formulation multi-échelle.
2. Être formulées strictement en terme de potentiels interatomiques.

La méthode tout indiquée pour accomplir cette tâche est la méthode du quasi-continuum (*quasicontinuum method* ou *QCM*) de Tadmor et collaborateurs [53, 87].

IV.1 La méthode QCM

L'objectif de la méthode QCM est de formuler le problème de l'équilibre élastique en termes microscopiques tout en tirant profit, comme dans les approches

continues, du fait que le champ de déplacement varie parfois assez lentement pour que la résolution atomique ne soit pas absolument requise. La QCM atteint cet objectif en deux étapes :

1. Décrire le champ de déplacement à tous les sites du réseau (ou, de manière équivalente, le vecteur des positions moyennes $\mathbf{r}$) en utilisant un nombre réduit de degrés de liberté.
2. Calculer, de manière efficace, l'énergie totale (équation IV.2) en évitant la sommation sur tous les sites du réseau.

La première étape s'effectue en construisant une représentation basée sur un nombre réduit, $N_{rep} < N_{tot}$, de sites représentatifs. La QCM originale atteint cet objectif en ne traitant comme variable libre que la valeur des positions des sites représentatifs et en utilisant les fonctions d'interpolation de premier ordre des éléments finis pour obtenir les positions moyennes sur des sites non-représentatifs. Cela suppose évidemment que la densité de sites représentatifs soit suffisante pour construire une représentation fiable de la solution microscopique exacte.

L'équation IV.2 devient alors :

$$E(\mathbf{p}, \mathbf{r}) \simeq E^h(\mathbf{p}, \mathbf{r^h}) = \sum_i^{N_{tot}} E_i(\mathbf{p}, \mathbf{r^h}) \tag{IV.4}$$

où $\mathbf{r^h}$ est le vecteur des positions moyennes des sites représentatifs. Même avec le nombre réduit de degrés de liberté utilisés pour décrire l'état mécanique de l'échantillon, la sommation de l'équation IV.4 est toujours extrêmement coûteuse en terme de calculs car elle contient des contributions provenant de chaque site du réseau.

La deuxième étape consiste à approximer efficacement la valeur de cette sommation. Plusieurs avenues ont été proposées pour atteindre cet objectif. Dans la présente étude, nous avons adopté la formulation non-locale basée sur l'énergie (*non-local energy-based formulation*). Dans le cadre de cette approximation, la sommation sur tous les sites du réseau est remplacée par une sommation sur les sites représentatifs ou, plutôt, sur les régions associées à chaque site représentatif. En effet, on peut considérer que l'énergie du site représentatif correspond en fait à l'éner-

gie moyenne des sites se trouvant à l'intérieur de sa région d'influence. L'énergie devient alors :

$$E(\mathbf{p},\mathbf{r}) \simeq E^{h'}(\mathbf{p},\mathbf{r^h}) = \sum_{i}^{N_{rep}} w_i E_i(\mathbf{p},\mathbf{r^h}) \tag{IV.5}$$

où w_i est un poids associé à la région du site représentatif i. Puisque E_i est l'énergie d'un seul site du réseau, on doit avoir

$$\sum_{i}^{N_{rep}} w_i = N_{tot}. \tag{IV.6}$$

Au premier ordre, w_i peut donc être considéré comme le nombre de sites du réseau contenu dans la région associée au site représentatif i.

À l'aide de la QCM, nous avons donc transformé un problème non-linéaire de taille N_{tot} (équation IV.1) en un problème de taille N_{rep}

$$\frac{d}{d\mathbf{r^h}} E^{h'}(\mathbf{p},\mathbf{r^h}) = 0. \tag{IV.7}$$

IV.2 Particularités de notre implémentation

IV.2.1 Interpolation

Tel que mentionné à l'annexe II, nous avons préféré la méthode d'interpolation de Laplace à celle des bases linéaires des éléments finis. Ce choix ne cause aucune complication particulière au niveau de l'implémentation de la QCM. Il permet toutefois d'utiliser un formalisme unifié entre le traitement des probabilités d'occupation à l'aide de la TDDFT et celui des positions moyennes à l'aide de la QCM. En effet, la région associée à chaque site pour le calcul en volumes finis des équations de la TDDFT est la même que celle utilisée pour la QCM. Cela permet donc de réutiliser la tessellation de Voronoï ainsi que le calcul des fonctions de base de Laplace.

IV.2.2 Solution du problème non-linéaire

Comme dans le cas de la TDDFT discuté à l'annexe III, il nous faut maintenant résoudre le problème non-linéaire de l'équation IV.7 pour déterminer les valeurs de

$\mathbf{r^h}$ (et donc de $\mathbf{r}$) requises pour l'évaluation des activités. Plusieurs approches sont possibles puisqu'il s'agit en fait d'un "simple" problème de minimisation de fonction. On peut donc avoir recours à des méthodes bien connues de type gradient conjugué [71]. Nous avons plutôt décidé de capitaliser sur l'infrastructure déjà implémentée pour intégrer les équations de la TDDFT et donc de recourir de nouveau à la méthode de Krylov. Dans ce cas, on reformule le problème de la manière suivante : autour d'une solution $\mathbf{r_0^h}$ de l'équation IV.7, la fonction $E^{h'}$ admet le développement

$$E^{h'}(\mathbf{p}, \mathbf{r_0^h} + \mathbf{dr^h}) \simeq E^{h'}(\mathbf{p}, \mathbf{r_0^h}) - \mathbf{F}^{h'}(\mathbf{p}, \mathbf{r_0^h} + \mathbf{dr^h}) \cdot \mathbf{dr^h} + [\bar{H}^{h'}(\mathbf{p}, \mathbf{r_0^h} + \mathbf{dr^h}) \cdot \mathbf{dr^h}] \cdot \mathbf{dr^h}, \tag{IV.8}$$

avec

$$\mathbf{F}^{h'}(\mathbf{p}, \mathbf{r^h})|_i = -\frac{\partial E^{h'}(\mathbf{p}, \mathbf{r^h})}{\partial r^h{}_i} \tag{IV.9}$$

une force généralisée et

$$\bar{H}^{h'}(\mathbf{p}, \mathbf{r})|_{i,j} = \frac{\partial^2 E^{h'}(\mathbf{p}, \mathbf{r^h})}{\partial r_i^h \partial r_j^h} \tag{IV.10}$$

une matrice Hessienne généralisée. À partir d'un état quelconque $\mathbf{r_0^h} + \mathbf{dr^h}$ on peut donc atteindre $\mathbf{r_0^h}$ en résolvant le système linéaire

$$\bar{H}(\mathbf{p}, \mathbf{r_0^h} + \mathbf{dr^h}) \cdot \mathbf{dr^h} = \mathbf{F}^{h'}(\mathbf{p}, \mathbf{r_0^h} + \mathbf{dr^h}) \tag{IV.11}$$

pour $\mathbf{dr^h}$. Cette dernière étape est réalisée à l'aide de l'algorithme du gradient biconjugué présenté brièvement à l'annexe III.

Puisqu'une certaine erreur est commise à travers l'approximation IV.8 lorsque $|\mathbf{dr^h}|$ ne tend pas vers 0, il est possible qu'on doive itérer à quelques reprises en posant $[\mathbf{r_0^h}]^\mathbf{m} + [\mathbf{dr^h}]^\mathbf{m} = [\mathbf{r_0^h}]^{\mathbf{m-1}} - [\mathbf{dr^h}]^{\mathbf{m-1}}$ et en resolutionnant l'équation IV.11 pour $[\mathbf{dr^h}]^\mathbf{m}$. Cependant, ceci n'est nécessaire que lors de la relaxation initiale du système, lorsque notre estimé pour $\mathbf{r_0^h}$ est de très mauvaise qualité. Par contre, à l'intérieur de la boucle d'intégration, la valeur de $\mathbf{r_0^h}$ au pas de temps précédent procure un excellent point de départ, et la convergence est normalement atteinte en une seule itération.

Cette méthode peut paraître inutilement complexe étant donné que des tech-

niques comme le gradient conjugué ne requièrent que le calcul des forces généralisées pour solutionner le problème. Le gradient conjugué requiert, par contre, un grand nombre de calculs de force et d'énergie pour atteindre son but, alors que notre méthode n'a habituellement besoin que d'un seul calcul de force et d'un calcul de la Hessienne. Puisque la Hessienne est extrêmement éparse, le coût associé à sa construction est du même ordre que celui d'un calcul de force. La méthode de Krylov transfert l'effort numérique du calcul des forces, généralement fortement sous-optimal, vers le calcul de produits matrice-vecteur ou de produits scalaires qui peuvent être implémentés de manière très efficace.

Annexe V

L'avenir de la TDDFT

La présente étude démontre l'utilité de la TDDFT lorsque appliquée à l'évolution microstructurale de systèmes multiphase. Cependant, la méthode est encore loin d'avoir révélé son plein potentiel. En effet, bien qu'elle repose sur une base théorique solide, sa précision est limitée par la disponibilité de fonctionnelles d'énergie libre de qualité. Même si, dans sa forme actuelle, elle se compare avantageusement aux méthodes de type *phase-field*, la TDDFT ne pourra vraisemblablement s'imposer comme un substitut aux méthodes de simulation microscopiques conventionnelles, telle le Monte Carlo cinétique, tant que des méthodes générales pour obtenir et améliorer les fonctionnelles ne seront pas disponibles. En effet, certains problèmes comme, par exemple, ceux impliquant des phases ordonnées, ne peuvent être traités de manière satisfaisante à l'aide de la fonctionnelle de Bragg-Williams. Le traitement de l'élasticité se doit aussi d'être amélioré pour permettre un accord quantitatif avec les calculs Monte Carlo. Le but de cette dernière annexe est de proposer des pistes de solution qui permetteront d'atteindre ces objectifs et ainsi d'étendre les possibilités de la TDDFT.

V.1 Fonctionnelles d'énergie libre

Tel que l'indique son nom, l'applicabilité de la TDDFT repose sur la disponibilité d'une fonctionnelle d'énergie libre. Comme on l'a vu au chapitre 4, la dite fonctionnelle se doit d'être uniquement fonction de $\mathbf{p} = \{p_i^\alpha\}$, l'ensemble des probabilités d'occupation de chaque site du réseau. L'approche la plus simple est donc de construire une fonctionnelle n'impliquant aucune référence aux fonctions de corrélation d'ordre supérieur, comme, par exemple, les fonctions de corrélation à deux sites $p_{i,j}^{\alpha,\beta}$ correspondant à la probabilité d'observer à la fois un atome de type α au site i et, *simultanément,* un atome de type β au site j. Dans ce cas, on obtient la

fonctionnelle de Bragg-Williams utilisée au cours de la présente étude :

$$F(\mathbf{p}) = \frac{1}{2} \sum_{i,j \in nn(i),\alpha,\beta} V_{i,j}^{\alpha,\beta} p_i^\alpha p_j^\beta + k_B T \sum_{i,\alpha} p_i^\alpha \ln p_i^\alpha. \tag{V.1}$$

Par contre, rien n'interdit, l'utilisation de fonctionnelles plus précises tenant implicitement compte des corrélations.

V.1.1 La méthode variationnelle par amas

À cet effet, nous proposons l'utilisation de la méthode variationnelle par amas (*cluster variation method* ou CVM) de Kikuchi [38]. Cette technique est basée sur un calcul variationnel de la matrice de densité ρ. Cette dernière peut en effet être obtenue en minimisant le potentiel thermodynamique approprié, comme par exemple, dans l'ensemble canonique,

$$\rho \ni F(\rho) = \min_{\{\rho_t\}} F(\rho_t). \tag{V.2}$$

où

$$F(\rho) = \mathrm{tr}[H\rho] + k_B T \mathrm{tr}[\rho \ln \rho] \tag{V.3}$$

avec H est l'Hamiltonien du système et $\{\rho_t\}$ représente l'ensemble des matrices de densité physiquement possibles. Cependant, cette relation n'est pas utilisable directement, car la matrice de densité est gigantesque (sa dimension est égale au nombre d'états possibles dans le système). La première étape de la méthode est donc d'exprimer l'équation V.3 sous une forme plus simple à l'aide d'une expansion des cumulants. Pour ce faire, nous devons introduire la notion de matrice de densité réduite. Comme leur nom l'indique, les matrices de densité réduites sont obtenues à partir de la matrice de densité totale en utilisant successivement des opérations de trace pour éliminer certains degrés de liberté. De manière générale, une matrice réduite d'ordre n s'obtient à partir d'une matrice d'ordre $n+1$ par une relation du type :

$$\rho^{(n)}(1,2,...,n) = \mathrm{tr}\rho^{(n+1)}(1,2,...,n,n+1), \tag{V.4}$$

avec, comme cas particulier :

$$\mathrm{tr}\rho^{(1)}(i) = 1. \tag{V.5}$$

Ici, les nombres entre parenthèse représentent les indices des degrés de liberté concernés (les différents sites du réseau par exemple). À chacune de ces matrices, on associe successivement une fonction d'amas $G^{(n)}$ et des fonctions de cumulant $g^{(n)}$:

$$G^{(1)}(i) = \mathrm{tr}[\rho^{(1)}(i) \ln \rho^{(1)}(i)] = g^{(1)}(i), \tag{V.6}$$

$$G^{(2)}(i,j) = \mathrm{tr}[\rho^{(2)}(i,j) \ln \rho^{(2)}(i,j)] = g^{(1)}(i) + g^{(1)}(j) + g^{(2)}(i,j), \tag{V.7}$$

$$\begin{aligned} G^{(3)}(i,j,k) &= \mathrm{tr}[\rho^{(3)}(i,j,k) \ln \rho^{(3)}(i,j,k)] \\ &= g^{(1)}(i) + g^{(1)}(j) + g^{(1)}(k) + g^{(2)}(i,j) + g^{(2)}(i,k) + g^{(2)}(j,k) + g^{(3)}(i,j,k), \end{aligned} \tag{V.8}$$

et, ainsi de suite. On peut maintenant utiliser ces fonctions pour effectuer une expansion des cumulants de l'énergie libre. L'équation V.3 devient dans ce cas :

$$F(\rho) = \mathrm{tr}[H\rho] + k_B T \left[\sum_i g^{(1)}(i) + \sum_{i<j} g^{(2)}(i,j) + \sum_{i<j<k} g^{(3)}(i,j,k) + \ldots + g^{(N)}(1,2,\ldots,N) \right] \tag{V.9}$$

où N est le nombre total de degrés de liberté du système. Notons qu'aucune approximation n'a encore été effectuée. L'intérêt de cette transformation devient évident lorsqu'on étudie d'un peu plus près les propriétés des cumulants. Considérons, par exemple, $g^{(2)}(i,j)$; à partir des équations V.6 et V.7, on obtient :

$$g^{(2)}(i,j) = \mathrm{tr}[\rho^{(2)}(i,j) \ln \rho^{(2)}(i,j)] - \mathrm{tr}[\rho^{(1)}(i) \ln \rho^{(1)}(i)] - \mathrm{tr}[\rho^{(1)}(j) \ln \rho^{(1)}(j)]. \tag{V.10}$$

Or, supposons que les sites i et j sont suffisamment éloignés pour que leurs états ne soient pas significativement corrélés ; on a alors :

$$\rho^{(2)}(i,j) \simeq \rho^{(1)}(i)\rho^{(1)}(j), \tag{V.11}$$

et, par conséquent :

$$g^{(2)}(i,j) \simeq 0. \tag{V.12}$$

Toutes les fonctions de cumulant partagent cette propriété d'être nulle pour des degrés de liberté non-corrélés. C'est ici qu'intervient la CVM. Cette dernière procure un protocole pour tronquer, de manière rigoureuse, l'équation V.9. Pour obtenir une fonctionnelle approximative, on procède comme suit :

1. On choisit une matrice de densité réduite comme base de notre approximation. Notons qu'il ne s'agit pas seulement de spécifier un ordre, mais aussi de spécifier les relations entre les degrés de liberté représentés par la matrice. Par exemple, on peut choisir $\rho^{(3)}(i,j,k)$ avec i,j,k formant un triplet de sites du réseau mutuellement voisins. Ce choix définit *l'amas parent* de notre expansion ; ici un triangle de premiers voisins. On préfère habituellement des amas compacts, puisque les corrélations devraient être plus fortes à courte portée.
2. On identifie toutes les fonctions de cumulant associées à l'amas parent à l'aide des définitions des fonctions d'amas. Dans notre exemple, on devrait conserver les fonctions de cumulant d'ordre 1, d'ordre 2 correspondant à des paires de voisins, et d'ordre trois correspondant à des triplets de voisins. Les amas associés à ces cumulants sont les *sous-amas*.
3. On tronque l'équation V.9 en gardant seulement les fonctions de cumulant correspondant aux sous-amas.
4. On détermine la forme finale de l'énergie libre en reformulant la version tronquée de l'équation V.9 en terme des fonctions d'amas ou, de manière équivalente, en terme des matrices de densité réduites.

Par exemple, si on choisit comme matrice de densité principale $\rho^{(1)}(i)$ (et donc comme amas parent un site isolé), et on suppose un Hamiltonien qui ne contient que des termes à deux corps entre premiers voisins, on obtient :

$$F = \sum_{\langle i,j \rangle} \mathrm{tr}[H_{i,j}\rho^{(1)}(i)\rho^{(1)}(j)] + k_B T \sum_i \mathrm{tr}[\rho^{(1)}(i)], \tag{V.13}$$

où $\langle i,j \rangle$ indique une paire de premiers voisins. Cette fonctionnelle correspond exactement à la fonctionnelle de Bragg-Williams (équation V.1).

De la même manière, si on choisi comme matrice de densité principale $\rho^{(2)}(i,j)$ avec i,j une paire de sites voisins, on obtient :

$$F = \frac{1}{2}\sum_{i,j} \mathrm{tr}[H_{i,j}\rho^{(2)}(i,j)] + k_B T \left[\sum_i (1-z)\mathrm{tr}[\rho^{(1)}(i)] + \sum_{\langle i,j \rangle} \mathrm{tr}[\rho^{(2)}(i,j)\ln \rho^{(2)}(i,j)]\right], \quad \text{(V.14)}$$

avec z le nombre de premiers voisins. Cette dernière équation est aussi connue sous le nom d'approximation de Bethe. De la même manière, on peut utiliser la CVM pour générer toute une série d'approximations d'ordre croissant en choisissant des amas parents de plus en plus gros et en incorporant, par le fait même, l'influence des corrélations à plus grande portée.

Par contre, l'objectif fixé en début de section n'est pas encore totalement atteint. En effet, ces fonctionnelles améliorées ne sont pas uniquement fonction des $\{\rho^{(1)}(i)\}$ (ou encore, de manière équivalente, des $\{p_i^\alpha\}$) mais aussi des matrices de densité d'ordre supérieur qui, elles, sont inconnues. La fonctionnelle recherchée est plutôt de la forme,

$$F(\{\rho^{(1)}\}) = \min_{\{\rho^{(2)}\},\{\rho^{(3)}\},\ldots} F(\{\rho^{(1)}\},\{\rho^{(2)}\},\{\rho^{(3)}\},\ldots). \quad \text{(V.15)}$$

Dans certains cas simples, il est possible d'effectuer la minimisation de manière analytique. Par contre, cette approche devient rapidement très complexe dû aux nombreuses contraintes imposées par les différentes relations de réduction (équation V.4). On peut alors avoir recours à la *natural iteration method* [39] ou simplement à une méthode plus traditionnelle en reformulant le problème contraint à l'aide de multiplicateurs de Lagrange. On peut aussi simplement paramétrer une fonctionnelle à l'aide de la CVM, puis ensuite l'utiliser lors des calculs TDDFT. L'avantage de cette dernière approche est qu'on peut alors concevoir d'utiliser un Hamiltonien *ab initio* en conjonction avec la CVM par l'entremise d'une procédure de type

cluster expansion [12].

V.2 Traitement de l'élasticité

Tel que mentionné au chapitre 4, notre traitement de l'élasticité en champ moyen implique qu'un même champ de déplacement $\mathbf{r} = \{r_i\}$ est utilisé autant pour calculer l'énergie moyenne d'un atome de type A que celle d'un atome de type B à un site donné. Bien que nous ayons montré aux chapitres 5 et 6 que cette approximation permet à la TDDFT de bien reproduire ce qui est attendu sur la base des calculs QCM, la situation pourrait être améliorée. Malheureusement, contrairement au cas des fonctionnelles d'énergie libre, nous ne connaissons pas de manière systématique d'alléger l'approximation utilisée pour traiter l'élasticité.

On peut quand même concevoir quelques modifications simples qui amélioreraient la qualité de l'approximation. À cet effet, nous proposons une stratégie en deux étapes, soient : i) permettre une relaxation indépendante des atomes A et B et ii) tenir compte l'effet de la relaxation locale. La première étape peut être implémentée simplement en utilisant des champs de déplacement distincts pour les différents types d'atomes. Dans ce cas, le potentiel interatomique original :

$$V_{i,j}^{\alpha,\beta} = k^{\alpha,\beta}(|\vec{r}_i - \vec{r}_j| - \sigma^{\alpha,\beta})^2 - \epsilon^{\alpha,\beta}, \tag{V.16}$$

devient simplement

$$V_{i,j}^{\alpha,\beta} = k^{\alpha,\beta}(|\vec{r_i^{\alpha}} - \vec{r_j^{\beta}}| - \sigma^{\alpha,\beta})^2 - \epsilon^{\alpha,\beta}. \tag{V.17}$$

et l'équilibre élastique est atteint en minimisant maintenant $\mathbf{r} = \{r_i^{\alpha}\}$. Cette modification permet un meilleur traitement des configurations fortement asymétriques, comme les interfaces, où les deux types d'atomes sont susceptibles d'occuper des positions moyennes assez différentes.

La deuxième étape consiste à tenir compte, de manière effective, de l'effet de la relaxation locale. Cet effet est particulièrement important lorsqu'un type d'atome se trouve minoritaire dans un environnement donné. En guise d'illustration, considérons un site i situé dans une matrice où $p^A = 0.99$. Dans ce cas, l'approximation

de champ moyen sera très adéquate pour décrire l'énergie élastique moyenne d'un atome A placé au site i. Par contre, si $\sigma^{A,B} \neq \sigma^{A,A}$, l'énergie élastique d'un atome B au site i sera surestimée par la même approximation puisqu'en réalité l'atome B devrait repousser ($\sigma^{A,B} > \sigma^{A,A}$) ou attirer ($\sigma^{A,B} < \sigma^{A,A}$) les atomes A voisins dans le but de minimiser l'énergie. Ceci est lié au fait que le traitement en champ moyen approxime bien l'énergie des configurations les plus probables (qui ne comportent pas d'atome B au site i) mais commet une erreur plus importante sur les configurations improbables. Au premier ordre, cet effet pourrait être partiellement corrigé par l'ajout de termes à un corps à l'Hamiltonien. Ces termes, fonction des p^{α} à chaque site (pris comme représentatif de l'environnement immédiat), pourraient être facilement paramétrés à partir de simples calculs d'énergie élastique. Bien sûr, on pourrait utiliser des termes plus complexes pour rendre compte de l'environnement local de manière plus raffinée.